The Construction and Testing of a Multi-mode Scanning Confocal and Atomic Force Microscope

Russell Edward Vanhouse

July 2020

A thesis submitted for the degree of
Doctor of Philosophy

School of Physics and Astronomy
University of Nottingham
Nottingham, NG7 2RD

Abstract

At the University of Nottingham, two research groups fabricate atom chips and hexagonal boron-nitride (h-BN) devices. These prototypes require characterisation to provide information about their functionality to the researchers. Electroluminescence and photoluminescence data is required of h-BN devices, atom chips and spintronic devices require measurement of their magnetic field strength.

An instrument capable of performing this would be similar in design to a nitrogen-vacancy (NV^-) magnetometer. The requirements of this instrument that differ from others are that it should accept larger samples, scan over a larger range, function in ambient conditions and be highly flexible with regards to the types of measurements it can perform.

The aim of my studies was to construct such an instrument, capable of imaging the surface of samples whilst measuring reflectance, photoluminescent and electroluminescent emission and measuring the surface topography with an AFM probe, whilst probing the sample with microwaves and a DC magnetic field. The resultant instrument should also be suitable to convert into an NV^- magnetometer.

This thesis describes the equipment selected and the construction. Functionality is demonstrated by performing tests on samples of nanodiamonds and h-BN devices. The tests provide information about the electroluminescent and photoluminescent properties of these devices which has added to the understanding of how they work.

A photoluminescence source was located on one h-BN device, coupled with the knowledge of how it was fabricated, this demonstrates that photoluminescence is also observed in samples of very high purity. Electroluminescence was detected and located on a different device, the instrument confirmed the origin of the emission, in a region of overlap between two thin flakes of h-BN. It also showed that heat generated by the tunnelling current caused deformation of the layers, resulting in a bulge on the surface.

The instrument investigated thin flakes of h-BN, to use the information in conjunction with data taken with an imaging ellipsometer. This ellipsometer is unique in its ability to probe samples with 6.5 eV photons, it is used to measure h-BN at and above its band gap. A model is fitted to the data, which gives the refractive indices of h-BN. The results indicate a birefringence of $\Delta n=2.2$ at 6 eV, making h-BN one of the most birefringent materials recorded.

To summarise, the instrument has been proven to be functional and flexible. It is suitable to be used as an NV^- magnetometer when an appropriate nanodiamond is located and it has provided information on the h-BN devices and aided in the discovery of new information about h-BN as a material.

Acknowledgements

My PhD research experience has been quite extraordinary. It has been challenging, rewarding and highly educational in many ways, there have been many memorable moments and I have changed a great deal since the start. It is an experience I will always cherish and look fondly back on.

From the moment that I decided to apply, all the way through my studies, my parents, Graham and Sheila, have supported me and offered love, advice and encouragement at every opportunity. My sister and grandmothers were there alongside them throughout providing me with a stable bedrock on which to build. Grandmama's motivational speeches were always welcome and never fell on deaf ears!

Thanks, of course, must go to my supervisor Dr Chris Mellor, the mastermind behind this project, whose endless knowledge on the subject (and on a great many more subjects) we could not have done without. Thank you for the guidance and for the many hours of proofreading.

Ashley Tyler's hard work in the lab brought progress on in leaps and bounds, he arrived at exactly the right time. His company in the lab was most welcome and entertaining, hours spent struggling are not as grim when there are two of you in the thick of it.

My thanks also go to the various members of Cripps Hall SCR over the years, who provided laughter at mealtimes and occasionally even a thought-provoking conversation! The time spent tutoring with them taught me many things, put me in many different situations, and introduced me to such a diverse group of people, the likes of whom I would be otherwise very unlikely to meet, and I am much improved for it.

In particular, I would like my friend Sayantan, who has been there from the start. He inspires me to be cleverer, faster, fitter, stronger and most of all, to self motivate and to work harder. Thank you for the support, the sounding board, the conversations, the breakfast and the coffee, and most of all for introducing me to the gym. Look how far we have come, and how far we can yet go.

Végül, köszönöm a páromnak. Köszönöm a segitséget és a stabilitást, a szerelmet és a megnyugtatást. Veled fényessebb a világ és boldogabb az életem. Köszönöm a kedves családodnak is, hogy mindig befogadóak velem, mostanság úgy érzem hogy már a családod része vagyok. Köszönöm az utazásokat és a jó vidámságot a népköztársaságban, kívánom, hogy legyen még sok közös szép nyáralásunk. Köszi Zsóf.

Contents

Chapter 1

Introduction

This project was funded by the UK National Quantum Technologies Programme (referred to as the National Quantum Technology Hub for Sensing and Metrology, or simply the QT Hub). The Hub is a group of departments from Universities of Birmingham, Glasgow, Nottingham, Southampton, Strathclyde and Sussex. The long term ambition of this consortium is to find practical applications for ultra-cold atoms experiments.

The Ultra-cold atoms group in the University of Nottingham focuses on the design and production of measuring devices which allow measurements to be performed at far greater precision than using classical techniques.

It is currently possible to create the experimental setups to cool atoms and make measurements on a lab-sized scale. In order to make more practical quantum sensors however, it is important to make the atom cooling devices far smaller in order for them to be portable. At Nottingham, techniques are being developed to create miniature versions of the optical and magnetic components of the cooling setup, with the devices contained on one 4 cm^2 chip. The fabrication of these microfabricated chips is not only tricky, but it is also time-consuming, and characterising performance is also difficult outside of the cold atom experiment itself.

The goal of this project is to design and build an instrument which will measure the microfabricated atom chips built within the department. It will scan the surface of the chip to observe the topography, whilst simultaneously measuring the strength and direction of the magnetic field generated by the chip using defects in nanodiamonds known as NV-centres. After only several hours of scanning, the required information will be obtained and can be immediately fed back to the chip microfabrication team, greatly improving the efficiency of the process.

The functionality of measuring small magnetic fields above a surface with high spatial precision would also be useful for investigating spintronics devices in order to investigate their magnetic characteristics. The spintronics group at the University of Nottingham has expressed interest in using such an instrument to map the magnetic domains of antiferromagnetic materials [1].

In projects of this nature, where the instrument takes several years to design and build, the goal can become slightly fluid as designs are adapted and equipment or samples vary over the course of the research. In my final year of this project, we began a collaboration with Professor Beton's group who were making devices from exfoliated flakes of hexagonal boron nitride (h-BN). In the initial stages of fabrication of the devices, it was noticed that the pure layers of h-BN emitted light when a current was passed through the flake (i.e. it displays electroluminescence), an unexpected result. The mechanism behind this is unknown and whilst Prof. Beton's group were able to use a spectrometer to identify the wavelengths emitted, the NV magnetometer was ideal to identify the precise location of emission. For this reason, we extended the measurement capabilities of the NV-magnetometer to include electroluminescence.

The resultant instrument is a multipurpose measuring device which has Atomic Force Microscopy (AFM) imaging capabilities as well as a confocal microscope with constituent parts working interchangeably with each other, allowing a study of both NV^- centres in nano-diamonds, as well as an investigation into the behaviour and properties of h-BN.

For clarity, from hereon in the combined AFM / confocal microscope being described in this thesis shall be referred to as "the instrument".

The thesis will progress as follows. The motivation for the construction of this instrument is explained before the physical construction process is described. This begins with the theory, construction and testing of the AFM. Then the theory behind confocal microscopy, the integration of the setup into the AFM and testing. Followed by NV-magnetometer theory and how the setup is modified and added to in order to allow magnetometry using NV^- defect. Experiments on nanodiamonds are described and discussed with a view to converting the system to perform magnetometry. The theory of h-BN is reviewed and the instrument is used to investigate luminescent properties of h-BN devices as well as imaging the surface of the devices. The ellipsometer is then used to perform further study on h-BN in general before our instrument is used to investigate these flakes of h-BN. A conclusion and ideas for future investigation will form the end of the thesis.

1.1 Statement of contributions

I started my research and the construction of this machine in October 2015. In October 2016 a second postgraduate student, Ashley Tyler, joined the project. I had already begun the process of setting up the AFM so he began designing the confocal microscope, the construction of the optics was very much a joint effort. Later on, he focused on making Qudi produce output signals via a National Instruments DAC card whilst I focused on procedures required to make the different elements work together. The h-BN devices and flake samples were fabricated and kindly provided by Dr James Kerfoot. All data presented is my own unless otherwise stated.

Chapter 2

Motivation

The purpose of this instrument is to provide a method of collecting pertinent and useful information about atom chips, hexagonal boron nitride structures or other samples, with similar properties, that we choose to image.

2.1 Miniaturisation of cold atoms devices

The motivation behind the atom chips is to miniaturise existing cold atoms machines and add greater functionality [2]. Miniaturising a system from the size of an optical bench to the size of an atom chip would allow an array of such systems to be used in conjunction with one another to provide directional and positional information of the quantity being measured e.g. gravity sensors could be used together to make a gravity gradiometer [3]. Atom chips have the potential to perform the optical tasks as well as the magnetic ones required in cooling and trapping atoms, they can generate the appropriate magnetic fields as well as split laser beams and guide them in the right directions. The only additional requirements to the final atom chip product would be an external power supply, a light source and an ultra-high vacuum environment; everything else would be contained, solid-state on the chip [4] [5].

The development of these chips and the microfabrication processes require reliable and comprehensive ways of imaging the chip and examining its properties. The developers must receive feedback on the physical size of the features they are growing e.g. has the correct thickness of metal been deposited as expected, are the edges of the features smooth or has the fabrication process led to some roughness around the edges and finally do the wires function correctly? The wires on an atom chip are designed to produce a magnetic trapping field; so the current density along the wire, via the measurement of the generated magnetic field, should be measured and fed-back to the developers.

One can test these chips by attempting to use them for their intended purpose, trapping atoms and seeing the potential well generated by the wires. However, this requires insertion into an ultra-high vacuum chamber and performing a cold atoms experiment that even with ideally functioning equipment can take several weeks. It would, therefore, be highly advantageous to test these chips in ambient conditions, which would make the process significantly faster as well as provide highly precise spatial and magnetic information about the chip.

Once the magnetic fields have been imaged the current densities producing them can be inferred using reconstruction algorithms [6]. This can provide more information on how well the growth of the gold wires occurred and information on the homogeneity of the evaporated metal.

2.2 Spintronics devices

The spintronics group at the University of Nottingham is focused on producing antiferromagnetic devices with a long term view to investigating their use in commercially viable items, particularly as a replacement for current computer memory devices. The ability to manipulate the magnetic spin would allow the storage of data, with much faster theoretical read/write speeds than traditional capacitor-based memory [1]. Once a device has been manufactured, an instrument such as ours would provide detailed information on the shape of the magnetic domains, the behaviour at the interface of neighbouring domains, and information on physical structure and shape of the device. Spintronic materials such as copper manganese arsenide (CuMnAs) have antiferromagnetic domains which are submicron in size and have weak magnetic field strengths. This means that any instrument capable of measuring them must have a high spatial resolution as well as high magnetic sensitivity.

2.3 h-BN

The hexagonal boron nitride devices being made in Nottingham, are designed to hold molecules which would emit light when a voltage is applied and a current is passed [7]. h-BN is a wide bandgap semiconductor (bandgap $= 6eV$) and there is great interest in using this type of material, to form ultra-violet emitting diodes with much higher efficiency than is currently possible. Doped h-BN layers are expected to have improved quantum efficiency compared to silicon-based LEDs, and this would reduce the energy converted into waste heat [8] making it an attractive prospect for future research due to the potential commercial viability of such devices.

In order to develop devices such as this, which still have a very experimental build process and by which a great variety of device structures are produced, it is important to be able to inspect both the physical properties of the device as well as those of the light emitted from the device. In the case of these devices which produce light by an unknown mechanism, the location of emission and being able to place that on a physical map of the device is of great interest.

Some samples of hexagonal boron nitride are known to fluoresce when probed with green light [9], it would also be of interest to know whether this occurs at the same location as the electroluminescence.

The instrument is therefore required to scan across the sample and build up a map of data. It should be able to produce a visible-light image of the sample, a photo-luminescence map and an electroluminescence map. As our instrument is built around an AFM it will also be able to generate a surface topography map of the h-BN sample. All of these maps can then be overlaid to allow for a clear comparison and to create a fuller image of the properties of the device.

2.4 2-D materials

Magnetic field measurements above the surface of 2-D conducting materials such as graphene [10], and above 2-D semiconductors such as h-BN flakes, can also be inserted into the current reconstruction algorithm [6]. This could provide further information about how the current flows through these 2-D materials, and/or on the internal structure of them. This is a method which has not been extensively explored thus far.

2.4.1 EP4 Ellipsometer

The arrival of an Accurion EP4 imaging ellipsometer provided the opportunity for further investigation of the h-BN samples. Mono-layer or multi-layer samples created with different methods by different groups do not necessarily have the same properties. This ellipsometer is able to produce probe light down to a wavelength of 190 nm and therefore can probe the 6 eV (206 nm) bandgap of h-BN. This will provide information about the dielectric function, including the birefringence in these particular samples. Ellipsometry of h-BN at bandgap wavelengths has not been widely researched before, so this may provide useful information regarding the behaviour of the h-BN devices. In this thesis we study exfoliated h-BN flakes, these results can then be compared to the already known values of MBE grown h-BN samples [11].

2.5 Further uses

By design, our instrument has the capability to apply DC external magnetic fields and microwave frequency magnetic fields to samples. This is included specifically to image NV^- defects in nanodiamond samples, however, this can be applied to any sample to investigate microwave dependency of emission (ODMR/ESR) or indeed to investigate the magnetic response of a sample. The system is extremely flexible and capabilities can be turned off or removed as required, a small component can be added and it is also possible to provide an AC magnetic field of any frequency up to 20 GHz to the sample (the upper limit of our microwave generator).

2.6 Conclusion

The requirements at the beginning of the project led us to design and build an instrument with a wide array of different imaging capabilities, allowing fast consecutive measurements in each mode and as each imaging method operates over the same area of the sample, the data is directly comparable.

Most of the samples we shall measure are opaque, the instrument must therefore probe, detect and perform AFM from the same side of the sample. There must be a range of motion of tens of µm in all three axes in order to measure the wires on an atom chip and the field strength at trapping height above the chip whilst retaining lateral resolution in the 10 nm range. Magnetic field sensitivity should be in the region of 100 µT to be able to see the fields generated by atom chips to sufficient resolution, meaning that resolution of applied microwave field should be as high as possible, and the coupling of the field to the NV defect should be optimised for maximum contrast. Fast measurement speed is viewed as an added bonus, however, the time taken to perform the alternative method of testing atom chips is on the order of weeks, this instrument is expected to complete the entire range of different measurements in less than one day.

The following thesis describes the construction and testing of the atomic force microscope, then the confocal microscope, and then the first attempts to bring all the parts together to make an NV^- magnetometer. The tests on nanodiamonds and h-BN sample will be demonstrated and evaluated.

Chapter 3

Atomic Force Microscope

The NV^- magnetometer instrument is based upon an Atomic Force Microscope (AFM). In this section, the theory of how AFMs function will be explained followed by a literature review of other AFMs used in NV^- magnetometry as well as some AFMs that represent the peak of modern scanning ability. The construction of our AFM will be described along with the methods of operation before it is compared to some of those covered in the literature review. Characterisation of the AFM will then be performed using standard calibration samples as well as the derivation of some important values including the free space amplitude of oscillation of the probe.

3.1 Theory

Intermittent contact and frequency modulation Atomic Force Microscopy (AFM) are methods of imaging the surface of a sample with a spatial resolution much higher than that of visual light microscopy. The probing of the sample is performed by a sharp tip on the end of an oscillating cantilever (excited by a small piezo-actuator) and as the tip comes into contact with the sample, the height of the surface at that location is recorded. The tip interacts with the sample through a variety of forces. As the electrons on the outside of the tip approach the electrons of the sample, short distance repulsive forces are felt by the tip[12]. Van der Waal's (temporary dipole induced dipole) forces cause the tip to be pulled towards the surface. When the tip approaches the sample from afar, covalent forces attract the tip to the surface as the electrons attempt to form covalent bonds[12]. If the sample is measured in air, then a thin water layer will form on the surface and so capillary action will also cause an attractive force, pulling the tip towards the sample[12]. This causes hysteresis in the displacement of the tip as it is approached and retracted. These forces act at the same time and affect the motion of the tip and cantilever. The overall interaction is displayed in Fig.3.1.

A sharp tip is used to probe the sample, sharp enough that ideally, only one atom is interacting with the surface of the sample in order to maximise spatial resolution. This tip is attached to a cantilever which is then oscillated above the sample, moving the tip vertically towards and away from the surface. The cantilever has a resonant frequency, f_0, and a quality factor, Q.

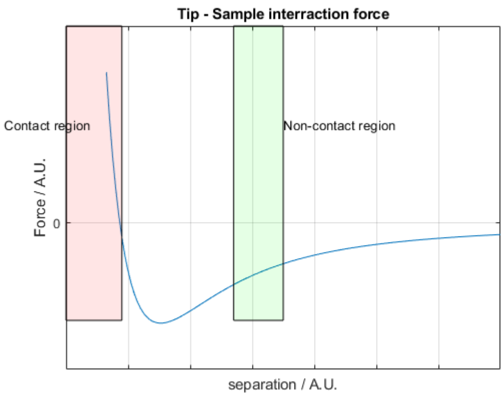

Figure 3.1: Diagram showing the interaction force between the AFM tip and the sample surface vs separation distance.

For small oscillation amplitudes, as the tip approaches the sample, the cantilever oscillation is sensitive to the force gradients and to extra dissipation of energy into the sample. The force gradients cause oscillation frequency shifts, and the dissipation decreases the Q-factor, decreasing the oscillation amplitude of a cantilever driven with a constant drive force.

Initially, on approach, the resonant frequency of the cantilever decreases as attractive force gradients dominate. When moved even closer, the repulsive forces between the tip and the sample dominate, increasing the resonant frequency. For a given drive amplitude, the oscillation amplitude is greatest at the resonant frequency, so a shift away from resonant frequency will decrease the oscillation amplitude of the tip. In general, Pauli repulsion forces, the strong repulsive interaction between atomic orbitals, dominate over very smallest separations. At several Å, attractive van der Waal's and capillary forces dominate, the resultant potential of these force acting together is known as the Lennard-Jones potential[13].

The equation of motion of the tip of the cantilever can, for small oscillations, be modelled as a driven, damped, simple harmonic oscillator,

$$\ddot{z} = \frac{F(z)}{m} + \frac{F(t)}{m} - \frac{c}{m}\dot{z} - \frac{k}{m}z \tag{3.1}$$

where $\dot{z}$ and $\ddot{z}$ represent the first and second time derivatives of displacement, F is the force exerted by the interaction between the tip and the sample, $F(t)$ is the driving force, typically a sinusoidal function, c is the coefficient of damping, k is the effective stiffness of the cantilever and m is the effective mass of the cantilever.

Rearranging for F and differentiating with respect to z gives,

$$\frac{dF}{dz} = k \tag{3.2}$$

where,

$$k = k_0 + k_{ts} \tag{3.3}$$

k_0 being the stiffness of the cantilever and k_{ts} is the change in stiffness due to the tip-sample interaction. k_{ts} is given by

$$k_{ts} = \frac{-\partial F_{ts}}{\partial z} = \frac{\partial^2 V_{ts}}{\partial z^2} \tag{3.4}$$

For oscillation amplitudes, over which the force gradient, k_{ts}, is constant,

$$\omega = \sqrt{\frac{k}{m}} \tag{3.5}$$

where ω is given by

$$\omega = \omega_0 + \delta\omega \tag{3.6}$$

can be used to infer (using the Taylor expansion approximation for a square root) that

$$\Delta f = \frac{f_0}{2k_0} k_{ts} \tag{3.7}$$

where f_0 is the resonant frequency. As tip-sample separation varies, so does the natural resonance of the cantilever, this shows that the change in resonant frequency,

$$\Delta f \propto \frac{dF}{dz} \tag{3.8}$$

i.e. the oscillation frequency shift is proportional to the force potential experienced by the probe. This allows us to infer the force between the tip and the sample from frequency shift, and therefore to calculate the tip-sample separation from the force/separation graph [12].

AFMs use either the amplitude of oscillation or the frequency of oscillation as the control parameter for the height of the tip. When surface tip separation is constant, the frequency/amplitude will remain constant. When scanning a sample to measure the surface topography, a change in surface-tip separation will have an effect on the amplitude and frequency of oscillation. AFMs record either the shift in frequency/amplitude or alter the height of the tip in order to return the oscillation to the set value, recording the height change required to do this. This process is known as feedback and the mechanism for this is described in section 3.1.1. Imaging can be performed in constant height mode, where the tip is held at a constant z-position relative to the lab frame and change is recorded. This can be performed with the tip in contact with the surface (contact mode AFM), or oscillating above the surface (non-contact AFM, NC-AFM), and is used for extremely flat surfaces which produce very little cantilever deflection, or where very fast scanning is necessary [14]. Alternatively, frequency or amplitude locking can be performed, where the height is altered to negate the change in frequency or oscillation amplitude.

The most basic form of AFM imaging is known as contact mode where the tip is brought directly into contact with the sample, deep into the repulsive regime. As scanning occurs, either a constant deflection of the cantilever is maintained by adjusting the height, or the height is kept constant and the change in deflection is recorded. The downsides to this method include wearing of the tip and damage to the sample as capillary forces can cause the tip to snap to contact with the sample during approach. Problems can also occur when the sample is soft and the tip penetrates the surface, meaning the surface topography is not correctly recorded.

In ultra-high vacuum when measuring inorganic samples, dissipation is low and so Q is very high. This means the oscillation amplitude is slow to respond to changes in the force gradient or dissipation, meaning that it is hard to track the amplitude. For this reason, the resonant frequency of the cantilever, and changes in it, are tracked, whilst the excitation frequency is varied to match this using a feedback loop and a phase-locked loop (PLL) (also described in section 3.1.1), this is known as frequency modulated atomic force microscopy (FM-AFM). The cantilever is driven either with a constant excitation force, or a second feedback loop is used to maintain a constant oscillation amplitude.

To image a sample using the method described above, a parameter is chosen to be kept constant, usually the resonant frequency of the cantilever, and this is achieved by using a feedback loop to vary the height of the tip. This is, essentially, imaging the force gradients above the sample. Constant drive excitation is most commonly used as a second feedback loop can generate artefacts in the data.

NC-AFM can be performed in the repulsive regime or the attractive regime, depending on the tip-sample separation and the force gradient experienced by the tip. As the probe approaches the sample, it first experiences an attractive force to the surface, which decreases the resonant frequency. Moving past the attractive regime, the probe begins to experience a repulsive force which increases the resonant frequency. The effect of these regimes can be seen in Fig.3.2, displaying the frequency shift as the probe moves vertically above the sample surface. Operating in the attractive regime means the probe is less likely to collide with the surface, something which could cause damage to the probe and/or sample, however, this can be harder to control and is typically only used in UHV environments. The repulsive force can initiate a far larger frequency shift making the probe more sensitive to smaller changes in height. NC-AFM means that tip-sample forces are minimised, and the tip is less likely to sustain damage or collect debris from the sample. The probe is oscillated at the cantilever resonant frequency. For cantilevers with a very high Q-factor, or in a medium with very little resistance e.g. ultra-high vacuum (UHV), it takes more time to dissipate kinetic energy, therefore shifts in amplitude are slower to occur and slower to correct. Frequency shifts, on the other hand, occur faster with a higher Q and can be tracked faster. Factors like this can affect the potential speed of the scan. NC-AFM may also be defeated by a liquid layer forming on the surface of the sample.

In ambient conditions, there is significantly more dissipation into the air, resulting in a lower Q-factor. It is, however, still possible to perform the FM-AFM method despite this [15]. Measuring the force gradients is information which would not be achievable using the more commonly used (in ambient conditions) using an intermittent contact method.

The third imaging mode is known as intermittent contact mode or 'tapping mode', which operates in the attractive region for the top part of the cycle and the repulsive region of force at the bottom of the cycle. The cantilever is oscillated at

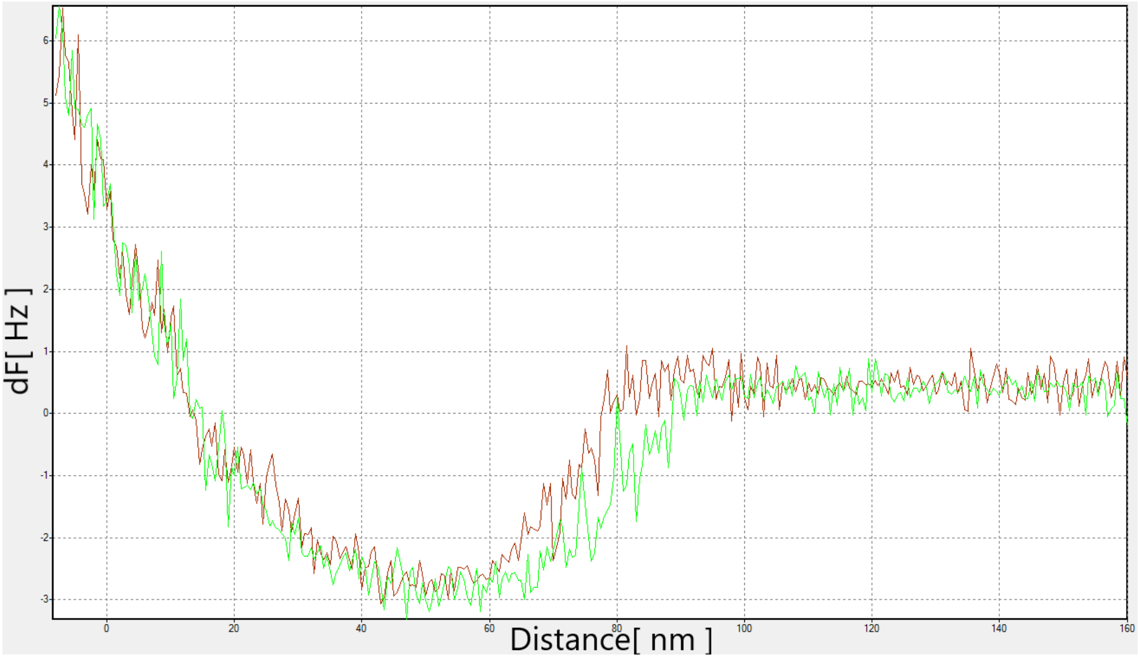

Figure 3.2: Graph showing how dF, resonant frequency shift, varies as the AFM probe is brought towards the surface. The red trace shows the approach, and the green the withdrawal. This nicely demonstrates that adhesive forces close to the sample keep pulling the tip in until it is stepped far enough back to escape this region of attraction.

a fixed drive frequency, typically ∼10% below the free space resonant frequency and with a fixed amplitude driving force. When it is brought towards the surface, the tip makes contact towards the bottom of the oscillation. The repulsive force from the sample surface increases the resonant frequency and more importantly reduces the amplitude of oscillation through dissipation. The resultant amplitude is measured and is maintained by adjusting the height of the cantilever as the height of the sample varies with scanning. The magnitude of the change in amplitude due to the tapping of the tip onto the surface is related to how much energy is dissipated by the probe hitting the surface. If a small amplitude drop is used as the locking parameter, then it is tapping more lightly and is less likely to drag along the surface or damage a softer sample material. Tapping mode, therefore, has elements of tip and sample preservation from NC-AFM and is able to penetrate any liquid layers to the actual upper surface of the sample like contact mode AFM. It is able to break the 'jump to contact' seen in contact mode with a soft cantilever in ambient conditions.

In most commercial AFMs the motion of the tip is measured by reflecting a laser beam off the back of the cantilever and observing the motion of the reflected spot. The laser beam reflected off the back of the cantilever is aimed onto the centre point of a quadrant photodiode with each of the quadrants receiving some proportion of the beam. The intensity seen by each diode allows the calculation of the position of the centre of the spot. Cantilever designs vary widely as there are many possible applications and different requirements for each of them. A cantilever designed for use in tapping mode will have a moderate stiffness to have sufficient kinetic energy to escape the adhesive force potential between the tip and the sample, and a high Q-factor for improved sensitivity. Low stiffness cantilevers are required to image biological samples in water, high stiffness is required to achieve atomic resolution in ultra-high vacuum. In frequency modulated AFM (FM-AFM) and tapping (amplitude modulated / AM-AFM) mode, oscillation frequencies tend to range from a few kHz to a few MHz [16] and oscillation amplitudes from 1nm to 10nm [17]. Cantilever stiffnesses are dependent on the dimensions of the cantilever as well as the material from which it is fabricated. Cantilevers designed for soft samples have low stiffness ∼80 $\mathrm{mNm^{-1}}$ and high scan speed cantilevers are the stiffest, typically > 80 $\mathrm{Nm^{-1}}$, cantilevers used for intermittent contact AFM typically have stiffness on the order of 1 $\mathrm{Nm^{-1}}$ [16]. The length of a cantilever tends to be between 3 µm and 100 µm and the radius of curvature of the probe tip from 30 nm to 10 nm for the highest lateral resolution.

3.1.1 Feedback loops

Of equal importance to the high quality cantilever/tip and the high precision 3-axis stages on which the sample is mounted, is the feedback loop which controls the measurement. A parameter, or several parameters, are chosen to be control parameters and the feedback loops adjust other parameters, e.g. frequency, amplitude, drive voltage, or height, and varies these in order to lock to the chosen value.

The phase relationship between the driving force and the oscillating cantilever can best be explained when the analogy is made, comparing the system to a mass on the end of a driven, vertical spring, a system which is to all intents and purposes, almost entirely undamped, similar to the AFM cantilever oscillating far from the surface. The motion of the mass can be compared to that of the centre of momentum of the cantilever, and therefore the end of the probe, and the driving force on the spring to that driving the AFM cantilever.

When driven significantly below resonant frequency, the spring compresses and extends a minimal amount. The driving head, attached to the spring, therefore, moves up and down in phase with the mass on the end of the spring. The phase difference between the displacement of these is 0°as the separation between the driver and the mass remains constant.

As the drive frequency is increased, the phase difference becomes non-zero and increases. When the driving force has frequency equal to the resonant frequency of the mass-spring system, the oscillation amplitude of the mass becomes large, many times larger than the drive amplitude, depending on the Q-factor of the spring, i.e. how quickly it dissipates the kinetic energy it receives from the driver. The phase difference between the driver and mass displacements at this point is 90°. The mass moves upwards through the centre as the driver reaches its top (retracted) position, and the mass reaches its top as the driver moves downwards through its middle position. The displacement of the mass always trails the displacement of the driver by $\frac{\pi}{2}$ of the cycle.

Increasing the drive frequency above resonance, the driver and mass displacements will reach 180°phase difference. The two move in opposite directions to each other and are out of phase.

Feedback loops work by measuring the current position and comparing it to a setpoint value. The difference between the present value and the setpoint, and the integral of the error with respect to time, decide the strength and direction of the signal which is sent back to the system to initiate movement towards the setpoint value(s).

In FM-AFM for instance, A phase-locked loop (PLL) locks to the phase of the oscillation by measuring the phase difference between the cantilever oscillation and the driving force. The drive frequency is delayed or advanced to maintain the 90°phase difference as the resonance of the cantilever changes due to changes in the force gradient caused by changing tip-sample separation. A PID feedback loop is used to adjust the tip-sample separation in order to keep the resonant frequency constant and a further feedback loop can be used to modulate the drive voltage if constant amplitude oscillation is required.

In AM-AFM, a feedback loop can be used to maintain a constant amplitude of oscillation of the cantilever. The cantilever is stepped away from or towards the sample in order to change the tip-sample force gradient, or to alter the damping and therefore to keep a constant amplitude.

Data from the feedback loop operation is recorded and this contributes to the sample topography data.

The PLL feedback loop operates about 10 × faster than the z control loop which maintains constant height to maintain a constant oscillation frequency and so a constant force gradient.

The most important component of a PLL is the phase detector or phase comparator. This is a piece of electronic circuitry which receives two input voltages, (in the case of the instrument described in this thesis) the current from the AFM probe representing the velocity of the tip, and the driving voltage driving the oscillation of the cantilever, and calculates the phase difference between the two. There are several slightly different methods by which the phase difference can be calculated, however, the simplest and most common, when the incoming signals are expected to be sinusoidal, is by using an analogue multiplier. This is a circuit, made up of several transistors, which receives the two input signals and produces an output signal proportional to the product of the inputs[18]. Taking the product of two sine waves, with a small phase difference, returns a constant voltage, proportional to the phase difference, and an oscillating sine wave voltage with the frequency being the sum of the frequencies of the inputs. The oscillating voltage is filtered out using a low pass filter, leaving the constant voltage, from which the phase difference is extracted.

The rest of the PLL contains a low pass filter, voltage amplifiers and the voltage controlled oscillator. The filter is used to filter out other frequencies and the voltage controlled oscillator to generate the oscillating voltage signal which will be sent to drive the cantilever.

In the AFM controller used in this project, the PLL is entirely digital; the incoming voltages are passed through analogue to digital converters (ADCs) before the software performs the function of the PLL.

The measured parameters are compared to the predefined setpoints, the difference between the two is known as the error, and feedback calculated based on three measurables: (i) proportional feedback, the difference between the setpoint

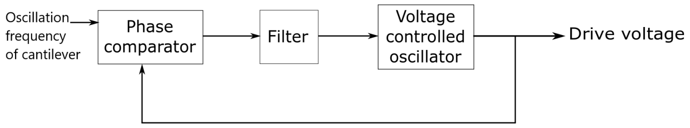

Figure 3.3: Simple diagram of a phase-locked loop. The reference signal is one input and the drive voltage is the other. The phase difference between the two is the output of the phase comparator.

and the current value, (ii) integral feedback, determined by integrating the size error over the time for which it has persisted, and (iii) derivative feedback, the rate at which the current value is moving away from the setpoint. Together the three are known as proportional-integral-derivative (PID) feedback.

For the AFM described in this project, the measured status can be the resonant frequency of oscillation, the amplitude of oscillation or the deflection of the cantilever. The feedback signal can be sent to a variety of effectors, altering the drive voltage, the drive frequency, the height of the probe or possibly other variables.

Typically, and in the case of the instrument described in this thesis, AFMs use only proportional and integral (PI) feedback [19]. Using derivative feedback loops tends to increase noise. The feedback loop is controlled by digital signal processing hardware, requiring low noise conversion of the analogue detected signal into digital form, and then the digital feedback into analogue signals.

In the case of tapping mode, the frequency is fixed at a value below the free space resonant frequency and the amplitude is used as the setpoint. The cantilever is first allowed to oscillate in free space at a pre-determined drive voltage, it will then have a fixed amplitude of oscillation which can be measured by the AFM. A target amplitude is then provided by the user and the tip-sample separation is decreased, causing the probe to tap the surface with increasing force until the amplitude is reduced to the setpoint value. If the tip-sample distance decreases, the oscillation is damped more and the amplitude of the cantilever oscillation decreases and the error signal to the feedback loop will cause the tip to withdraw resulting in an increase in amplitude, and vice versa for an increase in tip-sample separation.

In NC-AFM the frequency of oscillation is the primary set-point variable, often specified as an offset from the free space resonant frequency of the cantilever (typically -10 - $+10$ Hz). Once the setpoint is selected, the AFM controller uses the PLL to compare the phase of the incoming measured oscillation to that of a reference signal. The PLL demodulates the incoming signal and extracts the phase information. A diagram of a basic phase-locked loop can be seen in Fig.3.3. The PLL setpoint is defined as a particular phase between the signal and reference and it tracks the resonant frequency by keeping the phase constant [20]. The feedback loop then adjusts the tip-sample separation in order to keep the resonant frequency constant.

The AFM control hardware used in our instrument, and in the commercial AFM (Veeco Nanoscope V) in the lab use only proportional and integral feedback. Practically, for a flat sample, most of the feedback can be best performed with an integral feedback loop, especially for low scan speeds. For larger step sizes the

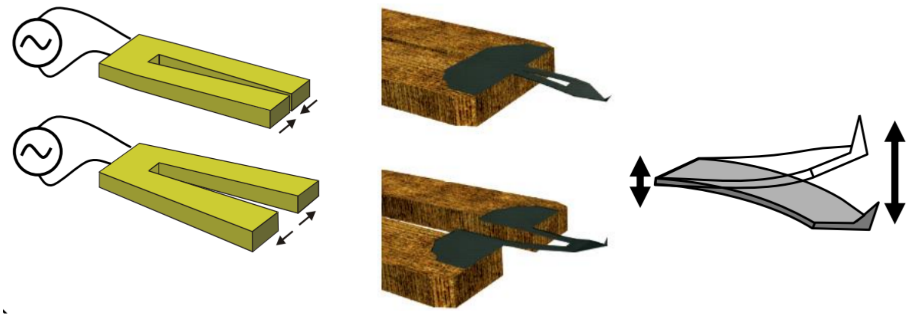

Figure 3.4: Primary vibrational mode of the Akiyama probe tuning fork and cantilever. It is possible to drive it at its first harmonic, but the returning current signal is extremely small.

proportional feedback is of much greater importance to ensure accurate tracking over large height steps.

3.1.2 Akiyama Probe

There are a large variety of probe types depending on the purpose for which they are required, however, the vast majority of them work by having a reflective upper surface to reflect a laser beam onto the quadrant photo-detector. In the case of the NV$^-$ magnetometer, the nano-diamond will be on the top side of the probe, and it is important that it is possible to collect all photons emitted from the NV$^-$ centre when a green laser is shone onto it. It is important that any laser used for beam reflection does not interfere with, or wash out, the red photons which will provide the magnetic field information and that the green laser does not interfere with cantilever beam deflection measurements.

A useful alternative, used in our instrument, is the Akiyama probe. This uses a quartz tuning fork as the actuator and sensor, and a tip on a silicon cantilever interacts with the sample surface, thus detecting the motion without the use of light which could interfere with the fluorescence. The probe tip has a radius of curvature of ∼15 nm providing excellent spatial resolution [21].

The primary vibrational mode of the quartz tuning fork is laterally, inwards and outwards, much like a musical tuning fork. The silicon cantilever is split in two and has two connection points, one on the end of each fork tine. As the tines move inwards and outwards, so do the connection points on the cantilever, this is visible in Fig.3.4, taken from the Akiyama probe guide [21]. Due to the surface shape of the cantilever and the attachment to the tuning fork, this is translated into a vertical up and down motion at the tip. This causes the probe to oscillate up and down with the same frequency as the tuning fork, albeit with a different amplitude.

The quartz tuning fork of an Akiyama probe is piezoelectric and therefore is the actuator in the system. The drive voltage is applied directly to the crystal via the metal contacts running along the surface, and the voltage causes stress and deformation of the crystal structure, generating the flexure. This directly results in the vertical movement of the probe tip.

The other tine of the tuning fork is electrically isolated from the first, but

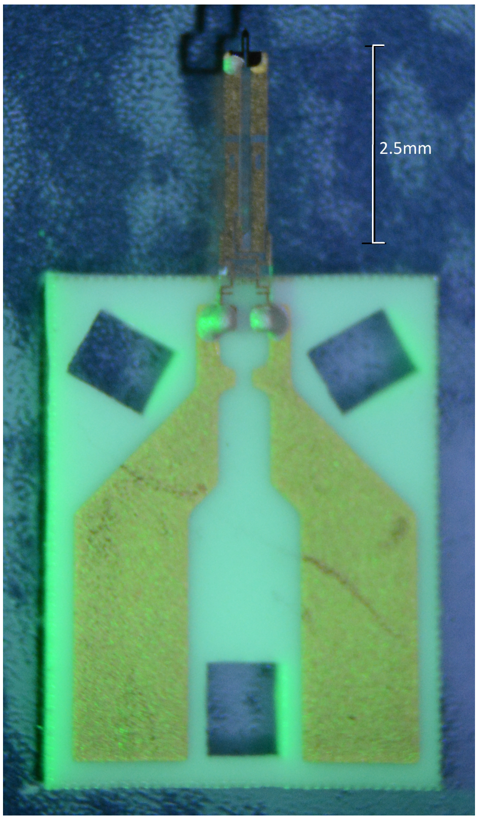

Figure 3.5: Optical microscope view of the Akiyama probe. The gold contacts are visible as is the tuning fork, the cantilever is at the top of the image on the end of the tuning fork. The tip of the probe is pointing upwards towards the camera.

this also is covered in a metal contact, which is the measurement connection to readout the motion of the probe. The piezoelectric effect in the quartz means that the movement of the crystal generates a current which can be detected and measured. The frequency and magnitude of the current directly relate to the frequency and velocity of oscillation.

As the output current from the second tine corresponds directly to the velocity of the tip, the current can be monitored to infer the displacement of the tip. Increased damping and therefore dissipation reduces the amplitude of oscillation. Changing effective stiffness of the cantilever, due to a change in force gradient, changes the resonant frequency of the cantilever. Both of these effects can be observed by measuring the output current from the second tine.

An Akiyama probe, visible in Fig.3.5, has the specifications displayed in Table 3.1 and its form can be seen in figure 3.5 (Close up images in figures 3.8 and 3.9).

The amplitude and phase response of one of our A-probes to a change in frequency is visible in Fig.3.6.

The frequency change of the oscillation of the Akiyama probe was measured with respect to displacement over a small region around the setpoint. The data is visible in Fig. 3.2. The non-contact region, where df < 0 Hz, is around 30 nm in size. This is significantly larger than other AFM cantilevers [12] and provides a far greater chance of successfully operating the AFM with the probe in the

Cantilever length	310 µm
Thickness	3.7 µm
Width	30 µm
Bulk resisitivity (n+ silicon)	(0.01 – 0.025 Ω.cm)
Tip radius	< 15 nm
Tip height	28 µm
Force constant (Si cantilever)	5 N/m
Resonance frequency	∼ 50 kHz

Table 3.1: Table displaying the typical physical characteristics of an Akiyama probe. Data from Nanosensors [21].

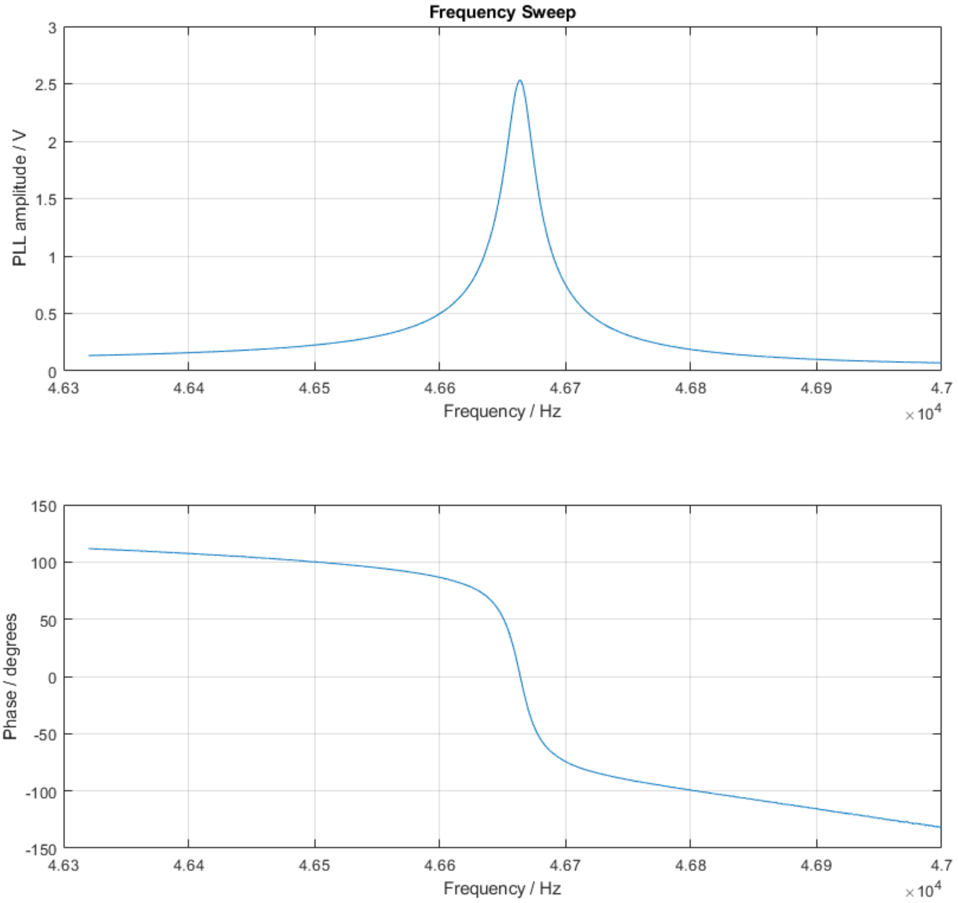

Figure 3.6: The top graph shows the amplitude of oscillation of the Akiyama probe vs drive frequency. The second plot shows the phase of the probe oscillation with reference to the drive signal. The zero degrees, in this case, is set to indicate where the driving force is $\pi/2$ ahead of the oscillation of the cantilever, i.e. the cantilever is being driven on resonance.

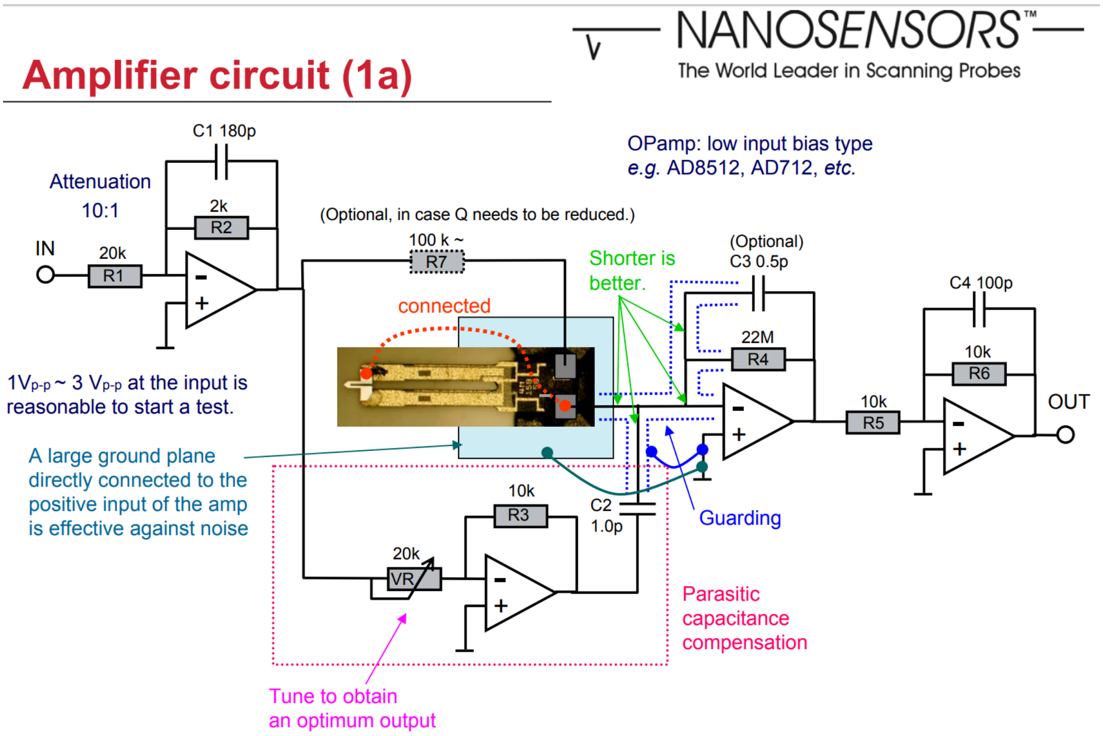

Figure 3.7: Circuit schematic of the preamplification circuits that accompany the Akiyama probe. Source: NanoSensors [21].

attractive regime. One possible reason for this extra-large non-contact region is that the cantilever oscillates with such large amplitude and possible as the Akiyama probe, a hybrid of a quartz tuning fork and silicon cantilever, has a higher Q-factor than a standard silicon cantilever. A higher Q broadens the non-contact regime (vs tip-sample separation) but reduces the magnitude of the ost negative value of dF [22]. The main difficulty with this regime is that there are two height values for a given negative frequency offset, meaning jumping between the two locations is likely to occur whilst scanning. In the case of the Akiyama probe, there is a much larger distance between two locations of equal frequency offset, meaning jumping between the two is less likely.

This method is significantly more compact than a beam deflection sensor. It requires the Akiyama probe and the ceramic plate to which it is attached to be clipped onto a printed circuit board visible in Fig.3.7. On the PCB are two pre-amplifiers, one which lowers the drive voltage to an appropriate level for the tuning fork without altering the waveform and another which amplifies the measured signal from the cantilever for processing in the controller. This frees up significant space around the probe and the sample, most of which will be occupied by the microscope objective lens which will be part of the confocal microscopy setup of this machine. The geometry of the Akiyama probe is designed in such a way that the probe extends away from the cantilever as well as down towards the sample, meaning that when viewed from above, the upper surface of the tip is visible. This is useful as on the final version of the NV-magnetometer, the nano-diamond will be attached close to the tip on the top surface of the probe, allowing emitted photons to be collected by the objective lens with greater efficiency. The

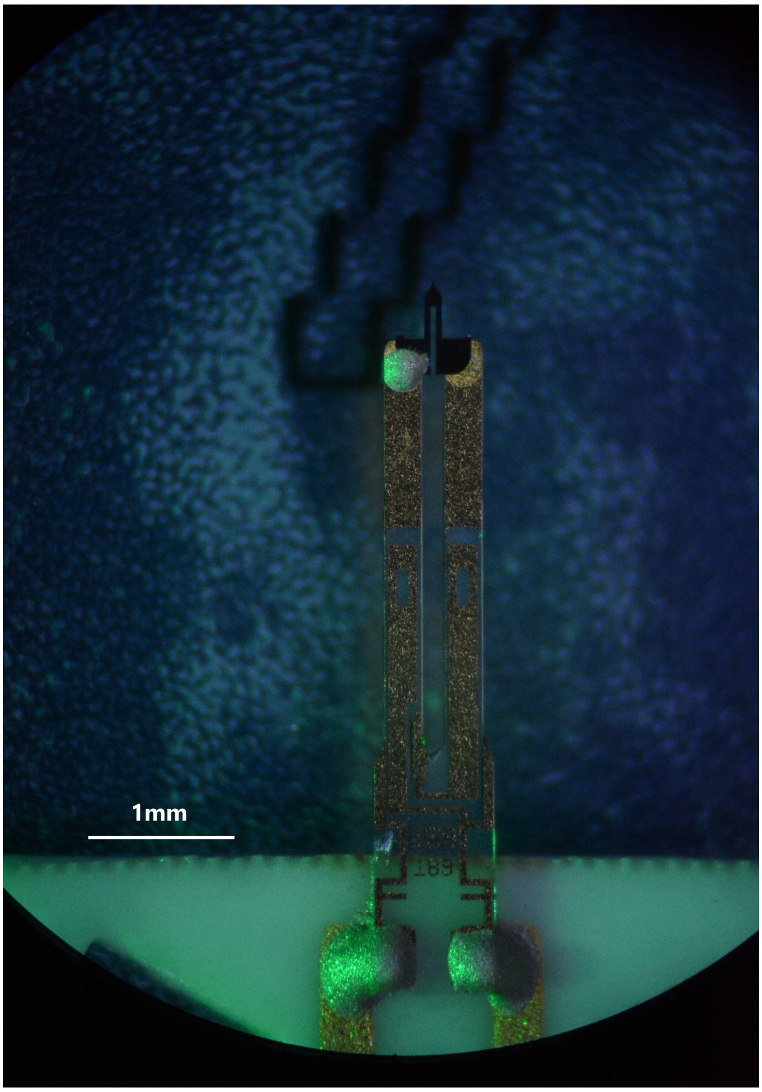

Figure 3.8: Magnified optical microscope view of the tuning fork and cantilever. Again, the probe tip is pointing towards the camera.

overriding reasons for using the Akiyama probe are its compact size providing room above the probe and the compatibility with fluorescence experiments [23].

3.2 Construction and Methods

We began the construction of the NV$^-$ magnetometer by building an AFM and then working around that. A combination of budget constraints, but mainly the need for exceptional flexibility meant that the AFM was constructed from separate components, rather than using a commercial AFM. An AFM can be largely boiled down to three fundamental parts: the tip/cantilever, three-axis motion to scan the sample and adjust tip-sample separation, and the feedback loops and control systems.

The AFM controller chosen was the RHK R9, a scanning-probe microscope controller, capable of driving an AFM or a scanning tunnelling microscope (STM).

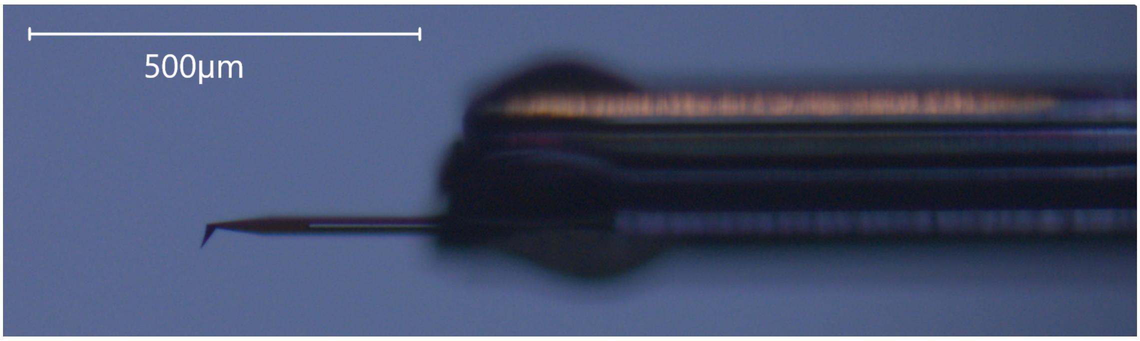

Figure 3.9: A side view of an Akiyama probe cantilever, viewed through an optical microscope. The AFM tip is visible at left-hand end of the cantilever, itself on the left-hand end of the tuning fork. The tip height is approx 30 μm and the radius of curvature of the tip is $\leq$ 15 nm.

RHK Technology is a Michigan based company which specialises in SPM instruments and other nano-scale applications. The R9 controller is capable of providing all of the control signals required for scanning, including the PLLs, probe drive, scanning signals and data collection. The instrument comes with its own proprietary software.

The software uses a system, referred to as an Iconic Hardware Description Language (IHDL), to describe the physical and electronic setup of the current system; in essence, every physical component, or group of electronics necessary for scanning. Physical connections are represented by solid lines and internal, electronic pathways within the control box are dotted lines. This method is intended to provide a simplified, user-friendly way to set-up the controller. It is in this software space that calibrations are provided for stages, to indicate what voltages should be applied and the physical distance to which this corresponds. It is also here where the feedback locking variable is specified, for instance, to change between tapping and non-contact mode AFM.

Within the IHDL is an area known as the procedure space, where protocols and algorithms can be created and named for automatic use during scanning or for the user to call as required. Again this has been executed with the intention of being user friendly, with block-based programming used instead of the usual written scripts.

Programmed into the procedure space is the capability for multi-pass imagining. This allows the user to set a number of repeat scans to be performed consecutively. It is possible to repeat the scan in normal measurement mode, however, more applicably to NV$^-$ magnetometry, the repeat measurements can be performed at different heights. Either by scanning at a fixed height relative to the surface which was just measured or by withdrawing the sample a fixed distance and scanning over a horizontal plane. In both of these cases, dF and PLL amplitude and other data are still collected, but this is particularly useful for magnetometry as the magnetic field measurements can be carried out over a volume above the sample.

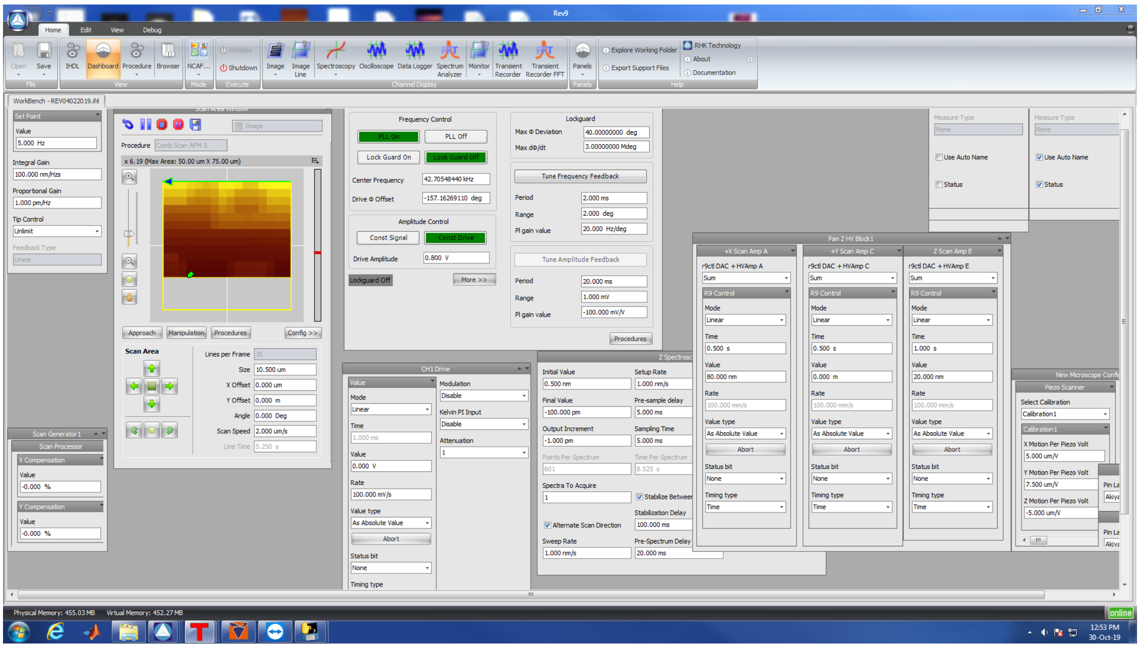

Value 5.000 Hz
Integral Gain 100.000 nm/Hzs
Proportional Gain 1.000 pm/Hz
Tip Control Unlimit
Size 10.500 um
X Offset 0.000 um
Y Offset 0.000 m
Angle 0.000 Deg
Scan Speed 2.000 um/s
Center Frequency 42.70548440 kHz
Drive Φ Offset -157.16269110 deg
Drive Amplitude 0.800 V
Max Φ Deviation 40.00000000 deg
Period 2.000 ms
Range 2.000 deg
PI gain value 20.000 Hz/deg

(a) Screenshot of the left-hand computer monitor displaying the RHK software controlling the AFM during a scan.

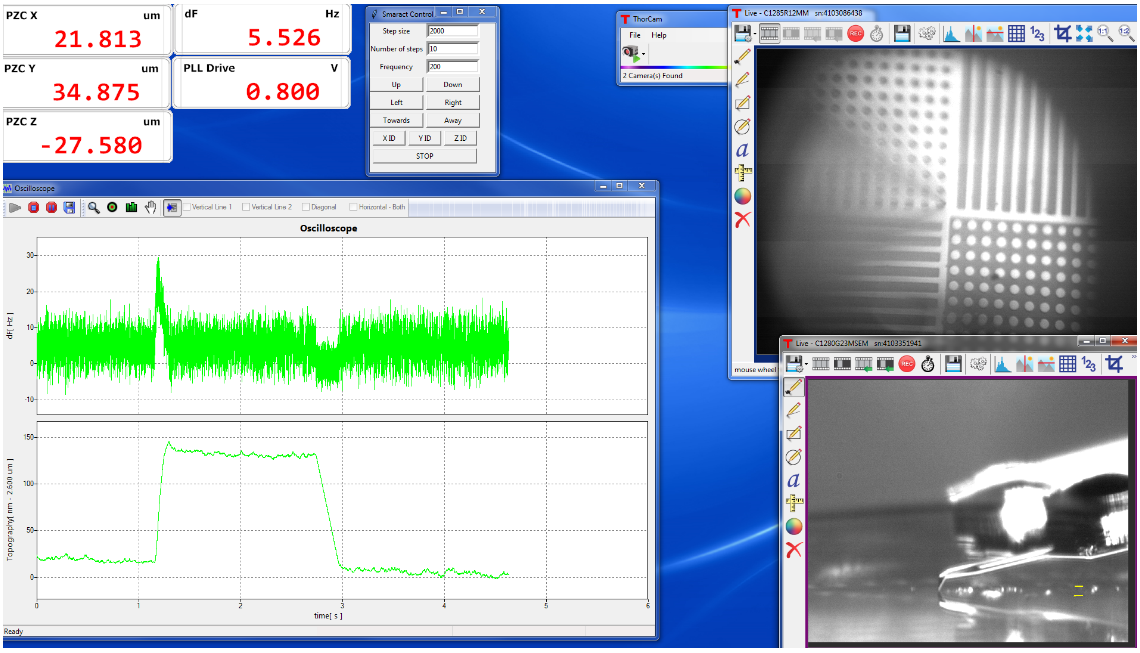

PZC X um 21.813
dF Hz 5.526
PZC Y um 34.875
PLL Drive V 0.800
PZC Z um -27.580
Step size 2000
Number of steps 10
Frequency 200

(b) Screen shot of the right-hand computer monitor (listed anti-clockwise from bottom left) is the oscilloscope plotting frequency shift and surface height vs time, a side view and a top-down camera view of the sample scanning, the SmarAct probe stage GUI, and information panels from the RHK displaying scanning stage positions, dF and PLL drive voltage.

Figure 3.10

3.2.1 Tip positioning

Whilst the tip is not moved during scanning, it has to be positioned in the centre of the objective lens whilst confocal microscopy is performed, withdrawn sufficiently far in order to remove or replace samples, and to be brought close to the sample in coarse approach before scanning begins. For this reason, the AFM cantilever and pre-amplifier are mounted onto a three-axis positioning stage manufactured by SmarAct. The stages chosen are three SLC-1720 Linear Piezo stages, mounted together to provide three axes of motion. They have a 12 mm range of motion and sub-nm resolution. These are also closed-loop stages and constantly measure their position to ensure accuracy. The motion is generated by piezo-electric slip-stick motors, which "shuffle" the stage around, this means that remaining stationary requires no voltage to be maintained. The stage setup can be seen in Fig.3.11.

The motion can be controlled by transistor-transistor logic (TTL) pulses, which could be provided from the R9. The downside of this is that a single pulse is required for every step, and the step size (and, therefore, the speed of motion) is not adjustable. Using an RS-232 cable from the PC allows the stage to be controlled by ASCII encoding. This method allows a request for a certain number of steps to be sent, along with step frequency and step size. This also allows an emergency stop button to be programmed into a user interface. As the tip never needs to move during scanning it is not necessary for this to be utilisable by the R9, and it is sufficient to have a graphical user interface (GUI), written in Python, for the operator to manually positioning the tip where required.

3.2.2 Sample scanning

In order for this AFM to be converted into an NV$^-$ magnetometer, it is required that the NV$^-$ defect and the AFM probe which will carry it, remain stationary in the centre of the microscope objective (MO) lens. The MO can move only along the z-axis and is fixed in x-y, therefore the sample will be scanned across underneath the stationary probe. In order to do this, motion stages for the sample made by French company Piezoconcept were chosen, the stages are the LFHS2.50 for x/y and the Z-STAGE.50 in z. The x and z axes both have a range of 50 µm and the y-axis 75 µm. These are three-axis flexure stages with motion controlled by a single piezo stack for each axis. Due to the inherent variability of piezo-electric crystals, the stages are calibrated directly after manufacture and each stage is encoded so it works only with the correspondingly calibrated controller unit. The piezo-crystals receive 0 V - 150 V from the controller and expand and contract with voltage. The calibration removes any need for the user to deal with the non-linearity of expansion of piezo-crystals, the stage controller is itself provided with an input analogue control voltage, 0 V - 10 V in this case, with 0 V being fully contracted and 10 V equating to maximum extension. Change in stage position is linear with this signal voltage. The stage controller receives voltage signals from the analogue output of the R9.

The stages themselves are closed-loop systems, they constantly measure their own position. This ensures that the stage has moved properly, as well as helps to negate any drifting effects or changes in temperature. This, coupled with the high precision voltage generator in the stage controller allow the stages to have a positional resolution of 0.05 nm, a noise floor of 5 pm, and the stages can extend across their entire range and arrive back to within 0.1 nm of the same point. The stages have a resonant frequency between 1.5 - 3 kHz which is far away from the resonance of the cantilever and scanning frequency to ensure that no issues arise [24]. These stages are highly suitable for AFM and therefore for NV^- magnetometry also. The R9 is capable of sending driving signals of up to $1V$ to the AFM probe. This is a generic voltage, as the R9 is designed to work with custom microscope designs.

3.2.3 Coarse approach of the tip towards the sample

An extremely useful addition to the AFM set-up was a CMOS camera and a 12× zoom lens with a focal length of 98 mm, both from ThorLabs. The camera is positioned at the height of the sample stage so it has a view of the tip. This provides a view of the tip approaching the surface at such resolution that 1 pixel = 1 µm in the plane of the tip. This allows the tip to be brought to within a few microns of the surface without the need for the standard 'sewing' approach used by most AFMs.

The sewing approach is a safe method of bringing the tip into contact with the sample. Typically there are a coarse and fine adjustment approach motors. The coarse stage is manually brought towards the surface until the user judges, by their own eye, that it is as close as they can safely make it. The AFM controller then takes over by moving the fine stage through its entire range of motion looking for the contact point. If the fine adjustment stage does not bring the tip into contact then it is fully withdrawn and the coarse stage takes one step of between the half and the full range of motion of the fine stage. The process then repeats. Therefore the manual approach usually brings the tip to 500 - 1000 µm from the surface. The sewing method would then bring the tip into contact, a process that usually takes several minutes.

Using the side view camera on our instrument allows the manual approach to bring the tip well inside the 50 µm range of the fine adjustment motion stage, meaning that once manually approached final approach is already completed and scanning can begin immediately.

The high zoom and close focal length of the lens on the camera mean that the numerical aperture is very small and that ambient room lighting is insufficient to view the tip. An array of green LED's is used, seven diodes each drawing 50 mA at 24 V. The LED array is positioned behind the probe pointing towards the camera, slightly off the axis of the lens. This reflects sufficient light off the tuning fork, cantilever and probe that it is clearly visible in the camera image.

This setup greatly improves efficiency in approaching and scanning a new sample and also improves the ease with which the AFM is operated.

3.2.4 Probe pre-amplifier

The Akiyama probe comes with a specific tuning fork sensor controller (TFSC) pre-amplifier, designed and manufactured by Nanosensors (Switzerland). The controller contains electronics to reduce the input voltage by a factor of 10, in

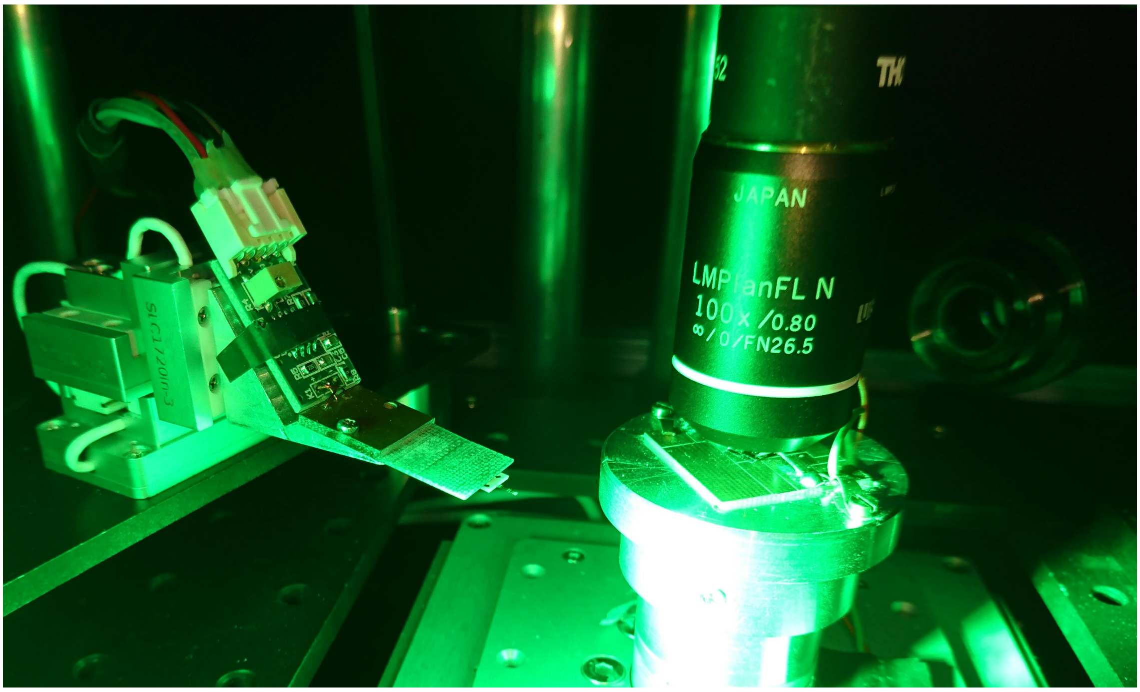

Figure 3.11: Overview of the scanning parts of the instrument. On the far left is the Smaract SLC-1720 stage, used to position the AFM probe in the centre of the MO and to bring the tip into contact range with the sample. The side view camera which allows the tip to be brought so close to the surface is on the far right of the image. Attached to the z-axis Smaract stage is a mount which holds the Akiyama preamplifier, which receives the drive voltage, converts it to a safe level for the A-probe, receives the induced current from the probe and converts it to a voltage for it to be measured by the RHK R9. The mount ensures that the A-probe, visible at the end of the preamplifier PCB extending into free space, is at an angle of 11^o above horizontal. This ensures that the probe contacts the sample vertically and no other parts of the chip or preamplifier impinge on the sample. On the bottom of the image is the PiezoConcept XYZ stage, used for scanning the sample. The mount on top of the stage is holding a PCB which is used to apply a voltage to h-BN chips. The mount is removable so the sample can be loaded and the terminals aligned in a more spacious environment. The microscope objective lens is visible entering from the top of the image. This provides the top down view of the AFM scanning, focuses the laser onto the sample and collects light emitted from samples. The MO is focussed on the sample surface, lens sample separation is 3.4 mm. The Smaract stages and A-probe are rotated away from the sample to provide a clearer image for this thesis. During normal operations this system is rotated anti-clockwise and secured so the probe is in contact with the sample and underneath the MO.

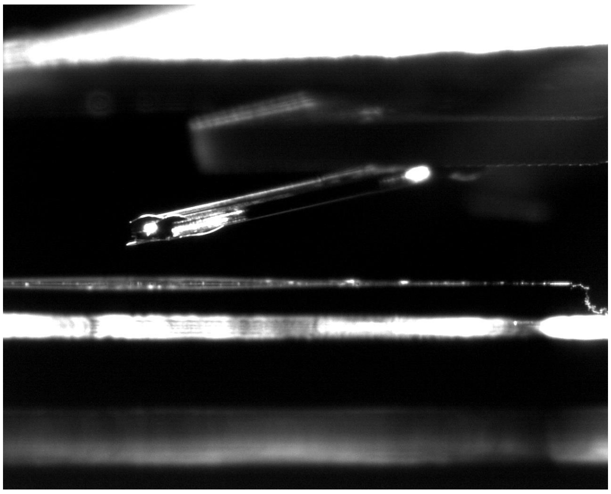

Figure 3.12: View of the cantilever and sample surface as seen by the approach camera with widest possible field of view.

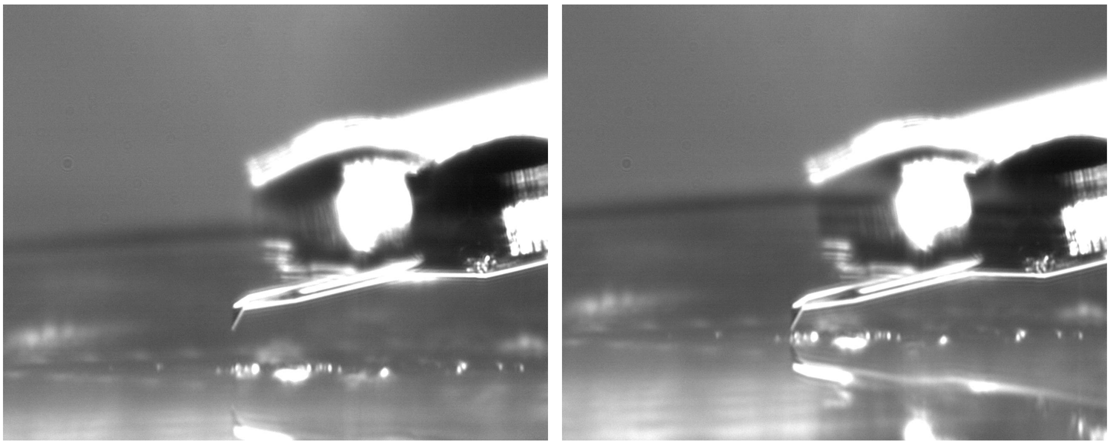

(a) View of the tip and the sample surface, with the side camera at maximum magnification. Sample z-stage is in the fully retracted position (z = 0 µm).

(b) Same view as in a), but the sample z-stage is at full extension, 50 µm above retracted position. The tip is just out of contact with the sample.

Figure 3.13: The reflection of the cantilever off the surface aids a great deal in seeing the tip-sample separation. The SmarAct probe stage can take sub-nm steps, which is far greater precision than is required, making this a very comfortable method of safely bringing the probe into contact.

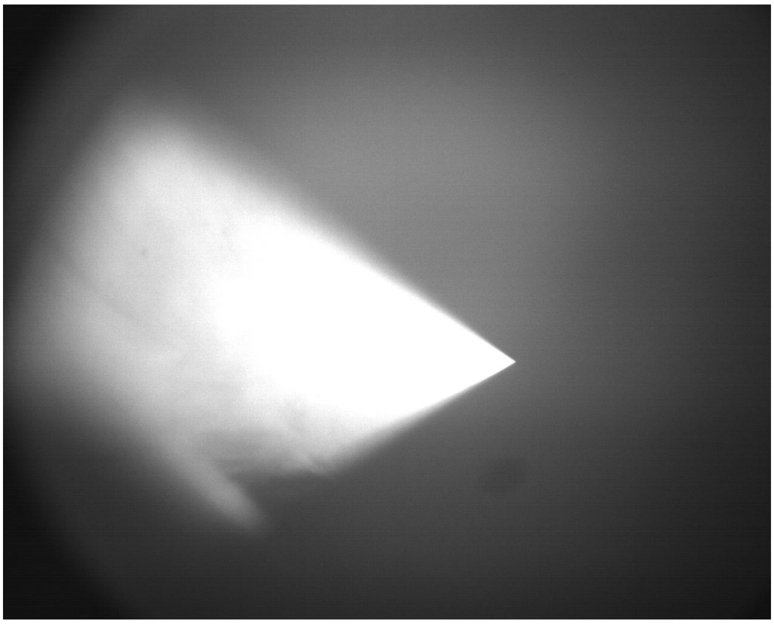

Figure 3.14: View of the AFM probe on the CMOS camera looking down the MO lens. By reducing the height of the lens using the focusing stages, the focal plane can be lowered, taking the probe out of focus and bringing the sample plane into focus.

our case coming from the R9, and a transimpedance amplifier (22 V/µA) to amplify the induced current in the oscillating tuning fork. On the output side, there is an op-amp loop with gain 1, which acts as a buffer. Between the input and output sides is a circuit containing a variable resistor, which can be manually adjusted to correct for capacitance in the system. Capacitance can be present between the electrodes on the quartz tuning fork. This correction is performed whilst tuning the cantilever in order to make the resonance curve symmetric and it is necessary to do this whenever a new cantilever is used. The schematic circuit diagram is shown in Fig.3.7.

3.2.5 Scan view

The final piece of equipment required to perform AFM is a way of seeing where the probe is going to scan on the sample. This is accomplished by using the microscope objective lens, which forms part of the confocal microscopy set-up, and another CMOS camera from Thorlabs. A variable intensity, green, LED projects light onto the sample through the MO by being reflected into the camera's view by a beam splitter. The light reflects off the sample through the MO, a proportion of it then transmits through the beam splitter and is focused by a pair of lenses onto the camera sensor. This view can be seen in Fig. 3.14 and the setup diagram in Fig.3.15.

The Piezoconcept fine control motion stages are mounted on a manual, micrometer driven stage. This provides the coarse positioning in X and Y with 25 mm of range in both axes. This allows the area of interest on the sample to be brought into view and centralised under the AFM probe before approach and

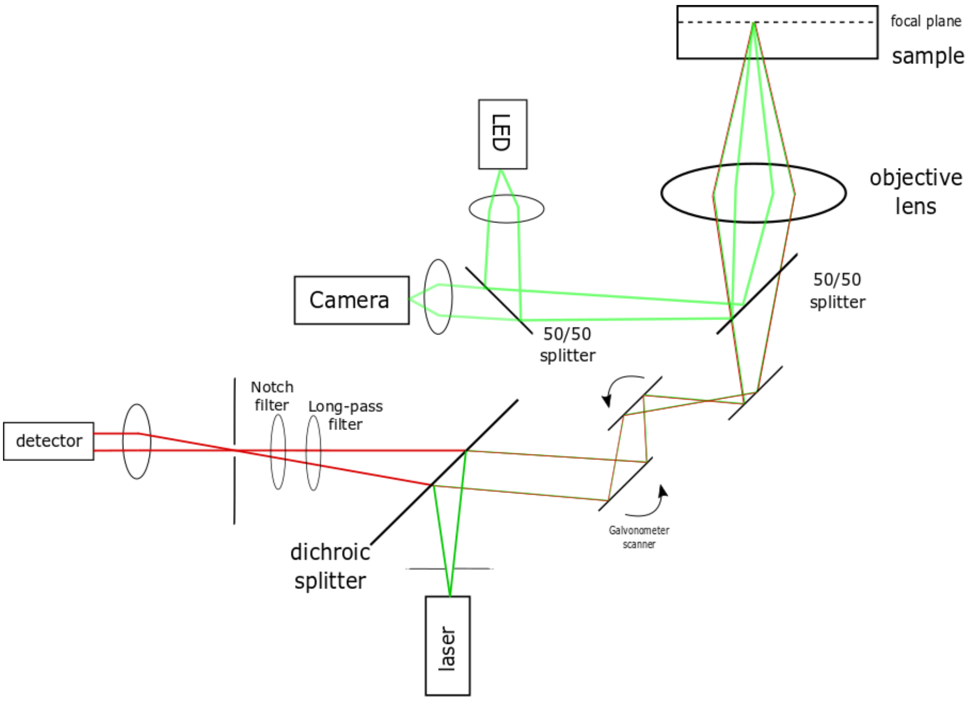

Figure 3.15: Diagram showing the camera and beam splitter responsible for providing the view of the sample and cantilever through the objective lens. See figure 4.1 for information on the other parts of the system. The camera view and LED illumination is achieved using the beam splitter nearest the sample.

scanning begins. The layout of the computer control system for the AFM can be seen in Fig. 3.10.

3.3 Literature Review

Amin-Shahidi et al. describe a high-accuracy AFM head, designed to be used in conjunction with the sub-Atomic measuring machine, a magnetically-suspended scanning stage developed by a joint team from MIT and the University of North Carolina at Charlotte[25]. It has an x-y range of 25 mm with a resolution of 0.1 nm [26]. The AFM head provides z-range of 20 µm. Scan speeds of 5 – 10 µm/s typically provide clear images, and depth measurement reliability is very high, agreeing with measurements provided on a 25 nm AFM standard sample. The scan range of this AFM is huge and is due to their use of an already existing machine, previously built in-house. This provides a very large area over which to image, however, at the maximum AFM scan speed, a 25 mm^2 scan area would take a very long time to cover. The z-range is larger than most commercial AFMs.

The Dimension FastScan AFM [27] has a maximum scan speed of 12 mm/s, although the use of this speed would be highly dependent on cantilever properties. The system senses tip motion using deflection of a laser beam from the back of the cantilever, and the scannable volume is 35×35×3 µm, and z-axis resolution is quoted as 40 pm. Due to the necessity of measuring oscillation by the reflectance method, and the way in which the machine is encased in protective panels, adaptation for other purposes is rendered difficult. It would require a lot of modification before this instrument could be modified for the purpose described in this thesis. The z-range is significantly smaller than on our instrument and is the same as that on the Dimension 3100 AFM in our lab, which is 20 years old. The maximum scan speed is truly impressive, if the settings are defined correctly then this would make taking an AFM measurement of 35×35 µm area just as fast as optically viewing it.

Gaoliang Dai et al. based at Physikalisch-Technische Bundesanstalt, developed a high accuracy, high speed, long scan range AFM to avoid the issue of drift during long-range scans [28]. The AFM scans a calibration grid attached to the sample in order to allow their software to correct for distortions caused by the scan speed. They show that scanning speeds of 100 µm/s and 500 µm/s are possible and produce an accurate image of the sample surface when using this real-time calibration technique. The sample is scannable over a 25×25×5 mm range, this is achieved by having multiple stages stacked together. The maximum scan speed is given as 1 mm/s, however, measurements at this speed are not provided. The range of motion of this is also huge, particularly that in the z-axis. The fact that this is performed by having multiple stages, stacked together, for each axis brings thermal and other types of stability into question. The necessity of having a calibration grid attached to the sample being measured reduces the adaptability and potentially the variety of samples which can be measured. The use of the optical beam deflection from the cantilever would limit the applicability of such an AFM in our area of application, however, an Akiyama probe could be used and such a system could work well for us. Such a massive range in every axis is not required in our application, samples are of a fixed size and features on the surface also should not be so large on standard atom chips. Whilst extra range can be useful, for us it would be unnecessary and would undoubtedly come with compromises in other areas, such as ultimate resolution.

Isaac et al. [29] describe an instrument and series of protocols used to align a probe and scan a sample on a magnetic resonance force microscope (MRFM). The system is cryogenically cooled and is designed to measure gold current-carrying wires in waveguides on silicon wafers. The range of motion of the system is 3×3×1 µm in XYZ axes and it provides a highly reproducible alignment technique. There is no optical observation of the system, either top-down onto the sample or side on to view tip-sample separation. The approach is performed with a visual coarse approach and then the 'sewing method', where larger vertical steps are taken with the probe, then the sample stage scans vertically to see if the tip is near enough to come into contact with the sample. The motion of the tip is detected using a fibre-based laser interferometer. The lack of cameras viewing the sample would make aligning our types of samples quite difficult, and the interferometer setup used to detect the tip motion would be very hard to work around whilst adapting the system. The dynamic range of this system has an accuracy of ∼1% of the maximum range.

Chang and Degen at ETH Zurich [30] use a scanning AFM to perform NV^- magnetometry. Their home-built AFM has a scan range of 200x200x200 µm and resolution of 1 nm. This is a large range and sufficient precision for carrying out their research, measuring current density in microscale current-carrying devices. Their AFM is used to perform magnetometry but does not image the topography of the sample, the AFM is purely used to scan the sample underneath the diamond.

3.4 Tests and Results

A frequent problem with many forms of nanoscale scanning instruments is that of drift. Fluctuations in temperature and voltage supply can cause the stage to move its position slightly. If a stage is required to hold a fixed position for a long time, the nature of piezoelectric crystals can mean that the stages drift slightly due to creep. The Piezoconcept stages constantly measure their position and feedback to the controller, this provides some degree of drift prevention. The system works extremely well on these stages and drift is not an issue. High resolution 50 µm FM-AFM scans were performed over the course of a weekend, each scan lasting up to 7 hours for the slowest scans (1 µm/s); the sample did not drift and four scans matched to within 200 nm.

Most FM-AFM scans are taken at speeds of 5 - 10 µm/s. Samples with much smaller features require slower speeds, down to 1 µm/s. For an ideal sample with correctly tuned feedback loops in tapping mode, a scan speed of 50 µm/s produces clear scans, scanning faster than this has not produced useful data.

3.4.1 Oscillation Amplitude

To understand better what is happening as the probe senses the sample, one must know the amplitude of oscillation of the tip. The drive voltage is set by the computer software, and the return voltage is measured by the AFM controller and is referred to as the PLL Amplitude, the voltage being used as the feedback signal by the phase lock loop. The Akiyama preamplifier has known amplification gains, there is a step-down voltage amplifier on the input and a current-voltage amplifier on the output. This can be used to convert the ”drive voltage” and ”PLL Amplitude” into the actual voltage experienced by the tuning fork and the current generated by it.

Plotting the PLL Amplitude against z-height can allow the inference of the free space oscillation amplitude of the AFM probe.

Figure 3.16 shows the plot of PLL Amplitude, corrected to tuning fork current, vs z-height whilst approaching and receding from the sample surface. The probe was driven by 800 mV drive signal, which was stepped down to 80 mV at the tuning fork. The best fit line is drawn over the linear region: 0 nA indicates where the probe would have reached the sample surface. This data shows that this Akiyama probe had free space oscillation amplitude of 822 nm ± 12 nm. This is a large amplitude compared to other types of AFM probe [31], however, this can be attributed to the way the tip is attached to the quartz cantilever.

3.4.2 AFM standard sample

AFM calibration standards are widely used to test AFMs across the world. The ones we used were manufactured by Budget Sensors and come in 100 nm and 250

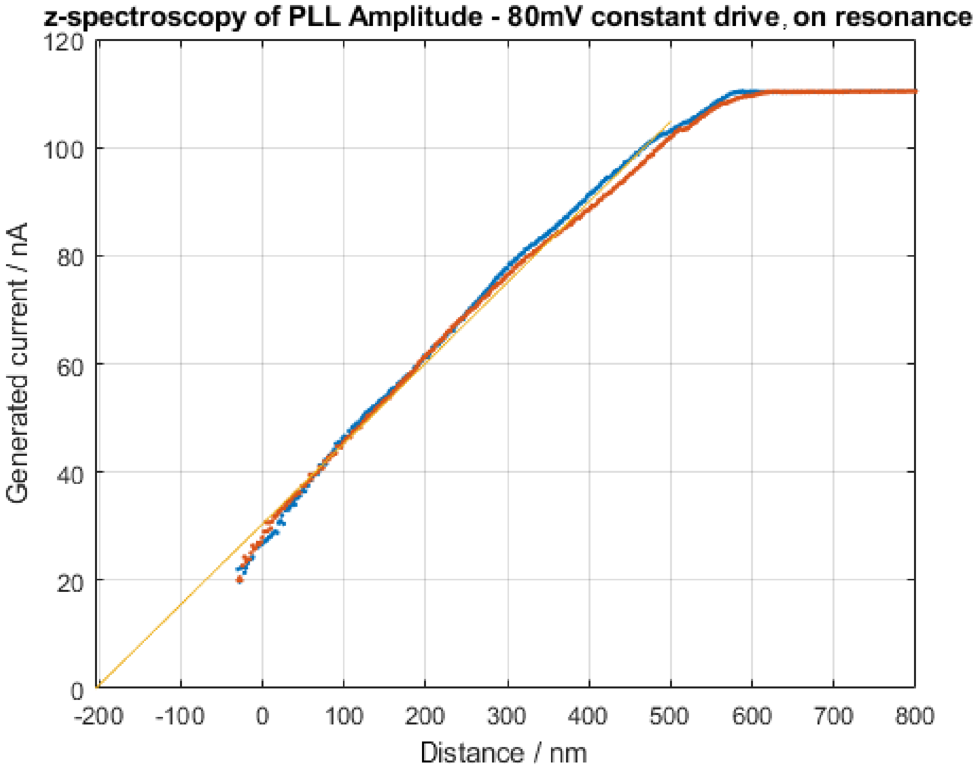

Figure 3.16: Tuning fork current vs z-height. This data is averaged over several approaches and retractions. The height is measured with respect to the initial PLL set-point and is arbitrary; the surface would be at the height at which the current would reach zero. Measuring this location is not possible and a fit of the linear section is required to extract the position. From this, the free space amplitude measured at 822 nm ± 12 nm. The blue points are averaged approach data, the red are averaged retraction data, the yellow line is the best fit of the linear section.

nm step heights. The layout of such a sample is visible in Fig.3.17 which displays the separation of the features as well as their heights.

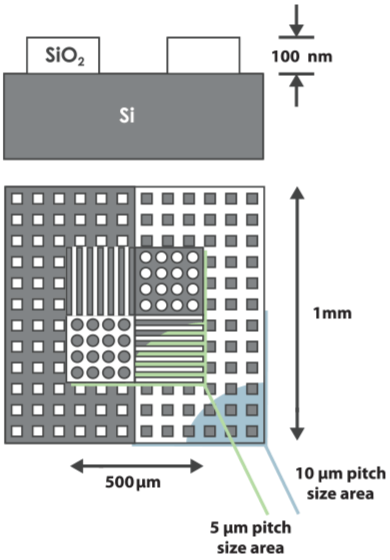

Figure 3.17: Diagram of the AFM calibration standard used to test the accuracy of our AFM. Image taken from BudgetSensors website.

The calibration standard has an identical height for every feature, which have high contrast colours when viewed optically, due to high and low reflectance surface finishes. The features have sharp edges and are high or low, separated in height by 113 nm ± 2 %, to provide high contrast on AFM scans.

Fig. 3.18 shows the camera view through the objective lens. This is the view used to align the AFM probe over the sample in order to know which area of the sample is being scanned. The confocal microscope can also be used to produce an optical image of the sample which will match up very closely with the AFM data as the same scan stages move the sample to perform the scan. Such an image can be seen in Fig. 3.19.

Figure 3.20 shows a post-processing image of the topography data set collected when measuring the surface of the sample with the instrument. Small errors in the sample mount can cause a slope across the sample which can be removed by data processing. This was a 15 µm × 15 µm scan and height data was collected over a 200 nm range.

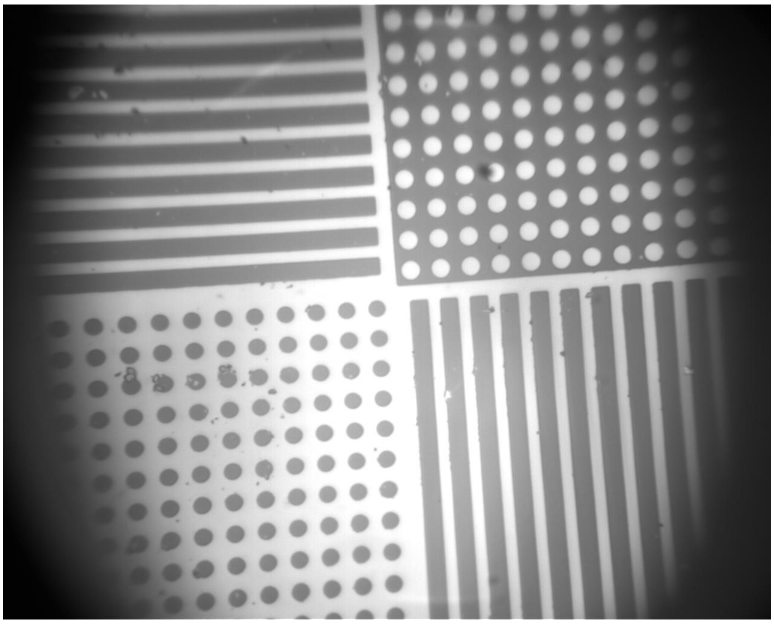

Figure 3.18: The top-down camera view of the AFM standard sample, viewed through the 100× magnification Olympus LMPLFLN100x microscope objective lens.

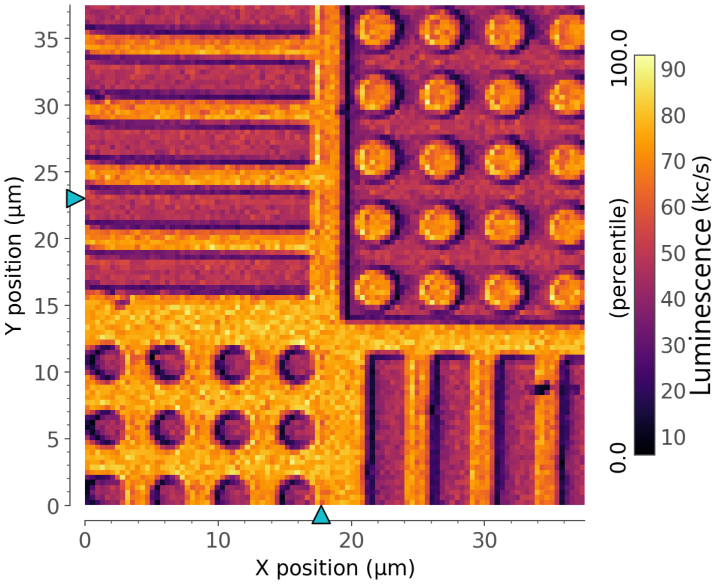

Figure 3.19: A confocal reflectance scan of the AFM standard sample using the confocal microscope to record relative intensity of the green laser light reflected off the sample. Image taken with a resolution of 100 lines with 100 pixels per line.

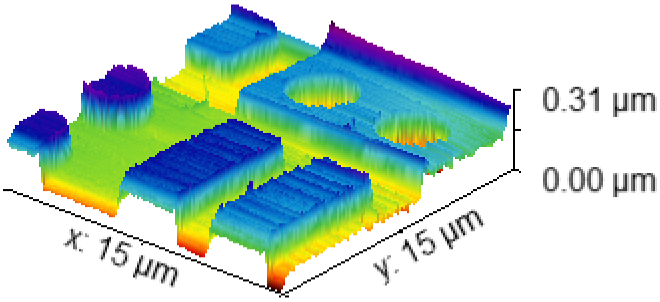

Figure 3.20: An AFM topography scan of the 100 nm step height AFM standard

Data processing software allows a line across the sample to be selected and the height data along that line to be displayed. This is the method used to test the accuracy of the AFM height readings. Lines are selected along the direction of measurement to allow for any drift between measurement passes. The step heights are then measured and analysed to provide a height value with error, the height of the sample is measured by the manufacturer and quoted on the sample box as 113 nm ± 2%. The calculated value from the data taken by our AFM is 113 ± 1 nm.

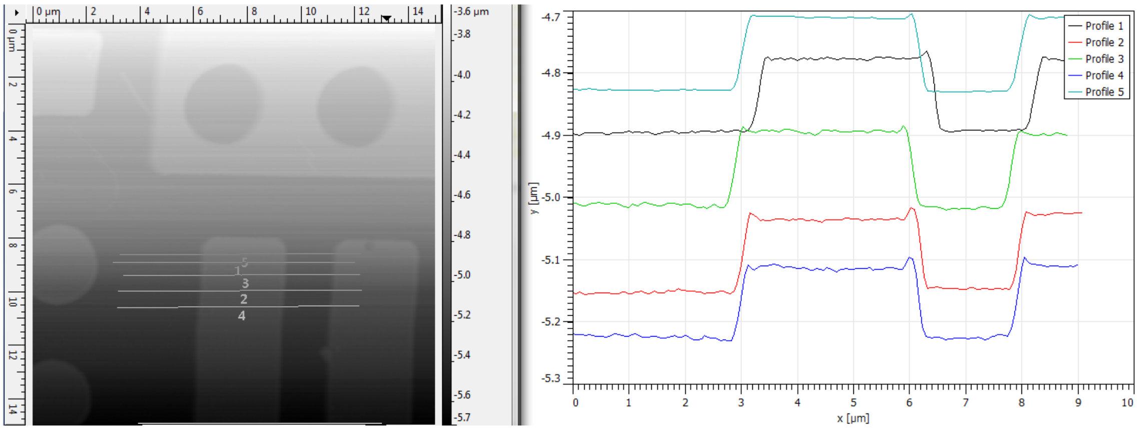

Figure 3.21: Topography profiles along lines drawn on the photo on the left. Height values are plotted on the right. The sample measured was the 113 nm AFM height standard.

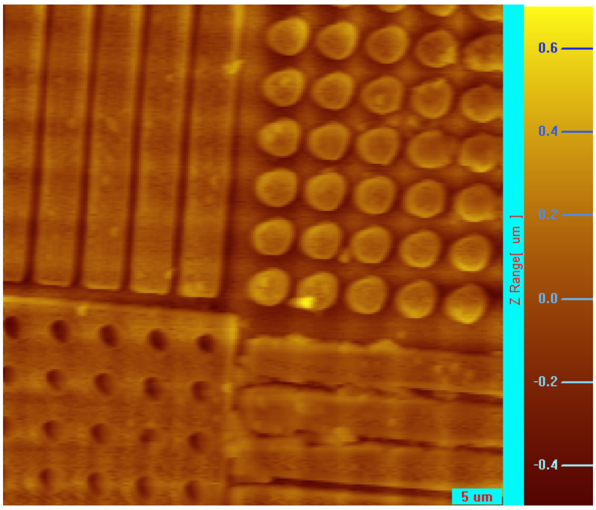

Figure 3.22: 50 µm × 50 µm square AFM topography scan of the AFM standard standard. Scan speed was set to 10 µm/s.

Figure 3.22 is a scan of the 250 nm high calibration standard from BudgetSensors. The spacing of the features is the same as in Fig.3.17 the only difference being the feature height. This scan displays the ability of our AFM to accurately measure, with low noise, across a 50 µm× 50 µm range. A small mark of dirt is clearly visible in the middle of the image, rising half a micron above the surface, demonstrating the ability of this AFM to image with clear definition even small, sharply rising features.

3.4.3 Comparison to AFMs in the literature

One property in common with the AFMs discussed in the literature review, and indeed many others I came across, is the necessity to use the sewing-style approach to bring the tip into contact with the surface. This can take up twenty minutes and may make the user less willing to switch samples as frequently as they might if the approach procedure was less time consuming; it increases the complexity of operation. With the side camera on our system, the sample can be changed and the tip brought safely back into contact in around two minutes. There is a large variety in scan ranges, with a couple of very large ones, and most smaller than ours (50×75×50 µm - XYZ, with 50 pm resolution). It was convenient for us to have a scan range which could measure samples that are as high as they are wide, this means that we are unlikely to encounter atom chips, h-BN or spintronics devices which we are unable to image with the instrument. The z-axis resolution is limited by the noise in stage position which is around 1 - 2 nm. Whilst measuring thin flakes of hexagonal boron-nitride, step heights of 4 nm were resolved, showing that this AFM is fit for the purpose required of it. This setup provides the ability to measure surface topography and then repeat the scans either at a constant height or at a fixed distance from the sample surface, this is an imperative functionality for magnetic field measurements using an NV^- centre.

3.5 Summary

This AFM does not have the finest spatial resolution or highest scan speed of any AFM, either custom-built or available commercially. However, it has a large scan area, suitable for measuring atom chips, the height sensing is accurate and can sample a line across the sample in 5 s at normal operating speed. Depending on the resolution requested, this means that a reasonably detailed scan containing 256 lines of 256 samples over a 50×50 µm area would take less than half an hour. The approach method also significantly reduces the time taken to load a sample and begin measuring the surface.

The next chapter will concern the confocal microscope. A system which is built above the AFM in order to probe samples on the AFM stage after they have been scanned by the AFM.

Chapter 4

Confocal Microscope

Construction of the confocal microscope began whilst the AFM was still in development. Whilst I constructed the AFM, the lead on the confocal microscopy side of the project was taken by Ashley Tyler. He reviewed different, specific types of confocal microscope and chose the majority of the components required to build ours, the laser, the galvanometer scanner and the photon detectors having already been chosen, ordered and received by myself. Assembly of the components and the extensive process required to align the system and position the components correctly was a joint effort and involved many hours of work on both our parts, independently as well as together.

This section will cover the theory of confocal microscope, explain its purpose in this instrument, and review and compare other confocal microscopes used for similar purposes. Occasionally, references to nitrogen-vacancy defects will be made in order to put the information into context. A full description of NV^- centres and their behaviour can be found in Chapter 5. Construction and initial testing of the device will then be explained by, again, using an AFM standard calibration sample.

4.1 Theory

Confocal microscopy has, for over fifty years [32], been used to image both biological and material samples in higher resolution than with traditional optical microscopes. It strictly controls the location from which light is received and so light coming from areas other than the area of interest is not collected. The word confocal refers to the fact that light in focus on the sample is focused at a pinhole in front of the final detector. There are various types of confocal microscopy used in research, in this project we have built a laser scanning/sample scanning instrument. A diagram of this basic version of the instrument can be seen in Fig.4.1.

A point on the sample is illuminated with focused light from a single coherent point source and the reflected light observed by a detector. The point is scanned across the sample to build up an image.

The source light is formed using spatial filtering techniques, whereby the light is passed through two convergent lenses, separated by the sum of their focal lengths. At the focal point between the two lenses, a pinhole is used to select

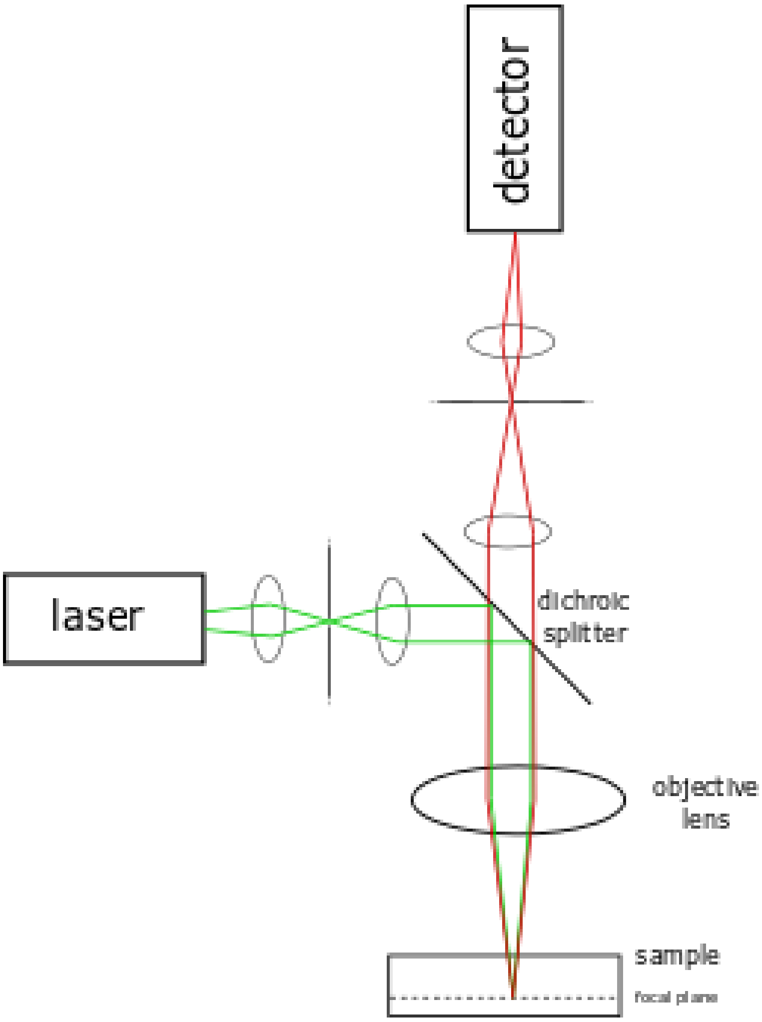

Figure 4.1: The basic components required to perform confocal microscopy.

only the most tightly focused light, allowing the transmission into the system of a very clean, Gaussian in profile, highly spatially coherent beam of light. The light is then passed through the system and focused onto the sample using an objective lens at a finely adjustable distance from the sample.

Light collected from the sample is selectively observed using the principles of Fraunhofer diffraction and spatial filtering. When an object is placed in front of a converging lens, the Fraunhofer diffraction pattern of the image will be formed at the focal distance behind the lens. If the image is placed at the focal distance from the lens, then the Fraunhofer diffraction pattern (at focal distance) is the spatial Fourier transform of the initial image. If this light is then passed through another converging lens, also focal distance away, then this lens will focus the light back into the original image.

In the case of confocal microscopy, a pinhole is used to accept only a very narrow band of light at the centre of the image in the Fourier plane. This light is the light originating from the focal point of the first lens, light originating from any other point, either to the side or in front or behind the focal point, is blocked by the pinhole. This technique is useful because the image formed by collecting the light after it passes through the pinhole is that of a very specific volume of space, known to the user and calculated by knowing the size of the first focal spot and the depth of field of the lens.

To make this technique more efficient at observing only the desired volume, as opposed to light from the entire stack of material on the optical axis of the observation lens, the sample is illuminated by a laser, which is directed via a beam splitter through a microscope and exits the objective lens onto the sample. The laser light is passed through a pinhole to ensure a very coherent beam is produced, the beam is then reduced in diameter and focused onto the sample by the microscope. The intensity of the beam is, therefore, highest at the focal point and so the majority of the light is reflected from this point. That coupled with the system only collecting light from the focal point improves the filtering and selects light only originating from the desired spatial volume.

In summary, the light leaves the laser and passes through a pinhole, is reflected by a beam splitter into the microscope lenses where it is focused into a spot on the sample, reflected back up the objective lens and transmitted through the beam splitter, passed through a pinhole in the Fourier plane and then detected by any of a variety of detectors, the type used being dependent on the purpose.

For the purpose of detecting single quantum emitters, like NV^- centres, it is important to have a small collection spot, to be able to scan it across the surface of a sample and to have a good view of such small objects. A high magnification microscope objective lens is therefore frequently used in order to focus the illuminating beam tightly to ensure only a small part of the sample is illuminated at a time and to ensure maximum light collection efficiency. Some method of scanning light across the sample is also required to build up an image from the pinpoints of light. Typically there is a system of two tilting mirrors, perpendicular to each other, between the beam splitter and the microscope. With the inclusion of a scan lens in the microscope to correct for changes in beam direction, it is possible to use the mirrors to change the angle at which light enters the objective, thereby scanning it across the surface of the sample whilst

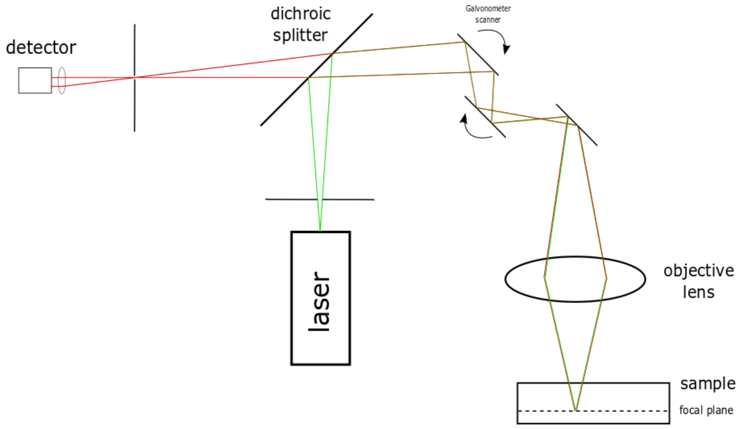

Figure 4.2: A galvanometer was added to setup to provide the ability to scan the focused laser beam/collection spot across the sample.

maintaining the focus of the light in the plane of the sample.

Recording the intensity of light at each point builds up a picture of the sample pixel by pixel. As the focus is changed, further layers of the sample can be measured, providing the illumination is able to penetrate and return successfully, and therefore a three-dimensional picture can be developed.

As well as applications such as ours, looking for light emitted from materials, confocal microscopes also have applications in life sciences [33]. As they are non-invasive and non-destructive they can be used to image biological materials which naturally fluoresce, or marker/dye molecules can be implanted into the sample which will photoluminesce and be observed by a confocal microscope [34]. This can be used on a cellular level and dye molecules can be chosen so they will only travel to specific locations, for example, ion streams through cells can be imaged.

4.2 Design and Construction

The confocal microscopy apparatus is based on the diagram in the previous chapter, which shows the main components. The microscope objective lens (MO) has already been referred to in the AFM section where it is used to observe the location of the AFM probe on the sample. It is an Olympus LMPLFLN100x, with 100× magnification, numerical aperture, NA=0.8, and a working distance of 3.4 mm. This was chosen as the large magnification provides a good view of the sample/diamond, the large aperture will allow efficient collection of the PL photons whilst the very long working distance means the diamond can be brought into focus without the housing of the lens fouling upon the AFM probe support system. The theoretical limit of resolution is,

$$\text{Resolution} = \frac{\lambda}{2\text{NA}} \tag{4.1}$$

where lambda is the wavelength of light and NA is the numerical aperture of the lens [35]. In our case, this gives a minimum resolvable size of 321 nm.

To make the system work with our instrument, a few alterations are required. The first is an extra beam splitter to provide the top-down camera with a view of

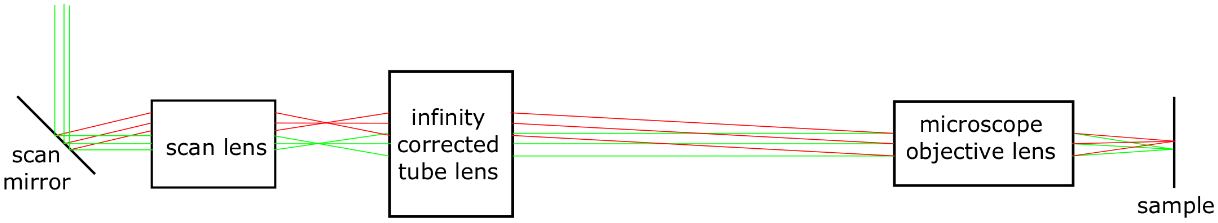

Figure 4.3: Diagram showing positioning and purposes of the scan lens and the ITL. The scanning mirror referred to in the diagram is the galvanometer scanner in our setup. Varying the angle of entry into the back of the MO results in lateral translation of the focal spot across the focal plane. Diagram adapted from ThorLabs. Red rays indicate an alternative path taken by the excitation and returning fluorescent light due to the change in angle of the scan lens.

the sample. This is placed above the microscope objective and below the infinity-corrected tube lens, to reflect the illumination LED towards the sample, and reflecting some of the light returning from the sample towards the camera. This is particularly useful for confirming the location of the laser spot on the sample before scanning begins. The position of this camera can be seen in Fig.3.15.

In scanning confocal microscopy instruments, a pair of orthogonal galvanometers with attached mirrors are used to scan the beam across the sample. The galvanometers rotate about a pivot, the angle rotated varies linearly with current. A very stable current supply is therefore required to reduce noise in angular position whilst the mirrors are being held at a fixed angle. A scan lens and an infinity-corrected tube lens (ITL) form part of the magnification apparatus of the confocal microscope, as well as allowing the beam to scan whilst still hitting the back of the microscope objective at the same point. The angle at which the light enters the objective dictates the lateral translation of the focal spot of the objective lens. The galvanometers translate the beam across the scan lens, this is also a translation across the ITL, the light then leaves the ITL at a different angle but still enters the MO at the same point. This is visible in figure 4.3.

The galvanometers are provided current by dedicated electronics, which in turn are instructed on the level of current to apply by a voltage from a digital to analogue converter (DAC) controlled by the confocal microscopy software. On construction of the setup and during test imaging, it became clear that scanning the laser across the back of the lens would not work in our case. There was difficulty aligning the system so the light could scan the full range of the back of the objective lens without clipping on other components, in addition to this, transmission and reflection were not uniform across the entire area. When pushed to the extremities of the range, the intensity of the returning light dropped off significantly, giving any collected data a large skew.

To avoid the clipping and light capture issues, it became apparent that a better mode of operation used the galvanometers to aim the beam directly through the middle of the objective lens and fixing it there, before scanning the sample under the microscope objective using the sample stages from the AFM side of the instrument. The beam is directed to the point of maximum transmission and reflection, and so by moving the sample, variances in the lens do not affect the data.

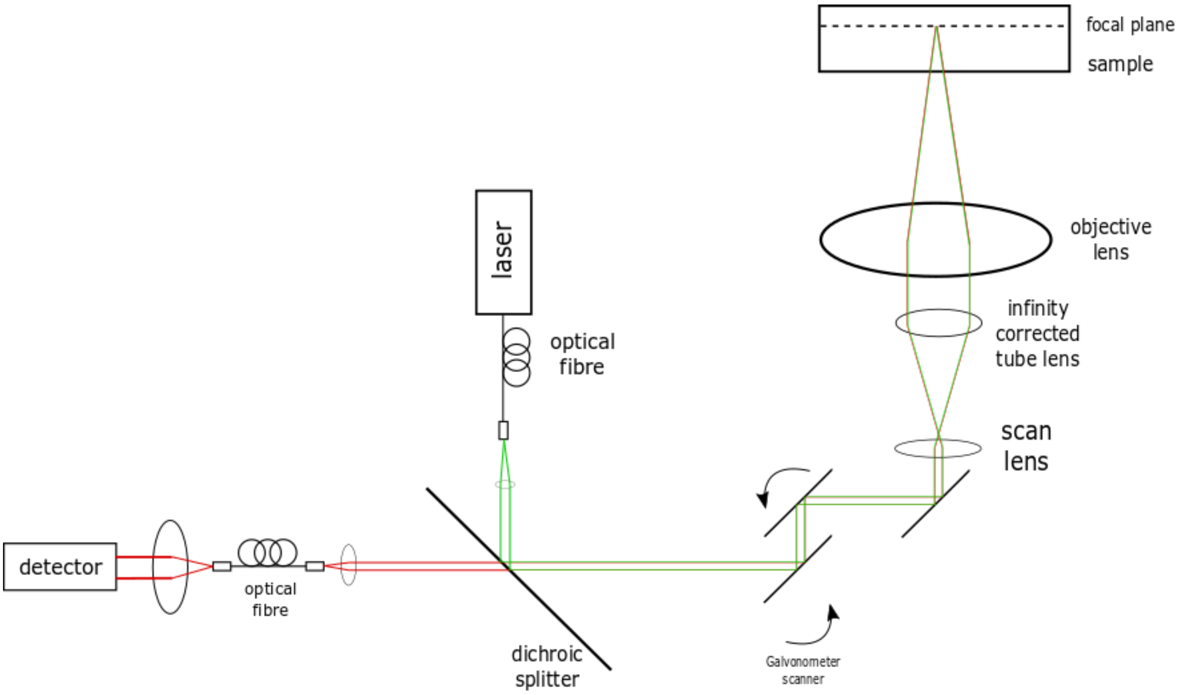

Figure 4.4: Confocal microscope setup including the scan lens and tube lens to provide the ability to scan the probe beam across the sample using the galvanometer scan mirrors. Optical fibres are used as pinholes in the setup, these have a core diameter of 25 µm which is the ideal size, matching the size of the focal spot when the magnification of the system is taken into account. They also provide the useful functionality of moving the laser beam around the instrument, allowing for compact design, efficient use of space and for the direction of detected luminescence into the light-tight detector box. For clarity, some components have been omitted.

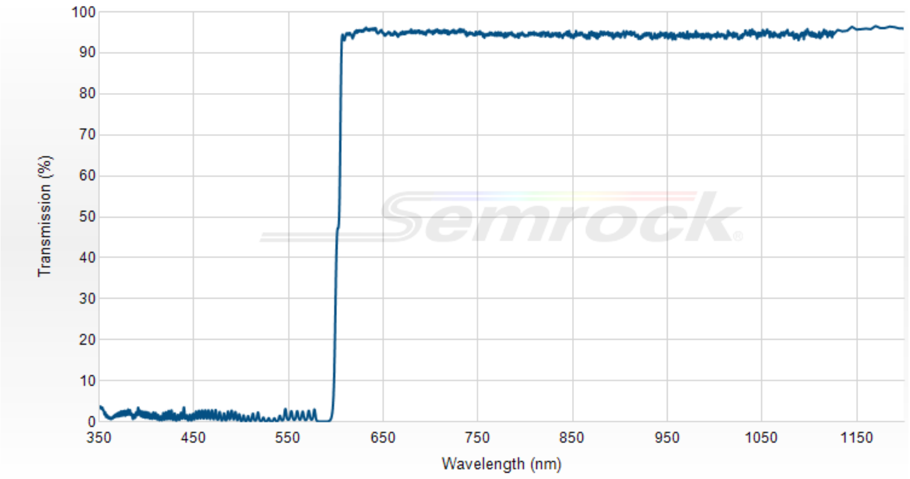

Figure 4.5: Transmission/Absorption percentage vs photon wavelength of the dichroic beam splitter. Its purpose is to reflect the green laser towards the sample and then to remove the returning green light, allowing emitted red straight through to the detectors [36].

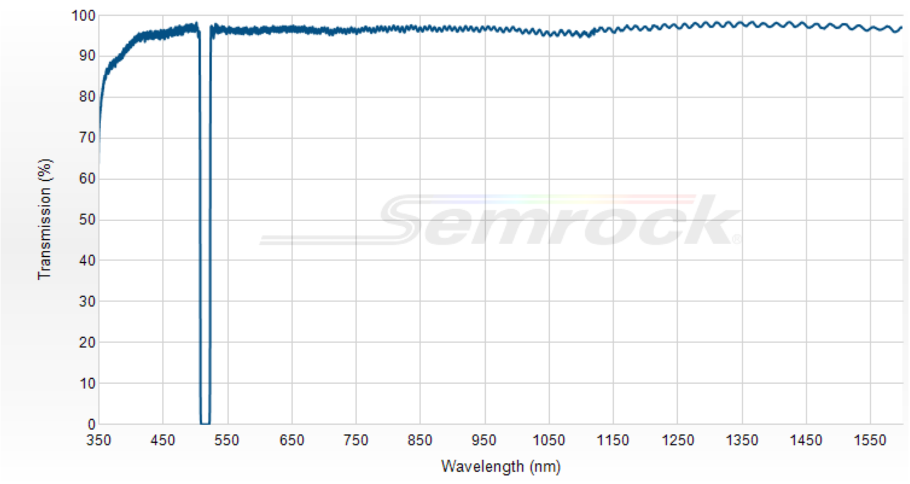

Figure 4.6: Transmission spectrum of the notch filter [37].

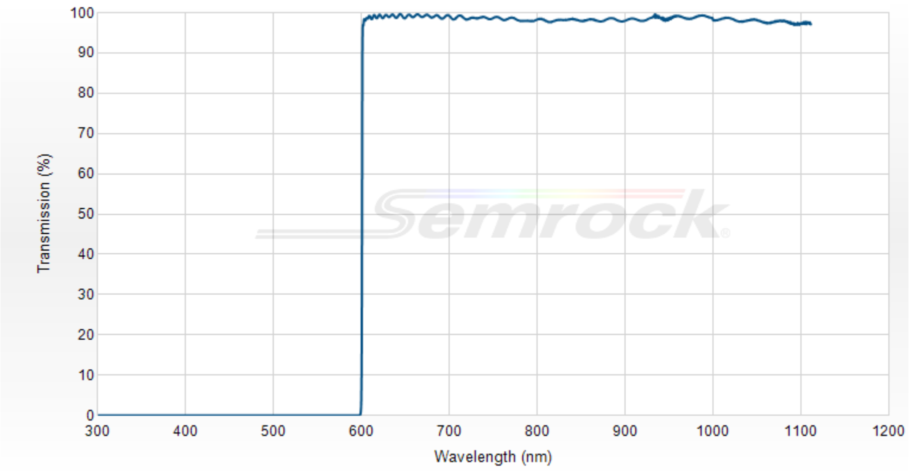

Figure 4.7: Transmission spectrum of the LP filter [38].

The splitter used to separate the green laser light from the red fluorescent light is a dichroic beam splitter made by Semrock (Di02-R514-25x36). The transmission and reflectance spectra are visible in figure 4.5. Whilst it reflects green light, it is not 100% reflective at 514 nm and so some illuminating light passes through onto the detectors. During photoluminescence scanning, this is reduced to a level comparable to the base noise level of the detectors by using a notch filter (Semrock Stopline 514 nm, NF03-514E-25) and a long pass (LP) filter (593 nm blocking edge BrightLine long-pass filter FF01-593/LP-25). Transmission of the notch filter can be seen in Figure 4.6 and that of the LP filter in Fig. 4.7. The combined effect of the three filtering optical elements is an optical density (O.D.) of $\sim$ 14 at the wavelength of the probing laser and an O.D. of $\sim$ 0.1 at 630 nm.

If these two are removed, then with a laser power of 1 mW, enough green photons are produced and transmitted through the dichroic splitter that a reflectance scan image can be made. This provides an image, very similar to that visible on the inline CMOS camera. Scanning to generate this image has the added benefit of quantifying the reflectance at each point on the sample whilst also providing higher spatial resolution than the camera and a higher fidelity image due to the narrower line width of the illuminating light.

After being filtered and before the light is passed to the detectors for photon counting, one more element is required. The pinhole before the detector ensures that only light from the focal plane is counted. The light emitted from the sample passes through the objective and the scan lenses, magnifying the image. After this microscope, the beam is collimated and it propagates through the galvanometers, splitters and filters without diverging or converging. A converging lens then focuses the light collected by the MO such that the focal point occurs on the end of a multi-mode fibre. The fibre core is 25 µm and this is sufficiently narrow to act as the pinhole of the confocal microscope. The fibre is also necessary as the photon detectors are housed inside a light-tight box, the fibre passes through the walls of the box and is the only route by which light can enter.

When performing experiments on NV^- centres, which will be described in chapter 5, it is, in some instances, necessary to measure a single emitter. It is also the case with the h-BN devices, which will be described in chapter 6, that we might need to test whether an emitter is by itself or whether a cluster of defects is producing the light. The detection of the number of emitters is done by testing for anti-bunching, a phenomenon described in the next section. To perform anti-bunching detection experiments, high-speed photon counting detectors and a time-tagger are required. Time tagging involves recording the arrival of a photon, and the time at which it arrived, with sub-nanosecond precision, this allows the software to calculate the time differences between the arrival of consecutive photons and plot the correlation graph. A representation of this graph can be seen in the next section in Fig. 5.4.

The light exits the fibre, is re-collimated and then is randomly divided in two by a 50/50 beam splitter in order to test for correlation. If there is a single quantum emitter, there will be no occasions where two photons arrive at both detectors at the same time.

The single photon avalanche diodes (SPADs) used are two SPCM-AQRH-TR made by Excelitas, they are most sensitive to red photons, with a quantum efficiency of 75% at 650 nm [39] and have timing resolution of 250 ps. The SPADs generate a 3.3 V pulse for every photon detected, these pass to the time tagger, in this case, the PicoHarp 300 made by PicoQuant is used. The PicoHarp accepts signals of 0 V - -800 mV, therefore the signals are passed through attenuating invertors before entering the counter. The counter has a time-tagging resolution of 4 ps and can accept count rates up to 10^7 cps [40], this is due to the 10 ns dead time, the time it takes to recharge the capacitors in the detection system. The data is collected inside the PicoHarp and transferred to PC via USB and displayed on QuCoa software, also developed and marketed by PicoHarp. Single NV^- centres are expected to emit up to 1 Mcps (mega-counts per second). This, split between two detectors, is many times lower than the maximum count rate. The detectors are cooled by internal Peltier cooling to reduce dark counts, which is specified at 250 cps. In our experiment, one detector has a dark count of $\sim$ 140 cps and the other has a dark count of $\sim$30 cps.

Whilst performing initial ODMR of the NV^- defects (this process and the reason behind it are explained in Chapter 5), a continuous wave (CW) laser is used to continuously excite the defect whilst scanning the microwave frequency and observing the fluorescent emission dip at particular microwave frequencies in order to detect magnetic field strength. Further accuracy can be obtained by applying NMR-style pulse sequences. It is possible to do this using a CW laser and an electro-optic or acousto-optic modulator to rapidly deflect the laser to create a laser pulse at the sample. It was decided that the system would be neater and more easily operated if a laser that could do this itself was used. The chosen laser is the Vortran Stradus 514-60, which produces light of 514 nm and has a maximum power of 60 mW, most NV$^-$ magnetometry uses around 1 mW of excitation power, therefore this laser is operated at a power that produces a beam with a clean profile and narrow linewidth and then neutral density (ND) filters are used to reduce the intensity of incident light. The laser can be operated in stand-alone mode or via PC control. Whilst being digitally modulated, the flashing can be performed as rapidly as 200 MHz, due to the rise time of <2 ns and fall time also of 2 ns [41]. This ability to produce laser pulses means that the laser will be useful for pulsed measurements as well as the CW NV experiments performed during the initial evaluation of the instrument.

Details of NV$^-$ centres and experiments that use them are provided in the next chapter. The SPADs are an integral part of the confocal microscopy instrument and during simple scanning, the counts are summed, or the data from the quieter counter is used, this is why their presence has been described at this stage.

4.3 Confocal Microscopy in NV$^-$ centre and h-BN experiments

In her thesis, Childress [42] describes using an AOM to pulse the laser, producing a rise time of 25 ns. Again an oil immersion lens (100× magnification, N.A. 1.3)) was used to improve collection efficiency, and the lens was focused using a piezo-electric stage to which the lens was mounted. The Hanbury Brown and Twiss (HBT) interferometer was formed using a fibre splitter which also acted as the pinhole for the confocal microscope to perform background de-selection. The laser was scanned across the sample using a galvanometer in the confocal microscope, this provided a field of view of 100×100 µm. The use of a fibre splitter improves the simplicity of a confocal microscopy setup, taking the place of the pinhole, the splitter also provides a way to isolate the detectors from background light. However fibre splitters are not as accurate as beam splitters in dividing the light 50-50, there is usually a greater imbalance and no possibility for adjustment. A fibre splitter also reduces flexibility; a beam splitter cube can just be removed if only one detector is required or operational. Scanning the laser beam and collection spot across the sample using the galvanometers provides a very large scan area. We found, however, that it is difficult for the MO to transmit light evenly across such a large area. This method clearly provides excellent range and images in this case, but for our instrument, this could not be replicated. An oil immersion lens has the benefit that the numerical aperture is maximised (compared to a lens in air), and so more light is collected from the diamond and channelled into the MO. Additionally, due to the decreased refractive index difference between the diamond and the outside medium, more photoluminescent light will exit the diamond and be detected. This method is an excellent way to improve collection efficiency, which in turn would improve the accuracy of data collected. Oil-immersion is not utilisable in our case due to the AFM, which would not work inside an oil droplet.

The observation system described by Togan in his thesis [43] employs a continuous wave (CW) laser and is pulsed using an AOM. The microwave setup is more sophisticated than ours and can provide two microwave frequencies to the sample at once in order to simultaneously probe both transitions. The AOM leads to a laser rise time of 20 ns which is sufficient for initial tests but may begin to limit progress as faster pulse sequences are required. The instrument measures field strength experienced by the NV$^-$ defect and its reaction to probing microwaves. This is not a scanning setup but with some sample-scanning stages could be converted into a device to spatially record the field strength of samples.

Arai in his thesis [44] also describes the use of an AOM to pulse the laser and has the capability to scan, in three dimensions, the sample to position the diamonds under the objective. An oil-immersion microscope objective is used to collect light emitted from the sample. This is another example of an AOM, an EOM could be used to produce a shorter rise time, however, it would operate at a lower pulse frequency.

Öckinghaus et al. were able to use new laser diodes (Nichia NDG1116) [45] to perform state lifetime measurements on NV$^-$ defects in nanodiamonds. The laser used in their confocal microscopy setup was driven by a simple diode driver and a MOSFET (metal-oxide-semiconductor field-effect transistor) to control the current (laser power), this system could switch the laser on with a rise time of 800 ps. This is a very fast rise time, outperforming AOMs, EOMs and indeed our pulsed laser which has a 4 ns rise time. The entire system as described also costs significantly less than our laser, however, this diode produces light that is less monochromatic, the bandwidth is significantly wider than ours, and the profile of emitted light is less clear and would require more cleaning up, as would the polarisation of the emitted light. Our laser emits light in a tight linear polarisation, which can be manipulated if desired to improve the interaction with our samples.

Toan Trong Tran et al. carried out experiments on hBN using a confocal microscopy setup to measure the photoluminescence characteristics of the sample [46]. A 532 nm laser was used with a power output capability of up to 2 W. Detection was performed by two Excelitas SPADs, feeding into a PicoHarp and supplied by a fibre beam splitter. Scanning stages have ranges 100× 100× 100 nm in XYZ and 0.4 nm spatial resolution. The power output of the GEM532 laser is huge (50 mW - 2000 mW) [47]. Whilst extra power can be useful and can be reduced using N.D. filters, powers this large are unnecessary for any of our purposes: NV$^-$ centre and hBN emitters both saturate at around 1 mW surface incidence in a diffraction-limited spot.

Every experiment designed to perform confocal microscopy on NV$^-$ defects uses very similar microscope objective lenses, either Nikon or Olympus that have minimal change in focal length between green and near infra-red wavelengths. They all have a magnification of 100× in order to obtain a good view of the

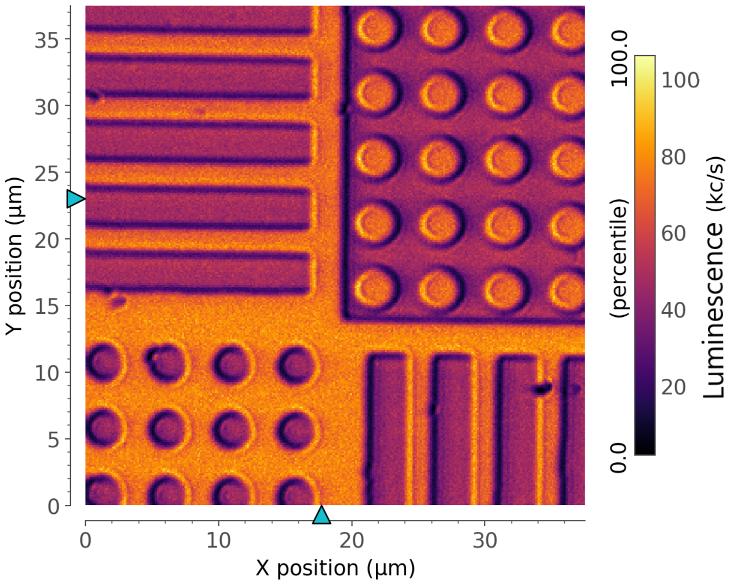

Figure 4.8: A confocal reflectance scan of the same scan area and sample as in Fig.3.19, but increased sampling resolution, 300 pixels per line over 300 lines. Note this does not change the size of the sampled area at each point, only an increase in the number of sampling points, a decrease in spacing between them and an increase in oversampling.

sample and reduce the difficulty in isolating emitters. An aperture of 0.9 or larger is also common, allowing high collection efficiency. A wide acceptance angle means more emitted photons are likely to be collected and detected. There is variation as to whether the MOs require immersion in oil or can be used in air; both options have positives and negative aspects. Oil immersion is not possible with many of our samples.

4.4 Testing of the confocal microscope

Figures 3.19 and 4.8 are reflectance scans taken of the AFM height calibration standard. These are taken using the confocal microscope by measuring the intensity of the green laser light reflected from the sample. Actual intensity values are not important unless the normal reflectance of 514 nm light is a desired parameter. The relative intensity, however, allows a clear and uniform optical image of the sample to be formed without any error obtained from differences in optical path. The scans show the difference caused by increasing samples per line. The 300 pixel scan took 9 times as long to complete as the 100 pixel scan, but the slight oversampling reduces the effect of electronic detector noise on the image.

Figure 3.17 shows a diagram of the standard height calibration sample and the measurements associated with it. This allows verification that the confocal microscopy software and the motion stages are correctly calibrated. Testing of the confocal microscope in fluorescent conditions requires a sample which fluoresces. This will be covered in the next chapter, concerning nano-diamonds.

The 100× magnification lens provides a narrow focal plane. This is visible in

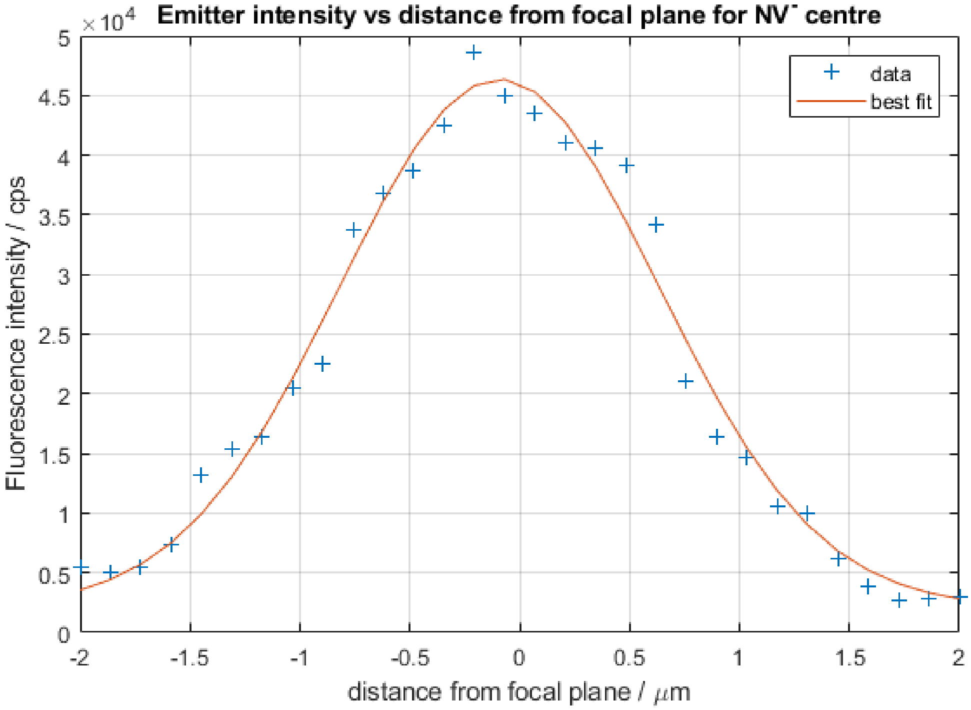

Figure 4.9: Intensity vs z-height of sample. This shows the intensity peaking sharply at focal distance, depth of focus is about 1 µm.

Fig. 4.9, which shows the fluorescence intensity of an NV^- centre vs focal height. From the figure, it is visible that intensity is halved at a distance of 1 µm away from the focal plane and intensity falls to one-quarter of the maximum value at 1.5 µm away from focus. This tight focus is important as it assists in selecting light emitted only from the target region.

In order to test the X-Y resolution of the instrument, a known sample is required. This is work for the future as such a sample would probably need to be produced on an electron beam lithography machine at the University of Nottingham.

4.5 Summary

The scanning is generated by the AFM scan stages rather than the galvanometers, this provides a 50 µm scan range with high spatial resolution and avoids the transmission variance caused by the light hitting the MO at different angles. This is not the largest scan range of any of the confocal microscopes reviewed, however, it is a very reliable system and sufficient for scanning the h-BN samples and samples of nanodiamonds. The SPADs have a dark count of ∼100 cps and therefore can detect emitted light with greater intensity. When the integration time is reduced then the dark count rises to a maximum of 500 cps at 2 ms measurement time, this allows much faster scanning for brighter samples. It is very simple to switch between PL and reflectance mode by inserting and removing the notch/LP and ND filters. Testing PL intensity at different wavelengths would be possible as the system is easily adaptable. The laser could be replaced with one of a different wavelength, as the laser light is inserted into the system via a fibre then the fibre could simply be connected to a different laser. The dichroic splitter could also be swapped out for one which operates at appropriate wavelengths, lending the system to studying many other types of photoluminescent samples. The system has also been adapted for electroluminescence and the wavelength changes could be made with relative ease. The flexibility of this system greatly increases the potential for use in other investigations on different materials.

The next chapter will cover NV^- centres in diamond and their application to perform magnetometry.

Chapter 5

Scanning NV$^-$ microscope

This chapter covers the theory of NV$^-$ centres, the construction of our instrument and compares it to similar NV$^-$ magnetometers. Some experiments are then carried out on nanodiamonds and the results are reviewed at the end of this chapter.

5.1 The NV$^-$ centre

Carbon occurs naturally in only two allotropes, graphite and diamond [48]. In graphite, each carbon atom is covalently bonded its three nearest neighbours, forming flat sheets in a hexagonal lattice which in non-layer form is called graphene. These sheets layer on top of each other, with the fourth electron in the outer shell forming van der Waals bonds between the layers holding them together. In diamond, each carbon atom covalently bonds with its four nearest neighbours, forming a diamond cubic lattice. Bonding is an extremely complex topic and to go into more detail than this would consume significant time and space without adding greatly to this thesis.

Whilst pure diamond would be a material made entirely of carbon atoms, in nature it is found to contain many defects and non-carbon elements within the structure [49]. Indeed even when fabricating diamond under laboratory conditions, it requires a lot of effort to prevent impurities from entering the lattice from the surrounding atmosphere [50]. Of specific interest to the instrument described during this thesis, is a naturally occurring, magnetically sensitive, diamond defect known as a negatively charged nitrogen-vacancy centre.

Nitrogen-vacancy centres have either a neutral or negative charge equal to that of a single electron. These are referred to as NV$^-$ centres [51]. The neutrally charged NV^0 defect is more difficult to interact with than the negatively charged one [52] and is outside the scope of this thesis. I shall, therefore, be referring to the negative NV^- defect as simply the NV centre. The defect is formed when two adjacent carbon atoms are instead replaced by a nitrogen atom and a vacancy - an absence of an atom.

Whilst carbon atoms contain four electrons in their valence shells, nitrogen contains five. In an NV defect, three of these electrons bond with the three surrounding carbon atoms and the other two are referred to as a lone pair. At the vacancy site, there are three electrons from the three surrounding carbon

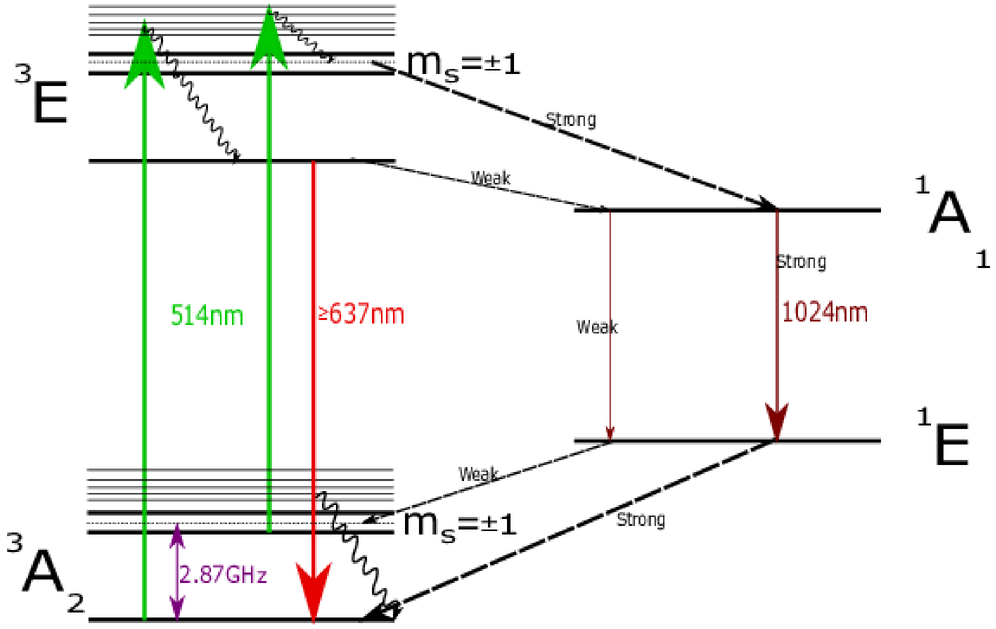

Figure 5.1: Energy level diagrams of an NV$^-$ defect in a stress-free diamond lattice. A green laser excites the system up into the vibrational continuum above the energy level. Phonons are radiated away and the state de-excites emitting a photon, possibly to the continuum above the ground state, where more phonons would be emitted, before returning to the de-excited state. Microwave spin polarisation puts the electrons into non-zero spin states which when excited decay preferentially via the two singlet states. This decay emits a photon in the near infra-red which is not detected if the experimental system is correctly configured. This gives rise to the distinctive troughs in the ESR spectral graph (visible in Figs. 5.2 and 5.3) [58].

atoms, two of these form a pair and the third forms a pair with an additional electron (probably from the lattice according to [53, p.146]) which is only present in the NV^- defect. The two lone pairs form a dipole which can be manipulated with magnetic fields and observed by measuring their magnetic field [54] [55].

The energy level diagram of an NV$^-$ centre (see Fig. 5.1) has been mapped out using a combination of optical and magnetic techniques [56] [57]. These defects display the interesting property of fluorescing, emitting red light when excited by green photons.

There are two radiative excitation/de-excitation modes. Between $^3A_2$ and ^3E, with a bandgap of 1.945 eV (637 nm) and between ^1E and $^1A_1$ of 1.190 eV (1042 nm) [59]; red photon and infra-red (IR) emissions respectively. $^3A_2$ is the ground state for this system, electrons can be excited from this state if they absorb photons of energy greater than 1.945 eV, they are excited to the ^3E level or beyond into a continuum of levels where they can have non-discrete energy values.

The ^aB_c notation is used to denote the energy levels in the system. The ^{a} describes the degeneracy of the state, $a = 1$ describes a singlet state and $a = 3$ describes a triplet state with $m_s = 0, +1, -1$ spin states. For a single electron system, the B would be lower case, in this case, the system is multi-electron in nature and therefore is described by an upper case A or E, these letters refer to the symmetry of the excitation state.

The system can in fact be excited by photons of any wavelength between 480 nm and 636 nm [53, p.146]. After a few nanoseconds [60], these excited electrons de-excite radiatively back to the ground state. They emit either a photon of wavelength equivalent to the gap between the states (637 nm), this is known as the zero-phonon line emission, or they emit some phonons into the diamond lattice and then emit a photon of longer wavelength. The emitted photons are of wavelength 637 nm or longer.

The second possible radiative decay, between ^1E and $^1A_1$, is only accessible if the electron decays from ^3E to $^1A_1$. Angular momentum, and therefore electron spin, must be conserved during such transitions, therefore the $^1A_1$ state is only likely to be occupied if the electrons are already in a state with non-zero m_s. If such is the case that the $^3A_2$ is occupied with $\mathrm{m}_s = \pm 1$, then electrons hit by pumping photons are excited to ^3E with spin$= \pm 1$ which then will decay to the $^1A_1$ state, before radiatively decaying to ^1E, emitting an infra-red (IR) photon of 1042 nm, and then back to the ground state. It is also possible to access this decay by giving electrons already in the ^3E a non-zero spin, and then letting them decay by the preferable route. It is less preferable energetically, and therefore far less likely, for an electron to gain or lose spin during an energy level transition.

It is possible to perform spin polarisation on the electron in the NV$^-$ defect using microwaves. This is carried out by applying a microwave field at the resonant frequency of a particular state. To spin polarise electrons in the $^3A_2$ ground state a microwave field of 2.88 GHz [61] is applied, and 1.42 GHz [62] does the same for electrons in the ^3E state.

5.1.1 Electron Spin Resonance

Electron Spin Resonance (ESR) or Electron Paramagnetic Resonance (EPR) is a measurement technique which involves looking at the spins of unpaired electrons within the sample material by aligning the electron spins with an external field and observing their behaviour. In the case of NV$^-$ centres, this is performed by exciting the electrons (often with a green laser) and observing the fluorescent light emitted. The intensity of the fluorescence is measured selectively, only counting photons with wavelength between 637 nm and 850 nm, ensuring that the light is being generated only by the $^3A_2$ to ^3E transition.

During ESR, the NV$^-$ centre is pumped by a laser of wavelength ≤ 637 nm and the intensity of emitted light is recorded. Simultaneously a microwave field is applied to the sample and scanned through a range of frequencies, the resultant data can be plotted on a graph of emission intensity vs microwave frequency. For the majority of the time, electrons are in $m_s = 0$ states and light of wavelength > 637 nm is collected. If the frequency passes through 2.88 GHz or 1.42 GHz during the scan, the electrons are spin polarised into $m_s = \pm 1$ state, causing them to decay via a different decay pathway. This decay emits light $\lambda \geq 1042$ nm, and will be filtered out and not detected resulting in a drop in intensity, visible as a dip in the intensity vs microwave frequency plot Fig. 5.2.

The final physical characteristic which makes NV$^-$ centres relevant to mag-

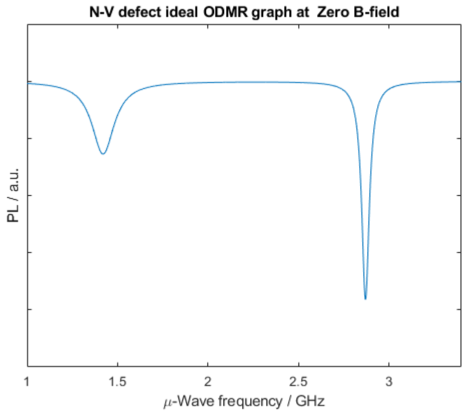

Figure 5.2: Depiction of the ODMR graph of an NV$^-$ centre experiencing zero external magnetic field, showing the resonances at 1.42GHz and 2.87GHz [63]. Plo of photoluminescence in arbitrary units vs microwave frequency.

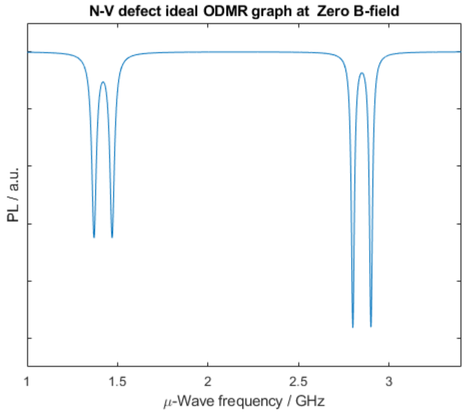

Figure 5.3: Depiction of the ODMR graph of an NV$^-$ centre, showing the Zeeman splitting due to the presence of an external magnetic field. The peaks from Fig.5.2 have separated into two and move apart linearly with magnetic field strength, up to $\sim$ 100 mT [64].

netometry is the presence of hyperfine energy level splitting. In a region of zero magnetic field, spin states of ± 1 have higher energy than that of spin $= 0$ state, but same energy as each other; i.e. $E(s_z = -1) = E(s_z = +1)$. However, when a magnetic field is applied to the system, the two states have different energies. This is due to one being parallel to the field, the other anti-parallel in a higher energy state. When the microwave frequency is scanned and the fluorescence intensity recorded, two dips appear on the plot where one did before as there are now two frequencies at which the IR emission decay route is more common, Fig.5.3.

It is noticeable that these two dips are symmetrical about the frequency of the resonance at zero magnetic field (B-field). The separation of these dips, ω, is given by the equation,

$$\Delta\omega = \frac{2\gamma B}{\hbar} \tag{5.1}$$

where γ is the electron magnetic moment. It is linear for magnetic fields up to 60 G and has a value of 28 MHz/mT [65]. γ and $\hbar$ are known constants, and the separation, $\Delta\omega$, is observable, allowing B to be inferred.

If the microwave can be scanned with sufficient precision and the luminescence intensity measured appropriately, then very small changes in magnetic field strength can be measured to high accuracy. As the NV$^-$ centre is on an atomic size scale, the spatial resolution of the magnetic field measurement can be very high, if a single NV$^-$ defect is used.

The spin Hamiltonian of the system is given by eqn.5.2,

$$\frac{\mathcal{H}}{\hbar} = \mathcal{D}\left(S_z^2 - \frac{2}{3}\right) + \gamma\mathbf{B}.\mathbf{S} + \epsilon_z E_z\left(S_z^2 - \frac{2}{3}\right) + \epsilon_{xy}\left\{E_x\left(S_xS_y + S_yS_x\right) + E_y\left(S_x^2 + S_y^2\right)\right\} \tag{5.2}$$

where the z-axis is the vector from the nitrogen atom to the centre of the vacancy site. Equation 5.2 [66] shows several components of the Hamiltonian. The term beginning with D is known as the zero field splitting (zfs), the $\mathbf{B}$ term refers to the magnetic interaction, and the final three E_i terms describe the interaction with electric fields and strain in the crystal. These components become significant when there is significant stress or strain in the crystal lattice which can cause large shifts in the ESR. For magnetic field measurements, crystals with minimal lattice stress are used in order to set the 'E' terms to zero.

Zero field splitting is the dominant spin interaction in the weak magnetic field ($<<$ 100 mT) region. An applied magnetic field causes there to be two spin resonances, as explained in the section above. This is due to the magnetic term where there are two values for m_s depending on the spin; for the positive spin state, $m_s = +1$, the energy is greater and for negative lower. The Hamiltonian in Equation 5.2 describes only spin states. Further terms are required if lattice stress is taken into account.

In the case of NV$^-$ magnetometry, only ideal samples are used, and the spin Hamiltonian of the ground state takes the form of eqn. 5.3 where $\mathbf{S}$ is the spin operator along the N-V axis.

$$\frac{\mathcal{H}}{\hbar} = \mathcal{D}\mathbf{S}^2 + \gamma\mathbf{B}.\mathbf{S} \tag{5.3}$$

Using NV$^-$ centres contained within nano-sized diamond particles to measure magnetic fields is an attractive prospect due, in part, to the physical attributes of the system. Due to the innate strength of the carbon lattice, the NV$^-$ centre is very resilient to external forces. Other physical systems used in photo-fluorescence applications alter their behaviour when heat or excess photon intensity is applied. NV$^-$ centres are extremely thermally stable and have remained reliable up to 600 K [67]. In fluorescence experiments, marker molecules can be susceptible to bleaching, a process during which the marker becomes less luminescent as it receives high photon flux. Eventually, an emitter may become permanently bleached and no longer photoluminesce. Bleaching of NV$^-$ centres is rare with very few occurrences reported, they tend to be able to withstand many hours of photon bombardment with little or no reduction of emitted photons. The bleaching occurs when the temperature of the defect is raised to a level sufficient for the extra electron to escape, leaving behind an NV^0 defect which does not fluoresce.

The photoluminescence exhibited by NV$^-$ centres makes them suitable for use as fluorescent markers in biological applications; diamond is non-toxic to cellular life and has very little interaction with organic organisms. This means that NV$^-$ magnetometry is compatible with the imaging of biological samples [68].

Whether a single defect or a cluster of defects is required, it is preferable to have a diamond of minimum possible size for magnetometry; it is important for the sample to be as close as possible to the defect/s with minimal matter between the emitter and detectors. The diamonds containing the defects are typically around 20 nm in size, they are therefore referred to as nano-diamonds. These can be fabricated by two methods. Chemical vapour deposition (CVD) is capable of producing layers of nano-diamond [69] and can control the occurrence of certain defects in order to create ideal diamond material. A layer of the CVD grown diamonds is separated from the substrate and mechanically ground into powder-like nanodiamonds. The more common method of production is known as the detonation method [70]. Detonation nano-diamonds are produced by packing either a synthetic (CVD) or a natural diamond in trinitrotoluene and detonating in an environment devoid of oxygen. The product is then heated in an autoclave for several hours to remove the unwanted products of the explosion. Diamonds produced by this method tend to be 5 - 10 nm in diameter [71]. The nanodiamonds are then observed using confocal microscopy in order to find how many if any, and what type of defects are present.

A nanodiamond for the purpose of NV magnetometry will ideally have the NV$^-$ defect near the surface to provide a greater probability of the emitted photons leaving the diamond in the direction of the observation device. It is possible, once a diamond with an appropriate defect is selected, to alter the surface shape, often to form a hemispherical dome around the defect, in order to maximise emission [72]. This means that emitted photons are more likely to intersect the surface of the diamond at angles close to the normal, greatly reducing the chance to total internal reflectance occurring.

The proximity of the diamond surface to the defect does, however, cause more lossy interactions between the defect spin and the surface bonds. This causes further spin de-phasing and reduces ESR coherence time [73].

The tetrahedral nature of diamond lattices means that the NV$^-$ centres are aligned along four possible axes. The Zeeman splitting occurs proportionally to the component of the applied external magnetic field, parallel to the defect axis. In a bulk diamond containing many NV$^-$ defects, the ESR spectrum contains many dips due to the four different defect orientations and the different magnetic field magnitudes experienced, due to the difference in the location of each. To extract absolute data about the external magnetic field, the orientation of each defect must be known. In the case of a nanodiamond containing a single defect, only the component of the external magnetic field in the direction of the NV centre axis is measurable. In bulk diamond with three or more non-parallel defects, the direction and the magnitude of the external field can be measured, this is a vector magnetometer [74].

5.2 NV$^-$ magnetometry theory

The starting aim of my PhD research was to construct a Nitrogen-Vacancy Magnetometer, in order to image samples up to 50 mm in diameter under ambient conditions. The system requires the ability to perform magnetometry using the NV$^-$ centre / confocal microscopy method, which requires scanning across the sample and maintaining a known distance between the sample and the NV$^-$ centre. It follows that the most straight forward way to achieve this is to make an atomic force microscope and combine it with a confocal microscopy system.

With this arrangement, it is possible to take a topographical image of a surface whilst simultaneously taking magnetic field strength measurements. This would require the AFM to operate normally, whilst producing a trigger signal to call the laser system to excite the NV$^-$ centre and the microwave field to scan, every time the nano-diamond (on the AFM tip) was at a particular position relative to the sample. At present, this high speed synchronisation is several improvement steps away, the process for using the magnetometer would be to run an AFM and then repeat the path travelled over the sample at a fixed height (using the AFM multi-pass mode) whilst performing confocal microscopy and scanning the microwave field to determine the magnetic field strength being experienced by the defect at each location. This re-scanning can be repeated several times with relative ease, allowing the collection of magnetic field data at several different heights, forming a data set of magnetic field strength over a volume of space above the sample surface. A single ODMR scan takes on the order of seconds, with accuracy improving proportionally to the square root of the number of scans taken.

Several adjustments have to be made to a standard confocal microscopy setup in order to use NV$^-$ defects to detect field strength. Any excitation laser light reflected back up the objective lens must be separated from photons emitted by the diamond, as this is the only information signal. This issue is particularly noticeable as the laser is many orders of magnitude brighter than the light emitted from a single NV$^-$ centre [75]. Whilst excitation can be performed with red light, it is preferable to use a wavelength further away from that of emission, in the case of this instrument a 514 nm pump laser is used. This allows the beam splitter in the confocal microscope to be replaced with a dichroic beam splitter. This has the same shape as a non-discriminatory splitter, but the reflective face is covered with a dichroic coating which has different transmission and reflection coefficients for different wavelengths of light. This allows the green light to be reflected, firstly down towards the microscope and objective lens, then any returning green light is reflected again away from the photo-detectors. The red light of the wavelengths which NV$^-$ centres are capable of emitting is transmitted through this splitter and towards the detectors. This provides an efficient way of separating the two wavelengths and counting the small number of photons emitted from a fluorescing NV$^-$ defect. As explained in chapter 4, a further long pass filter is used to filter out the remaining green photons.

Attaching the nano-diamond to the tip of the probe is made difficult by the short ranges and the variety of forces acting between the two. If the nano-diamond is sufficiently far away from others like it then there is less chance of picking up the wrong one. The outer surface of a diamond lattice tends to make bonds with hydroxyl (OH^-) molecules which form the outer coating [76]. A convenient way of "glueing" a diamond to the tip involves coating the probe in Poly-L-lysine, a positively charged polymer which will form an ionic bond with the surface of the diamond and hold it in place [30]. It has also been suggested that attaching the diamond to the tip may be possible using an ultraviolet-curable glue [77].

In naturally occurring diamond, the number and grouping of defects within the lattice is quite random. Only diamonds containing NV$^-$ defects are of any interest for magnetometry. The diamonds are confocally scanned and checked for photoluminescence. There are different benefits to having large clusters of defects or single NV$^-$ centres. A single defect will allow for greater spatial resolution of the generated image. The size of a single defect is very small ($<<$ 1 nm) and therefore the B-field only from that region is measured. A larger cluster of defects has a larger measurement area, lowering the spatial resolution of such a measurement, however, more defects increase the sensitivity to B-field. As the defects are likely to be at different orientations, the PL vs microwave frequency graph will have more features which all move with a varying field, allowing the field strength to be determined more accurately. Nanodiamonds with up to 100 NV$^-$ centres have been successfully used for high sensitivity measurements, achieving sensitivity of 100 pT/$\sqrt{\text{Hz}}$ [78]. Single defect magnetometry has achieved spatial resolution of 1 nm [79] and magnetic field sensitivity 10 nT/$\sqrt{\text{Hz}}$ [80].

When performing microscopy with a single NV$^-$ centre, it is important to know the orientation of the dipole which is always perpendicular to the N-V axis. The N-V axis is defined as the vector going from the nitrogen atom into the centre of the adjacent vacancy, this is along the $\langle 111 \rangle$ crystal axis [81] and is known as the major symmetry axis. This can point in one of four directions, parallel to the four possible orientations of bonds in the diamond lattice, the minor symmetry axis is orthogonal to the major symmetry axis and points from the major axis to one of the three carbon atoms nearest the vacancy [59]. The electron spin resonance effect is most visible when maximum Zeeman splitting occurs, this happens when the magnetic field is parallel to the N-V axis and the defect experiences maximum magnetic field strength [82]. Without this knowledge, the splitting and ESR can only provide information on the strength of the magnetic field projected along the defect axis and not the absolute strength of the field. This effect can be counteracted by knowing the orientation of the defect axis. The direction of the magnetic field can then be determined by taking further measurements at differing angles to the sample [59].

5.2.1 Photon Anti-bunching

When performing high spatial resolution magnetometry, the number of defects within the nanodiamond must be known, and a single defect diamond chosen. The number of defects can be calculated to a particular statistical certainty by observing the photoluminescence with two single photon counters. In our particular instrument, Single Photon Avalanche Photodiodes (SPADs) are used. These instruments are able to count single photons every few nanoseconds and coupled with the appropriate counter this makes it possible to detect a photon and assign a time of arrival to it inside the software.

To be certain of having a single defect, a single photon emitter, the collected luminescent light is passed through a 50-50 beam splitter and then directed into two SPADs, one on each output of the splitter. The counting and time-tagging is then performed. The software then plots the time between consecutive photon arrivals, and if a single photon emitter is producing light, then there will be no instances where two photons arrive at both detectors at the same time. A single quantum emitter will, like the SPADs, also have a refresh rate of a few nanoseconds, making it impossible for a single defect to emit two photons at once. The optical set-up is that of the Hanbury Brown-Twiss experiment [83].

The phenomenon of photons never being emitted simultaneously is known as photon anti-bunching. The software plots the time between photons (τ) vs the second order correlation ($g^{(2)}(\tau)$). This refers to the intensity of the incoming beam and the temporal separation, it is given by equation 5.4 [84, .p.60],

$$g^{(2)}(\mathbf{r}_1 t_1, \mathbf{r}_2 t_2; \mathbf{r}_2 t_2, \mathbf{r}_1 t_1) = \frac{\langle \mathbf{E}^*(\mathbf{r}_1 t_1)\mathbf{E}^*(\mathbf{r}_2 t_2)\mathbf{E}(\mathbf{r}_2 t_2)\mathbf{E}(\mathbf{r}_1 t_1)\rangle}{\langle |\mathbf{E}(\mathbf{r}_1 t_1)|^2\rangle\langle |\mathbf{E}(\mathbf{r}_2 t_2)|^2\rangle} \tag{5.4}$$

where $\mathbf{r}$ is the spatial location of the wave and is constant and the same in all instances above as the measurement is taking place at a single, fixed location; $\mathbf{r}_1 = \mathbf{r}_2$. t_1 and t_2 are the arrival times of the two photons which are being tested for correlation. In the case that photons arrive at the same instant, $t_1 = t_2 = 0$ and $g^{(2)}(\mathbf{r}_1 t_1, \mathbf{r}_2 t_2; \mathbf{r}_2 t_2, \mathbf{r}_1 t_1) = 0$. In the case that $g^{(2)}(0) > 1$ the light is described as bunched, for $g^{(2)}(0) = 1$, the light is coherent, when $g^{(2)}(0) < 1$ then the light is anti-bunched. In reality the correlation graph for an anti-bunched emission source would have a finite probability of photons arriving with $\tau > 0$, and the function would descend to a probability of zero for $\tau = 0$ symmetrically from the positive and negative direction. (See figure 5.4). The physical setup for the correlation counting can be viewed in the diagram in Fig.5.5.

5.3 Atom Chip theory

Clouds of ultra-cold atoms can be cooled to temperatures only a few nano-kelvin above absolute zero. At these temperatures they exhibit strange behaviours, groups of atoms with integer spins form a Bose-Einstein Condensate (BEC) [86]. This can be viewed as another state-of-matter, akin to solid or liquid, in which all of the atoms occupy the same quantum state, the lowest energy level. Experiments can be performed on BEC that test the validity of the current physical theories at the quantum level to see whether any breakdown occurs. Ultra-cold caesium atoms are currently used in the highest standard atomic clock, capable of keeping accuracy to around 1 part in 10^{15} [87] and are used to maintain the official stable, continuous timescale, International Atomic Time, on which global communications and satellite geo-location are totally dependent. Atoms at nano-kelvin temperatures are easily measured and observed using current techniques, therefore highly accurate sensors can be made using knowledge of quantum effects

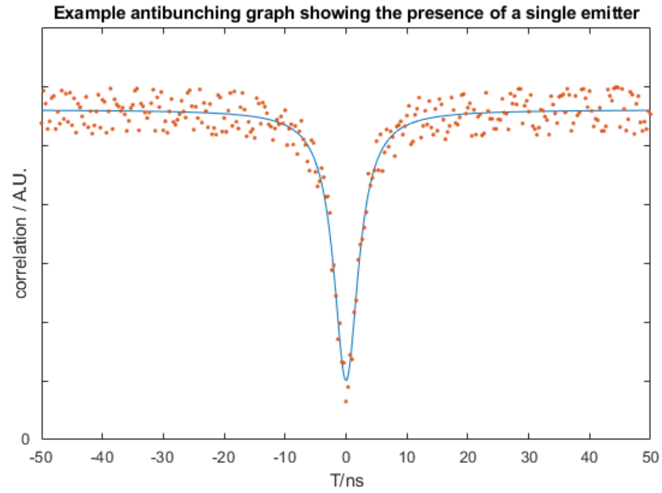

Figure 5.4: Example graph showing antibunching. The probability of two photons being detected zero seconds apart is very low; the value is non-zero as measurement resolution has a minimum limit [85].

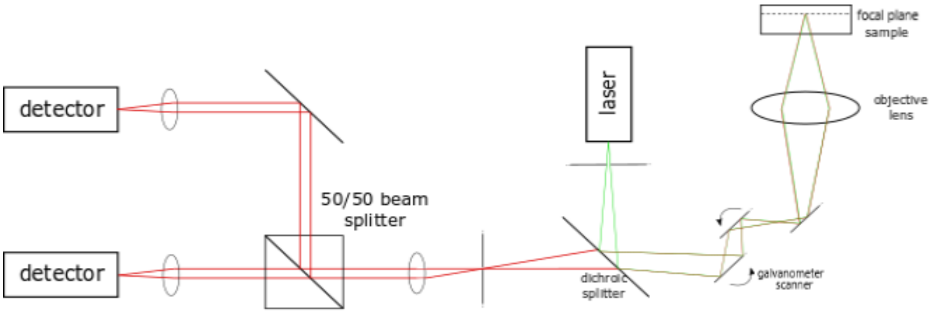

Figure 5.5: Confocal microscope setup including HBT interferometer with which to perform correlation counting/antibunching experiments on the photon emitters.

to extract data about local gravitational field strength, or to make gyroscopes or magnetic field-strength sensors [88].

Atom cooling is performed using a combination of techniques. Doppler cooling reduces the temperature of the group by aiming six laser beams into the centre of the sample. In the laboratory reference frame, the photon wavelength is Doppler shifted, so only when the atoms are moving towards the beams does the wavelength match an atomic transition of the atom. The photons are therefore absorbed only when moving in the opposite direction to the atom, allowing the kinetic energy of the atom to be absorbed and the momentum reduced. When the photon is absorbed the atom is in an excited state, spontaneous emission causes the photon to be emitted in a random direction, so on average over many cycles, the atom is slowed down. When the kinetic energy of every atom in the cloud is reduced, the temperature of the cloud is reduced. The atoms are contained by a magnetic field, and the combination of Doppler cooling reducing the energy, and the magnetic field preventing the escape of the atoms is referred to as a Magneto-Optical Trap (MOT). This type of cooling takes many thousands of photon absorptions per atom, and has a lower temperature limit; the energy of a single atom may not become lower than that of a single photon when cooling by this method. The minimum limit has actually been found to be higher than this due to the non-zero linewidth of the atomic transitions used for cooling, it typically has a value of $\sim$ 100 µK [89].

The Doppler limit can be beaten by using circularly polarised laser beams to absorb the kinetic energy of an atom as it moves against the polarisation gradient. This is called Optical Molasses for neutral atoms, or Sisyphus cooling. Minimum temperatures are experienced in the region of $\sim$ µK, dependant on which atoms are being cooled [90].

The final method of reducing temperature is known as evaporative cooling. Simply by reducing the field strength used to magnetically trap the atoms, the hotter atoms with more kinetic energy escape, leaving behind the cooler ones, reducing the temperature of the cloud. By this method, the temperature can be lowered to $\sim$nK.

These techniques are used in combination with each other, in order to cool atoms, however, every setup requires equipment to produce three pairs of orthogonal laser beams, magnetic trapping fields, and this takes place inside ultra-high vacuum (UHV) in order to eliminate the presence of any other atoms.

This equipment tends to take up a large percentage of the volume of a reasonably sized laboratory and is therefore not very portable. Methods of miniaturising the experiments are of great interest to those investing in quantum metrology.

One interesting idea is that of atom chips, that are fabricated on dielectric or semiconducting wafers. These could take one laser beam as the input and, through a series of splitters and mirrors built into the surface, generate the six overlapping beams with which to cool the atoms. Also etched onto the chip are current carrying nano-wires which will be shaped so that as current flows through them, the correctly shaped electric and magnetic fields are produced to confine a cloud of cooled atoms a fewµm above the surface [91].

The wires generating the local fields tend to be 2 µm thick thermally evaporated gold, are 5 - 10 µm wide and are separated from other wires by 5 - 10

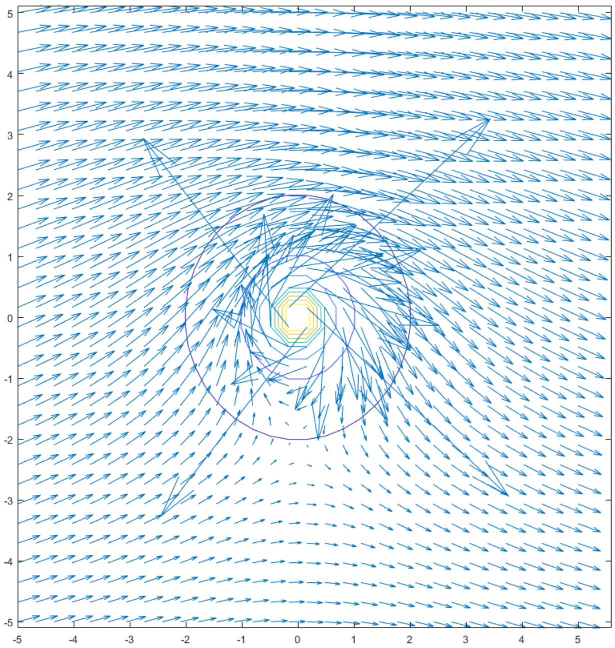

Figure 5.6: A current carrying wire on an atom chip generates a cylindrical magnetic field (in this case, current travels into the page). Lines on which all points have equal field strength are visible emanating radially from the wire (in the centre of the plot). An external magnetic field is applied at a distance, providing a uniform field strength across the region surrounding the wire, with little field curvature. The field strengths are adjusted so the field appears as in this figure, the trapping region, in this case, is just below the wire, if the current was reversed the trap would be just above the wire.

µm. Atoms can be trapped in the magnetic potential well 40 µm above the wire [2, p.385] formed from the local fields and a uniform magnetic field. Maximum magnetic fields generated are typically no more than 10 mT. Magnetic sensitivity of 0.1 mT is therefore required to image these fields with useful spatial and magnetic resolution.

At Nottingham, the focus is on developing the chips with gold wires on the surface. These wires can take several forms but they are often based on a very simple arrangement. A single wire, with a current passing through it, will generate a cylindrical magnetic field centred on the wire. If an external field is applied at a large distance, this magnetic field has a much larger radius of curvature than the field from the wire, the field vectors add together forming a field with a local minimum in a line along the wire but some distance above. This can be seen in Fig.5.6 and Fig.5.7 [2, p.40].

Field generating wires come in increasing complexity and increasing effectiveness. For example, "H", "Z", and "U" traps form two maximum magnetic fields either side of a minimum (see Fig.5.8), allowing trapping without the need for an external field. [2]

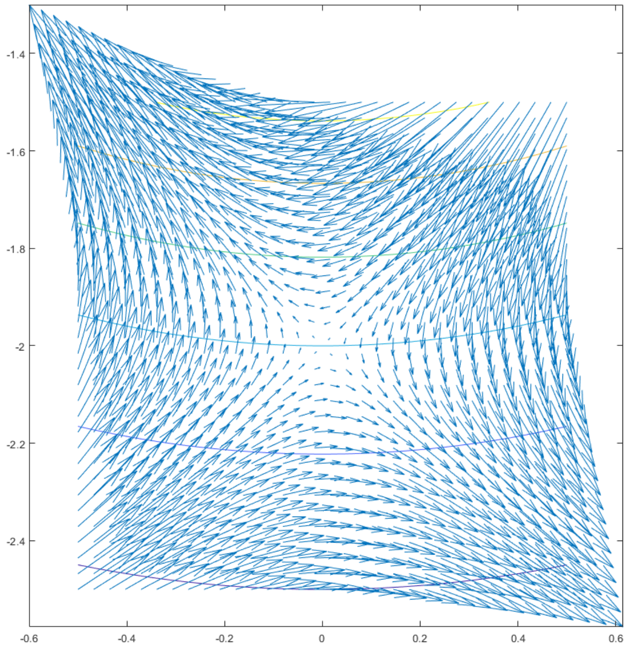

Figure 5.7: A plot of the field generated in Fig. 5.6 focusing on the trap region. The trap is saddle shaped and runs into the page, parallel to the axis of the wire, along its length. The solid lines mark lines of equal magnetic field strength generated by the current carrying wire on the atom chip.

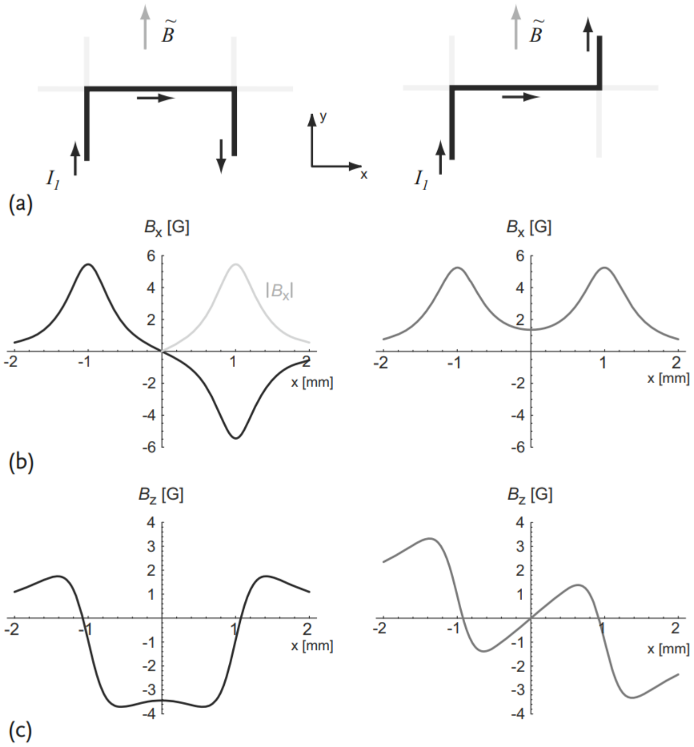

Figure 5.8: Diagram of H and Z traps, taken from [2, p.43]. (a) shows the wires and path taken by the current, (b) and (c) show the resultant fields, for each trap in two orthogonal planes.

Rotating traps can also be used, creating a simple magnetic potential well from an arrangement of wires. Two such arrangements are placed perpendicular to each other and powered one at a time sequentially. As the frequency of powering on and off is increased, this gives the effect of a rotating potential well, so the charged atoms remain in the middle at the lowest point of the potential and can never fall out the sides [2, p.44].

5.3.1 Fabrication

Atom chips have to be constructed in a clean-room environment and each stage of the process can take between several minutes and several hours.

The wires are deposited onto the surface of the chip by first patterning a thick photoresist and then evaporating 2 µm of gold onto the chip. When gold evaporation is complete the chip is cleaned with a solvent to remove the photoresist and any gold attached to it, leaving behind only the pattern of gold wires.

Microstructure within the wire can cause spatial variations in the current density and so the magnetic field minima. This is where the necessity for an NV^- magnetometer arises. To test a chip designed to produce magnetic fields, one can attempt to use it, to align cooling lasers above the surface in a vacuum, power the chip, and try to cool atoms. This, however, is a difficult process even when the chip is perfectly formed. The NV^- magnetometer would provide a method of measuring the surface topography of the chip as well as the magnetic field strength and direction in the space above the sample under ambient conditions within 24 hours of fabrication.

The nano-wires are typically in the region of 300 µm wide and ∼10 µm deep. An AFM image of the surface would provide useful information on how the wires have formed. Often the edges of the wires are not perfectly clean and straight, this can affect the shape of the magnetic potential above the wires and could be reflected in the magnetic field [92].

This, coupled with the imaging of the magnetic field generated, would provide far more rapid feedback to those growing the chips and allow the process of perfecting the chips to take place more efficiently.

5.4 NV^{-} centre microscopes

Maletinsky et al. describe the use of machined diamond nano-pillars to hold an NV^{-} centre close to a sample in order to measure magnetic field strength [93]. The surface sensing is performed by an AFM built in-house, mainly from Attocube components, the fine motion range is 40×40×4.5 µm with sub-nm resolution at room temperature. The microwave field was applied to the sample using a 25 µm diameter gold wire, placed within 50 µm of the defect on the surface of the diamond. Machining the diamond to bring the defect closer to the surface improves photon detection (and therefore magnetic field sensitivity) by making it easier for emitted light to leave the diamond. Requiring electron-beam lithography equipment and the specialist knowledge necessary to operate it successfully is an added barrier to functionality, but could be a useful way of improving our instrument in the future. The scan range of this magnetometer is significantly smaller than ours, particularly in the vertical axis. Delivering microwaves by a straight wire on top of the sample works, but is an inefficient way of generating a microwave field.

Rondin et al. combined an AFM with a confocal microscope to produce a scanning NV^{-} magnetometer [85]. Although the scan range is not specified, the largest scan referred to is a 5×5 µm scan and the tallest features measured in the paper are several hundred nm high. An Akiyama probe is used as the cantilever, a 50 µm pinhole selects the emitted light for measurement and a 100× magnification microscope objective with a working distance of 1 mm is used. Helmholz coils are used to apply a DC magnetic field up to a maximum value of 15 mT to determine the orientation of the defect. Whilst the magnetometer is very effective, the scan range is not very large and our instrument improves upon this. We found that using a microscope objective lens with a 1 mm working distance caused the housing of the lens to collide with the Akiyama probe preamplifier, the only way to avoid this would be to tilt the Akiyama tuning fork until it was horizontal, less than the required 11^{o} angle necessary to ensure the AFM probe contacts the sample at 90^{o} to the surface.

In his thesis [94], Kevin Kai Chang describes the design and build of an NV^{-} magnetometer, during which he, at first, attached nanodiamonds to the tip of an AFM probe, and subsequently fabricated pillars of diamond containing NV^{-} centres in order to use them as probes for an NV magnetometer. The XYZ range of motion of the sample stages is 20×20×6.6 µm, each with a resolution of 0.6 nm, the cantilever motion is detected by the reflectance of a laser beam and the system is in an inverted configuration with the cantilever and NV$^-$ defect above the sample and the microscope objective probing and observing from underneath. The laser is pulsed using an AOM which produces a rise time of 30 ns, a microwave synthesiser produces the microwaves and has a range of 200 MHz - 20 GHz and a resolution of 1 mHz. A 30 µm pinhole is used in the telescope to deselect background light and placed before band-pass and long-pass filters. The inverted nature of this microscope means that samples can only be imaged if they are transparent and the PL light can pass through it. The relatively slow rise time of the AOM means that faster pulse sequencing would be difficult, for instance, Rabi oscillations with reasonably strong microwave fields would be difficult to measure.

Schloss et al. at MIT use a nanodiamond containing several N-V centres to measure the magnitude and direction of sample magnetic fields [74]. The system is inverted, the emitted light is collected by a MO but the pump laser beam is applied from outside and has to arrive at a large angle of incidence to get past the lens, therefore this is not a confocal setup. The microwaves are applied by a small coil on the opposite side of the sample to the microscope lens. The microwave system is extremely complex, allowing four different microwave frequencies to be applied to the sample simultaneously. There are no scanning stages, the magnetic field is measured at a fixed location, but can be measured in real-time to observe changing fields. Such a complex microwave system would be unnecessary to basic perform NV magnetometry, where continuously swept frequencies or pulsing at a single frequency is sufficient, however, elements of the microwave setup could be incorporated into ours. The lack of scanning stages means that extensive modification to this system would be required to provide scanning magnetometry capability.

Stürner et al. used nitrogen-vacancy defects in diamond to devise a compact magnetic field sensor of 2.9 cm^3 volume [95]. This device is extremely compact, very portable, requiring a power supply of only 1.5 W to power the pumping LED, the Hamamatsu photodiode and the microwave source. Photon shot noise is not the limiting factor on magnetic sensitivity, however, a reasonable sensitivity of 31 nT/$\sqrt{Hz}$ is achieved. This is a fantastic exercise in miniaturisation and reveals the huge scope for using these sensors in greater numbers in far more portable instruments. Within the setup there is no AFM and little room for expansion of capabilities or adaptability to other tasks, there is no ability to scan a sample with any great precision.

Webb et al. constructed a similar device to Stürner [96], a solid-state, compact, NV magnetometer, designed for low power consumption and portability. This also has no AFM and no scan function. The microwave antenna is affixed to the top surface of the diamond, the wavelength filter and the photodiode to the bottom surface. This device is larger, however, it has a better sensitivity of 10 nT/$\sqrt{Hz}$.

NV magnetometers have to scan microwave frequency in order to view the ESR data. In most cases, microwaves are projected at the sample by passing the oscillating current through a very thin copper wire affixed to the surface of the sample, positioned as closely as possible to the diamond, with maximum power (typically 1 W) passing through the wire. By this method, a sufficiently strong magnetic field is generated in the region close to the wire that ODMR is visible. In a few cases, the microwave antennae are formed into spring-like coils and placed at a distance from the diamond, designed to project the microwaves along the axis of the coil directly towards the defect. Recently more groups have started to follow the example of Sasak et al. [97] in producing tuned flat coils on top of which the sample is mounted. Due to the improved efficiency in converting electrical current into a microwave field, this is the method used in our instrument.

Reviewing the literature from the preceding three chapters, it is obvious that whilst there are instruments with similar and in some cases better specifications than the one described in this thesis, none of them have the wide expanse of abilities that this instrument does. Our instrument will perform large range AFM scans before imaging a sample in reflectance, observing photoluminescence and/or electroluminescence, and then repeat any of these scans whilst applying a microwave field to the sample. The probe positioning, the spatial scanning of the sample, the scanning of frequency, and the photon flux count is all performed with high precision due to the high resolution of the equipment employed.

5.5 Nanodiamond observation methods

We received our nano-diamonds, which were generated using the detonation method, from Diasense. Once the diamond has been detonated, the resultant powder is filtered to try and reduce the concentration of graphite made during the explosion, and then suspended in a methanol solution or high-purity water. This sample appeared to be highly contaminated, this is visible in the results section.

We also used another sample of nanodiamonds, suspended in methanol, from The University of Warwick. These diamonds were grown by Element6, implanted with nitrogen and annealed by Warwick and then thinned and ground up using silicon balls in Cardiff.

The nano-diamonds are spread onto a substrate, in this case, a silicon wafer, in a thin layer to minimise the piling up of the particles. This should allow any single-defect diamonds to be visible and separate from others. The first method of application attempted was to simply place a droplet of the methanol suspension from Diasense onto the substrate and wait for the methanol to evaporate.

The result of this can be seen in the results section of this chapter and it is apparent that as the methanol evaporated, it did so from the outside inwards. During this process, surface tension caused the nano-diamonds to be dragged along with the receding edge of the methanol, resulting in the clustering of the samples. This is called the 'coffee ring effect' as the shapes produced is characteristic of the ring left by spilt coffee.

In Fig. 5.19, clusters of defects are visible, none of which exhibit anti-bunching characteristics. Also in the image is a dried-on layer, this could be some remaining methanol or other solvent. This also fluoresces slightly as the light returning is brighter than any reflected green would be after the splitter and filters. Many solvents fluoresce, so this is not unexpected.

It has been shown that nano-diamonds in suspension are best dispersed onto a substrate after being treated with ultrasound [98]. Initially, the suspension

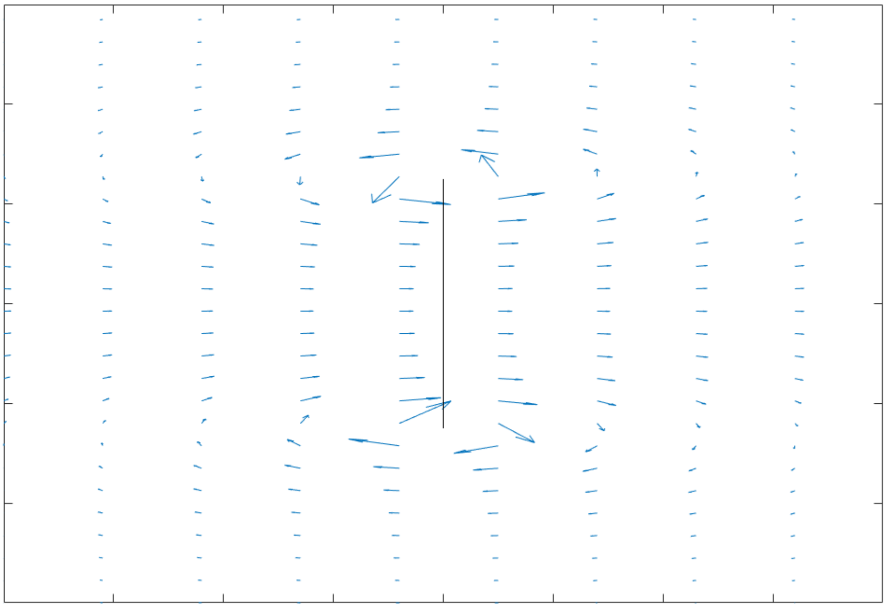

Figure 5.9: Side view of a single coil of the Helmholtz pair (indicated by the black line), and field produced in z-y plane through the centre of each coil (x=0). Vector direction of field is represented by the arrows, and magnitude of the field strength by the length of the arrows.

should be vibrated in an ultrasonic bath for several hours to break up the larger clusters of nano-diamonds which tend to clump together. A droplet of this can then be loaded into an applicator, for which most groups now use a nebuliser. In our case, we use an Omron MicroAIR U100 Portable Nebuliser, which uses ultrasound to separate the liquid suspension into a mist which then distributes much more uniformly over the sample.

Once the nano-diamond has been selected and attached to the upper side of the AFM probe using Poly-L-lysine, the orientation of the NV$^-$ defect must be determined in order to be able to use it to measure the strength of external magnetic fields. In order to find the orientation, NV magnetometry must be performed using known magnetic fields.

5.5.1 Magnetic field generation

Initially, the decision was made to use Helmholtz coils to generate a variable, known field strength at a defined angle, with three pairs of coils so that a field could be generated in any direction.

Helmholtz coils (HH coils) are pairs of electrical coils on the same axis, producing parallel magnetic fields, separated at such a distance that the magnetic field over a region at the centre is fairly uniform.

This property is necessary and a single coil is more difficult to use, as the position of the NV$^-$ centre relative to the coils is only measurable to a certain

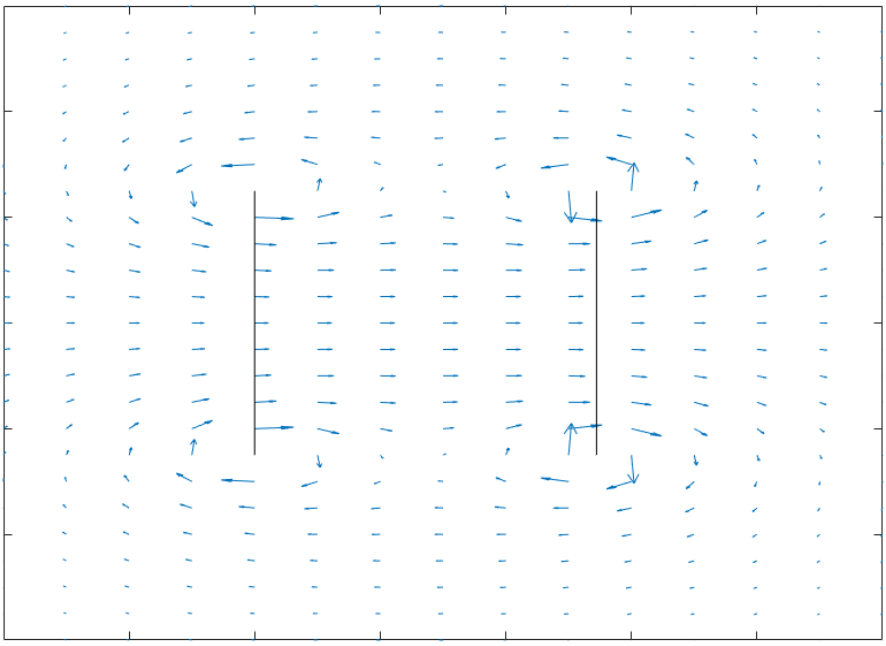

Figure 5.10: A pair of square Helmholtz coils at optimum separation. Field strength and direction are shown in the x=0 plane. The region in the middle, close to the symmetry axis of the coils has arrows pointing along the same vector with very similar lengths. This demonstrates how the coils generate a region of uniform field in their centre, allowing an NV$^-$ defect to be probed for changes in field strength and reducing the importance of its spatial position on the measurement. In the case of the observation of a cluster of defects, the larger region of uniformity of magnetic field increases T$_2$ relaxation time, reducing spin dephasing, by applying a more similar field to all the defects.

level of accuracy. A pair of coils can generate a B-field which varies only 0.1% over a 10 mm range at the centre, meaning the NV^- defect is experiencing a well-known field; however, such a large area of uniformity is only possible if the coils are separated by the correct distance [99].

For circular coils, the separation required for maximum central uniformity is given by [100],

$$x = \frac{R}{2} \tag{5.5}$$

where x is the axial separation of the coils and R is the radius of the coil.

Square coils provide an almost identical effect in the centre, however, they are often used preferentially over circular coils as they are easier to manufacture and support and they provide a larger internal volume giving more space for other experimental components.

For square coils, the optimum separation distance is given by,

$$x = 0.5445 * L \tag{5.6}$$

where L is the length of the side of a coil [101].

The biggest constraint for our NV magnetometer is the lack of available space due to the expected size of the atom chips (50 × 50 mm). A B-field strength of 1 mT would provide sufficient field strength for easily visible splitting; given HH coils are often used for cancelling the magnetic field of the Earth typically 250 µT - 650 µT [102], this is a strong field to generate. As coils get larger so does the distance between the centre of the coils and the origin of the B-field, and also the resistance of the wire increases. This means the magnetic field strength decreases in a square relationship with coil radius/side-length.

The nano-diamond must be in the centre of the HH coils, this is connected to the Akiyama pre-amplifier and the Smaract stage. The diamond must also be in the focal point of the objective lens which is only 3.4 mm away, vertically upwards. Nanometers underneath the probe is the sample, requirements of the instrument instruct that sample of up to 50 mm diameter must be loadable and scannable.

One of the biggest constraints was the vertical space, the nano-diamond is only to be ∼35 mm above the Piezoconcept x-y stage. This led us to propose that rectangular HH coils would provide the ability to load sufficiently large samples whilst keeping the coil separation and resistance of the wires to a minimum.

The coil separation distance for rectangular coils is less well known and there is little literature on the subject. There are some instances where researchers used the same separation ratio as for square coils picking either the longer or shorter edge to multiply by 0.5445 to find the separation. I wrote a Matlab script to model the magnetic field strength along the coil axis for rectangular coils to determine the separation required to provide a maximal uniform region in the centre. The script modelled each coil as four finite, current-carrying wires. An infinite current-carrying wire produces a magnetic field,

$$B = \frac{\mu_0 I}{2\pi R} \tag{5.7}$$

where B is the magnetic field strength, μ_0 is the permeability of free space, I is the current passing the wire and R is the distance between the location of measurement and the closest point of the wire.

The wires in the coil are, of course, of finite length, not infinite and therefore the B-field contribution from a finite wire is given by,

$$B = \frac{\mu_0 I}{4\pi R}(\cos\theta_1 + \cos\theta_2) \tag{5.8}$$

where θ_1 and θ_2 are the angles between the wire and the vector from the left end of the wire to the measurement point, and from the right end of the wire to the measurement point respectively.

The code calculated only the magnetic field along the coil axis, therefore $\theta_1 = \theta_2$ and the equation simplifies to,

$$B = \frac{\mu_0 I}{2\pi R}(2\cos\theta) \tag{5.9}$$

The code simulates four finite wires for every turn of the coil and calculates their distances from the centre. It adjusts for the fact that wires are wound so they stack in layers alternating between 10 turns wide and 9 turns wide in order to optimise packing. The calculation is then performed for the second coil and the magnetic field strength plotted vs distance along the coil axis. Coil separation is varied until maximum central uniformity is achieved and this value is plotted against the length of the long side and the length of the short side of the coil.

As more data is collected, this forms a 3-D plot and the data occupies a surface. The data were fitted using a least-squares regression method. The simulation was only run between 20 mm and 200 mm side length as the coils had to be within this size range, therefore the best-fit equation should not be expected to be valid outside of these limits.

The data surface had a gentle curve and x-y symmetry, but no overwhelmingly obvious shape, the best fit was achieved with a 3rd order polynomial expression relating side lengths to separation. This allows the ideal coil size and separation to be selected.

The best-fit plane was found to be,

$$\begin{split} s =& 0.1947 + 0.7229x + 0.04508y - 0.04425x^2 + 0.0535xy - 0.01434y^2 \\ &- 0.001566x^3 + 0.00425x^2y - 0.003202xy^2 + 0.0006486y^3 \end{split} \tag{5.10}$$

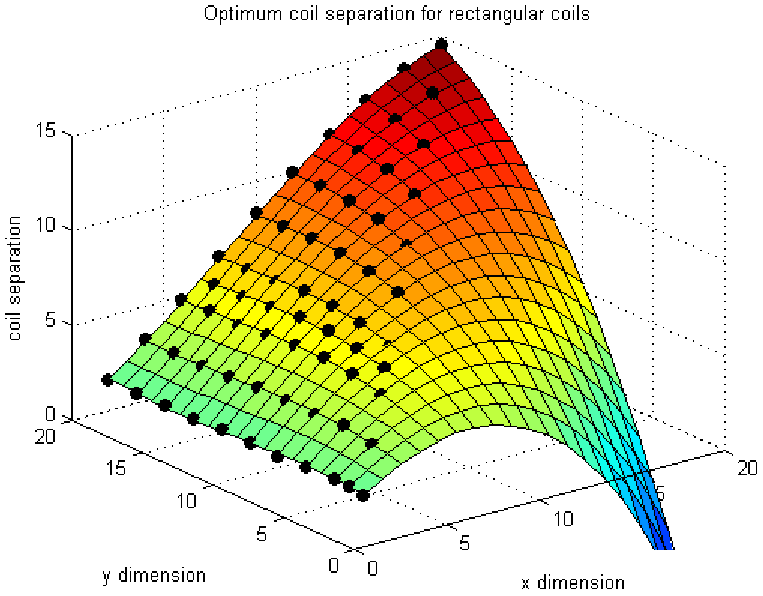

Figure 5.11: Graph of coil dimensions vs ideal coil separation for maximum field uniformity at the centre of the coils. Circles denote values obtained using Matlab model, surface is the best fit solution displayed in eqn.5.10

where s is the idea coil separation, x is the width of the coil and y is the height of the coil. The sum of squares due to error was 0.3142, and the R-square value was 0.9996 for this fit.

The frames for the coils were manufactured and the coils wound upon these. Testing revealed that coils of this size require significant power. To produce even 0.1 mT, the coils were not able to dissipate generated heat sufficiently well to prevent overheating. The coils were provided with 30 V initially, producing a current of around 10 A, although resistance increased with heat and the power supply could not provide enough power causing the current to rapidly decrease. It took a period of two hours for the coils to reach a stable temperature and therefore resistance and current. It was at this point that the magnetic field strength stopped decreasing and became stable. The coil surface temperature reached over 100 ℃ and the epoxy holding the coil in the mount began to melt. This temperature would be very unsuitable in the set-up as it would affect the resonance of the AFM cantilever, and if the MO were to become differentially heated then it may affect the alignment of the optics. There was no possibility for air cooling with a fan due to the effect this would have on the AFM tip or possibly on the stability of the sample.

The result was that the coils were unsuitable for use in this setup and another method was required to generate a known magnetic field across the sample.

The alternative method of applying a known field to the nano-diamond is by using a strong permanent magnet. Neodymium magnets can have extremely strong magnetic fields, sometimes ∼0.1 T on their surfaces, the field strength decreases in an inverse squared relationship with distance from the surface. The larger the magnet is, the stronger the field both on the surface and at a distance. It would, therefore, be possible to characterise a neodymium magnet, to measure the field strength along the axis extending from the pole of the magnet, and then use this as the magnetic field with known strength and direction vector to probe the NV^- centre. Using a stronger magnet allows the magnet to be further from the sample than a smaller one whilst still producing the same field strength, however, being further from the surface of the magnet means that the magnetic field gradient across the region of the diamond will be shallower. This results in a reduced change in B-field strength across the diamond; allowing us to know the magnitude of the B-field with improved accuracy.

The magnet must be moved around the sample, a minimum of three measurements over two or more different planes must be taken in order to determine the dipole vector. The magnetic field strength experienced by the defect must be known, and the simplest way to do this is by maintaining a constant separation between the magnet and the defect and by keeping the pole of the magnet pointing directly at the defect. This can be performed by mounting the magnet on two, orthogonal, rotating stages, whose axis of rotation both point directly at the NV^- centre. This allows the magnet to be moved around the sample by adjusting the azimuthal and polar angles. A linear motion stage could be used to bring the magnet closer or further from the centre, this would vary the field strength experienced by the nano-diamond. Stages used are made by Smaract, the same company as made the probe positioning stages, the controller can be attached to the existing frame for that of the other stages. The stage is not able to complete a full 360^o rotation due to space constraints, particularly the Akiyama pre-amplifier and motion stages will prevent the stage from passing on one side, however, this will not prevent the necessary measurements from being made.

This setup is currently not yet operational and integrated into the instrument but a CAD drawing is visible in Fig. 5.12. For the time being, the permanent magnet is manually placed at a known distance from the nanodiamond sample in order to provide a magnetic field. A distance of 100 mm provides a field of 2 mT and is theoretically strong enough to view Zeeman splitting in the ODMR spectrum.

5.5.2 Microwave generation

To apply the microwave field in order to measure ODMR, the signal must be generated, amplified and emitted using an antenna.

For initial tests, a simple configuration was used. The signal generator used is the Model 845 from Berkeley Nucleonics, which can generate 100 kHz - 20 GHz with 1 mHz resolution [103]. It is capable of performing frequency sweeps. In order to enable fast pulsing, an RF switch is used which is controlled by a 5 V TTL pulse, where a high pulse enables transmission of the signal through to the amplifiers. The rise time of the switch is around 10 ns. This switch is triggered by the Pulse Streamer 8/2 made by Swabian [104]. This receives a pulse from the Qudi software and it then sends TTL outputs to the microwave switch, the microwave generator to initiate output and/or frequency scanning, the laser to flash the laser on for the duration of the high pulse and to the SPADs, causing them to count photons for the duration of the pulse. It is simple to program the Pulse Streamer using a Python script and this is how ODMR scanning is

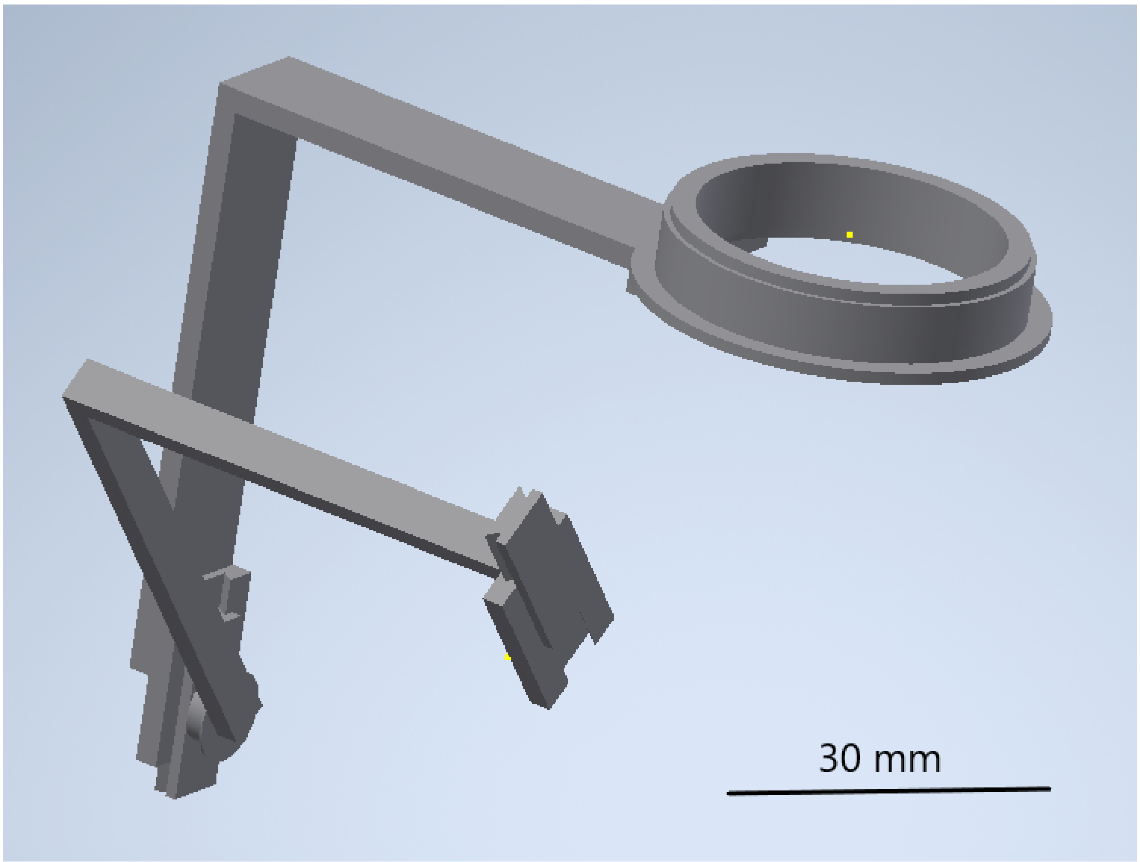

Figure 5.12: CAD (AutoDesk Inventor) drawing of the stage system which will rotate a permanent magnet around the nanodiamond. The rotation stage will be affixed around the MO so it rotates about the centre axis of the MO. One linear stage is used to adjust the second rotation axis to ensure it is aligned exactly with the diamond sample, the second linear stage is attached to the magnet and provides some degree of field strength control by moving the magnet nearer and further away from the sample.

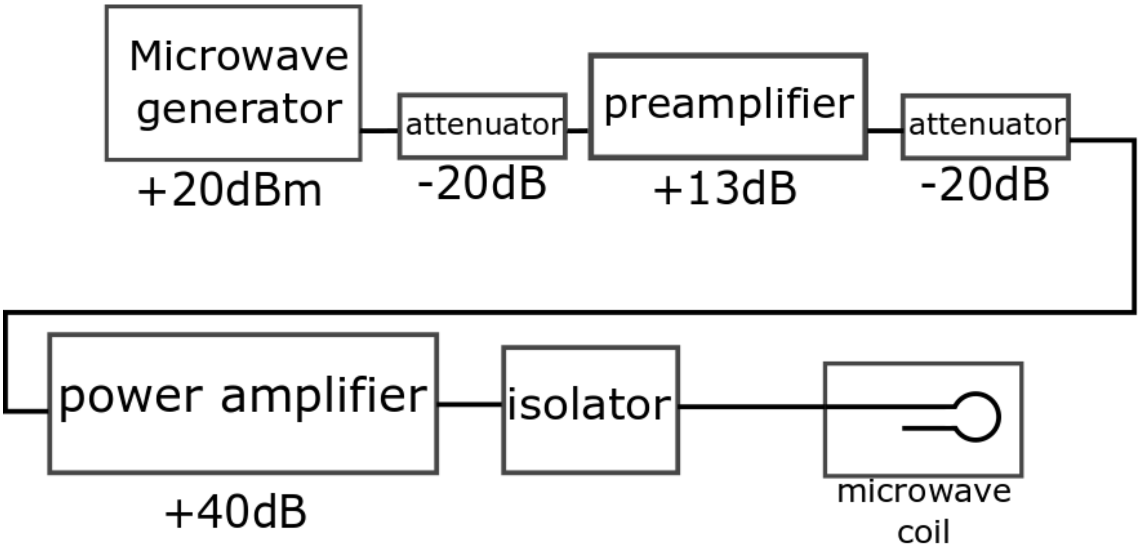

Figure 5.13: Component diagram of the microwave circuit. Microwave generator produces the waveform at the correct frequency, which is then amplified and fed into the microwave coil.

performed, and how other laser and/or microwave pulsing experiments will be performed.

A diagram of the circuit described below is visible in Fig. 5.13, the positioning of the switch is visible in Fig. 5.14. The system used in this instrument requires a preamplifier and a power amplifier to amplify the signal up to 1 W to be passed into the microwave coil. The preamplifier is a ZX60-4016E+ made by Mini-Circuits and has a gain of about 13 dB. The power amplifier is ZHL-4W-422X+, also made by Mini-Circuits, has a gain of about 40 dB for the ideal input power and has a maximum output of +36 dBm. Attenuators are placed before the input terminals of the pre-amp and the power amplifier to reduce any signals which are reflected back from the inputs of the amplifiers. These reflections are likely to be small as the components are all impedance matched at 50 Ω, so once they have been attenuated there will be no risk of pulses bouncing around the system and pulsing the sample when not required. It is likely that there will be more than sufficient amplification of the microwave signal and therefore extra attenuation for safety can be easily overcome and will not be detrimental to the eventual intensity of the generated microwave field.

A circulator or an isolator must be included in the circuit to protect it from back reflections from connections and interfaces. In our microwave circuit, an isolator is used, the difference being that this does not require external termination.

This is particularly important once the signal has been amplified to $> 1W$ as this level of energy passing into the amplifiers, or even back into the frequency generators, might cause damage to the electronics.

Many groups have passed the microwave signal through a simple straight wire, the diamonds are then placed directly on top of the wire, as close as possible, in order to maximise the field strength experienced by the defects. This has the added benefit of allowing a direct current (DC) field to be applied to the sample

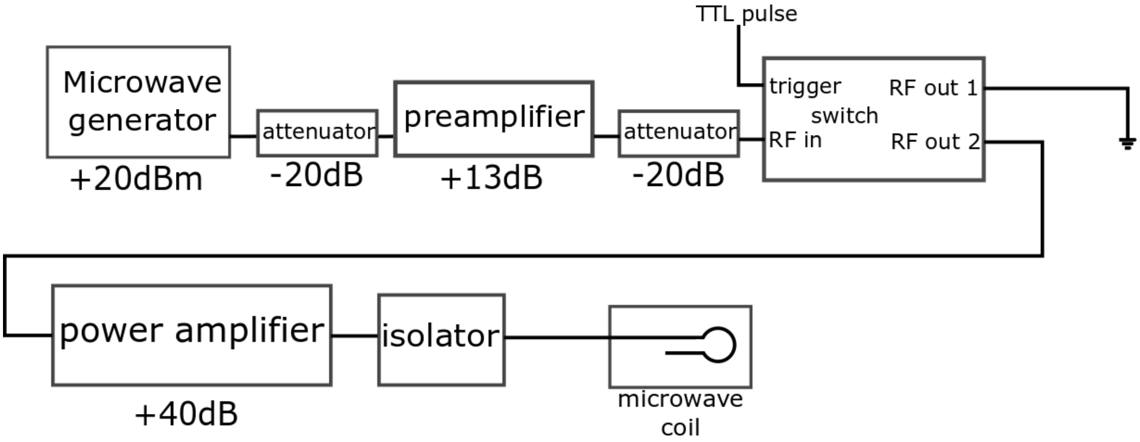

Figure 5.14: Microwave circuit including the switch. Used for rapid switching on and off of the microwave signal, when the trigger is low the microwave signal output at RF out 1 and goes to ground, setting the trigger high sends the signal to RF out 2 which goes to the power amplifier and to the coil, exposing the sample to a microwave field.

as well whilst performing initial NV$^-$ tests to observe Zeeman Splitting.

For this instrument, it was decided to produce a coil antenna with which to apply the microwave field to the sample. This design was based on that described in a paper by Sasaki et al. [97]. Using software made by Sonnet Software Ltd, called Sonnet-Lite, a coil was designed that would be resonant at or around the frequencies required for NV$^-$ ODMR. A resonant coil would provide much greater efficiency in terms of reducing reflections and producing a strong microwave magnetic field.

Care was taken to ensure that the impedance of the input rail matched that of the cable delivering the alternating current; this makes the interface between the two as seamless as possible and reduces reflections.

Sonnet-Lite allows a coil to be designed, Fig. 5.15, it models the microwave response of the coil, Fig. 5.16, and also displays the current density within the coil at each wavelength simulated, Fig. 5.17.

The coil itself is made on a printed circuit board (PCB), in this case, a 1.6 mm thick FR-4 PCB which has a layer of copper 35 µm thick on one side. The design to be applied to the PCB is drawn up in CAD software and a PCB machine, similar to a small milling machine, uses a thin drill bit to remove copper as required in order to form contact points, circuitry or wires.

A loop shape is used to generate a high strength field at one location; the nano-diamond would be positioned in the centre of the loop at surface height. As the inner and outer radii of the loop are varied, the inductance changes and the capacitance may also change depending on how close the end of the loop is to the input rail. The main way to vary the capacitance was to alter the length of the 'tail' end of the circle, to vary the distance for which it overlaps the input line. The inductance and capacitance of a coil determine it's resonant frequency and, although the ends do not meet, the loop is a partial coil and therefore acts in the same way. The method of tuning the coil was to change the dimensions methodically whilst running the simulation and recording the predicted resonant

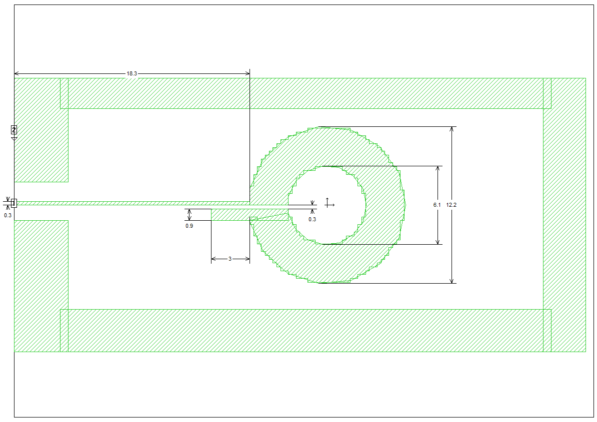

Figure 5.15: CAD drawing of the microwave coil which is to be simulated. The green indicates copper layer, the white area is FR4 printed circuit board. The oscillating wave enters via the copper tail at the left-hand side of the board. The larger copper area on the peripheries of the board is the earth plane.

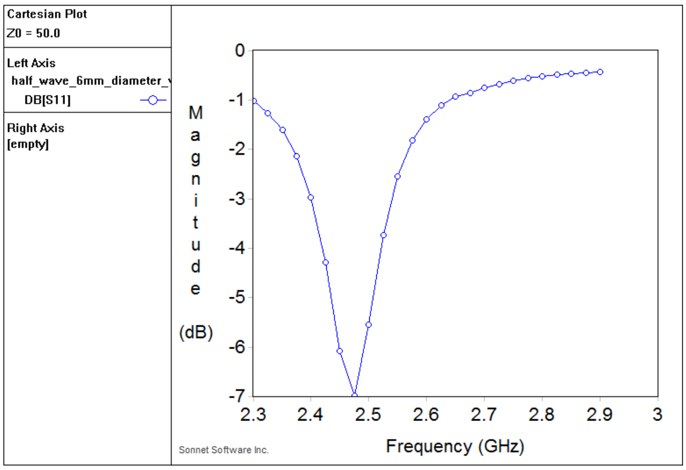

Figure 5.16: The simulated response of the microwave coil to microwave frequency signals. The resonance of the coil, which was designed in the software, was also predicted by Sonnet Lite's algorithm.

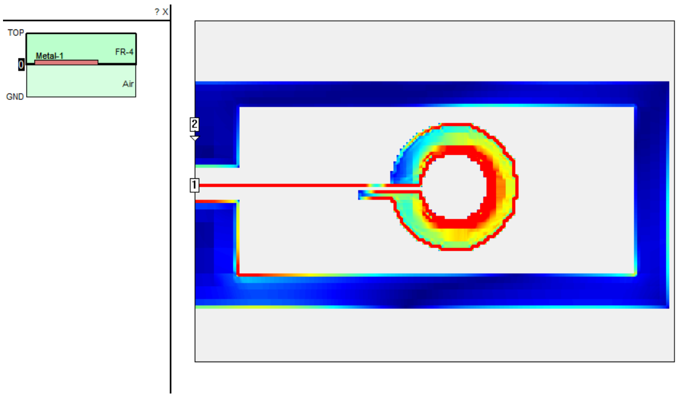

Figure 5.17: Simulated current density in the microwave coil at 2.7 GHz.

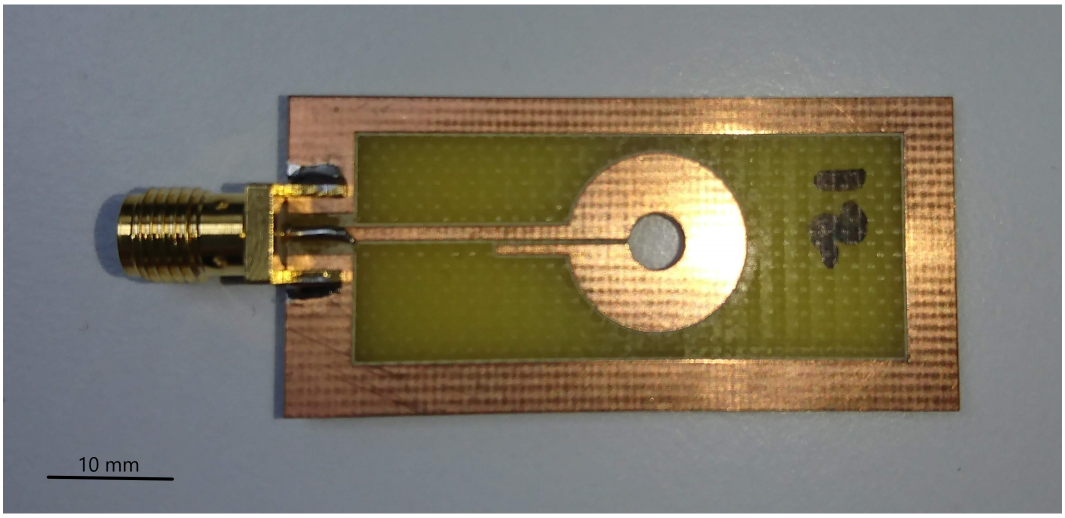

Figure 5.18: Photo of the microwave coil used to observe ODMR of the NV defect. The signal travels through the core of the SMA cable into the coil; the cable ground sheath is connected to the ground plane around the coil to reduce capacitance to other components. The NV^- defect is to be positioned as close as possible to the surface of the copper, within the region of the hole in the centre of the coil. This region experiences a very uniform microwave field strength.

frequency and the full width at half maximum (FWHM) of the resonance graph. The coil can be seen in Fig. 5.18.

Initial tests showed that the resonant frequencies generated by the simulation software had a slight offset from the manufactured circuit boards by a few hundred MHz. For the second tests, it was decided to produce an array of coils of varying sizes in order to cover a range of frequencies to ensure that a coil with resonance of 2.87 GHz, and a wide enough bandwidth to allow for scanning across the appropriate range, could be found.

It is to be expected that during testing in an ideal environment, the coil will have a particular resonant frequency, however, when brought into the larger setup this can change. This is due to large pieces of metal making up other components being at a different voltage to the coil and therefore causing there to be capacitance between themselves and the coil. This would reduce the resonance of the coil. In order to counteract this effect, a large ground plane was included in the design of the coil. Connected to the grounded sheath of the co-axial cable delivering the microwave signal and surrounding the coil, this provides some shielding and buffering of the coil, reducing the effect of taking the component out of the ideal testing regime. The final coil had a resonant frequency of 2.875 GHz and 118 MHz FWHM and the design is visible in figure 5.18. These values were slightly different from those predicted by the software, but both were within 10%, making a number of different coils allowed the ideal one to be selected.

The resonance of this coil was measured using a vector network analyser Wiltron 37217B, capable of scanning over a range of 22.5 MHz to 40 GHz.

5.6 Nano-diamond Method

Once the suspension of nano-diamonds has been ultrasonically applied to the substrate and the dispersion medium has evaporated (a process which could take an hour to ensure complete evaporation), the sample can be observed under the instrument.

5.6.1 Optical

The optical camera is used to position a specific area of the sample in the centre, at this point optical images can be collected. This is performed with a mirror or a splitter directing the light onto the sample and then back into the camera. Fig. 3.15 shows the setup which is being referred to, however, the 50/50 beam splitter immediately after the MO is replaced with a plane mirror. The laser can then be turned on to confirm correct positioning of the beam on the sample. With a beam splitter, the image of the sample is slightly faded and the laser beam appears bright, however, the mirror provides a very clear image of the sample, and the laser beam is greatly attenuated as it has to penetrate the back surface of the mirror before arriving at the sample. This provides a much dimmer laser spot which is still sufficiently visible for positioning purposes. The mirror or beam splitter is positioned at 45^o to the laser path, so the beam gains a horizontal offset of around 5 µm. When the mirror is removed in order to perform the various optical scans, a 5 µm adjustment is required to enable the camera images to be compared directly to the scanning images. The view from this camera can be seen in Fig.3.14.

5.6.2 Reflectance

The first scan taken is always the reflectance scan. The laser is aimed at the sample via the confocal microscope and then sent back towards the detectors. The dichroic beam splitter has an optical density of ∼2.3 at 514 nm [36] which is equivalent to attenuation by a factor of ∼500. When the laser power is sufficiently high, enough light passes the splitter that a bright, high contrast image is formed. The SPADs have a maximum count threshold of 30 Mcps before damage occurs, so a standard neutral density (N.D.) filter (typically, with O.D of 3 or 6), which has uniform attenuation across all visible wavelengths, is used to reduce the incoming photon flux to safe levels. The software used to perform scanning is Qudi [105] and was developed by the Institute for Quantum optics at Ulm University in Germany, then released as open-source software on GitHub. The software allows many variables to be controlled, most importantly the size of the scan, the scan resolution, and the time spent collecting light at each pixel (integration time), as well as the focus in the z-direction. In reflectance imaging, the count rate is high enough that pixels can be measured for only a few tens of ms and a low noise image is built up.

Each pixel represents the centre of one collection spot, the size of which cannot be changed. The collection spot is the focal spot of the MO lens, and therefore any number of pixels which causes consecutive sampling spots to be separated by less than the diameter of the collection spot leads to oversampling and can produce an artificial smoothing of the data. This can be counteracted by knowing the spot size and not exceeding this, or by taking the over-sampled image and "binning" the pixels. This is a process where a group of pixels are averaged and replaced by one single larger pixel. Binning number has to be a square number, e.g. 2 × 2, and is a noise reduction technique which in the case of large enough oversampling does not alter the true resolution of the image.

The reflectance scan provides an image of the exact area that will subsequently be scanned by the photoluminescence detection method. Example images will be given in the results section of this chapter and of chapter 6.

5.6.3 Photoluminescence

Whether it is emitted by NV^- defects or from the hBN grown here in Nottingham, it is known that photo-luminescent (PL) light will be of red (NIR) wavelength. Very little optical density is experienced by the red light and green light is heavily attenuated before the detectors. Any light detected during PL experiments will be red light generated by the sample.

With the notch and LP filters in, the rest of the process is identical to the reflectance scanning. The laser is turned on, the sample is scanned across, the integration time can be increased slightly, but typically is still at ∼10 ms. This changeover takes less than 60 s and scanning can commence immediately.

The PL scan can then be directly overlaid onto the reflectance scan to provide the x-y location of where the PL is being emitted, see examples in chapter 6.

The software uses the z-stage to focus the MO by varying z whilst re-scanning a line in x and displaying the intensity as an x-z plot. The brightest line displays the focal height. When scanning in reflectance, the focal height is always surface height, at the air-sample interface. For a PL scan, the photoluminescent location must first be located in x-y and then moved to the focal point of the MO. In the case of both the hBN and the nano-diamonds, the emitter is beneath the surface. The x-z focus plot can display the central height of the emission and provide further information as to the location of the emitter.

Once the three-dimensional location of the PL emitter is measured, the next step in the process when selecting a diamond for use in magnetometry is to check that the diamond contains a single defect. This is performed by selectively aiming the MO at the defect location using Qudi, and then connecting the SPADs' outputs into the PicoHarp and using the QuCoa software. The software is already prepared for correlation counting and anti-bunching experiments, it only requires the user to set which input channel should be used as the trigger to start measuring time. Once the start button has been clicked the software will collect arrival times of photons and plot a correlation graph in real-time, it will stop when instructed to, or after counting for a pre-set time if that option was selected. If count rates are high and high precision is requested from the software then there is the possibility that the RAM of the PC will fill up and the computer will crash. This happened several times after around 20 minutes counting when both channels were receiving ∼500 kcps.

A single quantum defect is taken to be indicated by a $g^2(0) < 0.5$.

5.6.4 ODMR

Another method of testing for the presence of a single defect, or indeed for confirmation that the observed emission is from an NV$^-$ centre, is to perform optically detected magnetic resonance (ODMR) on the sample. The microwave coil is placed on the sample stage facing upwards, the sample is then placed over the hole in the middle. As the sample and coil PCB are of similar thickness, the sample diamonds are very close to the plane of the coil wire, at this height and at the centre of the coil is the location of the strongest magnetic field.

A microwave signal can then be passed into the coil and applied to the sample and ODMR can be carried out, whilst observing the photoluminescent emission from the defect. The presence of ODMR about the correct microwave frequency indicates that the sample is definitely an NV$^-$ centre, and the number of troughs visible in the graph can infer how many defects are present.

5.6.5 AFM

At this point, the surface topography can be measured with the AFM part of the instrument. After the laser and the SPADs are turned off, the mirror is reinserted above the MO and the camera is used to view the sample again. The Smaract stages then move the tip into the centre of the MO, or to the region of interest and the side view camera is used to bring the tip to within fine approach distance of the sample.

The first step is to measure the frequency of the tuning fork. The cantilevers are measured when they are manufactured and the information such as resonant frequency and Q-factor provided. These measurements have so far turned out to be quite accurate, and allow a frequency scan of 2 - 3 kHz either side of the stated value to find the resonance with ease. The frequency is then chosen, depending on whether NC-AFM or Tapping Mode AFM will be carried out and the PLL is turned on. The size and position/orientation of the scan area and the number of lines/samples per line are also selected around this time.

Frequency shift (dF) is set as the locking variable, depending on the required tip-sample separation and the probe is brought into contact with the surface. Feedback gains can be tuned once scanning is underway, these depend on the speed at which scanning is carried out, the size of the features being measured and the gradient of the height changes on the sample.

The system can then be left to scan, the software saves files automatically and the default setting is to keep scanning the sample over and over until stopped by the user. The data is saved in .SM4 file format which is specific to RHK, it can be opened by the built-in RHK data analyser or by alternative freeware Gwyddion which has proved very useful for processing and analysing AFM data [106].

The SM4 file saves all the data collected by the scan. This includes PLL amplitude, PLL phase, dF, Topography, PLL drive and Current. Current is irrelevant to AFM, and would only make sense in a scanning tunnelling microscope, it is present because the RHK R9 is also capable of controlling an STM. PLL drive amplitude data can be relevant if constant signal mode is used, whereby the voltage to the tip is varied in order to maintain the same voltage returned from the probe. This is possible with our instrument, however, we tend to use constant drive mode, meaning that the PLL drive maps are a uniform flat plane. Topography map contains the surface height information, this can be compared to the dF map, which shows how far the phase is shifted from the setpoint on arrival at each pixel of the scan. This can be used to interpret the topography graph and to correct for errors and to produce a more accurate understanding of the surface height.

Due to the use of the Piezoconcept stages, the AFM has a large XY scan range (50 × 75 µm), an exceptionally large vertical range of 50 µm and a noise level of ∼1 nm dependent on the accurate setting of the feedback loops. This makes it ideal for scanning both smooth samples and extremely rough ones with large vertical features.

5.7 Initial NV$^-$ Investigations

5.7.1 Diasense diamond sample

The substrate is significantly more reflective than the diamonds which may be coated or mixed with the black compounds present in the suspension. It is likely that this other material is present as a result of the detonation method used to produce the nanodiamonds and was not filtered out afterwards.

In the scan, Fig. 5.22, the substrate is totally dark indicating that no laser light is able to reach the detectors. There is low level PL from around the sample, this could be due to defects in the diamond or photoactive systems in the impurities. The brightest photoluminescence, however, comes from a single spot in a chunk of diamond. It is visible in Fig. 5.23 that the emitter is bright only over a narrow z-range of ∼600 nm, meaning that this is likely to be a diffraction-limited spot and therefore is likely to be contained within a single submicron diamond.

The microwave coil was then used to deliver a signal in the region of 2.87 GHz in order to test for the presence of ODMR.

A strong resonance dip was observed with 15% contrast. This indicates that the coils are producing a strong microwave field which is strongly interacting with the sample. However, the resonance is not at the location expected for a nitrogen-vacancy centre in a diamond lattice. This could be due to stresses in the lattice, or environmental magnetic fields interfering with the resonance behaviour of the defect. This was a highly impure sample, and the droplet application method did not provide a widely spaced, thin layer of individual nanodiamonds. This meant that a lot of different factors could be contributing to the discrepancy between the expected and the observed resonance frequency, it is, therefore, difficult to extract much cause or meaning from the observations. However, this first experiment did demonstrate that the ODMR was affected by a microwave signal in the region of 2 - 3 GHz.

The sample of nanodiamonds was then scanned by the AFM, which produced the image visible in Fig. 5.25. There are a number of diamonds, visible as hemispheres on the scan, some are several layers deep on the sample, heights range from 20±1 nm to 40±1 nm for diamonds in this field of view. There is nothing visible on the AFM that separates the diamonds containing the PL emitter from the others, this is only known by matching up its location from the PL scans performed with the scanning confocal microscope.

Figure 5.19: View down the optical microscope of the nanodiamond suspension dropcast onto a Si wafer. The white streaks are impurities in the suspension dried on. The 'coffee staining' is visible in the small circular artefacts which have concentric rings. The circles are where the nano-diamonds are located, none were found outside of these circular objects during extensive searching and scanning. The impurities reflect green light, but there is no exhibition of any detectable photoluminescence above 600 nm.

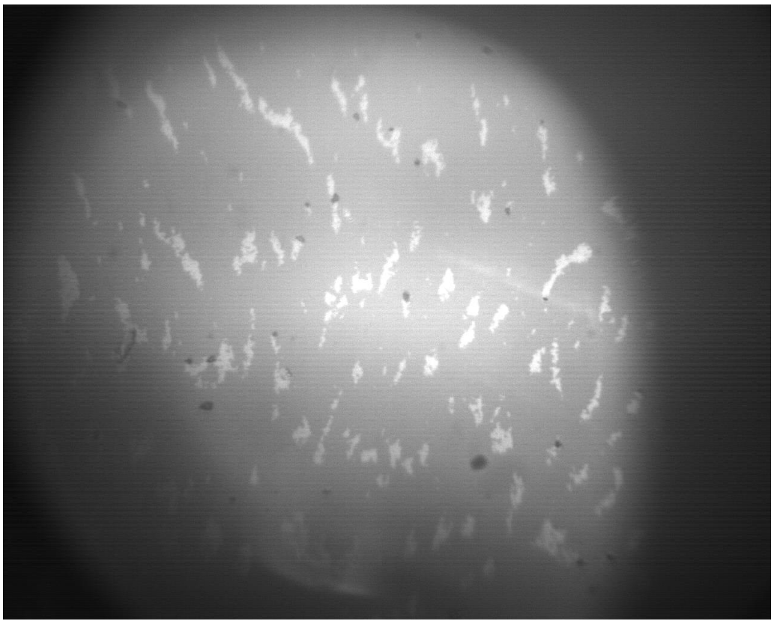

Figure 5.20: Camera view of the diamond deposit as applied to the substrate. The diamonds are clustered together in chunks, along with other graphitic compounds which gave the suspension its dark colour. The slight streaking effect, the lengthening along one axis, of some of the larger clusters indicated the direction to the centre of where the droplet was applied, the streaks being left behind as the solvent evaporated inwards towards the centre.

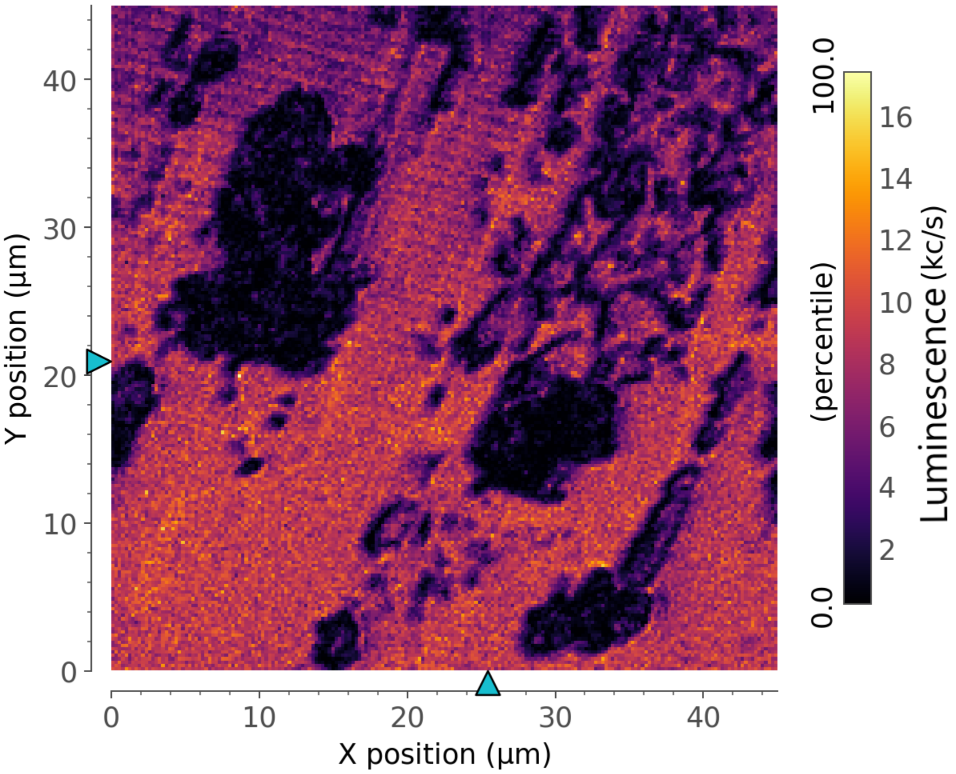

Figure 5.21: Reflectance scan of Diasense nanodiamond sample, applied to a silicon dioxide substrate, illuminated with a 514 nm laser.

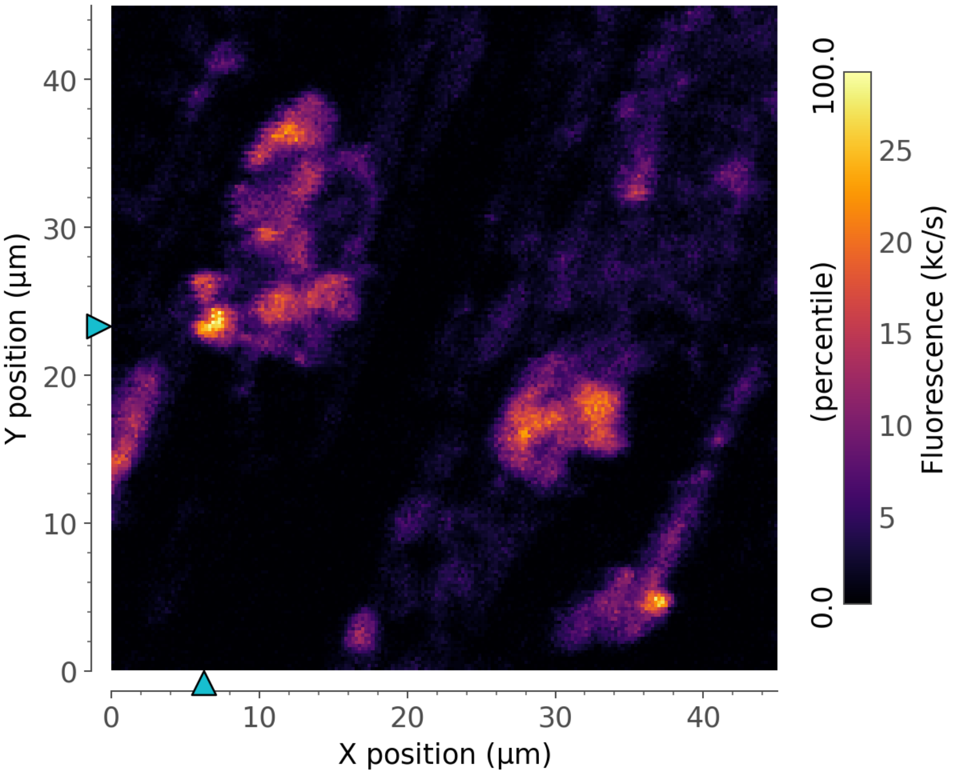

Figure 5.22: Photoluminescence scan of the Diasense nanodiamond sample, probed with 514 nm light, observed light is in the region 600 nm - 800 nm. The brightest spot is marked by the blue arrows on the axis, this is a photoluminescing defect in the nanodiamond. This demonstrates the proper functionality of the confocal wavelength filtering system.

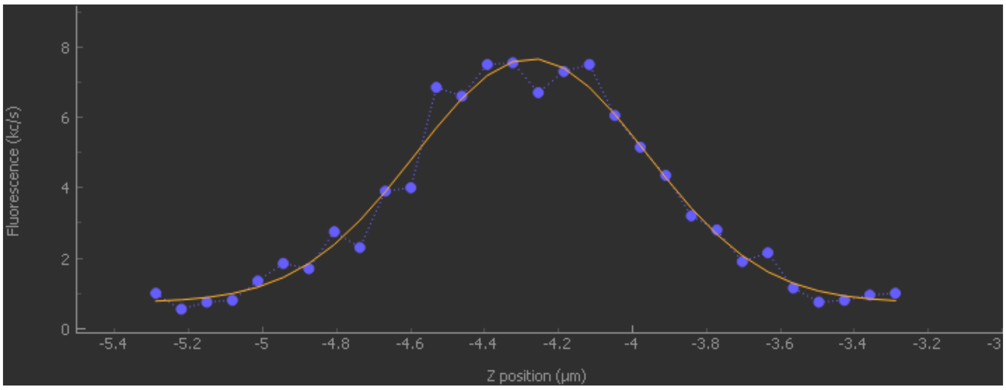

Figure 5.23: PL Intensity vs z-focus graph for PL emitter in nanodiamond sample shown in Fig. 5.21.

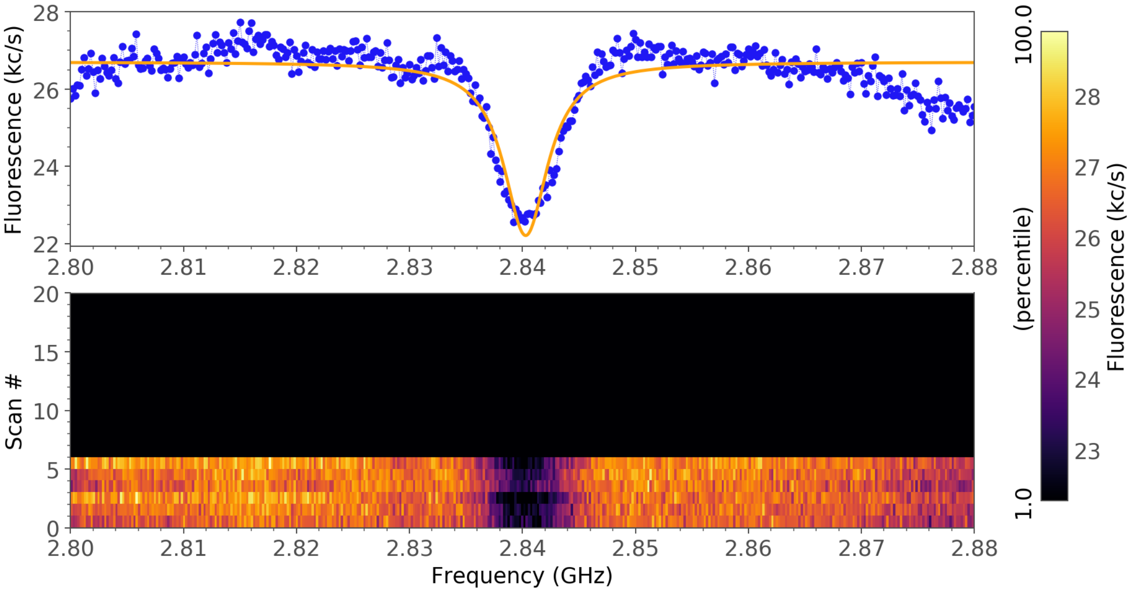

Figure 5.24: A strong ODMR signal is visible when a scanning microwave frequency is applied to the sample of diamonds with zero external magnetic field. This resonance is not at the frequency expected, were the emitter an NV$^-$ defect in a stress-free lattice.

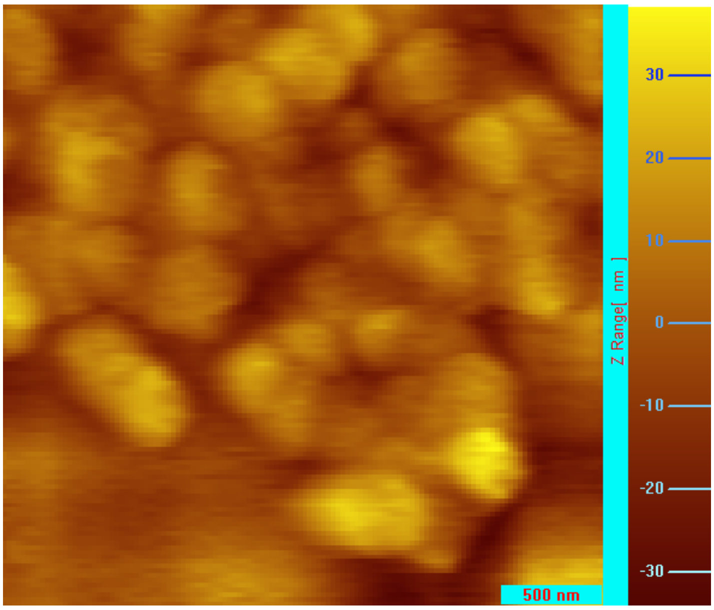

Figure 5.25: 3 µm × 3 µm AFM scan of a cluster of nanodiamonds deposited on a silicon substrate.

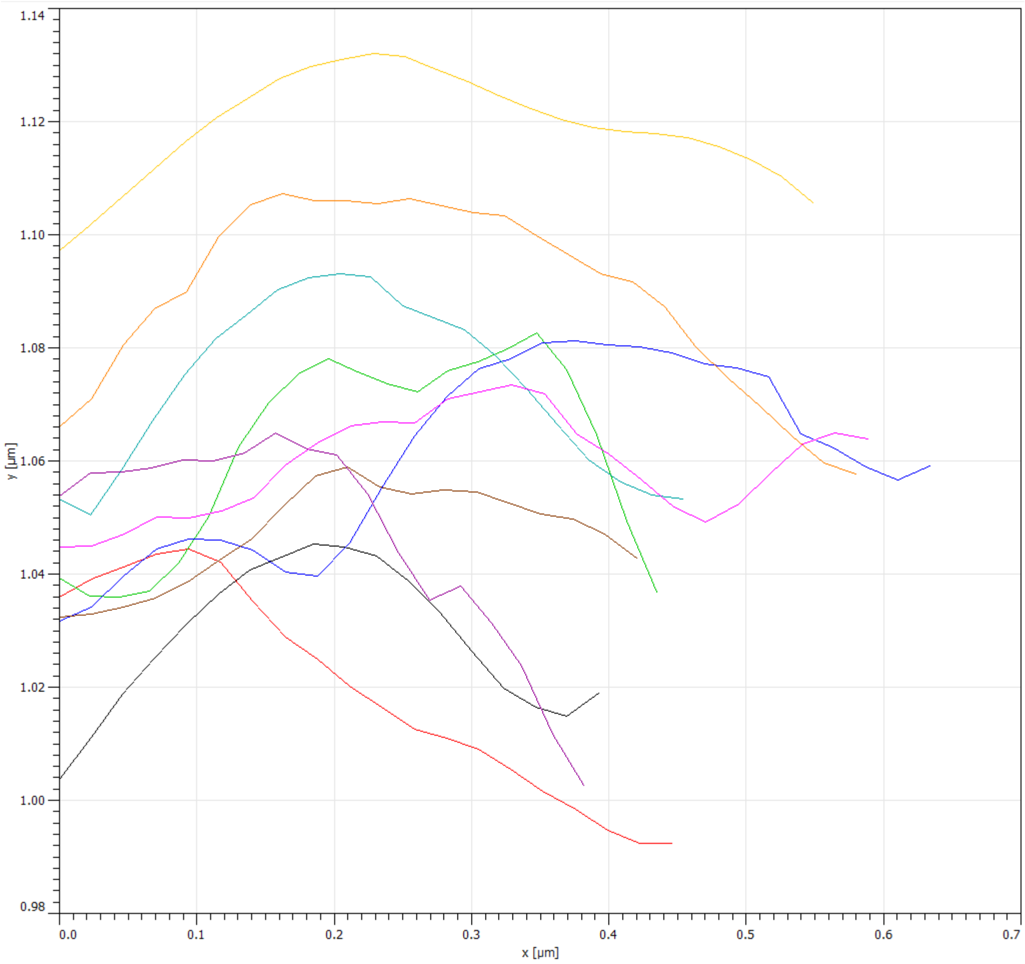

Figure 5.26: Line profiles extracted from the AFM topography scan of the nanodiamonds sample shown in Fig. 5.25.

5.7.2 Warwick diamond sample

The diamonds used in the nebuliser application method were produced by Dr Gavin Morely at the University of Warwick. The diamonds themselves were manufactured using chemical vapour deposition (CVD) in order to create a diamond lattice of very high purity. The diamonds are then irradiated with high energy electrons (∼1 MeV) in order to knock carbon atoms out of the lattice, creating vacancies. The diamonds are then exposed to nitrogen which diffuses into the material before they are annealed, a process which involves heating to ∼800 ℃ for several hours in order to allow the nitrogens and vacancies to move through the lattice and pair up forming NV$^-$ centres. A thin outer layer (∼20 nm) is then removed from the diamonds and these flakes are put into a tumbler, containing silicon balls, which then runs for several hours to smash the diamonds into nanodiamonds. The silicon balls get damaged by the diamonds during this process, adding some silicon powder into the product, this can then be removed by using a solvent which targets only the silicon, resulting in a clean nanodiamond product.

These diamonds were suspended in MilliQ water (1 mg of diamond in 1 ml of water), which was then diluted with 49 ml of methanol. This mixture was loaded into the nebuliser and sprayed into a glass vial which was then held over a silicon wafer, allowing the mist to settle onto the surface. The nebulise and settle process was repeated 8 times for one wafer and 4, 2 and 1 times for the others.

This process yielded very dark samples with very little photoluminescent material on them. In many hours of scanning, only two photoluminescent defects were discovered, these bleached under the laser before they could be studied. Whilst the nebuliser dispersion method is widely used as it produces a sample containing many small diamonds with appropriate (5 µm) spacing, it did not work for in this study and we did not have sufficient time to pursue this technique further before submission of this thesis.

In order to confirm that the diamonds were photoluminescent, a further sample was made, using the droplet technique described in the previous sub-section. This sample contained areas of nothing and areas which were dense with diamonds, approximately 5 emitters in every 50 µm square in these regions. These defects were illuminated with 200 µW of laser light and bleached after approximately 20 s of continuous wave (CW) illumination.

This sample is far cleaner than the one from Diasense, the Warwick suspension delivered to us was colourless and clear, as opposed to black and opaque. This is visible on the reflectance scan in Fig. 5.27 the diamonds, those which are large enough to see, are visible as black spots and there is far less other material on the sample, it appears that far more graphite, and in this case silicon has been removed after manufacture. The diamonds appear dark as they refract and reflect the light away from the MO, so less light is detected returning from them compared to the silicon surface which is smooth and highly reflective.

The photoluminescence scan of the same area, Fig. 5.28, shows that there is low-level fluorescence throughout the deposited material and there are two bright emitters in this sample. Due to the method of manufacture of this sample, these are likely to be NV$^-$ centres. Confirmatory investigations on these, and indeed any other emitters from this sample of diamonds, was not possible due to the fact that they bleached in a very short time. This property allows us to reject the possibility that these are NV$^-$ defects, which do not bleach at these laser powers on these timescales.

Whilst scanning for photoluminescence, each pixel was observed for 5 ms, leading to a total exposure time for each defect of about 50 ms per scan. This appeared to be little enough light so as not to cause bleaching; repeating these scans also did not lead to bleaching. The issue was observed when continuously probing the emitter in order to observe ODMR. Figure 5.29 shows the typical intensity reduction vs time plot for one of the emitters on this sample, the others behaved in much the same way. Within 50 s the fluorescence intensity was reduced to background level and was indistinguishable from the noise floor of the detectors.

ODMR was performed on one emitting defect, and this was only possible for less than a minute before the bleaching rendered the defect unmeasurable. This is visible in Fig. 5.30. The decay with time is the most obvious characteristic of the data, however, there are visible resonances. They are not at the frequency expected when looking at the NV$^-$ centre's Hamiltonian, much like with the Diasense sample they are at many frequencies, all below 2.8 GHz, again this could be due to strain in the lattice. Every care has been taken during the development of this instrument, and during the measuring process, to ensure that there are no stray magnetic fields in the vicinity of the sample, so this can be ruled out as a cause of this unexpected ESR behaviour.

In an effort to reduce bleaching, the laser was pulsed at 10%, 5% and 1% duty cycles with the laser being on for 0.1 ms in the fastest case. This did not improve the bleaching, the defect still became dark within 1 minute of observation. At faster pulses than this, or at shorter duty cycles, the fluorescence signal was lost in the background level.

The bleaching behaviour could be due to the diamonds overheating and reaching annealing temperature which would destroy the NV$^-$ centres. The power density at the focal point of the beam is on the order of 1 GW/m^2, and if the diamonds are particularly small in size, it may be more difficult for them to dissipate the heat. This may cause the defects to lose their electrons, resulting in an NV^0 centres which would be dark, to this observation setup, when probed with the laser. The bleaching behaviour was also observed on larger crystals of diamond on the sample. One such crystal was 30 µm × 40 µm in size and contained several emitters. This also bleached rapidly when the laser was aimed at the defect in order to probe its properties. Many groups pulse their laser at their diamonds, which would reduce heat build-up, but many other groups use CW lasers to probe their diamonds without bleaching, although this may be using bulk diamonds which are able to dissipate more heat away from the defect into the lattice than nano diamonds; pulsing did not work in this case. However, this is all speculation, further study of this sample and of other bleaching samples is needed in order to find a more definitive answer, as of now the emitters do not appear to be NV$^-$ defects.

It has since been suggested that the after the suspension has been applied to the substrate and has dried, that the laser is slowly scanned, at high power, over the sample in order to bleach any bleachable emitters. This should leave only unbleachable emitters which are more likely to be NV$^-$ centres. This process is

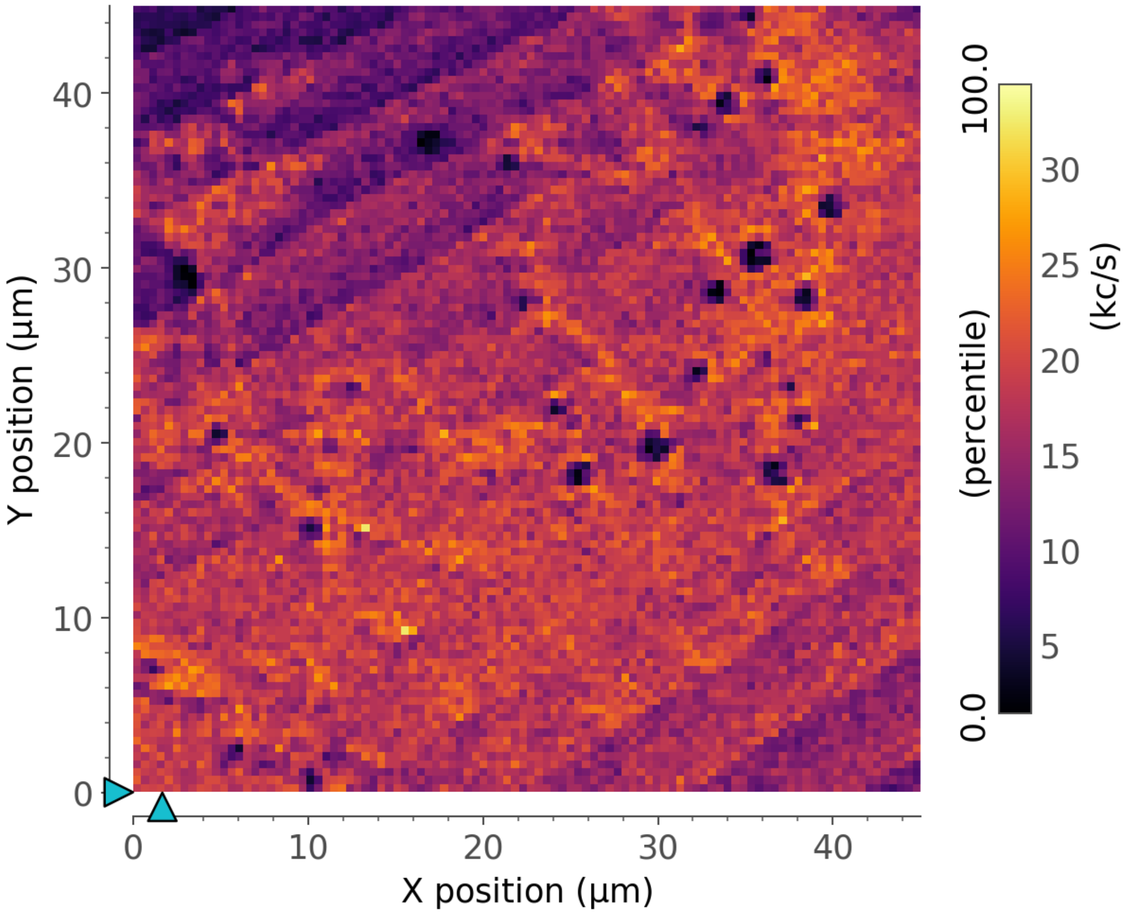

Figure 5.27: Confocal reflectance scan of the Warwick diamond sample, applied to the surface by the droplet method.

predicted to take on the order of 10 minutes for a 50 × 50 µm square of the sample. This method has yet to be attempted with this instrument, however it yields further possibility of successfully identifying an NV$^-$ defect.

The sample was AFM scanned with the instrument in order to investigate the size of the particles on the surface. The scan can be seen in Fig. 5.31. Everything on the surface is expected to be diamond or any other materials that were in the suspension with them, the sample was created in a very clean environment with little room for contamination. There are some larger features visible, however, the fluorescent objects (assumed to be diamonds) are the small bumps in the middle of the image. These were measured to be 40 nm ± 12 nm in height and were less than 1 µm in radius.

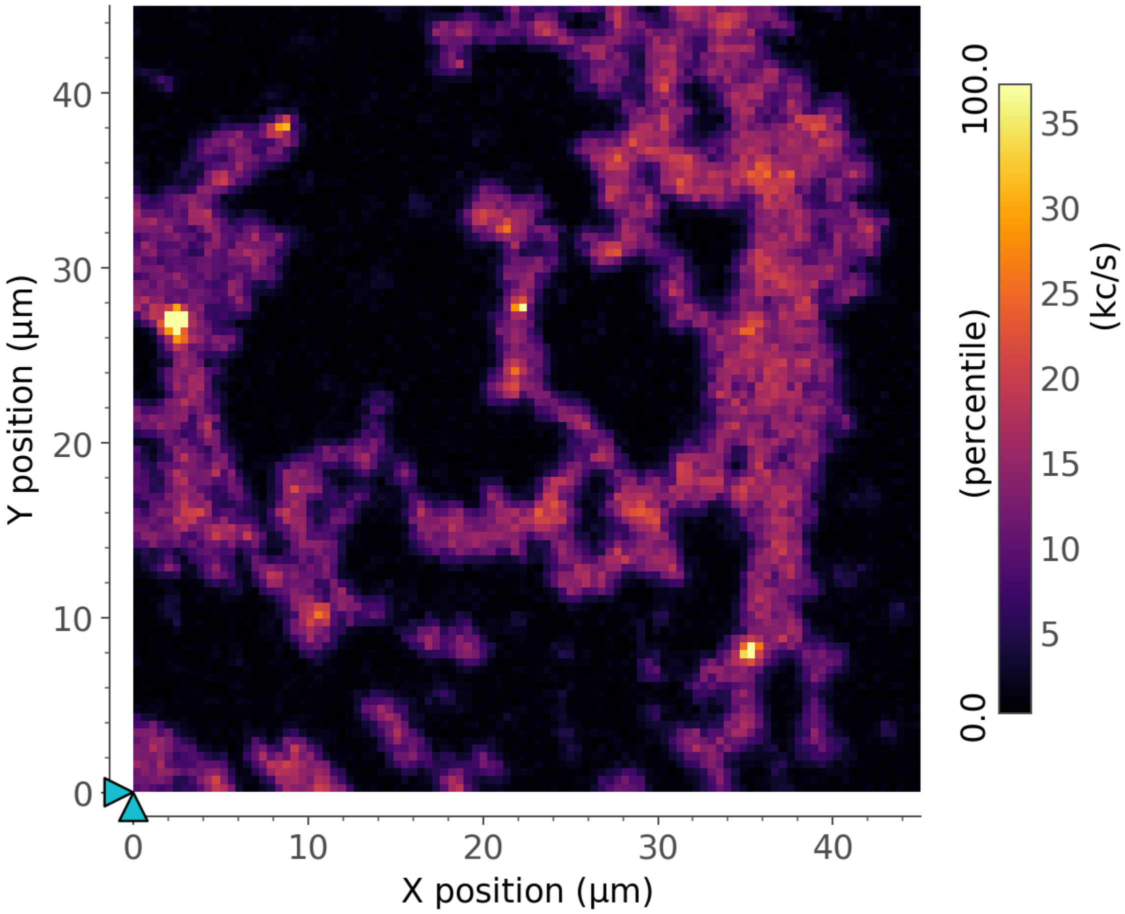

Figure 5.28: Photoluminescent scan of an area of the diamond sample from Warwick, over the same field of view as Fig. 5.27.

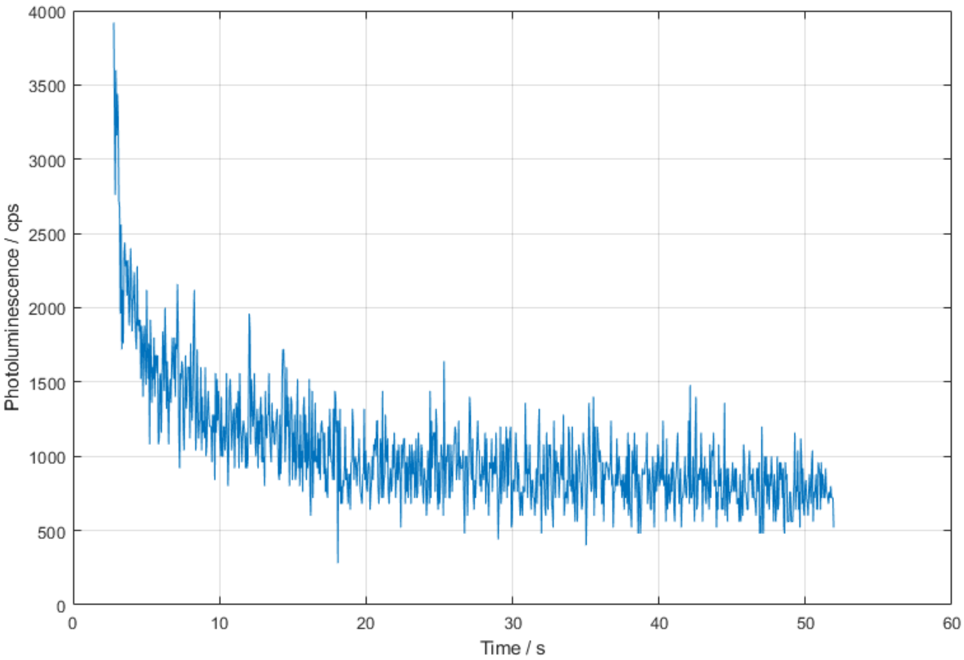

Figure 5.29: Plot of emitter intensity vs time. The bleaching of the defect is clear to see and occurs over a short timescale.

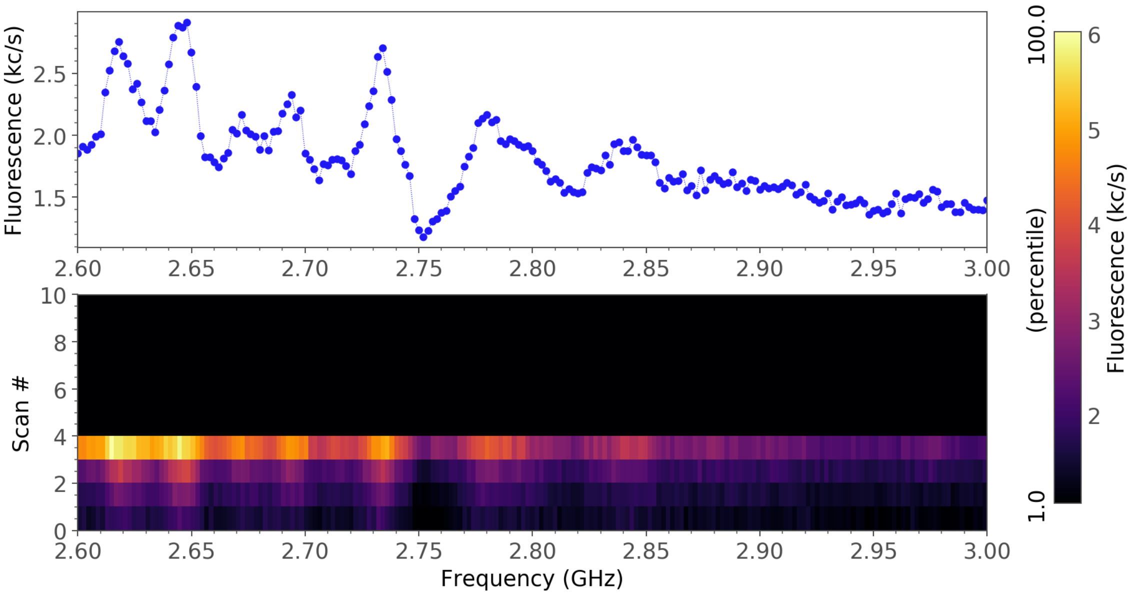

Figure 5.30: Plot of ODMR data, collected from the droplet deposited sample of Warwick's diamonds. Subsequent scans are darker as bleaching occurs until the contrast is reduced to the point where further collected data is no longer usable.

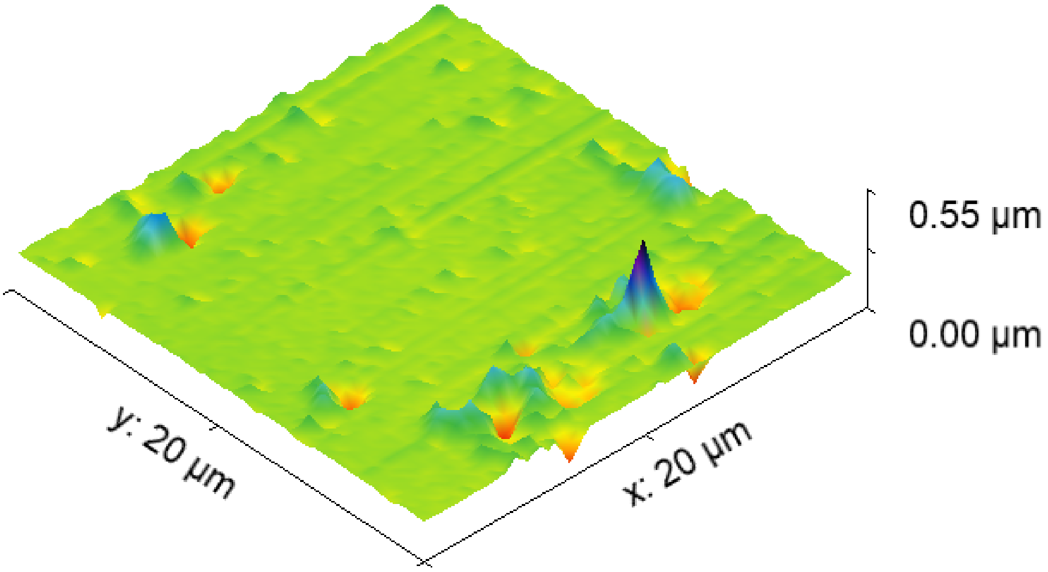

Figure 5.31: AFM topography scan of some of the diamonds visible in Fig.s 5.27 and 5.28

5.8 Summary

Whilst neither of the diamond samples provided any 'ideal' nanodiamonds which could be used in NV^- magnetometry, the suitability of the instrument to become an NV^- magnetometer has been proven. The anti-bunching set-up has not been tested due to the lack of suitable samples with which to test it. However, the instrument was able to rapidly confirm the unsuitability of the observed diamonds. It is able to measure the photoluminescence, the ESR spectrum, visually observing the sample and measuring the AFM topography of a 50 µm × 50 µm area to a 2 nm height resolution in under 1 hour. The most time consuming element is the AFM scan due to the number of sample points required to build up a data set capable of showing the heights of such small diamond samples. When searching for photoluminescent emitters using the confocal microscope a 50 µm × 50 µm could be covered in about 100 s.

The remaining work required to convert the instrument into a full NV^- magnetometer is to find an appropriate diamond, confirm that it contains a single emitter and attach it to the tip of an Akiyama probe. This probe can then be removed and stored when magnetometry is not required in order to preserve it. A standard Akiyama probe can be inserted in its place to perform normal AFM as required. The instrument has been designed and manufactured to be highly flexible with regards to its functionality, making it unique, certainly within the University of Nottingham, and with significantly better capabilities than many of the instruments reviewed. This is demonstrated again in the following chapter in which samples for which the instrument was not designed are investigated, producing new and useful data.

In the next chapter investigations into hexagonal boron-nitride devices will be made, using the instrument. The theory of h-BN will be covered as will methods of investigation and the results.

Chapter 6

h-BN investigations

This section uses our instrument, described in previous chapters, to investigate hexagonal boron-nitride (h-BN) devices manufactured at the University of Nottingham. The electroluminescent and photoluminescent properties of these devices are investigated as the surface topography is measured to provide information on their physical forms. Information on these devices is given, and other studies are examined, but first, some information on the h-BN.

6.1 Hexagonal boron-nitride

Boron nitride is a molecule formed when a single boron atom covalently bonds to a single nitrogen atom. It is found in three crystalline forms, only one of which (cubic-BN) occurs naturally. It is possible to manufacture hexagonal Boron Nitride (h-BN), forming a giant 2-D lattice of hexagons, each containing three BN molecules covalently bonded together. The 2-D lattices are flat, and form layers on top of each other, loosely bound together with van der Waal's forces. This is much the same arrangement as is found in graphene/graphite, with a monolayer of h-BN having similarities to graphene, it can be thought of as a non-conductive version of graphene. The strong covalent bonds cause it to have a high melting temperature and high thermal stability, and the weak temporary-induced dipolar bonds between the layers allow the layers to slide over each other, making h-BN flakes a good lubricant. Unlike graphene, there is little ability for electrons to flow freely either between layers or along the lattices, the covalent bonds are too strong. This makes h-BN more thermally insulating than graphene and electrically non-conductive in its pure form [107].

Hexagonal boron nitride has a wide bandgap, for a semiconductor, of 5.955 eV [108], which corresponds to photon wavelength of 208 nm. This is the widest bandgap currently known of any 2D material [109]. The lattice can be doped with atoms of carbon, sulphur or silicon to form semiconductors with a lower bandgap [110].

6.2 Previous work on hexagonal boron-nitride

Tran et al. measured PL emission at 632 nm from thin layers of MBE (molecular beam epitaxy) grown (at the University of Nottingham) hBN in 2016 [111]. Antibunching was detected indicating the presence of a single emitter, this and the 632 nm zero-phonon line was present for both monolayer and multi-layer crystals. The emitted light was strongly polarised. Very similar results were found by Exarhos et al. in 2017 [112] when using single-crystal exfoliated h-BN.

U. D. Dzhuzeev & P. E. Ramazanov found in 1969 that hexagonal boron nitride electroluminesces at almost identical wavelengths to its photoluminescent emission [113]. They concluded that this phenomenon only occurred when the hBN layers had been heated in the presence of carbon atoms. This is not the case for the exfoliated hBN samples, which are not exposed to carbon at high temperature, meaning that there must be another explanation for the behaviour explained in the next subsection.

More recently, in 2017, Gupta, Singh, et al. developed electroluminescent devices using exfoliated h-BN as a dielectric layer wrapped around a layer of emitting molecules [114]. This emission is not due to the h-BN which acts only to carry the current to the mixture of metal and metallic compounds which are the emitters.

There are many papers applying hetero-structures to h-BN sheets which result in electroluminescence, indeed this was the initial plan when the Nottingham group began developing these devices, however, they discovered that their clean and pure h-BN layers themselves emit light when a tunnelling current passes through. This behaviour is not well documented and does not feature in any publications at the time of writing.

6.2.1 Nottingham h-BN Devices

The devices produced in Nottingham by James Kerfoot and the group of Prof. Beton are made up of thin exfoliated layers of h-BN and graphene which act as the tunnel barriers and electrodes respectively, to a cluster of electro-luminescent molecules for use in future experiments. The samples tested using our instrument are made of mono-layers or multilayers of both of these materials, either one or several atoms thick, rarely more than ten layers. Making these is not a precise science and the most reliable method is that which was used to isolate graphene for the first time [115]; a strip of adhesive tape is stuck to the surface of the bulk material, then removed and applied to the substrate of the sample. When this is subsequently removed from the sample, several layers of atoms remain behind on the surface of the sample. This process is known as exfoliation. The bulk crystals of h-BN from which the flakes are exfoliated are made by the high pressure high temperature (HPHT) method by Watanabe and Taniguchi in Japan [116].

These devices are fabricated on a thick silicon wafer with a 90 nm SiO_2 layer on the top. Gold electrodes are deposited on the surface which can be connected to a current source. Layers of graphene and h-BN are then built up bridging the divide between the gold contacts and creating a continuous circuit. In the case of the final devices, the electro-luminescent molecule will be sandwiched between

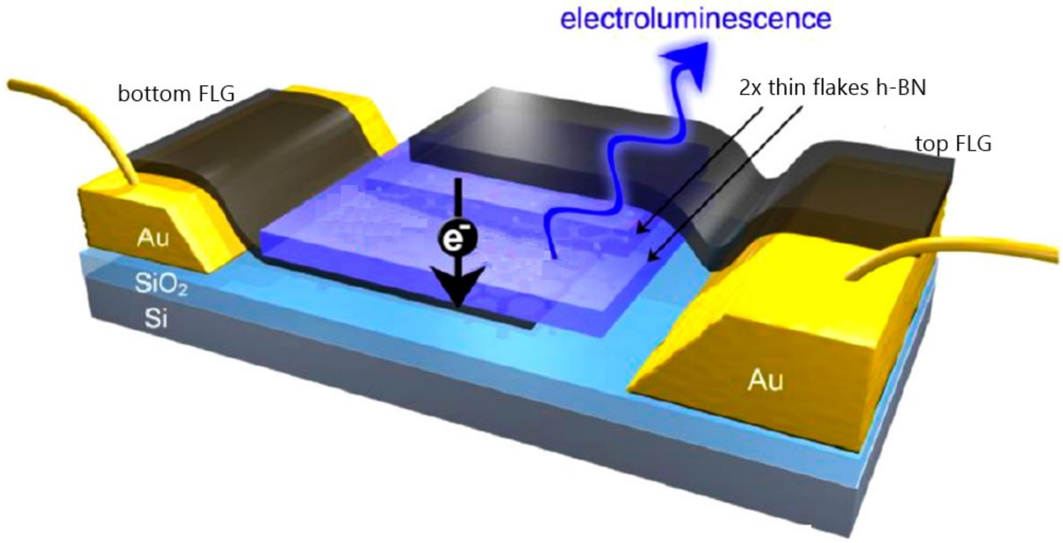

Figure 6.1: A modified version of a diagram, taken from a paper, co-authored by Dr Kerfoot [117] (Image not to scale). The device pictured had molecules positioned on the h-BN layer with the intent of measuring the electroluminescence from these molecules. Device D110, investigated in this thesis, has much the same structure, albeit with no extra molecules on the h-BN. There are two, overlapping, thin flakes of h-BN sandwiched between two flakes of few-layer graphene (FLG). D110 also has thicker flakes (few layers) of h-BN between both FLGs and their respective gold electrodes. It was postulated that D110 emits electroluminescence from the region of overlap between the two central thin flakes of h-BN.

two layers of h-BN, which in turn will be sandwiched between layers of graphene, both graphene sheets will be in contact with a gold electrode. The samples we are investigating, which electroluminesce, are of the form h-BN/G/h-BN/G/h-BN, with the h-BN touching the electrode. A similar device is visible in the Fig.6.1 layer view, the diagram is taken from a paper by Svatek et al. [117], the devices investigated were fabricated by Dr Kerfoot in an almost identical process to the ones investigated in this thesis.

The thicker layers of h-BN and graphene are deposited from a polydimethylsiloxane (PDMS) stamp, a method of soft lithography called micro-contact printing, which allows a surface layer to be applied, then selectively removed leaving only the parts which were protected by the stamp [118]. The thin, central layer of h-BN is then applied and flame annealed which causes the h-BN to form larger crystals [119]. The device is then tested for emission intensity and wavelength, as well as I-V characteristics before being passed to us for analysis.

The h-BN used in these devices was made in Japan using the HPHT method and then exfoliated from the bulk crystal in Nottingham. This method produces h-BN of extremely high purity, which should not electroluminesce without the presence of contaminants. As this has no contaminants, it is a surprising result that light is emitted and it is for this reason that we are using our instrument to help investigate these devices.

It should be noted that Beams et al. [120] documented electroluminescence from single layers of graphene, produced by a hot luminescence mechanism. This, however, is not the property exhibited in these h-BN devices.

6.3 Imaging method

The hexagonal boron-nitride sample grown by Professor Beton's group at the University of Nottingham consists of layers of hBN and graphene. The thin h-BN is sandwiched between two graphene contacts and is applied to the sample by exfoliating using sticky-tape. There is often polymer from the tape left on the sample, this does not always get in the way of imaging as it does not stick to the hBN due to the method of application, most of the material remains on the tape while a few layers of hBN attach to the sample. In some cases where the adhesive polymer is a problem, particularly when performing AFM scans, it is soluble in chloroform and can be cleaned off with relative ease.

The process for imaging an hBN sample is the same as described earlier. The sample is visually examined, then scanned with the laser to build up a reflectance image. Photoluminescence scanning can also be performed, any polymer material from the tape or other sources usually fluoresces at a low level, both from the body of the material as a whole as well as from points inside the mass of polymer, removing the polymer removes this extra source of luminescence. Hexagonal boron-nitride has been shown to photoluminesce [111], emitting red light when bombarded with green photons. The method of emission is not fully understood, which is why it is useful to perform PL measurements on these samples with the instrument.

6.3.1 Electroluminescence

If electroluminescence (EL) is possible or expected from the sample, as it is with the hBN made in Nottingham, it can be mounted on a specific EL stage. The sample is placed onto a square of printed circuit board (PCB) where it is contacted by the electrodes which are pre-loaded and pin it to the board. The PCB is then attached to the mount by a pair of retention clips which also act to earth parts of the PCB to the mount and the stage. This can be seen in Fig. 6.2

Current can then be passed through the sample, from a source-measure unit (SMU), in order to measure the I-V characteristics of the sample. All hBN samples tested by the instrument have been shown to electroluminesce and have emission wavelength, intensity and I-V characteristics measured and provided to us by Prof. Beton's group. It is, however, important to verify the data to ensure that nothing has changed during transport or use.

The SMU can then be set to a specific voltage to deliver a current of such a value that emission is expected and of observable levels by the system.

The noise floor of the SPADs is in the region of $100cps$ so emission of light at values lower than this are difficult to detect. The Qudi software has an upper limit for integration time of $1s$ per pixel, this leads to a rather slow scan time, taking several hours for a scan with a useful pixel resolution. In some cases, the emission is too dim to view, the solution to this is to repeatedly take scans with 1 s integration time and average them together. By this method, it is possible to replicate a scan with an integration time of more than 1 s.

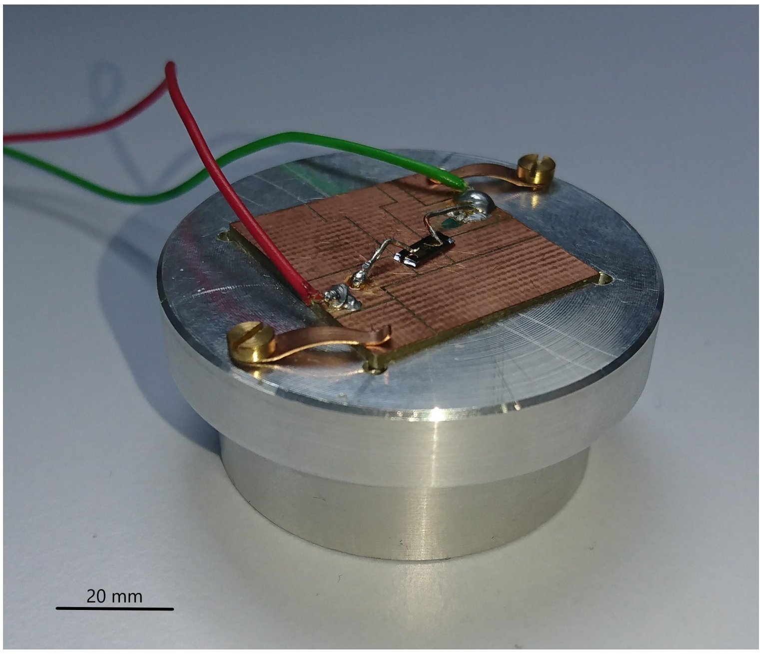

Figure 6.2: The stage mount designed to provide current to h-BN tunnelling devices whilst positioning the sample underneath the microscope objective, on the scanning stage.

The electroluminescence is expected to emit from only one location on the sample, therefore resultant images which positively detect EL are largely dark and covered by detector noise and have one area of emission. These images must then be superimposed onto the reflectance scans of the same area in order to show the location of the source of the emission.

This scanning detection capability is currently unique in the department and provides additional information to help understand the origin of the EL produced by the hBN samples as well as testing the usability and utility of the new instrument.

6.3.2 Spectral Analysis

Prof. Beton's group have a spectrometer and CCD sensors which can observe the EL with very long integration times and measure intensity vs wavelength. In our system we have not yet integrated a spectrometer, however, it is possible to verify the spectral analysis of the other group, albeit to a lower precision by putting various line pass or band-pass filters into the path of the beam. These band-pass filters are specified with a central wavelength and width of transmission. By switching filters and recording the intensity received at the SPADs, it is possible to calculate the spectral components of the emitted light. This method can be performed during PL scans as well as EL, but more often the scan is performed first to locate the emitter, and then the stage position is fixed and intensity measurement performed whilst looking directly at the emitter.

This method provides more information and certainty regarding the wavelength than just using the dichroic splitter, notch and long-pass filter.

6.4 h-BN device measurements

6.4.1 D41

Sample D41 was manufactured by Dr James Kerfoot at the University of Nottingham. This sample is constructed from top to bottom as: h-BN, graphene, thin h-BN, graphene, h-BN. The top half was picked up using thicker h-BN, the middle thin h-BN layer was flame annealed and the bottom thick h-BN and graphene was stamped from PDMS (note this has a different structure to D110, whose diagram is shown in Fig. 6.1).

Electroluminescence was detected from this sample using a cooled CCD and spectrometer, however, there was insufficient light emitted for it to be visible on our system with a higher spatial resolution, which requires ~50 cps emitted to rise above the noise floor of the SPADs after passing through a 50/50 beam splitter.

Photoluminescence was detected on our setup and it was able to be located to a specific point of emission.

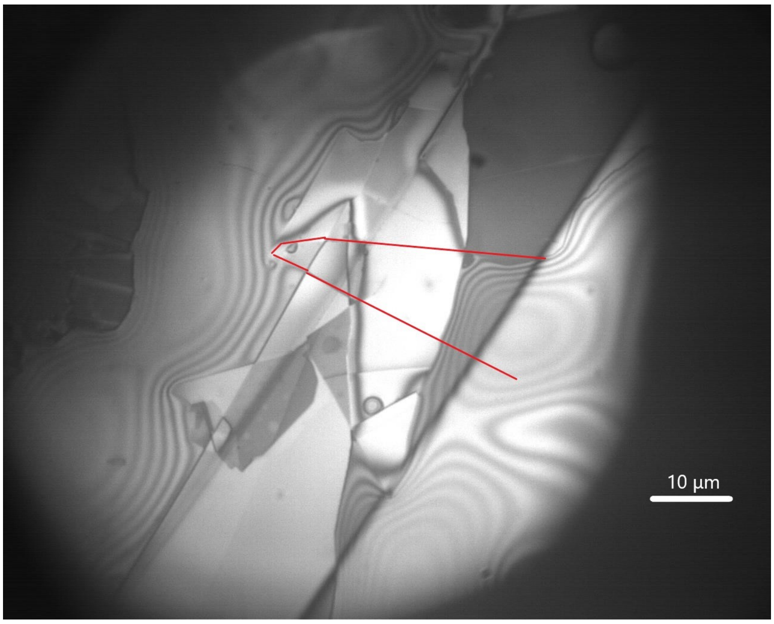

Figure 6.3: Camera view of D41 through objective lens. For clarity, the location of the thin h-BN flake is outlined in red. This flake is sandwiched vertically between two graphene flakes (not shown).

Figure 6.3 shows the camera view of the sample through the microscope objective. Not visible in this picture is the small laser spot produced by the laser passing through the back of the camera mirror showing the centre point of the confocal scan. In the centre is the small gap between the gold electrodes (visible over most of the image), the gap is bridged by the layers of graphene and h-BN as described above. The crystals are visible overlapping each other and can be identified when compared with the accompanying information provided with the sample.

Figure 6.4 shows the confocal reflectance scan, the laser power on the sample surface is 200 µW at 514 nm and neutral density filters are placed before the

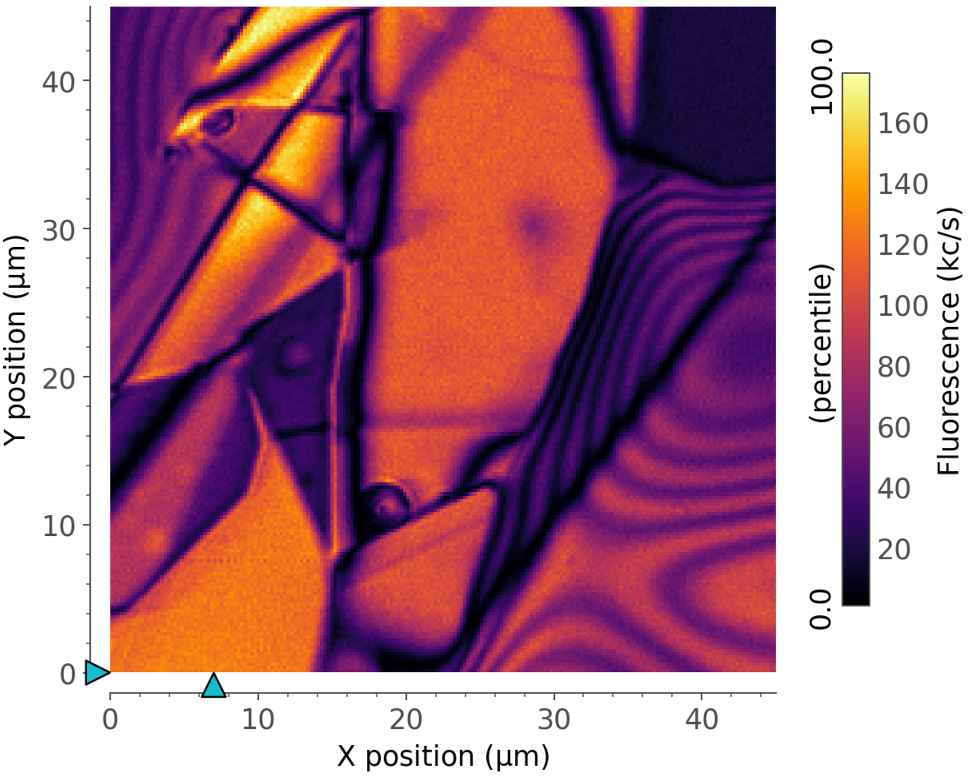

Figure 6.4: Confocal reflectance scan of device D41

fibre with $O.D.$ 6, which coupled with the optical density of the dichroic splitter, reduce the intensity to levels that are safe for the SPADs. More visible in this view than from the camera are the thin-film interference patterns caused by the polymer layers left behind after manufacture. These can be removed, but one can see in this image that the polymer has not come into contact with any of the important layers near the active area. The sampling rate is 100 lines of 100 pixels per line, measuring light at 100 samples per second. These parameters remained the same for all reflectance and photoluminescence scans of this sample.

After the reflectance scan, the neutral density filters are replaced by the notch and long-pass filters. This greatly reduces the absorption of the laser light whilst having relatively little effect on the expected red light. Figure 6.5 shows the photoluminescence scan of D41. Most of the sample is dark, some light is emitted from the crystal edges. This is probably because there is likely to be more defects and dangling bonds on the edges of the crystal. Most of the light, however, escapes within a short distance of the defect and is detected in that region.

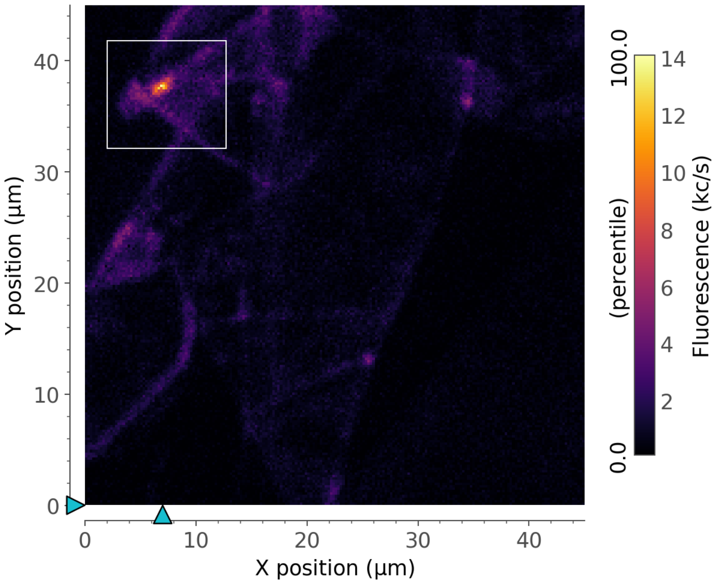

Figure 6.5: Confocal photoluminescence scan of D41 sample. Active photoluminescent region is highlighted by the white box.

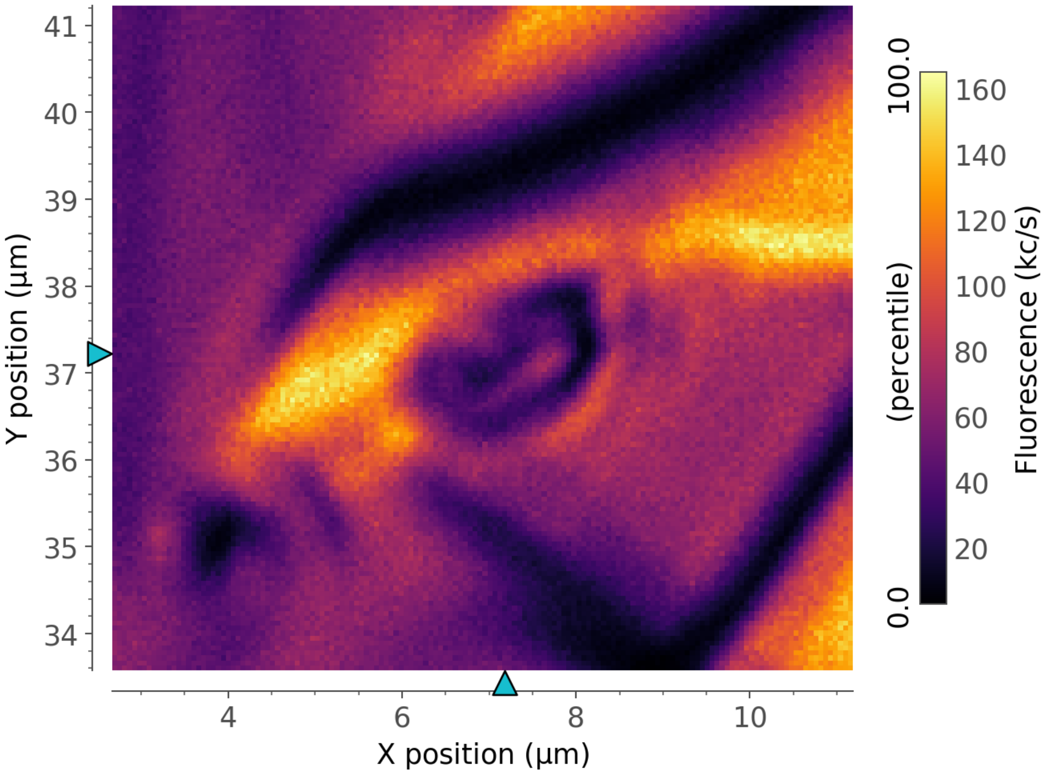

Figure 6.6: Confocal reflectance scan of D41, a smaller scan whilst maintaining the same number of sample points per image produces a magnified of the photoluminescent emitter location.

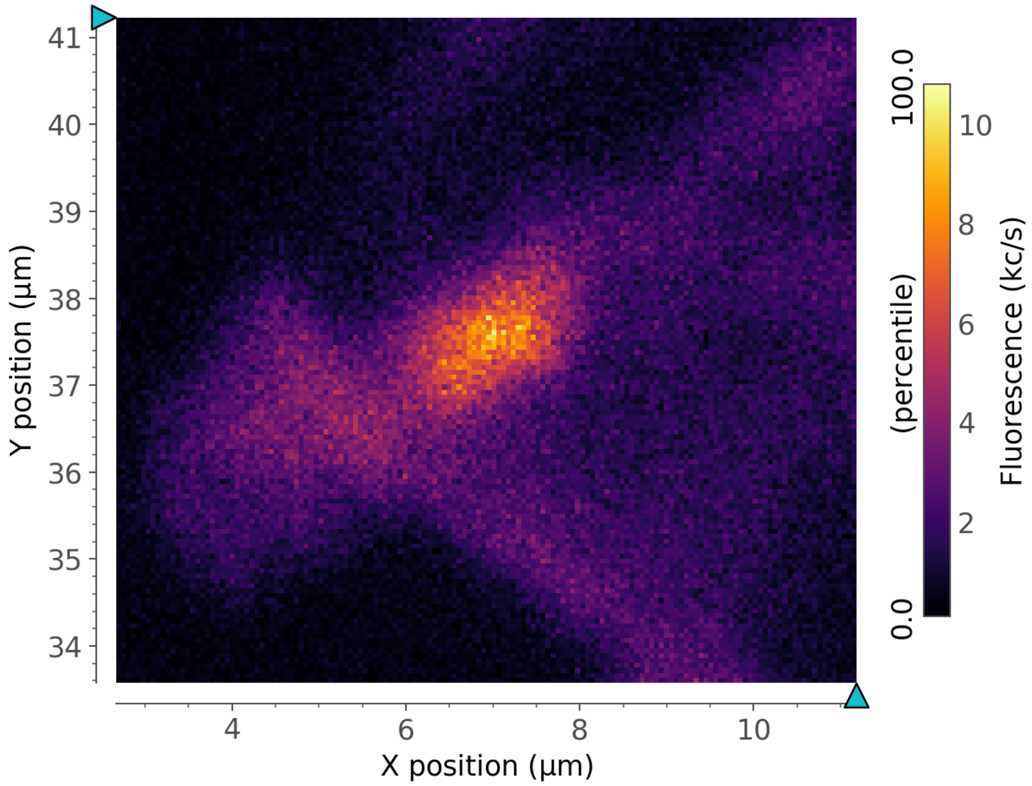

Figure 6.7: A repeat of the scan in Fig. 6.6 with a longer integration time and with the system in photoluminescence configuration. This provides a confocal photoluminescence scan of D41, zoomed in on the emitter location.

Figures 6.6 and 6.7 are taken by reducing the scan range to the area of interest whilst leaving the sampling at 100pixels. This produces a high resolution scan of a 10 µm square around the emitter with a 100 µm× 100 µm pixel size. As these two scans are of the same area, they can be overlaid to show the distribution of photoluminescent light on the sample.

Figure 6.8 is an overlay of the two full sized images, showing that the emission comes from some layers overlapping above the gold contact. Figure 6.9 confirms that the emission is coming from the edge of the 'bubble-like' defect in the overlapping layers.

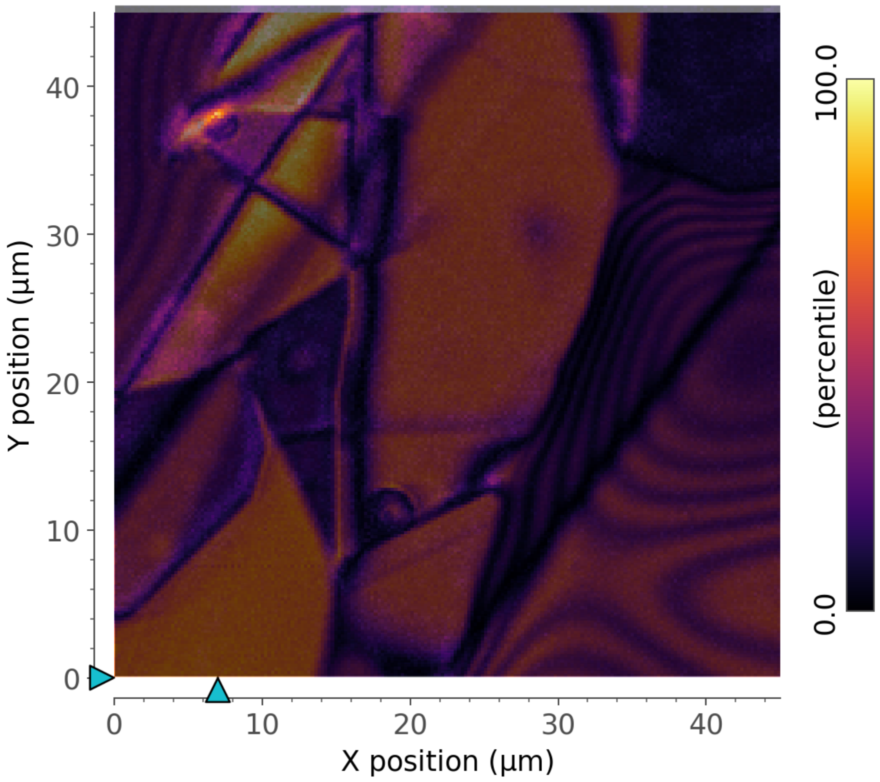

Figure 6.8: Photoluminescence scan overlaid onto the reflectance scan, showing the location of the PL emitter. Sample: D41.

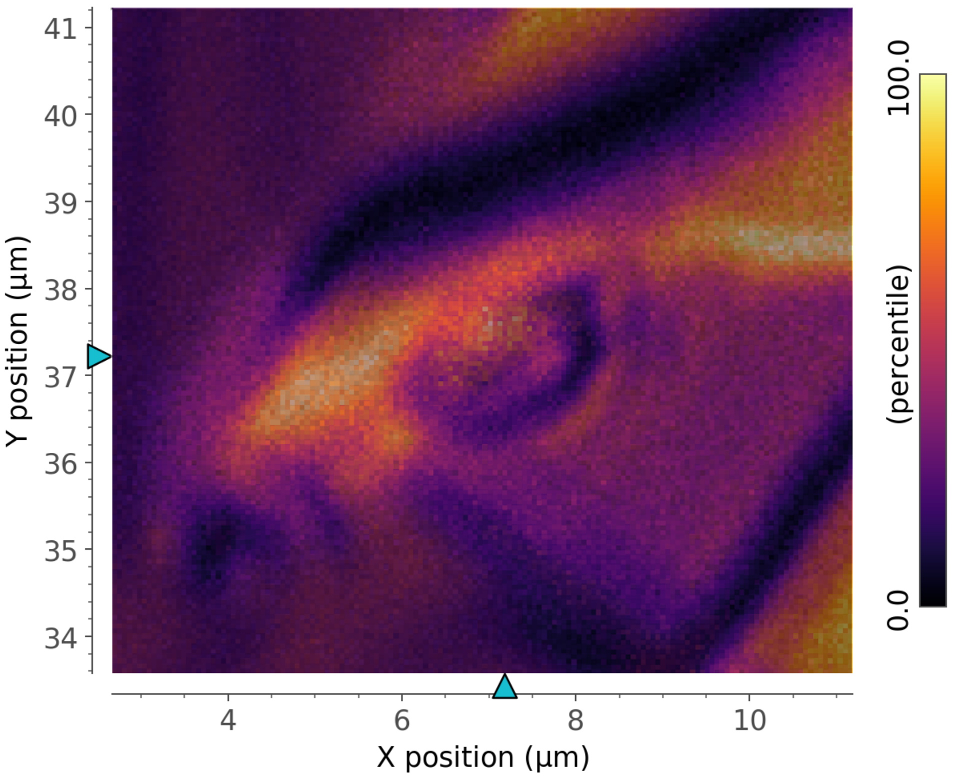

Figure 6.9: PL and Reflectance scans overlay image, zoomed on PL emission area. D41

At this point, the top camera can be used to align the AFM probe over the sample which can then be approached and a scan performed. The topography data and the PLL amplitude data are visible in figures 6.10 and 6.11 respectively. the second figure shows the features with greater clarity than the first, allowing us to be certain that the 'bubble-like' defect is lined up exactly with the large feature visible on the AFM scan. The topography scan then allows us to extract the height of this object which is 600 nm above the surface of the surrounding crystal. The PLL amplitude plot shows the change in dissipation of the cantilever kinetic energy and can provide information about the mechanical or material properties of the sample.

The focal height data from the confocal microscope shows us that the photoluminescence emission is brightest (and therefore originates from) the same height as the reflectance. This measurement is accurate to less than 500 nm due to the thin focal plane of the 100× N.A=0.8 lens. This indicates that the emission comes from a point level with the rest of the surface, and not at the top of the bulge. The shape of the bulge above the emitter can be seen more clearly in Fig. 6.12.

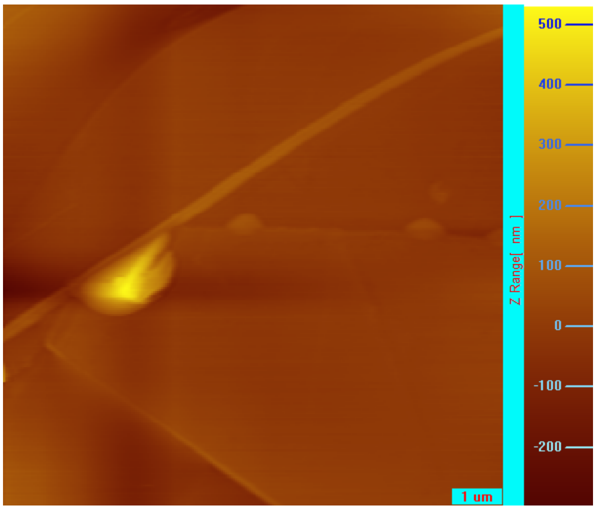

Figure 6.10: Surface topography of D41 in the region of the emitter. The feature in the middle is the exact location of the photoluminescent emitter, it is slightly pyramidal in shape. This shape could be due to the feature being sharper than the AFM tip is able to observe, therefore the shape is that of the AFM tip, but the maximum height of the feature is still measurable. The peak of the defect is 600 nm above the surrounding surface.

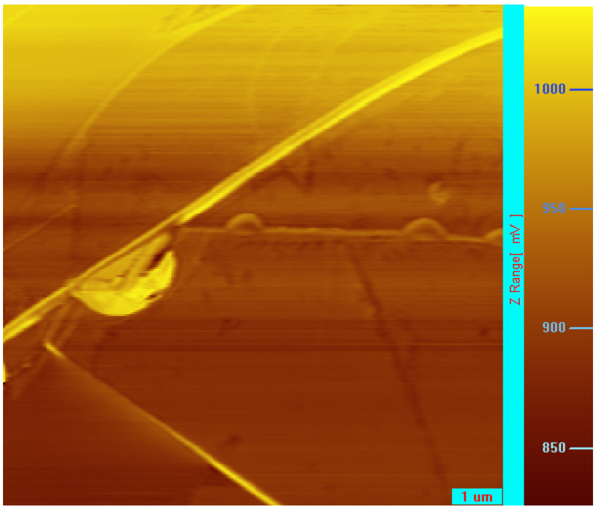

Figure 6.11: PLL amplitude plot. The change in voltage as the PLL maintains oscillation frequency.

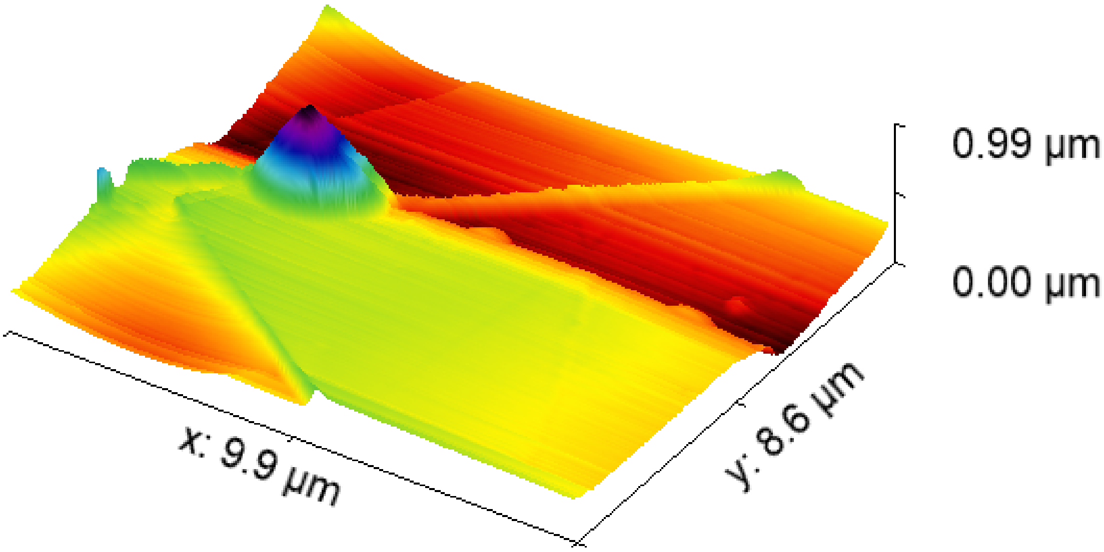

Figure 6.12: 3D projection of the surface topography data of D41. The height of the emitter artefact compared to the surrounding material is clearer in this representation.

6.4.2 D110

Sample D110 was also found to exhibit electroluminescence. This sample has a slightly different construction to D41. It is made up of the following layers, described from the top down: thick h-BN, graphene, thin h-BN flame annealed, thin h-BN flame annealed, graphene, thick h-BN. The two outer layers of thick h-BN are in contact with the gold electrodes and transfer current to the rest of the device. It is suspected that the two central layers of thin h-BN, both applied to the sample by exfoliation, have overlapping surface defects which may be the source of the electroluminescence.

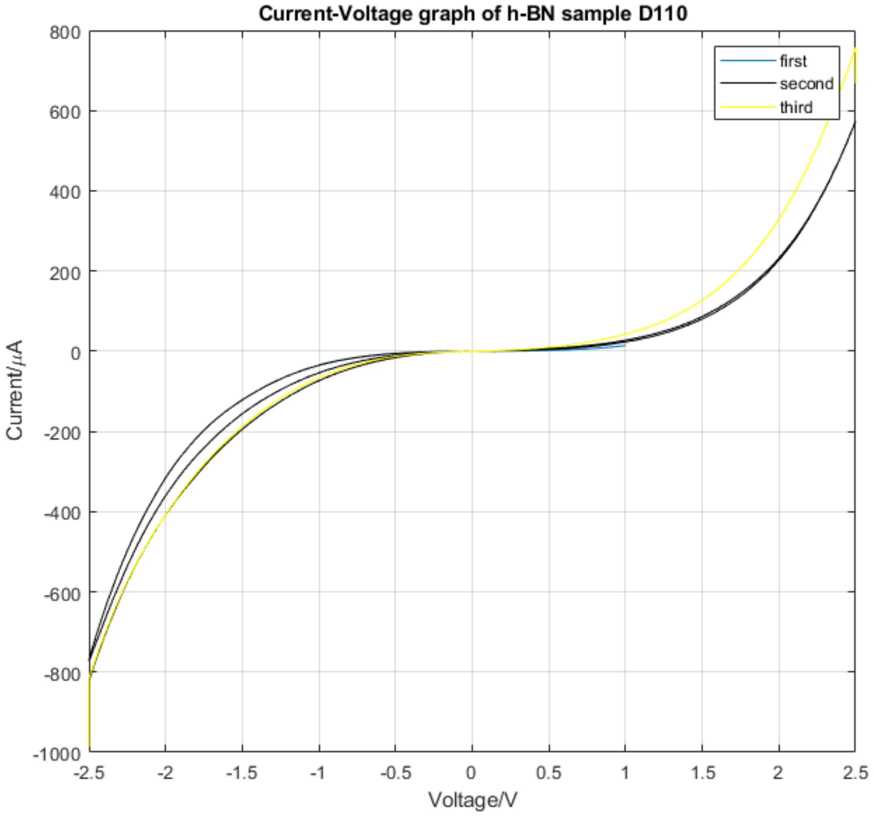

Figure 6.13: Graph of current-voltage characteristics of D110. This measurement was taken before EL testing commenced, the behaviour changed significantly during use. The sample was left off for a period of several days and the resistance increased, significantly lowering the current at the constantly held voltage.

Figure 6.13 shows the I-V characteristics of the sample. These were tested using the SMU. These values did not remain the same after many hours of emission, indicating that some sort of irreversible physical process was taking place inside the sample during emission.

Figure 6.14 is a microscopy image of h-BN device D110, taken and annotated by James Kerfoot. The location of the central h-BN flakes and of the two graphene flakes which sandwich them is shown. The active area is expected to be in the region where the four flakes overlap.

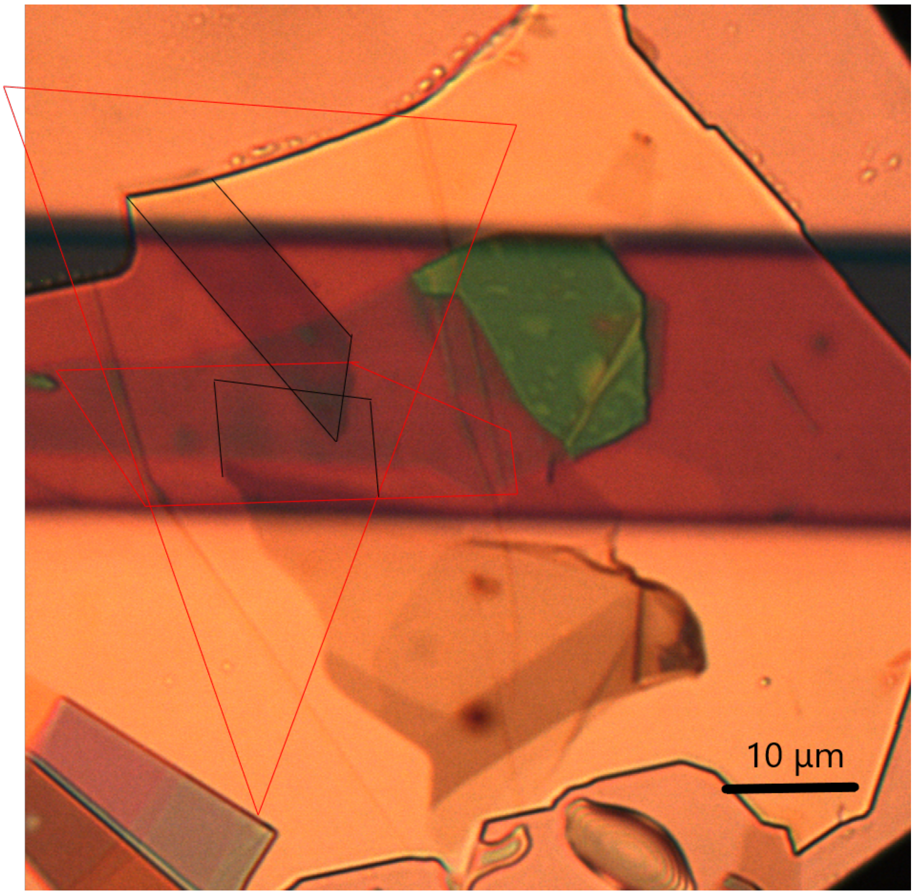

Figure 6.14: Optical microscope image of D110. Black lines outline the graphene flakes, red lines outline the two central thin h-BN flakes. It is thought that the interface between the two flakes is the source of the electroluminescent emission. Thanks to James Kerfoot for the image and annotation.

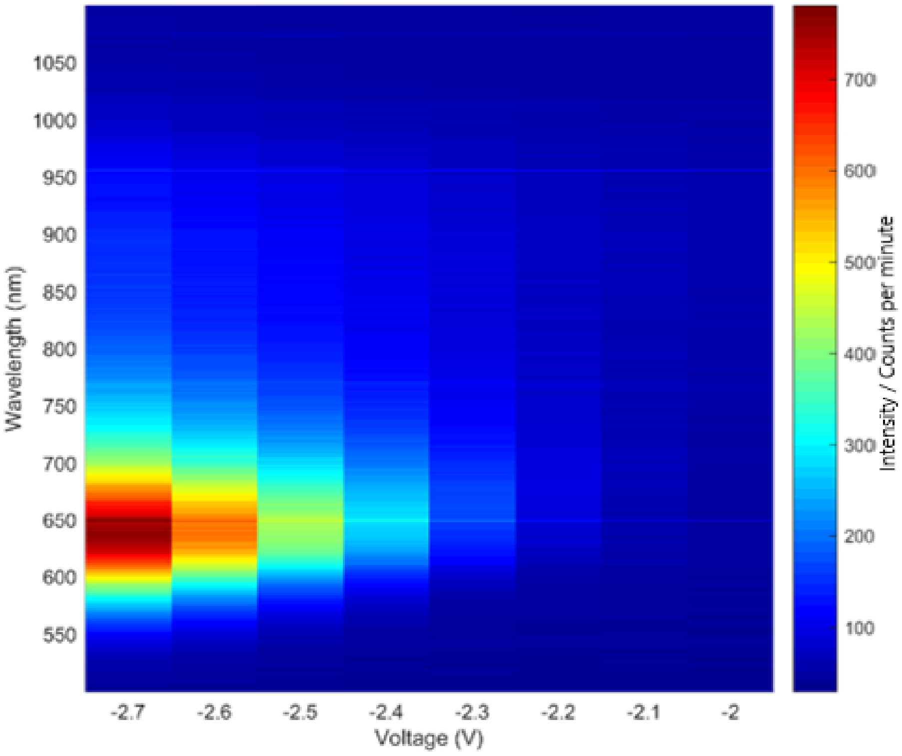

Figure 6.15: Electroluminescence spectrum of device D110. The graph shows that turn on voltage is in the region of 2.3 V and that peak emission is around 650 nm. Thanks to Dr Kerfoot for providing me with this graph.

Dr Kerfoot used a spectrometer with a cooled CCD camera to take spectra of the electroluminescent emitter on D110. This was taken with the tunnelling current flowing in the positive and subsequently the negative direction. This made no difference to the spectrum or the intensity of the emission. The spectrum of emission from the negative tunnelling current can be seen in fig. 6.15.

Figure 6.16 is a reflectance scan of the sample. The thick black diagonal line left to right, top to halfway down, is the edge of the gold contact with the gold contact beginning above this line. Some physical deformities on the surface are visible in the bottom right of the image, and just to the left of these the overlapping layers of h-BN can be seen clearly. The overlapping region is an acute-trapezoid shape and has some visible 'bubble-like' structures in the bottom left-hand corner.

Figure 6.17 is a 200 pixel scan, with an integration time of 1s per pixel; as such this scan took nearly 12 hours to complete. The scan was performed with the laser off and beam blocked, light-sources in the lab were covered up and the box containing the instrument was light-proofed to ensure that no stray photons could affect the data. No filters of any kind were placed in the beam path and the only obstacle was the dichroic splitter which has transmission of 95% at red wavelengths. Collection efficiency from the sample by the MO is very high; during tests reflecting a laser off a mirror in the sample plane at normal incidence, 95% of light arriving at the mirror arrived at the optical fibre (having accounted for the 90/10 beam splitter used for this test). In real experiments, the

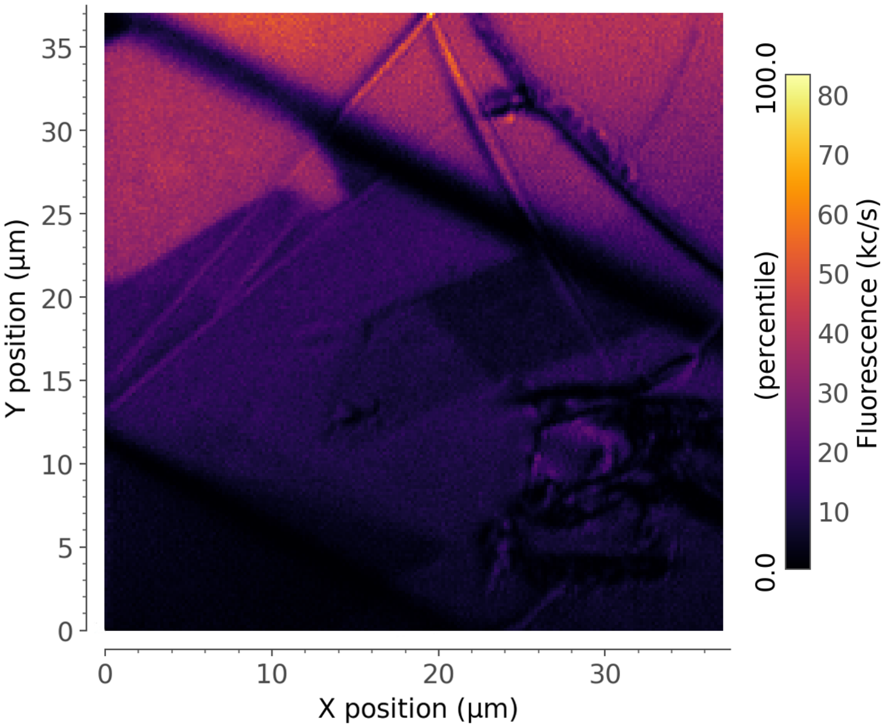

Figure 6.16: Confocal reflectance scan of D110, centred on the expected active region of electroluminescent emission, the region where the thin h-BN flakes overlap.

collection efficiency will be less than this as the lens will be 3.2 mm away from the sample and the emission will not be travelling exclusively upwards into the lens. The numerical aperture lens means it will only collect light travelling within a finite cone. The optical fibre acting as the pinhole and taking the photons into the light-tight SPADs' box transmits about 70% of light incident upon it. The inefficiency of the fibre should not be taken into account when calculating the actual intensity of emission, the fibre deliberately selects focused light in order to ensure that only light originating from the focal spot of the objective is counted. It is impossible to measure how much of the focused light is being lost at the fibre as replicating a 25 µm at the correct location/angle is difficult. The final element to take into account is the 50/50 splitter in the HBT interferometer setup, each detector receives only 50% of the photons. Taking into account the beam splitter, the dichroic splitter and the collection efficiency, actual emission intensity is ~2.2 times the detected intensity. This means that the brightest pixel on the image was emitting 332 cps from the sample. In reality, it is possible that the actual instantaneous count rate is higher than this, as the light appears to be emerging from an area of about 1 µm diameter. However as this scanning confocal microscope measures only one pixel at a time, i.e. only a fraction of the emission area at any one time, it is not possible to collect all the emitted light at once and therefore impossible to confirm the actual overall emitter intensity. This could be achieved if a lower magnification lens, with a collection spot larger than the emitter, was used.

The emission spectrum was analysed, by the group who grew the device, by

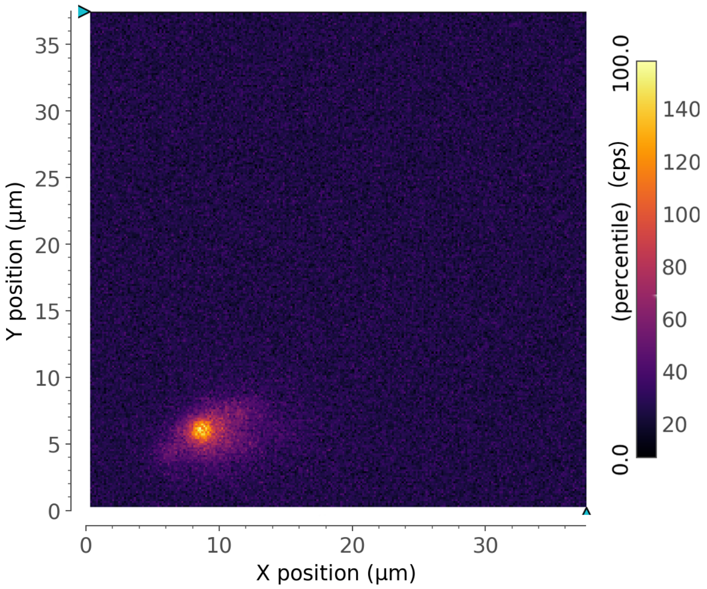

Figure 6.17: Electroluminescence scan of sample D110. This scan was performed with 1s integration time per pixel, meaning the data was collected over several hours. This was necessary to allow the emitted light to be distinguishable from the background noise of the detectors. The chip was provided with 2V DC and drew 45.66 µA.

collecting all light emitted from the sample in one large objective lens and passing it to a spectrometer. Count rates were collected in 1 nm bins, integrating across their data and dividing by measurement time gives a count rate of ~500 cps which would agree with our highest count rate on one pixel being less than the actually emitted count rate across the whole emitter region.

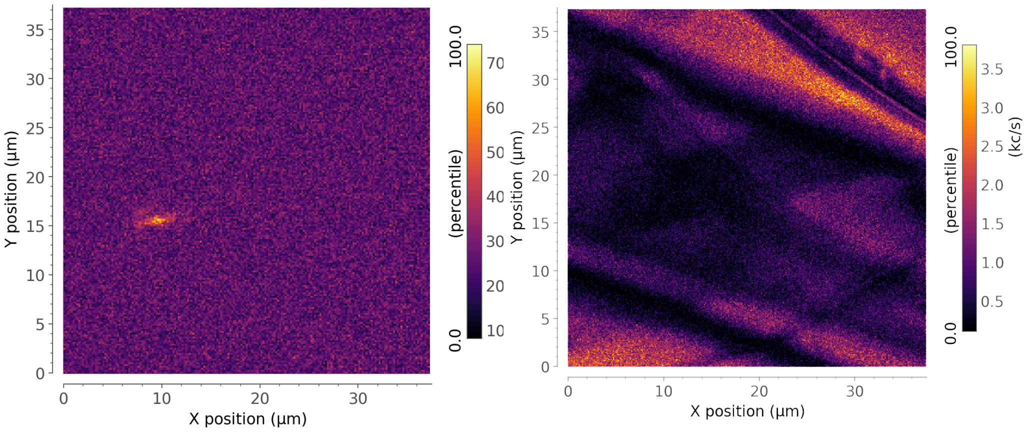

(a) Electroluminescence scan with a wider field of view than Fig.6.17.

(b) Reflectance scan with same FOV as Fig.6.18a.

Figure 6.18: Sample D110

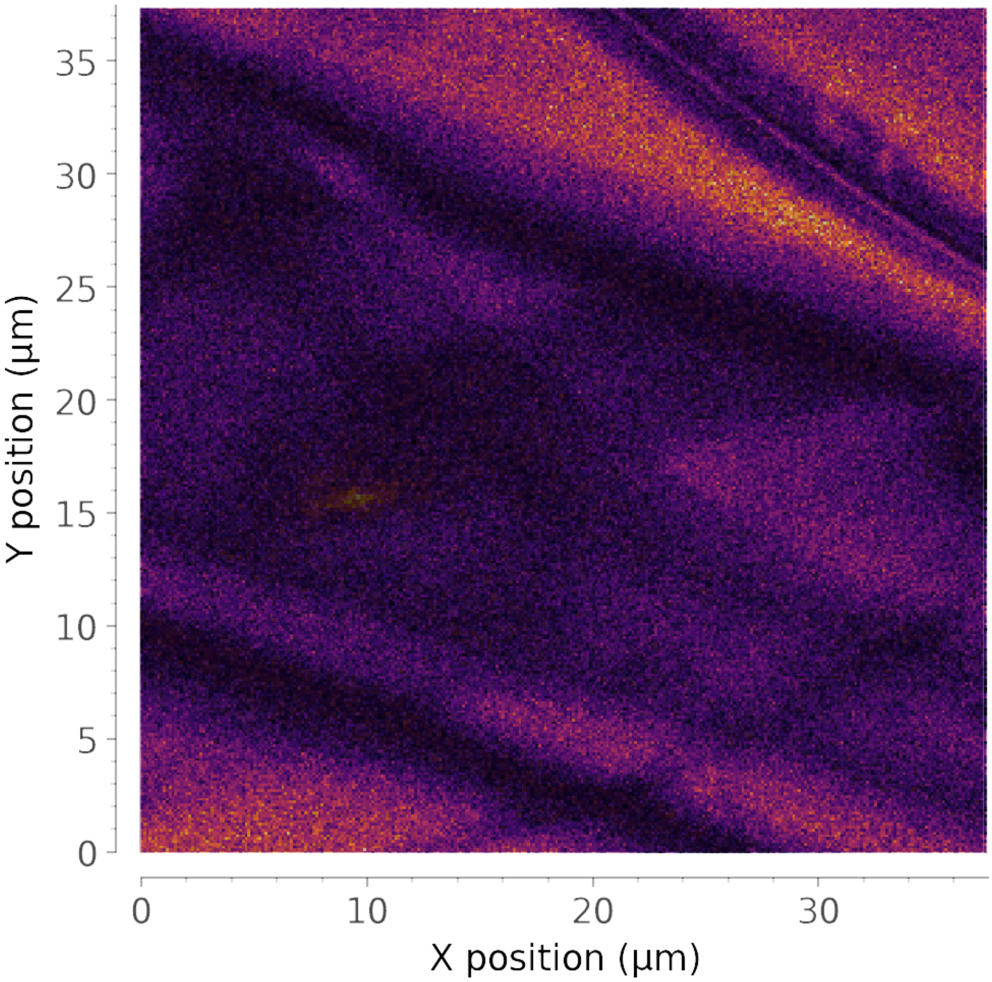

Figure 6.19: Image of Fig. 6.18a overlaid onto Fig. 6.18b.

The graph in Fig.6.20 displays the intensity of electroluminescent emission vs the voltage applied to the h-BN device. The voltage was not increased beyond 2.3 V even though it would probably luminesce with greater intensity in order to preserve the integrity of the chip and prevent breakdown or failure resulting from too much power dissipation.

After several weeks of use and a subsequent two weeks of not being used, the I-V characteristics of D110 changed dramatically. The chip drew only 15 µA at 3 V and no electroluminescence was observed for any voltage at any focal height. It appears that whatever causes the emission denatures slightly every time the power is switched off. It occurred on several occasions that powering down the device and then reapplying power resulted in a reduced current for the same voltage. This made it impossible to collect reliable data concerning the emission efficiency of this device, but such data would be of great interest and shall be investigated when new devices are available.

Visible in Fig. 6.16 are some circular features in the active region. These were not present at the time of the first scan and these defects appeared after several hours emission. They grew larger with emission time and coincide with the location of emission. It is possible that these are caused by the heat generated by the tunnelling current or by some of the emitted photons being absorbed into the material.

The electroluminescent emission from D110 (Fig. 6.18b), is visible in Fig. 6.18a. The overlay of these can be seen in Fig. 6.19. This shows that the emission is coming from the 'active region' where the crystals overlap, almost at the edge of one of the flakes.

There was insufficient light emitted by the electroluminescent emitter with which to test for antibunching. Even with many minutes of measurement, the light of the emitter could not be separated from the noise floor, the noise washed out the correlation counting data.

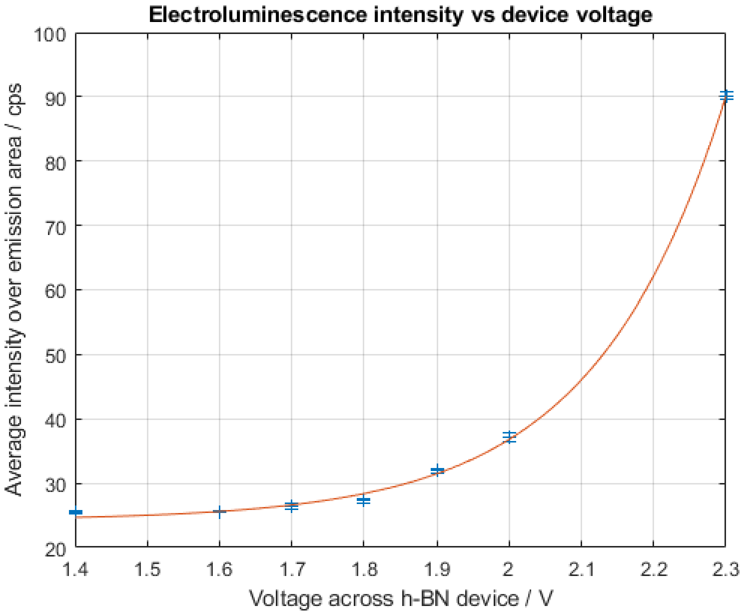

Figure 6.20: Graph of EL intensity vs voltage applied between the contacts. Points were best fit by an exponential curve of form $I = -24.21 + 2.02 \cdot 10^{-4} \cdot e^{5.52V}$.

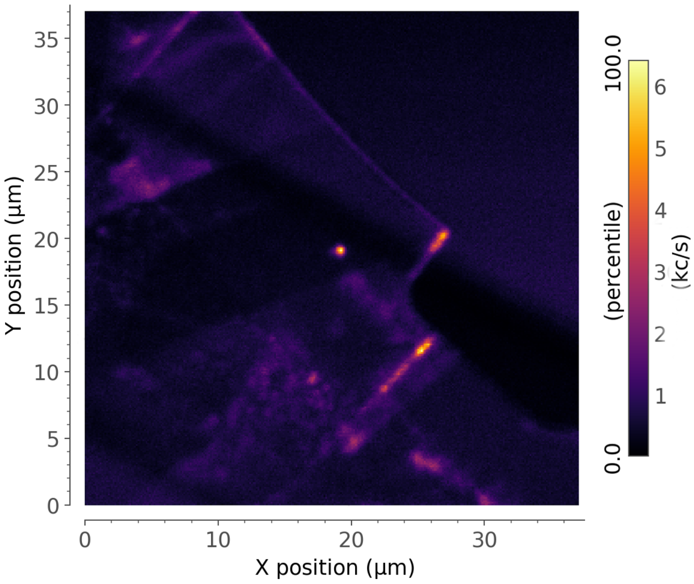

Figure 6.21: Photoluminescence scan of D110. Laser power was set at 1 mW which equates to 200 µW hitting the sample over the area of the focal spot (400 nm spot diammeter).

Sample D110 was also tested for photoluminescent behaviour. Figure 6.21 shows the resulting scan, with one bright point-like emitter in the centre of the image near the edge of the thin, flame annealed h-BN layer.

The PL emitter that is visible in the centre of Fig. 6.21 was probed and observed whilst different filters were placed in the beam path. The resultant data can be seen in Fig. 6.22. The horizontal bars display the transmission range of the notch filters used, in the transmissive region where transmission is 99%. For wavelengths outside this range, an O.D. of ≥ 2 is experienced. This information shows that most of the light emitted from the PL emitter has a wavelength between 600 nm and 750nm, with a peak near 650 nm. This agrees with Tran et al. [111] who detected PL at 632 nm.

Due to its diffraction-limited size, this photoluminescent emitter was tested for anti-bunching behaviour to see whether it was a single emitter or otherwise. The sample was probed with $\sim$ 10 µW of 514 nm light. However, after about 30 s of continuous illumination, the emission reduced to zero. The emission never returned, the emitter having bleached, therefore single source emission was never confirmed from this particular defect.

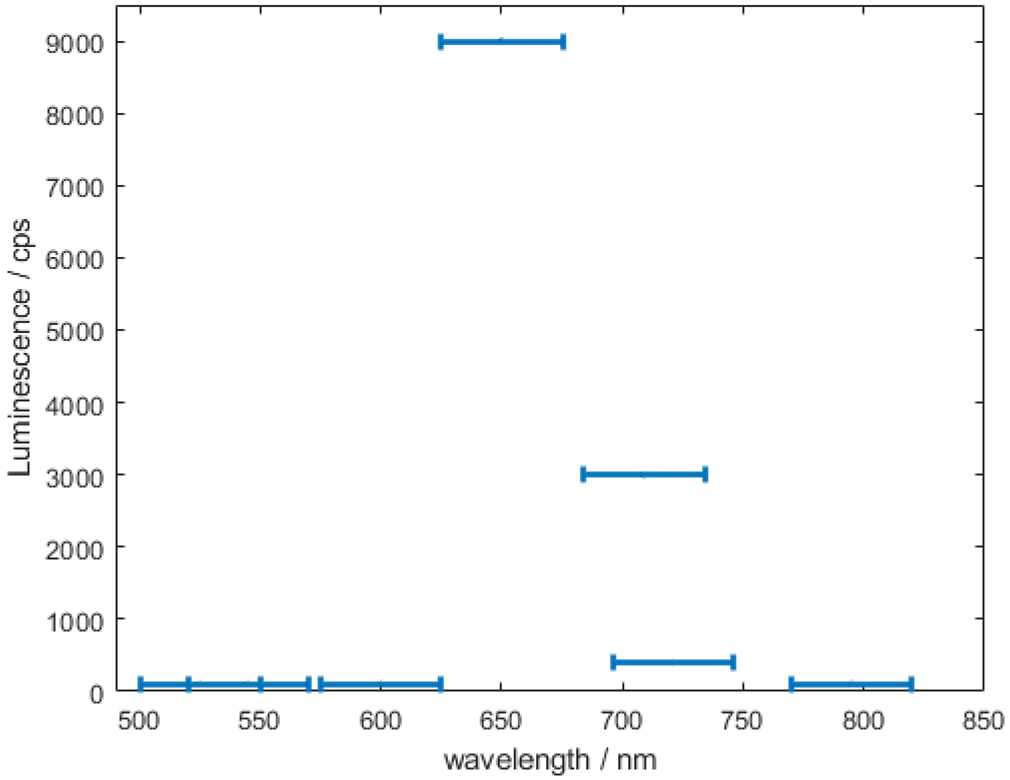

Figure 6.22: Emission spectrum of photoluminescent emitter in h-BN device, D110

The photoluminescent defect having bleached, it was decided to take a surface topography scan above the electroluminescent emitter. The camera view of the sample with the AFM scan area marked upon it is shown in Fig.6.23. The emitter location is visible here on the small white feature towards the edge of the overlap region.

Figure 6.23: Camera view of sample D110, with the area to be AFM scanned roughly marked upon it.

The topography data of a 40 μm× 40 μm scan can be seen in Fig.6.24 and the dF data in Fig.6.25. The frequency shift view provides a slightly clearer view of the locations of certain features. The deformation on the surface in figure 6.16 is clearly visible as 4 μm high feature at the edge of the scan area. With the correct feedback values, the AFM was more than capable of imaging this feature, despite its very large height and slope. This feature reduces the contrast across the rest of the scan making it more difficult to spot items of interest, however, in the dF scan, it is possible to pick out the location of the emitter and the surface feature above it. Moving to these coordinates on the topography graph allows height data to be extracted, which shows that this defect is 150 nm above the height of the surrounding layer. The feature at the emitter location can be seen more clearly in Fig. 6.26 and Fig. 6.27.

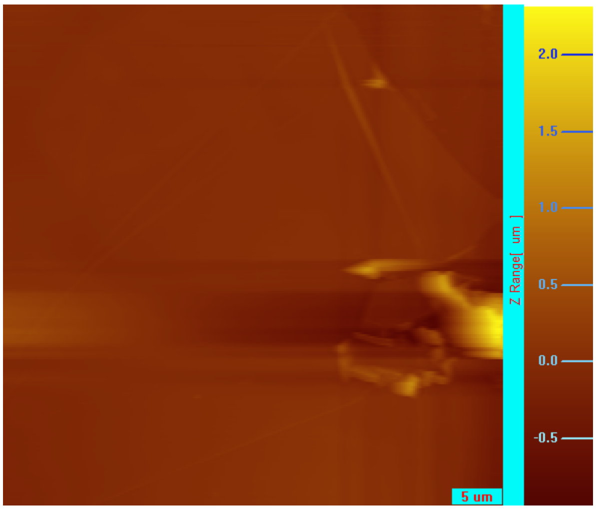

Figure 6.24: Large area AFM topography scan of D110. The feature at the location of the emitter is more visible on the dF data image. The large feature on the right of the image is 4 µm tall and is contamination on the surface of the device.

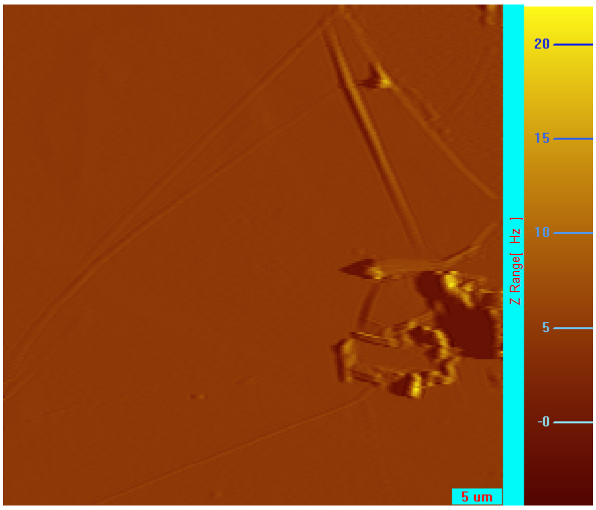

Figure 6.25: AFM scan dF data of sample D110. The emitter feature is more visible in this image and can be seen, just to the left of middle, approx 15 µm from the bottom of the image.

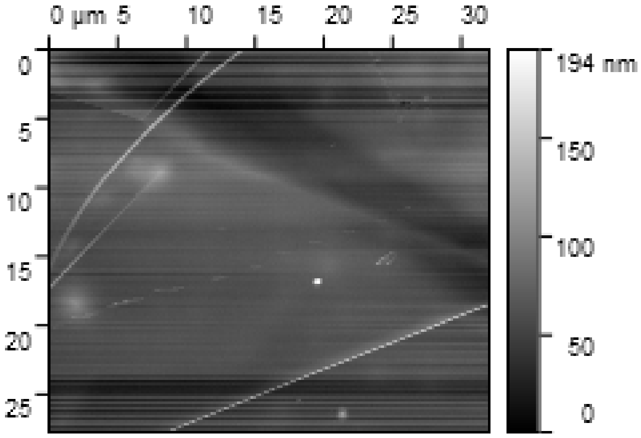

Figure 6.26: Cropped version of AFM scan in Fig. 6.24, the emitter location is more clear.

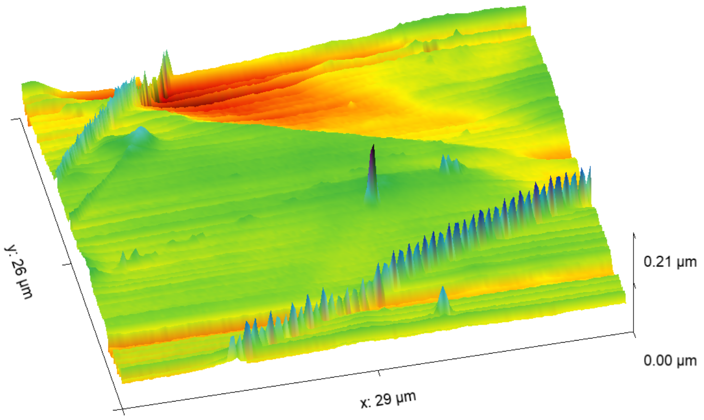

Figure 6.27: 3D image of topography data of PL emitter in sample D110.

6.5 Summary

Using the instrument, we were unable to detect electroluminescence from sample D41, however, photoluminescence was identified and located. The surface topography about the PL area was measured and a 600 nm bulge was detected above the emitter. It is known that the bulge and associated visible feature were not present before the PL emitter had been probed for several hours. It is postulated that the heat from the laser or the emission caused warping and distortion of the h-BN layers in the immediate vicinity of the emitter.

Sample D110 was scanned, electroluminescence was detected and located at a specific point in the active region, on the edge of a bubble-like feature which got larger with time spent electroluminescing. This provided useful information to the group who are making these devices as they previously had measured the intensity and spectrum of the photoluminescence but were unaware of the exact location, only where they expected it to come from, in the region of overlap between the two deposited thin h-BN flakes, the significance of this is a subject of further studies. Photoluminescence was also observed, emanating from a different location on D110. Our spectral analysis is not very precise, however, the emission was measured to be between 600 nm and 750nm with a peak near 650 nm. This is an area of the instrument which could be greatly improved, a spectrometer could be placed in the beam path, with the output coupled to the fibre optic cable which takes the light to the SPADs, this would provide higher precision of the spectral analysis. The surface was AFM scanned in the region of the emitter and a narrow feature, 150 nm tall was found at the location of the emitter.

This was another demonstration of the instrument working to the expected level of performance. The different imaging modes do not compromise each other and only minor adjustments are required to switch between them. This is an excellent demonstration of the highly specialised abilities of this instrument to extract photonic and topographic data of this kind from a sample, being the only instrument, in the University, suitable for the task. It was able to collect electro- and photoluminescence data over a 50 µm square area, optically observe the sample in high resolution and take AFM scans, measuring the topography and dissipation of the surface.

This chapter is concerned with specific devices constructed from h-BN. The next chapter shall investigate the fundamental physical properties of h-BN. This will be done by performing ellipsometry on high purity flakes of h-BN. Ellipsometry will be explained, in addition to the methods used to fit the data and extract physical values from it.

Chapter 7

Ellipsometry

This chapter explains the theory behind ellipsometry and describes the measurements made on various h-BN samples. A model is fitted to the data to enable optical properties to be calculated and other conclusions to be drawn from it.

7.1 Theory

The University of Nottingham has recently installed and commissioned a new imaging ellipsometer, the Nanofilm EP4 made by Accurion GmbH. This provides another instrument with which to extract interesting, fundamental information by imaging flakes of h-BN [121].

Ellipsometry is a non-invasive, contact-free method of measuring the properties of thin-film samples, probing the sample with polarised light. The method works most effectively when applied to a thin-film sample, on top of a thick substrate [122].

Light of a known polarisation is reflected off the sample and the change in polarisation is measured, effects will be different at different wavelengths of light due to the optical dispersion of the materials. Ellipsometers typically generate their light from a laser or from a white light source.

The light directed at the sample is elliptically polarised. Such light can be described as the sum of two, superimposed, linearly polarised waves in which the electric field vectors are perpendicular to each other, with differing amplitudes and a phase difference between the two. The sum of the electric field vectors rotates around the axis in an ellipse, with clockwise rotation referred to as right-handed polarisation.

The EP4 produces light from a laser-stabilised Xenon arc discharging between two electrodes in a low-pressure environment. This produces a continuum spectrum across the visible spectrum extending both into near UV, visible, and IR, albeit with reducing intensity as the spectral distance from visible increases. The light is then passed through a monochromator, with bandwidth 6 nm - 18 nm dependent on wavelength, to select only the required wavelength of light to be reflected from the sample. Light is produced in the range 190 nm - 1700 nm.

Once the wavelength has been selected the light is aimed at the sample and passed through a linear polariser and then a compensator (a quarter-waveplate). The compensator converts the linearly polarised light into elliptically polarised

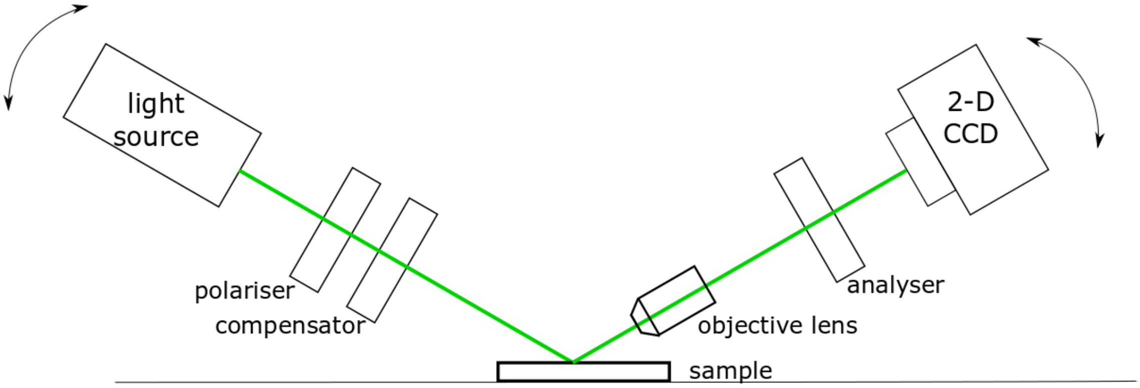

Figure 7.1: System diagram of the EP4 Spectroscopic Imaging Ellipsometer.

light which then hits the sample. The collimated light is reflected off the layer boundaries in the sample and is gathered by a microscope objective before it passes through the analyser (another linear polariser), before hitting the detector which measures intensity. The angle of incidence is adjustable and is, ideally, set close to the Brewster's angle of the layer beneath the thing film sample in order to maximise the contrast in the image on the detector. A diagram of the setup is shown in Fig.7.1.

The instrument sets the polarisation of the light being projected at the sample and measures the polarisation shifts of the light reflected from the sample. The variables measured are,

$$\rho = \frac{r_p}{r_s} = \tan\Psi \cdot e^{i\Delta} \tag{7.1}$$

where ρ is the complex reflectance ratio of p-polarised to s-polarised light, Ψ is the amplitude ratio of the two polarisations and Δ is the phase shift of each polarisation. p-polarised light is polarised parallel to the plane of incidence, and s-polarised is perpendicular. This reflectance can be derived from the Fresnel equations [123]. During measurements of a sample, the angle of the polariser and the analyser is varied whilst data is recorded, and the incident wavelength can also be methodically varied to collect extra information about the properties of the material.

The phase change of the light after reflection is affected by the thickness of the material, its dielectric tensor, and the complex refractive index at that wavelength. Theoretically, or experimentally determined models of materials are used to fit the collected data and to extract values for these properties. The Accurion fitting algorithm uses a Levenburg-Marquardt least squares regression method, which when given appropriate initial estimates can find the global best fit. When operating in the wavelength scanning mode, this instrument can be an efficient way of finding the band-gap of a semiconductor [124].

Although this is an optical measurement method, the resolution of thickness is not diffraction-limited. This is because phase change is the measured property allowing sub-nanometer resolution of thickness measurements [125].

7.1.1 Imaging Ellipsometry

The Accurion EP4 is specifically an imaging spectroscopic ellipsometer. It carries out the measurement on phase change and intensity using two CCD cameras (for different wavelength ranges) with square arrays of pixels making it possible to carry out one measurement per pixel per image captured. This, therefore, allows a view of the sample, prior to and during measurement, as well as the selection of particular regions of interest, where the phase and intensity change of the area are calculated by averaging every pixel in that region. This allows us to make spectroscopic measurements on exfoliated flakes with lateral dimensions less than 10 µm.

Due to the large angle between the camera axis and the sample plane, the depth of field is extremely thin, collecting light from only a narrow band across the sample. Therefore the focus is pulled across the sample for each different polarisation angle or wavelength increment by moving the objective lens. The size of the focal strip and the frame rate of the camera determine how long a measurement will take.

The most common imaging mode is called "EP4 nulling". This is used when thin films being measured are on top of a reflective substrate. The polariser and analyser are rotated to find the minimum detected light intensity, this provides high contrast images of the flakes and accurate measurements of Δ and Ψ.

7.1.2 The model

Optical properties of the material cannot directly be extracted from the values of Δ and Ψ. A model of the material must first be created, including the thicknesses of the various layers, using known models and by creating new models if none exist. This overall model can then be used to calculate what values of Δ and Ψ would be expected at given angles of incidence. These values are then plotted and compared to the experimentally obtained values. A Levenberg–Marquardt algorithm is then used to alter the parameters within the model until the predicted Δ and Ψ values are as close as possible to those measured. The model is checked for goodness of fit, and also for any cross-correlation between the fitting parameters, indicating redundant parameters. Once the model is considered correct and is a good fit, then values for permittivity of the observed material can be calculated, and from there, values for the refractive index and extinction coefficient can be produced, details of which are covered in section 7.3.

7.1.3 Relevance to h-BN

This particular EP4 made by Accurion is the first to perform measurements with wavelengths of light down to 190 nm, 50 nm below the previous limit. This makes it the first imaging ellipsometer able to use such high photon energy. It also makes it an interesting prospect for observing h-BN which has a band-gap at 208 nm, resulting in increased absorption, reflection at this wavelength. The purpose of this investigation is, therefore, to obtain information on the dielectric functions of h-BN at incident photon energies greater than that of the material band-gap.

Hexagonal boron-nitride is a van der Waals material, meaning the molecules are bonded together covalently, forming layers, which in turn are stacked together with van der Waals bonds between the layers. These properties mean that, for optical properties, h-BN is a uniaxial, anisotropic material. The single-axis referred to (by uniaxial) is any vector through the material, along which light can travel, and rotation about this axis does not affect the propagation of the light through the material. h-BN has only one such axis, normal to the layers of the crystal [126], making it a uniaxial material.

The layered nature of the material causes the electron clouds around each molecule, to be distorted into an oblate spheroid. The electron clouds are strongly confined to the molecular layers, perpendicular to the optical axis. This means that light passing through the material will experience different refractive indices dependant on polarisation and the material is, therefore, anisotropic [127].

For linearly polarised light passing through the material (perpendicularly to the layers), with electric field parallel to the incident/reflected beam axis, called the extraordinary polarisation, the field is oscillating in the light incident plane. Perpendicularly, ordinarily, polarised light has electric field oscillations perpendicular to the incident plane.

The ordinary electric field oscillates parallel to the layers of the crystal, along the major axes of the electron cloud spheroids, providing the potential for stronger coupling, absorption, or other energy transfer from the light to the crystal. Extraordinary light oscillates parallel to the minor axes of the spheroids, perpendicular to the layers of the h-BN, where less energy transfer is likely. A diagram showing the crystal layers, the optical axis of the h-BN, and the parallel and perpendicular electric fields can be seen in fig. 7.2.

The difference in the refractive index, Δn, experienced by the two polarisations of light, equivalent to the polarisation of the two perpendicular axes of the material, is called the birefringence. It is given by the equation,

$$\Delta n = n_e - n_o \tag{7.2}$$

where n_e is the extraordinary axis refractive index, and n_o is that of the ordinary axis.

The extent to which the electrons are confined to their layers is thought to be the reason for such large birefringence being exhibited by this material[128], a value for which will be determined in by the experimental process described in this chapter.

Investigating h-BN with UV light is important because the information acquired will aid further research and the creation of new devices, fabricated from this material. There is interest in using h-BN to form solid state neutron detectors (due to boron's, and therefore h-BN's, large thermal neutron cross section) [129], single photon emitters [130], but most relevantly to the ellipsometry investigation, to form high efficiency UV emitters and deep UV optoelectronics [131]. Quantifying the anisotropy of a high quality sample of h-BN, as produced by Dr Kerfoot, fills a gap in the current understanding of the optical properties of h-BN.

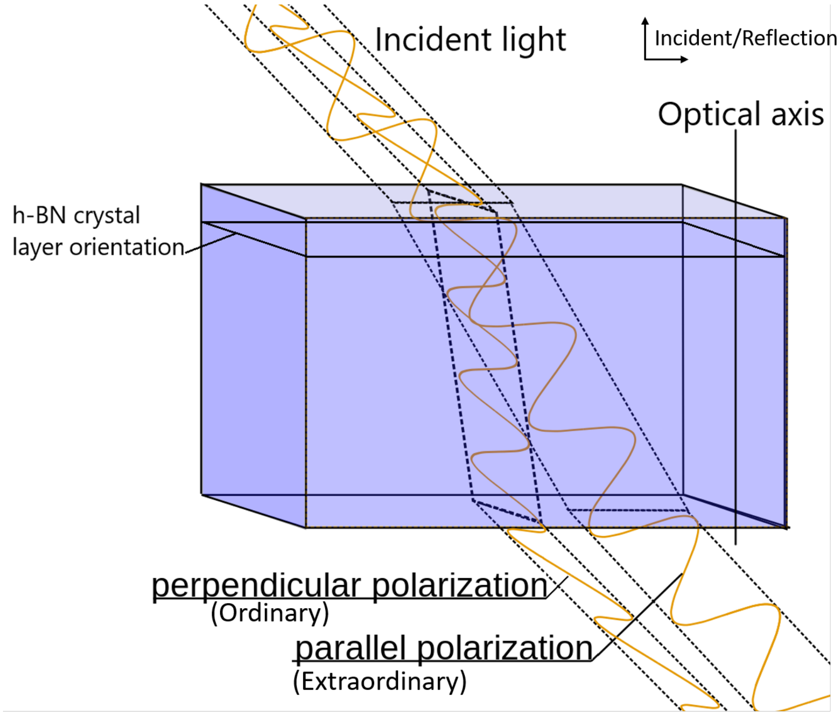

Figure 7.2: Diagram displaying p and s polarisations with respect to the incident plane of the beam. Also visible is the optical axis of h-BN with respect to the crystal layers. Diagram adapted from work by Mikael Häggström, used with permission.

7.2 Literature Review

A paper by Crovetto et al. [132] describes using ellipsometry to determine the thickness of hBN multi and mono-layers. The boron-nitride flake was attached to a Si/SiO_2 substrate and its thickness was measured before and after flame annealing.

A conference paper by Rah, Jin, Kim and Yu [133] describes the measurement of the birefringence of exfoliated flakes of hBN for wavelengths 400-750 nm. The team used an optical microscope and a spectrometer in combination to measure the reflectance of the hBN flakes at different wavelengths, and a spectroscopic ellipsometer was used to measure the refractive indices of the flakes along the different crystal axes.

Vuong et al. investigate the optical properties of MBE grown h-BN [134]. The material is probed with wavelengths down to 210 nm and they find that the MBE grown h-BN is of high optical quality.

Rah et al. used a spectroscopic ellipsometer to measure the refractive index and birefringence of h-BN (from HQ Graphene, Netherlands) from 100 nm to 400 nm [135]. This paper confirms the birefringent nature of h-BN, they find a Δn of between 0.3 and 0.35 dependent on wavelength.

McKay et al. perform spectroscopic ellipsometry on 200 µm thick, metal oxide CVD-grown epilayers of h-BN using photons of 309 - 243 nm in wavelength [128]. Their aim was to assess the quality of the crystal by measuring what proportion of the crystal's layers were not aligned horizontally (horizontal being the orientation of the majority of the layers). To do this, they quantified the degree of birefringence in the crystal, finding Δn = -1.2 at 280 nm wavelength. They found that this value rapidly increased approaching the band-gap, attributing this to the layered structure and the presence of stronger excitonic effects nearer the band-gap.

Segura et al. analyse interference patterns, in reflectance (555 - 1428 nm) and transmission (1700 - 184 nm), in HPHT-grown h-BN crystals [136]. Degree of birefringence ranged from Δn=-0.7 at 774 nm to Δn=-2 at 221 nm probing photon wavelength. The process used to find the values for the refractive indices is similar to that used by ellipsometry. The interference patterns are recorded, then models created and used to recreate such interference patterns. Thes models are then optimised to best fit the data and then values for permittivity are extracted from the model's parameters. The article notes that their data largely agrees with what is expected from ab initio calculations, but it does not present and data collected at or above h-BN band-gap energies.

Funke et al. used spectroscopic imaging ellipsometry to characterise flakes of h-BN on a SiO_2 on Si substrate [137]. They measured from 350 nm to 800 nm incident photon wavelength then fit the data using an anisotropic model with a Cauchy model for the in-plane dielectric function and a Lorentzian model for the out of (incident/reflection) plane components. The in-plane extinction coefficient was assumed to be almost zero. A maximum birefringence of $\Delta n = -0.5$ was found at 350nm incident wavelength. This study probes the material in the near-UV range but does not approach or exceed the band-gap energy of h-BN.

7.3 Methods

The Accurion imaging ellipsometer is very user-friendly and, providing a checklist is rigorously followed, reliable in collecting data. Coupled with a high magnification lens, the CCD on the EP4 can provide a lateral resolution of 1 µm. Polariser, compensator and analyser angles can be set to a precision of 10^{-3} degrees.

The sample is loaded onto the motorised XY stage and centred in the camera. The appropriate lens should be chosen beforehand with a variety of magnifications available (5x-50x) however it should be noted that most of the Olympus lenses are opaque to UV photons and therefore for imaging at 300 nm or shorter, a special (UV transparent) 7× lens must be used. Once the sample is centred, the camera must be focused, and as the sample is very far from perpendicular to the camera axis and the focus is just a thin band across the width of the sample, the focus is performed by scanning the working distance of the objective. The camera records as the focus is swept from top to bottom and a composite image is generated where every pixel is in focus. At this point, regions of interest (ROIs) must be drawn. ROIs should encompass uniform regions where the interaction with the light is expected to be the same across the whole area. The software averages over each of these areas and produces Delta (Δ) and Psi (Ψ) data for each area. The averaging of the readings improves the signal-to-noise ratio of the measurements.

The ellipsometer is programmed to take data whilst scanning over a range of incident angles and/or a range of wavelengths and can then be left to measure unattended. The data is saved as raw Δ and Ψ values vs wavelength, this can then be imported into the modelling software which fits models of the dispersion to the data and calculates the physical properties of the material.

The fitting is based on pre-existing models of the dielectric function ϵ(E), where E is photon energy, which are informed both by measuring materials with known properties and from theoretical considerations. There are well known dispersion models for silicon and silicon dioxide. The fitting is performed by using different models in conjunction with each other and allowing the software to vary the parameters in the models to minimise the root mean squared error (RMSE). The optimised parameter values allow the calculation of

$$\tilde{\epsilon}(E) = \epsilon_1(E) + i\epsilon_2(E). \tag{7.3}$$

where ϵ_1 and ϵ_2 are the real and imaginary parts of the complex dielectric constant. They are referred to as the permittivity of the material and the absorption product of the material respectively.

The dielectric function is related to the complex refractive index, $\tilde{n}$, of the material,

$$\tilde{n} = n + ik \tag{7.4}$$

n is the real component of the complex refractive index and is what we commonly refer to as the refractive index, it describes by how much light is slowed down when passing through a material compared to in a vacuum. k is the imaginary component of the complex refractive index, it refers to how much attenuation takes place when light passes through the material and is referred to as the extinction coefficient.

The relationship between these values is given by,

$$\tilde{\epsilon} = \tilde{n}^2 = (n + ik)^2 \tag{7.5}$$

$$n = \sqrt{\frac{|\tilde{\epsilon}| + \epsilon_1}{2}} \tag{7.6}$$

$$k = \sqrt{\frac{|\tilde{\epsilon}| - \epsilon_1}{2}} \tag{7.7}$$

allowing the calculated values of ϵ_1 and ϵ_2 to be converted into the complex refractive index.

Another property of these values is that they obey the Kramers-Kronig relations [138]. The dielectric function ($\tilde{\epsilon}$), and the complex refractive index ($\tilde{n}$), are both analytic functions in the upper-half complex plane, and as such ϵ_1 is inextricably related to ϵ_2 and n is inextricably related to k. I shall not include the formula relating the two parts in this thesis as I have not had to use it, the software performs the job of inferring k from n and ϵ_2 from ϵ_1. This relationship means the two are not independent of each other, fixing the value/function of one of them fixes the value/function of the other. This is an important property to take into account when fitting ellipsometry data.

Dr James Kerfoot prepared samples for us, producing flakes by exfoliation that were as thin as possible as well as some thicker crystals. Measurements were made on the samples using the EP4, and then the samples were measured with the AFM to determine the thickness in order to corroborate the fitted ellipsometry data.

The h-BN samples investigated in this thesis were all of the same type and from the same production batch. They were fabricated in Japan in the research group of Watanabe [116], using a high pressure high temperature (HPHT) method and then exfoliated in Nottingham by Dr James Kerfoot in order to deposit the flakes on wafers (in this chapter) or to make the electroluminescent devices (as in Chapter 6). There are other methods of making h-BN, including by molecular beam epitaxy (MBE) which is performed at the University of Nottingham, although the quality of the product is currently significantly lower than the material used in this thesis.

HPHT h-BN, and in particular the sample from this research group, are of extremely high purity making them ideal samples on which to perform ellipsometry. The data obtained from this material should be highly accurate. The problem in measuring the optical constants of this material until now has been that the exfoliated crystallites are too small to measure on conventional ellipsometers.

7.4 Ellipsometry on a thin flake of h-BN

The samples used were made by exfoliating the HPHT h-BN onto a silicon wafer with a 90 nm silicon dioxide layer on the surface. The sample was then raster scanned and imaged by an optical microscope, collecting images of the whole surface. Dr Kerfoot then sifted through these images looking for thin flakes of h-BN. Fig. 7.3 shows the optical view of an area of the sample which contains a thin flake in the centre. Fig. 7.4 shows the optical view of the flake under a 100× microscope objective on an optical microscope. A polariser was used to improve the contrast of the image, which underwent further contrast enhancement in post-processing.

Areas of interest on the flake were selected and wavelength scans were performed at a fixed angle of incidence, scanning between 190 nm and 1000nm, with the ellipsometer setting the camera exposure time at each wavelength before measuring the Ψ and Δ values by the EP4 nulling method.

This flake is extremely thin, measured on an Asylum-Research Cypher AFM to be 0.8 nm thick. This indicates that it is a bi-layer, two atoms thick. For this reason, the contribution to the Ψ and Δ vs wavelength plots was very small compared to that of the SiO_2. The only difference between this data and the silicon dioxide model was a small peak at the band-gap. This made the data impossible to fit and therefore no values could be extracted. For future ellipsometry experiments, it would be interesting to see if exfoliating the h-BN onto a silicon wafer with no oxide coating would give a clearer response. There should be little or no sharp structure in the dielectric function from the opaque silicon close to 6 eV which may allow the phase shifts due to the h-BN to be observed more clearly.

The sample was AFM scanned using the instrument (described in chapter 3) in an attempt to get a height measurement to aid the fit of the ellipsometry data. The Cypher AFM had determined the h-BN flake thickness to be 0.8 nm, significantly smaller than the 2 nm noise floor of the AFM on our instrument,

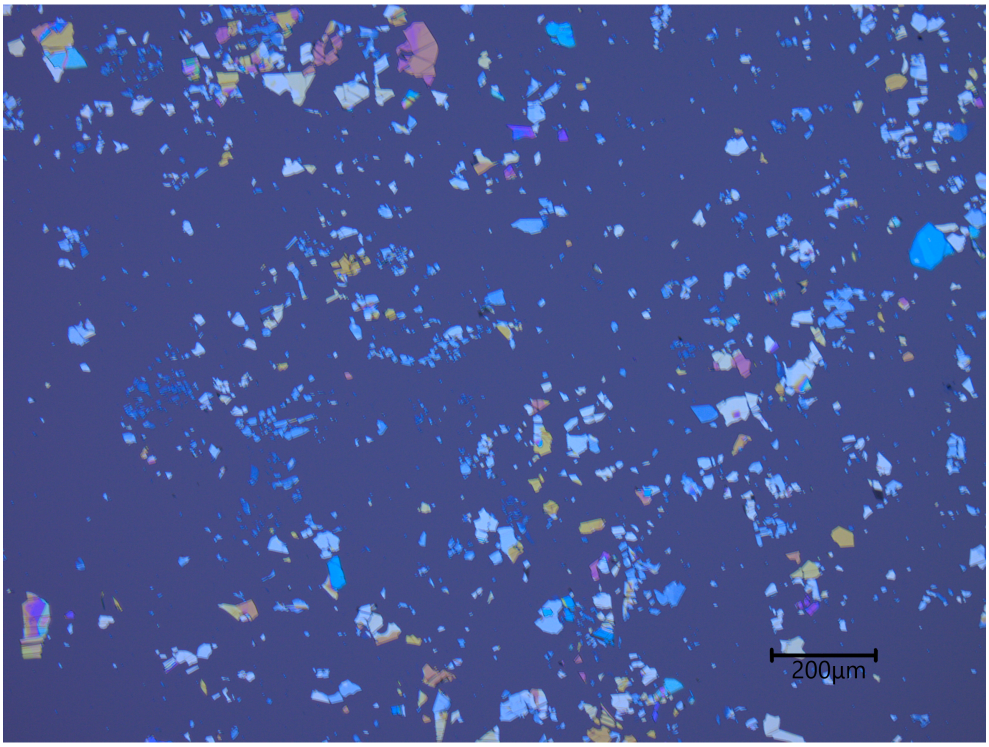

Figure 7.3: Wide angle, optical microscope, view of h-BN flakes on SiO_2 wafer.

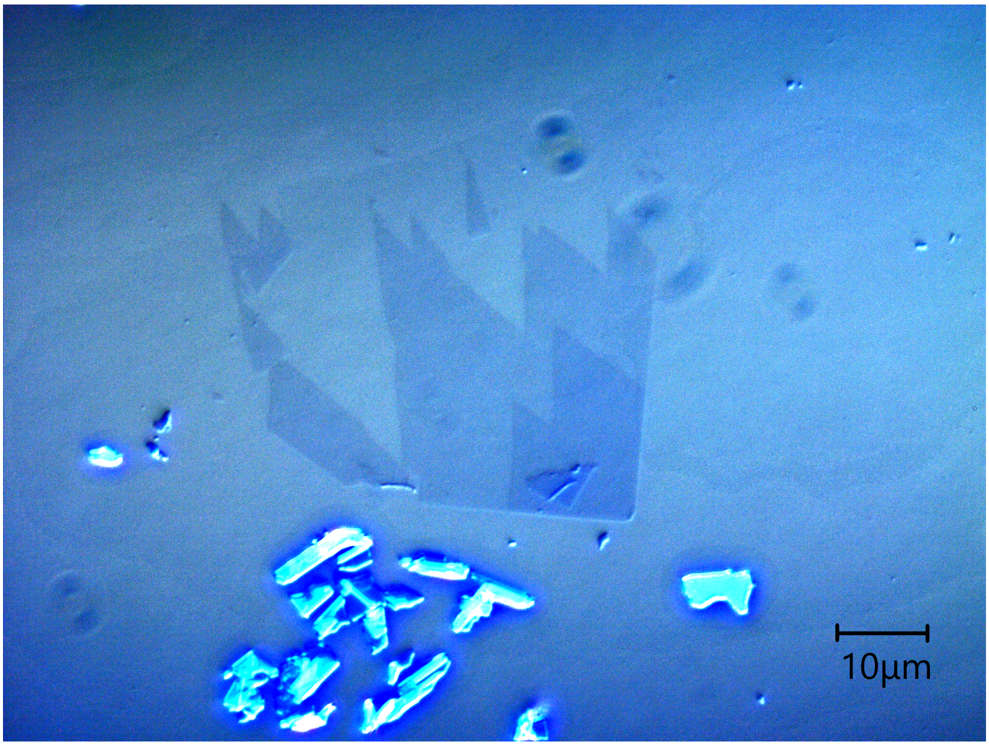

Figure 7.4: Optical microscope image (using differential interference contrast microscopy) thin h-BN flake on 90 nm SiO_2. The contrast of the image has been enhanced in post-processing.

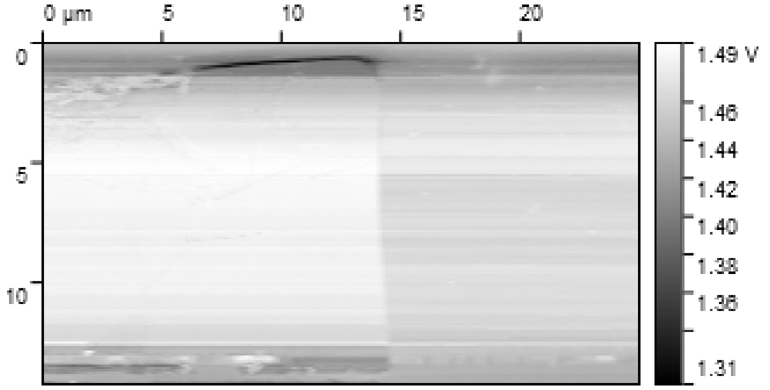

Figure 7.5: PLL amplitude plot from the AFM scan over the thin flake of h-BN. Scan is of the bottom right corner of the flake shown in figure 7.4.

and therefore the topographic data came back as noise. However, our instrument was not totally oblivious to the presence of the thin flake of h-BN. The PLL amplitude data (Fig. 7.5) clearly shows the flake (The bottom right corner in Fig. 7.4), despite the z-height feedback loop not adjusting to accommodate for the sample. When the AFM probe is scanned across the sample in constant excitation mode, the PLL amplitude data can be derived from the current, generated by the Akiyama probe, (which passes through a transimpedance amplifier and is converted to voltage, hence the voltage scale on the image) and is proportional to the oscillation amplitude of the cantilever. When the cantilever is on the surface of the h-BN, the amplitude of oscillation is larger than when it is on the silicon dioxide. This means that the h-BN is less dissipative, meaning less energy from the cantilever is lost to the sample. This is possibly due to the fact that the AFM probe is Si and the SiO_2 surface is likely to interact more with the tip as they have similar bonds. The surface of the h-BN adhesively interacts with the silicon cantilever tip less than the silicon dioxide surface.

The flake was then imaged using the confocal microscopy components. In reflectance mode, there was very little interaction with the 514 nm light and therefore the flake was not visible, see Fig. 7.6. In fluorescence mode when the green light was filtered out and only red light was allowed through to the SPADs, the outline of the flake was clearly visible and stood out from the completely dark silicon dioxide on silicon. There was also a reasonable degree of photoluminescence from areas of the h-BN. Emission was particularly bright in the corner of the flake where the h-BN has more layers and is stacked higher due to a smaller flake on top of the larger bi-layer flake. This photoluminescence could be due to impurities, possibly hydrocarbons, picked up during measurement in ambient conditions [139], particularly as it had been scanned by AFM prior to this measurement, however, the flakes at the top of the image had not been scanned and also display fluorescence. This shows that even bi-layers of h-BN emit >600 nm light when probed with a 514 nm laser. Observing this PL and measuring the emission spectrum is a possible future research direction.

Fig. 7.8 and Fig. 7.9 show the thin h-BN flake from the viewpoint of the imaging ellipsometer's camera. These images nicely display the what happens when photons incident on the crystal are above and then below the band-gap.

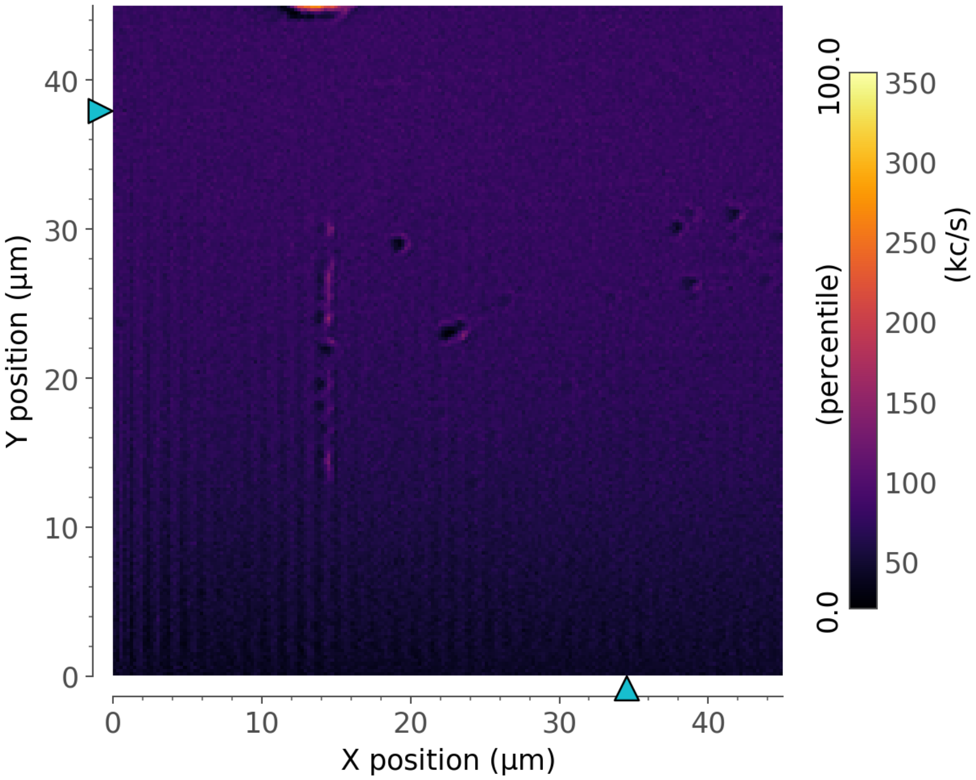

Figure 7.6: Confocal laser (514 nm) reflectance scan of the thin h-BN flake.

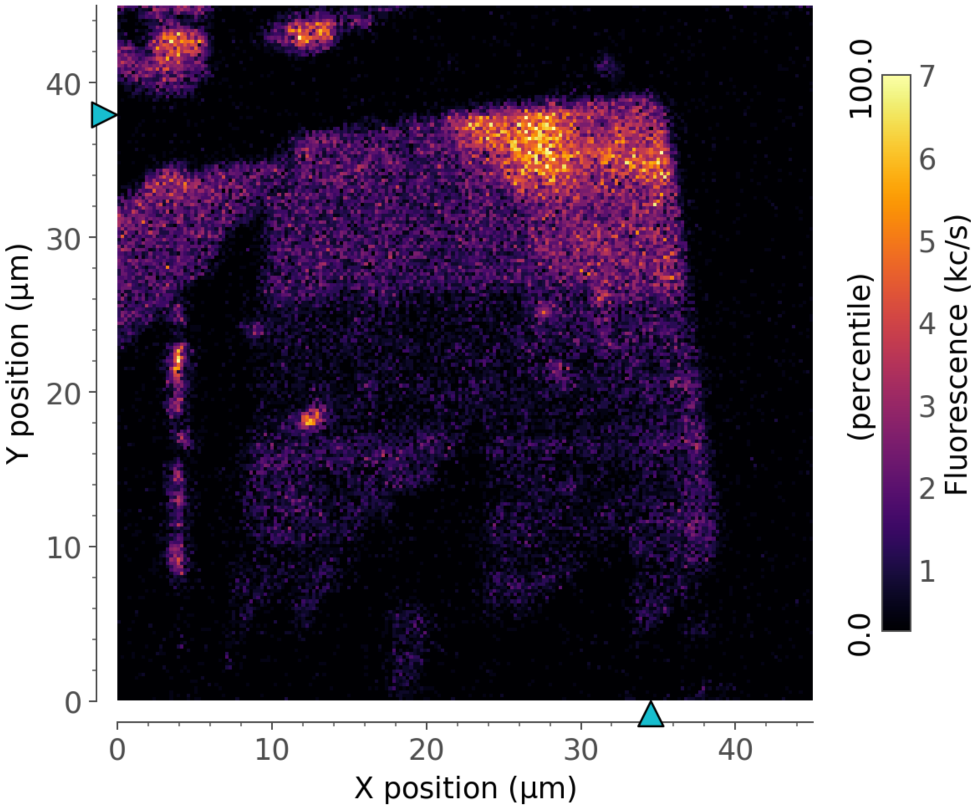

Figure 7.7: Confocal photoluminescence scan of the thin h-BN flake. Probed with 514 nm laser; emitted light is of wavelength longer than 637 nm

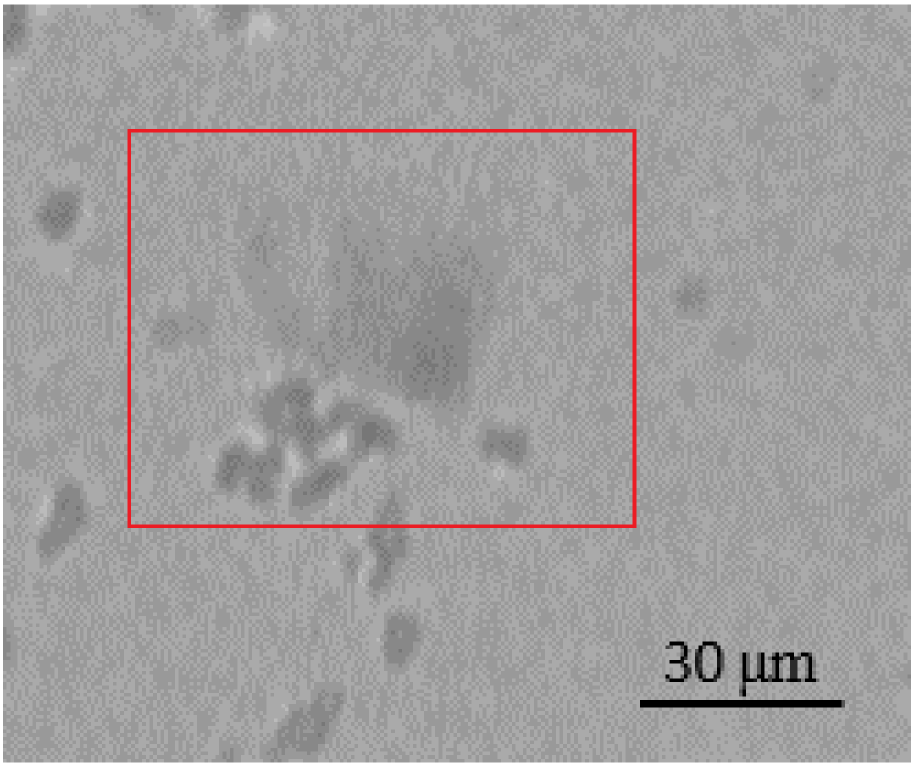

Figure 7.8: Bilayer flake of h-BN, viewed by the imaging ellipsometer, illuminated with 200 nm wavelength photons. Red box indicates the area visible in fig. 7.4. The contrast is the same for all h-BN flakes as light of this wavelength does not penetrate the full thickness of the flake.

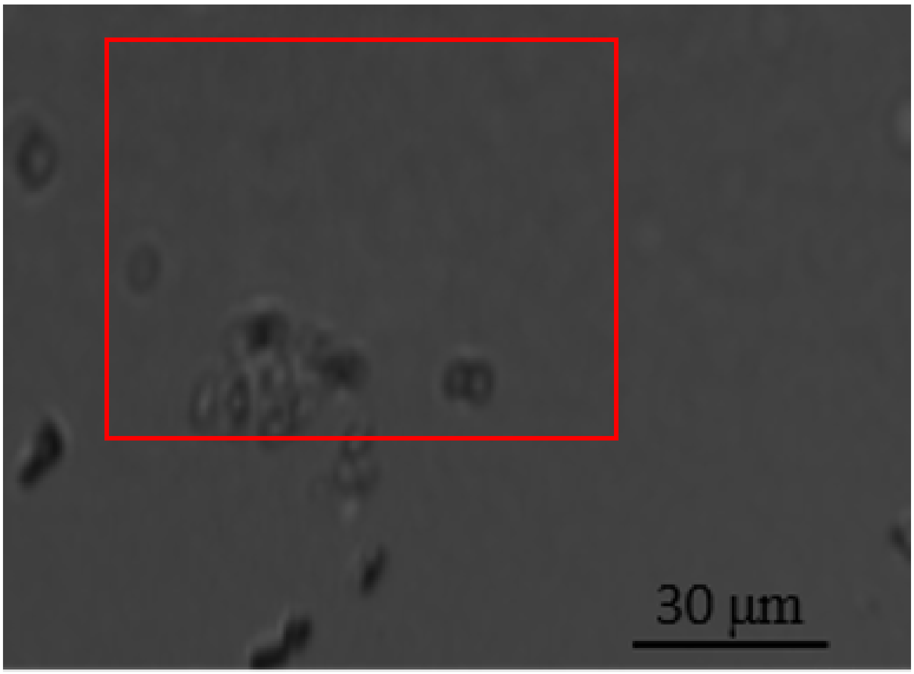

Figure 7.9: View of the same region as Fig. 7.8, illuminated with 250 nm wavelength photons. As the photon energy is below the band-gap of the h-BN, there is no absorption of the photons and so the h-BN is transparent at this wavelength. The image contrast varies from flake to flake due to the variations in flake thickness.

The band-gap of h-BN is about 6 eV and using,

$$E(eV) = \frac{hc}{e\lambda} \tag{7.8}$$

where E is photon energy in electron volts, h is Planck's constant, c is the speed of light in a vacuum, e is the charge of an electron and λ is the photon wavelength, this is shown to correspond to a photon wavelength of 206 nm. As will be shown later in Fig. 7.16, the extinction coefficient of h-BN, that is how much photons are absorbed when passing through the material, is almost zero below the band-gap and increases greatly at the band-gap. This means that sub-band-gap energy photons pass through the material, whilst photons of greater energy are absorbed and then re-emitted in random directions, or the energy is dissipated throughout the material as electron-hole pairs or phonons in a non-radiative loss process. This causes the flake to appear dark as photons emitted in random directions are far less likely to be collected and measured by the objective lens and the CCD.

Fig. 7.8 shows a dark flake, absorbing and re-emitting 200 nm photons which have energy higher than the band-gap, Fig. 7.9 show that the flake is invisible as the 250 nm (5 eV) photons do not interact with the h-BN and reflect off the SiO_2 surface below the flake.

During AFM scanning there was an unfortunate occurrence when the feedback loop lost control of the height and raised the sample to full approach, 25 µm closer to the tip than the contact point. The scan continued with AFM cantilever bent and the tip pressed hard into the sample (with a force of approximately 125 µN).

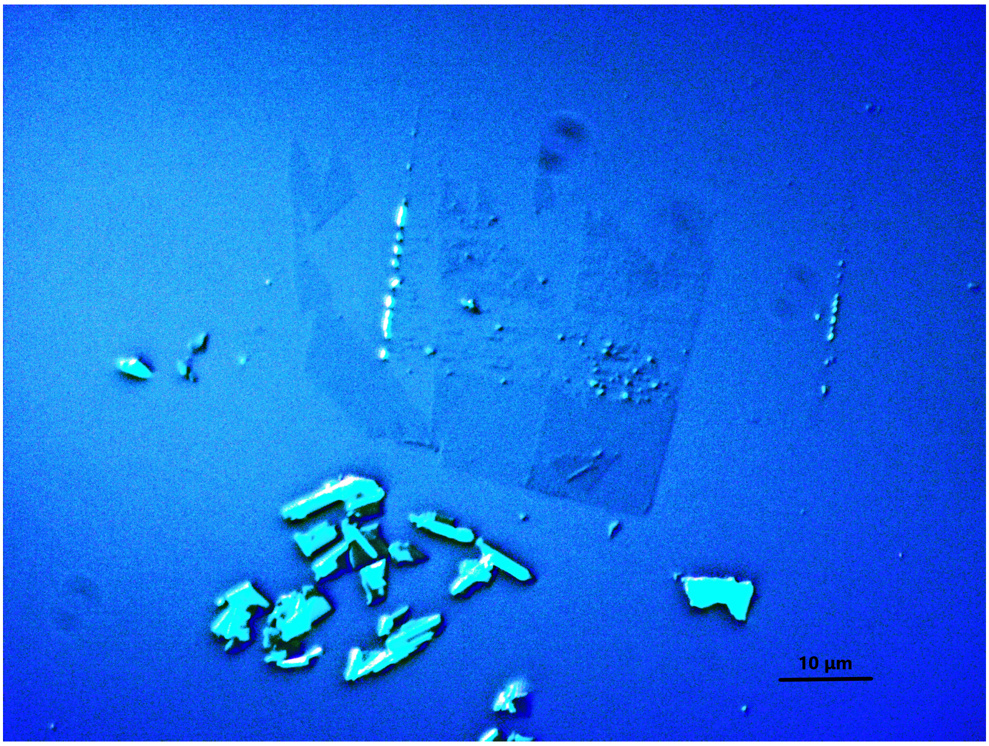

Figure 7.10: Image of the thin flake of h-BN (taken using a DIC optical microscope) after it was damaged when the AFM probe crashed and continued to scan. Distance between the two lines of piles of h-BN is 49.9 µm.

The scan continued for an hour after this, during which time the tip was pushed and dragged through the sample, the result of this is visible in Fig. 7.10. The error was spotted and the scan was restarted. There was some loss in lateral resolution due to the blunting of the tip, however, the tuning fork and cantilever were no worse for wear, the resonant frequency in free space and the Q-factor remained the same and the probe remained in use for several more scans. This demonstrates the robust nature of the Akiyama probe, it was bent upwards by 25 µm and remained usable afterwards.

This image (Fig. 7.10) shows that the h-BN has been cleanly scraped from the silicon dioxide surface leaving it in little piles at the end of the scan lines. This raises the possibility that our instrument, with the Akiyama probe, could be used for micromanipulation of h-BN devices (similar to those covered in chapter 6) in the future in order to isolate the active region from the rest of the flake. Micromanipulation of samples with an AFM tip is already a known process, however, being able to use the tip to perform AFM scans afterwards is not a common phenomenon. This has been performed by Island et al. [140], as an experimental method of thinning and exfoliating h-BN flakes, using a reflectance cantilever. They showed that only the AFM tip was required to do this, and not an entire AFM, their scratching was performed manually. It is not mentioned whether the tip was still usable for scanning after this process.

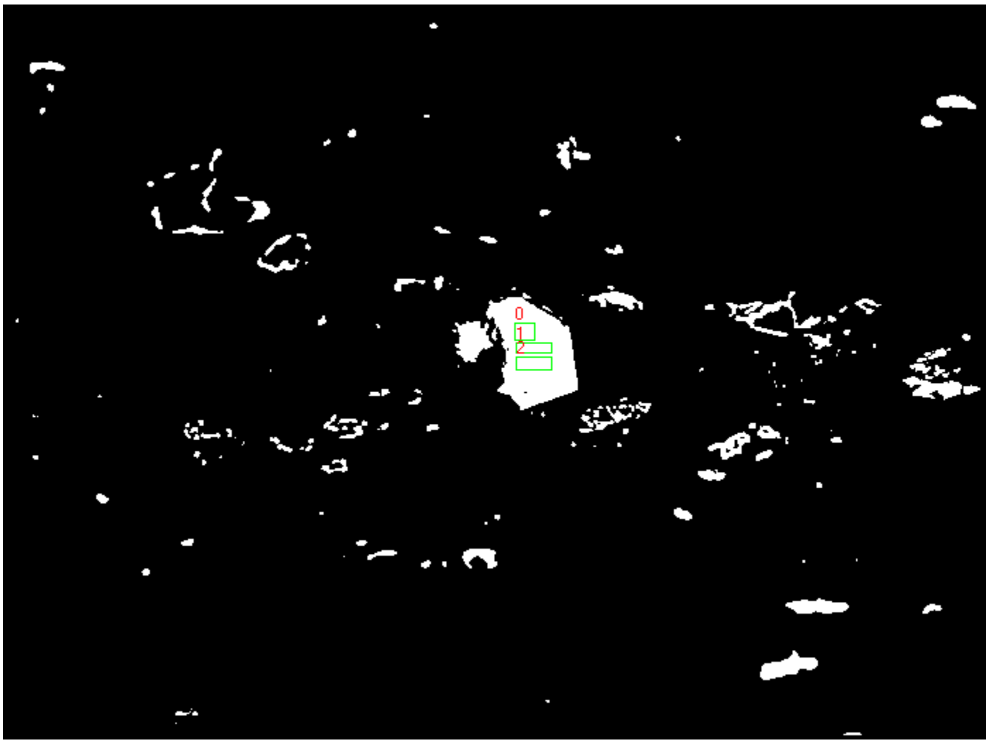

Figure 7.11: Image of the thick h-BN flake on which ellipsometric data was collected. Regions of interest are marked. The data fitted and referred to from here on in is from ROI 0. The image was taken at AOI 60^o with light wavelength 200 nm. The polarisers have been rotated to provide maximum contrast between the h-BN and the SiO_2 substrate.

7.5 Thick h-BN flake ellipsometry

The birefringent optical response of h-BN is known, but it has not been explored with photon energies at and above the band-gap. In order to do this, a thicker crystal of h-BN must be probed in order to ensure that the different refractive index in the z-direction has a noticeable effect on the data.

A large, clean flake was selected and regions of interest drawn upon it. Variable angle imaging spectroscopic ellipsometry (VA-iSE) was then performed on it. The wavelength was scanned from 190 nm to 300 nm in 2 nm steps, and then from 310 nm to 1000 nm in 10 nm steps. After each wavelength scan, the angle of incidence, the angle at which the probing light hits the sample with respect to the surface plane, was adjusted. This changes the polarisation change due to the change in travel in the vertical and horizontal planes and is performed to improve the modelling of the dielectric function and make the fitted data more certain. Data was collected at three angles, 50^o, 60^o and 70^o, providing three data sets all between 190 nm and 1000 nm. The data and resultant best fits derived from the final model are visible in Figs. 7.12, 7.13 and 7.14.

The dispersion models used are included in the Accurion software. They are either based on theoretically derived models or are non-physical models that work well over the wavelengths used.

A clean area of silicon dioxide, adjacent to the flake of h-BN, was measured

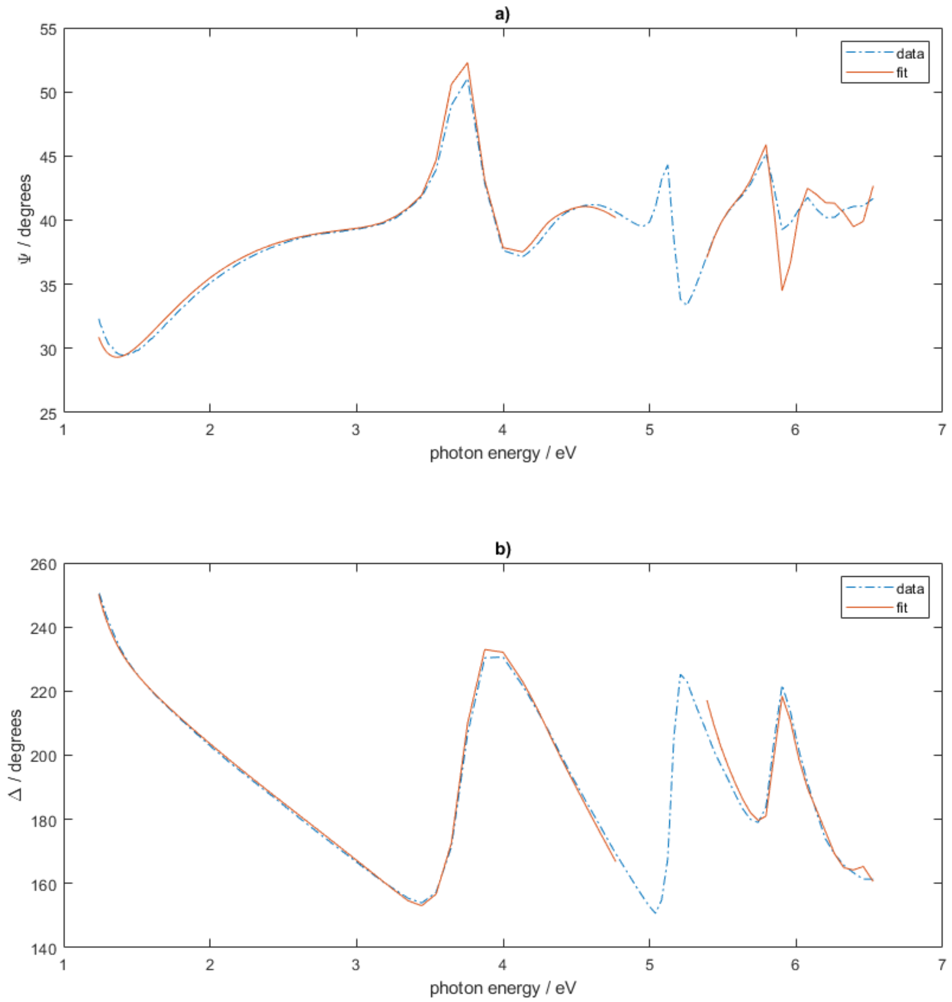

Figure 7.12: a) Ψ and b) Δ values and fits at 50^o angle of incidence onto the h-BN on SiO_2 on Si sample.

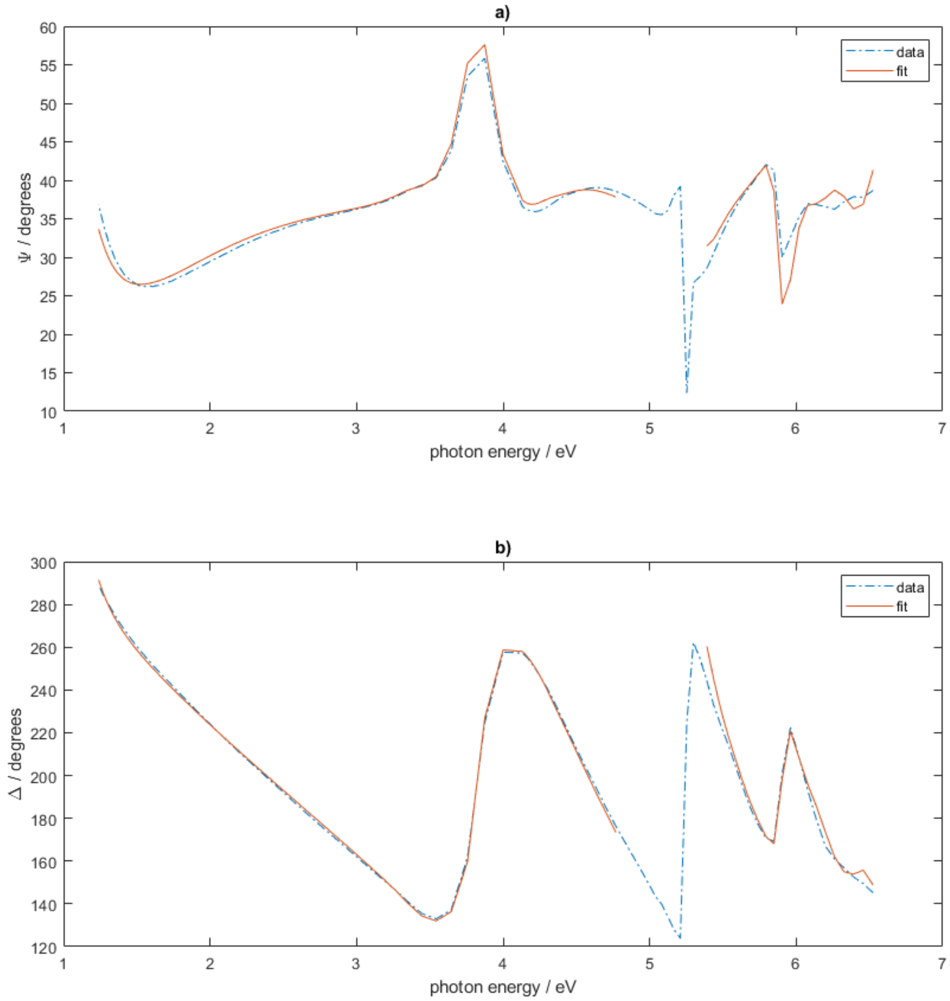

Figure 7.13: a) Ψ and b) Δ values and fits at 60^o angle of incidence onto the h-BN on SiO_2 on Si sample.

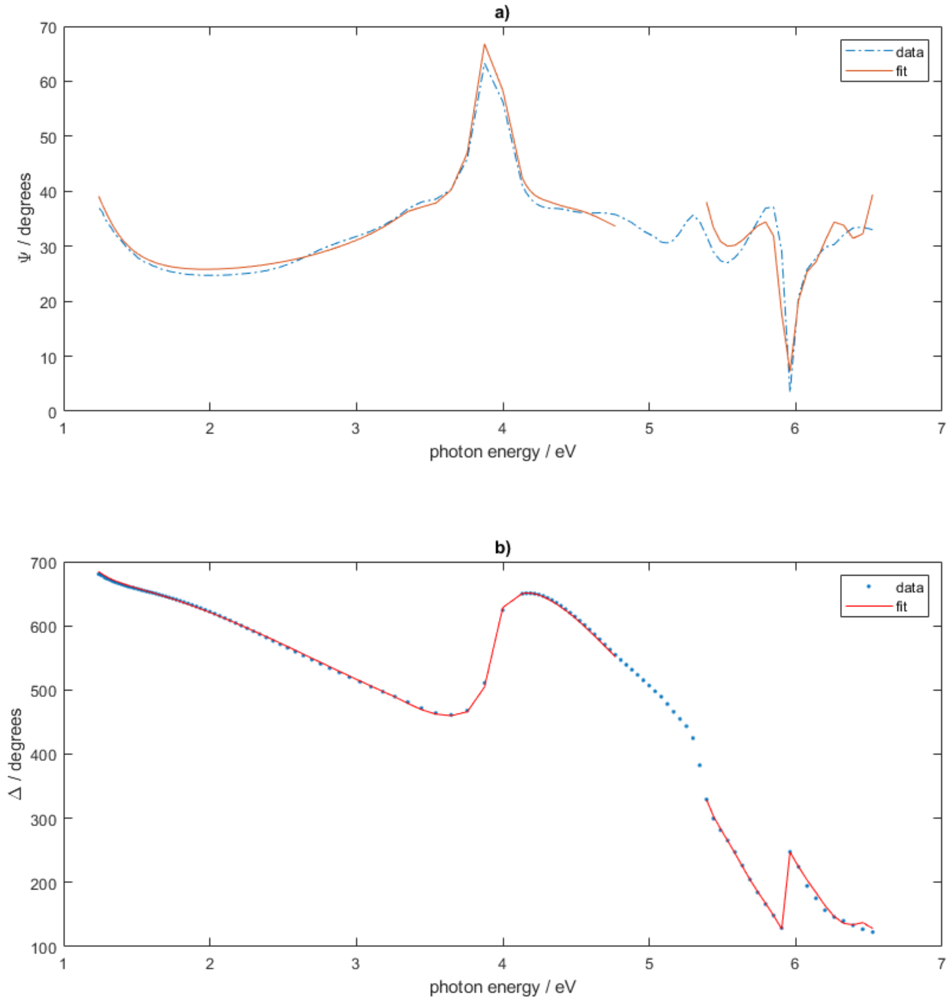

Figure 7.14: a) Ψ and b) Δ values and fits at 70^o angle of incidence onto the h-BN on SiO_2 on Si sample.

and fitted to a Sellmeier model of SiO_2 on Si. The fit from this model returned a SiO_2 layer thickness of 88 nm ± 0.6 nm and it defined the dielectric function of this particular batch of SiO_2 substrate. This data was then imported to the model and remained fixed for the rest of the h-BN data fitting process.

On all of the Ψ plots, in particular on the 50^o and 60^o data sets, are two sharp peaks, one at $\sim$4 eV and the other at just over 5 eV. These are resonances of the silicon dioxide layer. They are extremely sharp, making the data very difficult to measure accurately and therefore fit. As the spike in this region is definitely due to the silicon dioxide and, therefore, it was decided to omit a small range of data around 5 eV to allow the fitting to be more reliable.

The h-BN data was then imported and initial fits were tested at long wavelength values, far from the band edge. Cauchy equations are often able to fit well for materials at low energy, far from the band edge. In this case, an isotropic Cauchy approximation did not work. Funke et al. [137] provided details on an anisotropic Cauchy approximation for h-BN at long wavelength. Manual adjustment of the parameters, particularly for the thickness of the h-BN, allowed us to reproduce the Ψ and Δ data collected in the experiment for wavelength 500 nm - 1000 nm. The thickness was fine tuned using this method and then a Sellmeier approximation was fitted to the data in both the zz and the xy directions. The Sellmeier approximation is non-physical as it sets the extinction coefficient, k, to zero. This is forbidden by the Kramers-Kronig relations as k=0 would result in n=0 for all wavelengths, which is patently untrue. This approximation does, however, work in regions where k is very small, with values which are almost zero, as is in the case for h-BN with low energy photons. In the long wavelength regime, the non-physical Sellmeier model fits the behaviour of h-BN very well when a fixed real-epsilon ($\mathbb{R}\left(\tilde{\epsilon}\right) = 1$) term is included as standard to ensure that the high and low energy behaviour is correct and does not return non-physical values.

The Sellmeier model in xy and zz allows the thickness of the h-BN to be determined as well as the dielectric functions for the long wavelength region. Data down to 400 nm was then included, a good fit should mean that the fitting parameters do not change with the inclusion of the extra data, some fine tuning of the parameters was required to achieve this. At this point, the photon energy is approaching the band edge, where strong absorption occurs and so a more complex approximation is required to model the material.

It was noticeable that when optical viewing the similar flakes of h-BN on the substrate, rotating the polariser would cause some flakes to become more visible and others less so, the flakes having differing contrasts to the substrate. This is due to the different orientations of the crystal lattices. When photon energy was increased to the band-gap energy, all of the h-BN flakes became much more visible, as in fig. 7.8, an were uniformly highly contrasting with the substrate. This indicates that a great deal of reflection of the light from the h-BN was taking place, this in turn, indicating that much of the light was not penetrating the material along the vertical axis. With little light penetrating and returning vertically, very little of the Ψ and Δ data contains information about the absorption in the zz axis. This rendered it impossible to fit the vertical axis model whilst taking into account the absorption, accordingly, the Sellmeier approximation remained the best model developed for the vertical axis.

The photon energies used to probe the h-BN included and exceeded the band-gap, causing a peak in the data and leading to the expectation of a peak in the dielectric function at this value. It is therefore natural to use one of the models which would include such a peak, namely a Gaussian function or a Lorentzian function. Success has been achieved using a Gaussian function to model MBE-grown h-BN [134], however, the Gaussian did not fit this data, the peak was too broad. Possibly due to the heterogenity of the MBE flakes, the Gaussian fit was due to overlapping Lorentzians, attributable to areas of the flake. The increased homogeneity of these HPHT flakes means that the Lorentzian function is a better fit for the band edge peak. The Lorentzian and a fixed epsilon term were tested, but the behaviour above the band-gap was not quite correct, requiring a second Lorentzian term to correct. Various models were tried, some including the use of poles (narrow resonances), but none fit more satisfactorily than the one described in this chapter.

This model, using a Sellmeier and a fixed epsilon term in the zz and two Lorentzians and a fixed epsilon term in xy, was then best fitted by the software. All the parameters, except for the thicknesses and the fixed epsilon in the vertical axis model, were allowed to move in order to optimise the parameters to reduce the root mean squared error (RMSE).

The two Lorentzian functions used in the fit correspond to two absorption lines. One of these provides the peak at the critical point at the band-gap of h-BN, and the other is at a shorter wavelength just outside the range over which we are able to investigate.

The Sellmeier function is of the form,

$$n^2(\lambda) = 1 + \frac{B_1\lambda^2}{\lambda^2 - C_1} + \frac{B_2\lambda^2}{\lambda^2 - C_2} + \frac{B_3\lambda^2}{\lambda^2 - C_3} \tag{7.9}$$

where n is refractive index, λ is the photon wavelength and B and C are variable parameters. This is an example of a non-physical model that works for this purpose. In the fitting performed for this data, only one Sellmeier term was required.

The Lorentzian function is of the form,

$$\epsilon(E) = \frac{A}{E_0^2 - E^2 - i\Gamma E} \tag{7.10}$$

where E is the photon energy, A is the strength term, E_0 is the resonance energy and Γ is the damping.

There is no method by which to go from Ψ and Δ to a dielectric function for the material. For this reason, the fitting process involves giving initial values to the parameters of the model, which are used to calculate the Ψ and Δ values expected when light of the given wavelength is passed through the material layers of known thickness at a particular angle. These values are compared to the experimentally obtained data and the residual error of this is minimised by adjusting the coefficients of the model. This process returned the model described by equations 7.11, 7.12.

	best fit	+/-	unit
Layer thicknesses			
Silicon dioxide (SiO_2) layer	87.37	0.26	nm
Hexagonal boron-nitride (h-BN) layer	67.79	0.21	nm
zz model			
Sellmeier term B_1	1.495	0.021	1
Sellmeier term C_1	1.80E-2	7.5E-4	μm^2
Fixed epsilon$_1$ term ($\epsilon_{1,0}$)	1	0	1
xy model			
Lorentzian_0 frequency ($E_{0,0}$)	6.236	0.003	eV
Lorentzian_0 strength (A_0)	25.68	0.86	eV^2
Lorentzian_0 damping (Γ_0)	0.01998	0.003	eV
Lorentzian_1 frequency ($E_{0,1}$)	6.495	0.010	eV
Lorentzian_1 strength (A_1)	26.5	1.2	eV^2
Lorentzian_1 damping (Γ_1)	0.096	0.010	eV
Fixed epsilon$_1$ term ($\epsilon_{1,1}$)	3.245	0.018	1
RMSE	53.786		

Table 7.1: Best fit values of the coefficients of the function used to model ellipsometry data.

The parameters returned by the best-fitting process are displayed in Table 7.1.

It should be noted that the uncertainty values provided by the fitting software do not necessarily relate to the thickness of the physical sample. The uncertainty is that of these values providing the best fit to the Ψ andΔ data with this particular model and with the data collected in this experiment.

The best fit parameters from Table 7.1 are present in two equations, used to describe the material. One for vertical light propagation and one for propagation through the xz plane. The equations take the form,

$$\epsilon_{zz}(E) = 1 + \frac{B_1\left(\frac{hc}{E}\right)^2}{\left(\frac{hc}{E}\right)^2 - C_1} + \epsilon_{1,0} \tag{7.11}$$

and

$$\epsilon_{xy}(E) = \frac{A_0}{E_{0,0}^2 - E^2 - i\Gamma_0 E} + \frac{A_1}{E_{0,1}^2 - E^2 - i\Gamma_1 E} + \epsilon_{1,1} \tag{7.12}$$

where ϵ is the complex permittivity of h-BN in the specified direction and E is the photon energy in electron-volts. The values for the parameters can be found in Table 7.1.

The thick flake was then taken to the confocal microscope / AFM instrument in order to use the AFM to measure the height of the flake. The measured value was 65 nm ± 2 nm. This indicates that the value calculated when fitting the ellipsometry data is consistent with the AFM value.

These models provide values for $\tilde{\epsilon}$ for any wavelength of incident light, although these values are most reliable over the wavelengths used to collect the

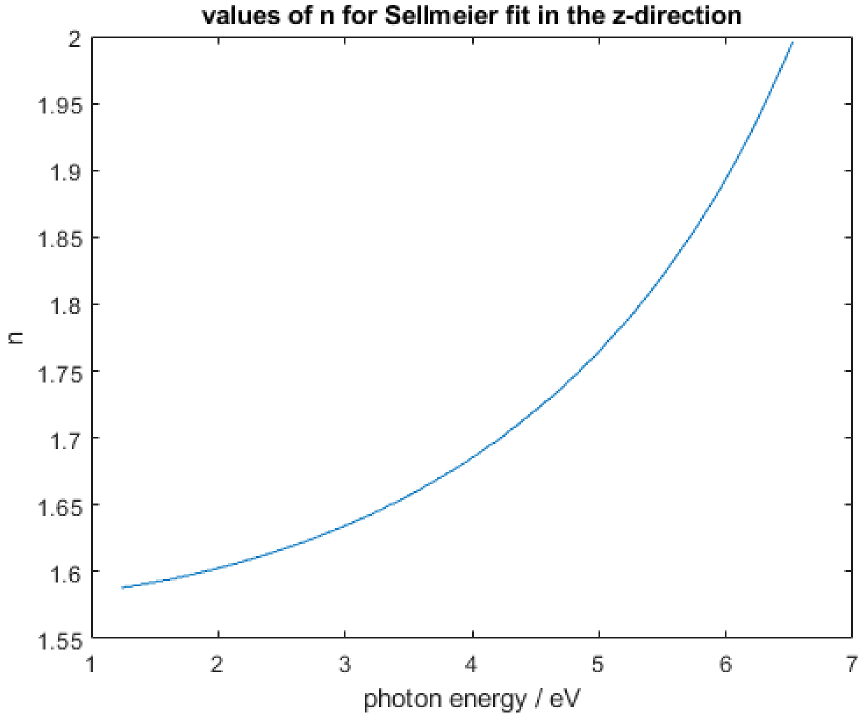

Figure 7.15: Refractive index of h-BN in the z direction.

data. The software can plot these in terms of n and k vs photon energy. These plots are visible in Fig. 7.15 and Fig. 7.16.

The graph for k, Fig. 7.16, shows that there is no absorption until the band-gap.

The refractive index data shows a large degree of birefringence in the h-BN flake, see Fig. 7.17. At low energy, n$_{zz}$=1.6 and n$_{xy}$=2, and by 6 eV, n$_{zz}$=1.9 and n$_{xy}$=4.12. This gives Δn=-2.22 at a 6 eV photon energy, making it an extremely birefringent material. The birefringence increases further above 6 eV, with a maximum value of Δn= $\sim$ -4. However, this further progression into far-UV reduced the reliability of the results due to the limitations of the equipment and the reduced sensitivity. There are currently no materials known of with a higher birefringence than h-BN in this result.

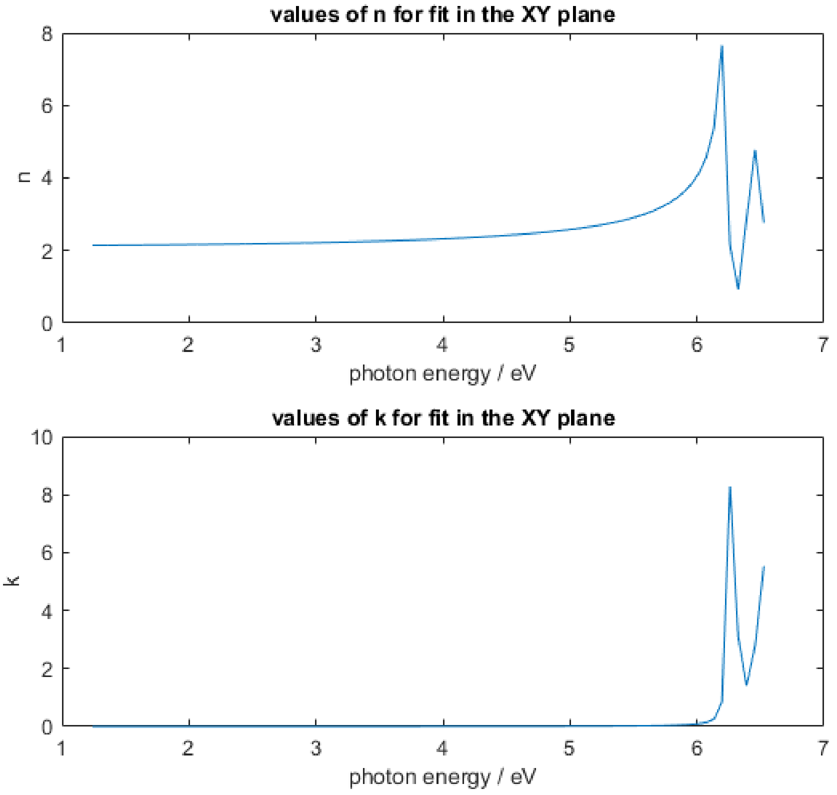

Figure 7.16: Refractive index and extinction coefficient of h-BN in the x-y plane.

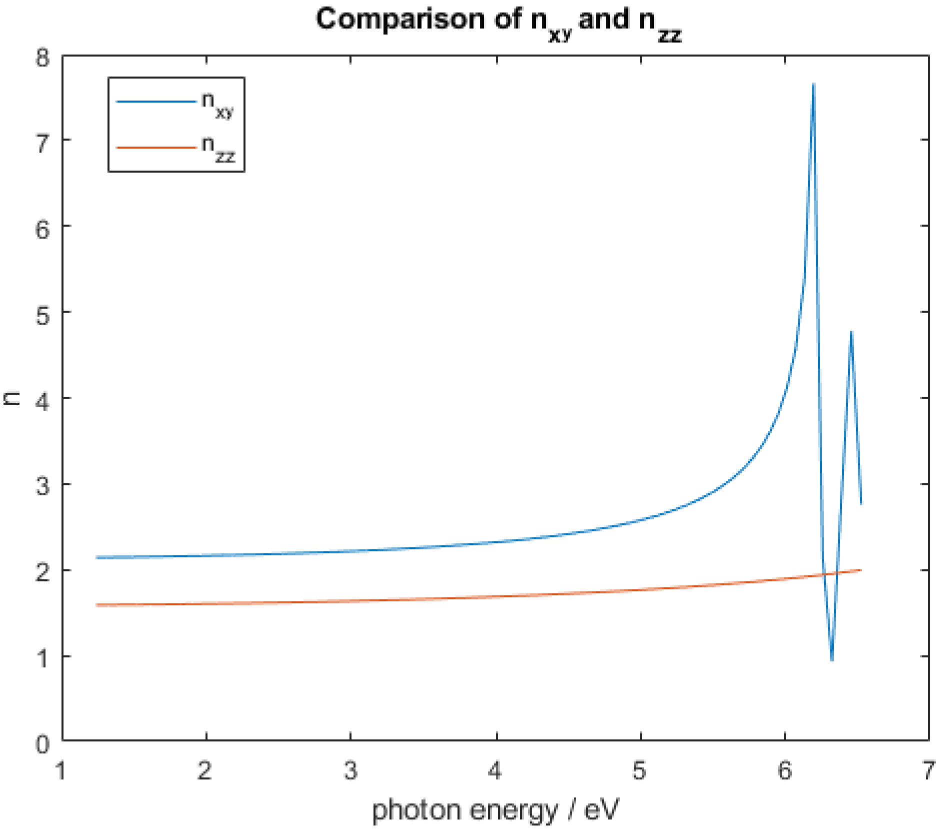

Figure 7.17: The two refractive indices of h-BN plotted on the same axes for comparison. A large spike in n_{xy} can be seen at the band-gap, it is at this value that the birefringence is expected to be largest, although measurements at 190 nm (6.5 eV) photon energy are likely to be less reliable due to the relative darkness of the light source and the reduced sensitivity of the camera at this wavelength.

7.6 Discussion

McKay [128] noted that the large charge inhomogeneity along the optical axis, i.e. through the layers in which the electrons are confined, means that excitons are tightly confined within the layers. This results in there being a larger oscillator strength for an electric field perpendicular to the optical axis. This causes an increase in n_o as photon energy approaches the band-gap of the material, but has very little contribution to n_e, resulting in the large birefringence. This large birefringence is confirmed by the data collected in this chapter, indeed the value was found to be larger than in any previous publication, due to the fact that the instrument used was able to measure with higher photon energy than before.

Segura [136] noted that higher purity h-BN is expected to have a higher anisotropy and therefore a higher birefringence. The h-BN used in this experiment is thought to be some of the purest samples produced anywhere in the world. This may also contribute to the extremely large birefringence measured using this method.

7.7 Summary

An 0.8 nm thick, highly pure, bilayer flake of h-BN was imaged on the ellipsometer, however, the flake was too thin to allow the optical properties to be measured. Under the confocal microscope, it interacted very weakly with green light, rendering it invisible on top of the silicon dioxide on silicon substrate. In photoluminescence detection mode, when it was illuminated with green light, the thin flake stood out strongly. The silicon dioxide remained dark, but the thin flake displayed photoluminescence, emitting red light from most areas of the flake, particularly the edges and the areas with more layers. This is largely attributable to dangling bonds on the edges of the flakes' layers, possible impurities adsorbed to the surface and defects formed where h-BN flakes meet.

A 67 nm thick flake of h-BN was measured on the imaging ellipsometer at different incidence angles and over a range of incident photon wavelengths (190 nm - 1000 nm), to determine the dielectric functions of the h-BN. Models describing the dielectric functions indicated that there is a high degree of birefringence in the material. The difference in refractive indices was found to be $\Delta\mathrm{n}$=-2.22 at 6 eV incident photon energy, with that value increasing further into the UV, up to the band-gap energy. This makes it one of the most birefringent materials discovered so far.

The values for degree of birefringence and the refractive index values, at 350 nm incident photons, agree with data presented by Funke et al. [137] (Δn=-0.5). The degree of birefringence also agrees with Segura et al., who found Δn=-1.8 at 5.6 eV incident photon energy.

Chapter 8

Conclusions and future work

8.1 Summary

At the beginning of my PhD studies, the goal was to build an NV$^-$ magnetometer, and whilst this has not yet been achieved, the instrument is, (a) ideally designed to become one, (b) close to being converted to one, and (c) an excellent measuring device in its own right.

The AFM has a large XY scan range and is capable of imaging surface step heights significantly higher than others whilst having a noise level of only 2 nm. The scans can be completed in a reasonable time as the scan speed is on a par with other AFMs, and loading and bringing the tip into contact with the sample has been made far more efficient with the use of the side camera which allows the tip to be quickly brought to within 'fine' approach distance to the sample. Both tapping mode and non-contact (FM-AFM) produce clear images.

The XYZ sample stage provides the scanning for the confocal microscope, which means that accurate and stable scans are performed in this operating mode. The photon detectors can detect emitters brighter than 50 cps when observing for an entire second, for brighter sources, >500 cps, they require only 5 ms counting. This provides great flexibility; scanning samples with very low emission intensity is possible, as is the fast scanning of brighter samples. The narrow focal plane of the microscope objective lens means it is possible to narrow down the location of an emitter to within 1 µm in the z-axis. The fast switching from reflectance scanning to photoluminescence or electroluminescence scanning allows data to be overlaid onto a visual image of the sample. This provides information on the location of an emitter to a precision of less than 500 nm.

The only remaining tasks to convert the instrument into an NV$^-$ magnetometer are to find a suitable diamond, attach it to an AFM tip and then to use the new magnet rotation system to find the defect orientation. The system has been proven to work when performing scanning, multipass AFM imaging, fluorescence detection, ODMR and laser pulsing on a test sample of diamonds containing NV$^-$ defects. Finding a nanodiamond, confirming that it contains a single defect and picking it up is a matter of a few days work, as soon as an appropriate nanodiamond comes along! The microwaves can be generated to such precision that, theoretically, the equipment should not be the limiting factor when the system is used for magnetic field detection.

Using this instrument to perform multiple imaging modes on a single sample is a fast process, limited only by scanning speed. Changing between AFM and confocal microscopy scanning requires only a couple of minutes to change which program is driving the sample scanning stages and to bring the tip into contact with the sample.

The instrument was used to image h-BN devices made by exfoliation at the University of Nottingham and was able to spatially isolate the source of the electroluminescent emission. To complement this information it also provided surface topography data of the region above the emitter, showing that the device bulged where it was heating up due to the tunnelling current. The instrument also detected photoluminescence from other areas of these devices and provided information on the spectrum of emission.

The instrument was used to detect photoluminescence from a bilayer of h-BN and although it was unable to measure the surface topography, it demonstrated that there is less dissipation of energy from the AFM cantilever over the h-BN than over the silicon dioxide.

The instrument measured the height of a thicker flake of h-BN, helping to confirm the validity of a fitted data set generated by the new imaging ellipsometer at the University of Nottingham. This imaging ellipsometer is unique in that it is the only one in the world which can probe samples with light with a wavelength as short as 190 nm. This is beyond the band-gap of h-BN allowing novel investigations to be performed and the refractive indices of this highly pure specimen of h-BN to be calculated. This led to the finding that h-BN has a birefringence of Δn=-2.2 at 6 eV photon energy increasing further into deep UV.

8.2 Future work

8.2.1 The instrument

There is much of room to develop the instrument further, starting with finding a single NV$^-$ defect and attaching it to an AFM tip. Magnetic fields can then be measured, beginning with known fields generated by a simple current carrying wire and then moving to unknown samples which require measurement. The sensitivity of the machine to magnetic fields can be measured and then improved upon by the use of microwave pulse sequencing or by selecting another nanodiamond with more NV$^-$ defects inside, trading off magnetic sensitivity for spatial resolution. With a bulk sample, if all of the defect orientations are measured this could provide vector magnetometry, providing information on the direction of the magnetic field at a particular location, as well as its magnitude.

At this point atom chips can be characterised, measuring the magnetic field in a three-dimensional space above the sample. This would allow the manufacture of these devices to become more efficient and improvements to happen at a greater rate.

Future directions and improvements to the instrument not associated with magnetometry might include the addition of a spectrometer to provide better spectral analysis of collected light. A spectrometer could be used to examine the photoluminescent light being emitted from the thin flake of h-BN, investigated in

Chapter 7. Possibly a secondary photon detector, such as a cooled CCD, could be installed to provide lower dark counts and allow detection of much darker light sources if scanning speed is not desired. Such an instrument might have aided in the measurement of electroluminescence from device D41 however the scan would have taken a long time.

In the near future, when an appropriate diamond is found, it should be possible to observe the Rabi oscillations of an NV^- defect by pulsing the laser for differing lengths of time whilst applying a CW microwave field to the sample. There appears to be endless room to continue experimenting with NV^- defects and with this instrument, e.g. measuring the magnetic domains of antiferromagnetic spintronic samples [1].

8.2.2 Ellipsometry

Future work involving the ellipsometric measurement of h-BN would involve taking high definition measurements of the silicon dioxide on which it is placed. This may help to fit the data around the sharp peaks and allow for a more complete model and more accurate data. If the h-BN is grown onto pure silicon, the need for this could be removed altogether.

Other samples of h-BN, grown by different methods, can be measured. This would provide more data on how the physical properties of the material change dependent on how it is produced.

The high energy capabilities of this ellipsometer mean there are a great number of avenues to explore. Prof. Beton's group at the University of Nottingham already has some samples of perylene-3,4,9,10-tetracarboxylic-3,4,9,10-diimide (PTCDI) which had been attached to flakes of hBN on a silicon chip [141]. This is a heterostructure of great interest to people in this area of research. Indium (III) selenide devices are also being produced at the University of Nottingham, and investigating the optical dispersion of this material is now possible using the EP4 ellipsometer.

8.3 Final conclusion

This instrument has been built from scratch, starting with the constituent parts of an AFM. Initial tests on different samples have been very promising, showcasing the instrument's ability, whilst also uncovering new information about certain materials. The instrument has the capability to open up several areas of exciting research including nanoscale imaging of the magnetic fields of atom chips or spintronic devices, and investigating single photon emission in van der Waals materials like h-BN.

Bibliography

[1] P. Wadley et al. Electrical switching of an antiferromagnet. *Science*, 351(6273):587–590, 2016.

[2] Jakob Reichel and Vladan Vuletić, editors. *Atom Chips.* Wiley-VCH, Boschstrasse 12,D-69469 Weinheim,Germany, 2011.

[3] A Trimeche, B Battelier, D Becker, A Bertoldi, P Bouyer, C Braxmaier, E Charron, R Corgier, M Cornelius, K Douch, et al. Concept study and preliminary design of a cold atom interferometer for space gravity gradiometry. *Classical and Quantum Gravity*, 36(21):215004, Oct 2019.

[4] Ron Folman, Philipp Treutlein, and Jörg Schmiedmayer. *Atom Chip Fabrication*, chapter 3, pages 61–117. John Wiley & Sons, Ltd, 2011.

[5] Mark Keil, Omer Amit, Shuyu Zhou, David Groswasser, Yonathan Japha, and Ron Folman. Fifteen years of cold matter on the atom chip: promise, realizations, and prospects. *Journal of Modern Optics*, 63(18):1840–1885, May 2016.

[6] Alexander Y. Meltzer, Eitan Levin, and Eli Zeldov. Direct reconstruction of two-dimensional currents in thin films from magnetic-field measurements. *Phys. Rev. Applied*, 8:064030, 2017.

[7] Seung Hee Lee. et al. Electroluminescence from h-bn by using al2o3/h-bn multiple heterostructure. *Opt. Express*, 27(14):19692–19701, Jul 2019.

[8] H Jiang and Joung-Yol Lin. Hexagonal boron nitride for deep ultraviolet photonic devices. *Semiconductor Science and Technology*, 29:084003, 06 2014.

[9] M Kawaguchi, K Nozaki, Y Kita, et al. Photoluminescence characteristics of BN(C, H) prepared by chemical vapour deposition. *Journal of Materials Science*, 26(14):3926–3930, July 1991.

[10] Sagar Bhandari and R. M. Westervelt. Imaging electron motion in graphene. *Semiconductor Science and Technology*, 32(2):024001, 2017.

[11] Zhongguang Xu, Hao Tian, Alireza Khanaki, and Renjing Zheng. Large-area growth of multi-layer hexagonal boron nitride on polished cobalt foils by plasma-assisted molecular beam epitaxy. *Scientific Reports*, 7(1):43100, 2017.

[12] S Morita, Franz J Giessibl, E Meyer, and R Wiesendanger, editors. *Non-contact Atomic Force Microscopy*, volume 3. Springer, Tiergartenstraße 17, 69121 Heidelberg, Germany, 6 2015.

[13] Shueei-Muh Lin, Chihng-Tsung Liauh, Wen-Rong Wang, and Shing-Huei Ho. Analytical solutions of the first three frequency shifts of afm non-uniform probe subjected to the lennard–jones force. *Ultramicroscopy*, 106(6):508 – 515, 2006.

[14] D. Sarid et al. Buckyball-substrate interactions probed by stm and afm. *Ultramicroscopy*, 42-44:610 – 615, 1992.

[15] Takeshi Fukuma, Takashi Ichii, Kei Kobayashi, Hirofumi Yamada, and Kazumi Matsushige. True-molecular resolution imaging by frequency modulation atomic force microscopy in various environments. *Applied Physics Letters*, 86(3):034103, 2005.

[16] Nanoworld. *USC-F5-k30, Ultra-Short Cantilevers (for High-Speed AFM).* NanoWorld AG Rue des Saars 10 CH-2000 Neuchâtel, Switzerland.

[17] Kislon K. Anharmonicity, solvation forces, and resolution in atomic force microscopy at the solid-liquid interface. *Physical review. E, Statistical, nonlinear, and soft matter physics*, 88:022407, 08 2013.

[18] Paul R. Gray, Paul J. Hurst, Stephen H. Lewis, and Robert G. Meyer. *Analysis and Design of Analog Integrated Circuits.* Wiley, Hoboken, New Jersey, 5 edition, Jan 2009.

[19] Maja Dukic, Vencislav Todorov, Santiago Andany, Adrian P. Nievergelt, Chen Yang, Nahid Hosseini, and Georg E. Fantner. Digitally controlled analog proportional-integral-derivative (pid) controller for high-speed scanning probe microscopy. *Review of Scientific Instruments*, 88(12):123712, 2017.

[20] Átila Madureira Bueno, José Manoel Balthazar, and José Roberto Castilho Piqueira. Phase-locked loop design applied to frequency-modulated atomic force microscope. *Communications in Nonlinear Science and Numerical Simulation*, 16(9):3835 – 3843, 2011.

[21] Nanosensors. *Akiyama-Probe (A-Probe) technical guide.* NANOSENSORS™ Rue des Saars 10 CH-2000 Neuchâtel Switzerland.

[22] M.E. Suddards. *Scanning Capacitance Microscopy in the Quantum Hall Regime.* PhD thesis, University of Nottingham, 7 2007.

[23] S. Stucklin, M. R. Gullo, T. Akiyama, and M. Scheidiger. Atomic force microscopy for industry with the akiyama-probe sensor. *IEEE explore*, pages 79–82, Feb 2008.

[24] PiezConcept. Lfhs3 nanopositioner. `http://www.piezoconcept.com/wp-content/uploads/2014/02/PAGE28-29-LFHS3.pdf`.

[25] R.J. Hocken, D.L. Trumper, and C. Wang. Dynamics and control of the uncc/mit sub-atomic measuring machine. *CIRP Annals*, 50(1):373 – 376, 2001.

[26] D. Amin-Shahidi, D.M. Ljubicic, J.L. Overcash, R.J. Hocken, and D.L. Trumper. High-accuracy atomic force microscope using a self-sensing probe. *Proceedings - ASPE Spring Topical Meeting on Control of Precision Systems, ASPE 2010*, 48:51–54, 01 2010.

[27] Bruker. Dimension fastscan the world's fastest afm. Bruker Nano Surfaces Division Santa Barbara, CA USA.

[28] Gaoliang Dai, Ludger Koenders, Jens Fluegge, and Matthias Hemmleb. Fast and accurate: high-speed metrological large-range AFM for surface and nanometrology. *Measurement Science and Technology*, 29(5):054012, apr 2018.

[29] Corinne E. Isaac, Elizabeth A. Curley, Paméla T. Nasr, Hoang L. Nguyen, and John A. Marohn. Cryogenic positioning and alignment with micrometer precision in a magnetic resonance force microscope. *Review of Scientific Instruments*, 89(1):013707, 2018.

[30] K. Chang, A. Eichler, J. Rhensius, L. Lorenzelli, and C. L. Degen. Nanoscale imaging of current density with a single-spin magnetometer. *Nano Letters*, 17(4):2367–2373, 2017.

[31] Frank Etzler and Jaroslaw Drelich. *Chapter 6. Atomic Force Microscopy for Characterization of Surfaces, Particles, and Their Interactions*, volume 4, pages 309–333. William Andrew, 12 2012.

[32] Marvin Minsky. Microscopy apparatus, 1961. US3013467A.

[33] Rachael L. Niederer, Divya Perumal, Trevor Sherwin, and Charles N. J. McGhee. Corneal Innervation and Cellular Changes after Corneal Transplantation: An In Vivo Confocal Microscopy Study. *Investigative Ophthalmology & Visual Science*, 48(2):621–626, 02 2007.

[34] Å. Flock, E. Scarfone, and M. Ulfendahl. Vital staining of the hearing organ: Visualization of cellular structure with confocal microscopy. *Neuroscience*, 83(1):215 – 228, 1998.

[35] Robert H Webb. Confocal optical microscopy. *Reports on Progress in Physics*, 59(3):427–471, mar 1996.

[36] Inc Semrock. 594nm laser brightline single-edge super-resolution, part number: Di03-r594-t1-25x36. `https://www.semrock.com/FilterDetails.aspx?id=Di03-R594-t1-25x36`. Semrock Inc, 3625 Buffalo Road, Suite 6, Rochesterr, New York 14624.

[37] Inc Semrock. 514nm stopline single-notch filter, part number: Nf03-514e-25. `https://www.semrock.com/FilterDetails.aspx?id=NF03-514E-25`. Semrock Inc, 3625 Buffalo Road, Suite 6, Rochesterr, New York 14624.

[38] Inc Semrock. 593 nm blocking edge brightline long-pass filter part number: Ff01-593/lp-25. `https://www.semrock.com/FilterDetails.aspx?id=FF01-593/LP-25`. Semrock Inc, 3625 Buffalo Road, Suite 6, Rochesterr, New York 14624.

[39] Excelitas. Spcm-aqrh-tr. `https://www.excelitas.com/file-download/download/public/60596?filename=Excelitas%20SPCM-AQRH-TR%20Family%20datasheet.pdf`.

[40] PicoQuant. Picoharp 300 datasheet. `https://www.picoquant.com/images/uploads/downloads/7304-picoharp300.pdf`.

[41] INC VORTRAN LASER TECHNOLOGY. Vortran laser technology, inc stradus® 514-60. `https://www.frlaserco.com/uploads/files/20180821134226_Stradus%20514-60.pdf`.

[42] Lilian Isabel Childress. *Coherent manipulation of single quantum systems in the solid state*. PhD thesis, Harvard University, Harvard University, Cambridge, Massachusetts, 03 2007.

[43] Emre Ismail Cengiz Togan. *Optical control of individual nitrogen-vacancy centers in diamond*. PhD thesis, Harvard University, Harvard University, Cambridge, Massachusetts, 12 2011.

[44] Tingting Lu, Xiaolei Li, Huaguo Zang, and Xiaolei Zhu. Comparison of high repetition rate Q-switched 355nm ultraviolet lasers with EOM and AOM. In Stefan Kaierle, Jingru Liu, and Jianlin Cao, editors, *2nd International Symposium on Laser Interaction with Matter (LIMIS 2012)*, volume 8796, pages 453 – 458. International Society for Optics and Photonics, SPIE, 2013.

[45] Thomas Oeckinghaus, Rainer Stöhr, Roman Kolesov, Julia Tisler, Friedemann Reinhard, and Jörg Wrachtrup. A compact, diode laser based excitation system for microscopy of nv centers. *Review of Scientific Instruments*, 85(7):073101, 2014.

[46] Toan Trong Tran et al. Quantum emission from hexagonal boron nitride monolayers, 2015.

[47] A Novanta Company Laser Quantum. gem high specification oem cw lasers. `https://www.laserquantum.com/download-ds.cfm?id=1102`.

[48] Eduardo HL Falcao and Fred Wudl. Carbon allotropes: beyond graphite and diamond. *Journal of Chemical Technology & Biotechnology*, 82(6):524–531, 2007.

[49] W. Zhu and Don R. Kania. *Defects in Diamond*, pages 175–239. Springer US, Boston, MA, 1995.

[50] Gordon Davies. *Basic Properties of Diamond: Phonon Spectra, Thermal Properties, Band Structure - CVD Diamond for Electronic Devices and Sensors*, chapter 1, pages 1–28. John Wiley & Sons, Ltd, 2009.

[51] F. Jelezko and J. Wrachtrup. Single defect centres in diamond: A review. *physica status solidi (a)*, 203(13):3207–3225, 2006.

[52] Ariful Haque and Sharaf Sumaiya. An overview on the formation and processing of nitrogen-vacancy photonic centers in diamond by ion implantation. *Journal of Manufacturing and Materials Processing*, 1:6, 08 2017.

[53] Derek F. Jackson Kimball Dmitry Budker, editor. *Optical Magnetometry.* Cambridge University Press, 2013.

[54] E van Oort, N B Manson, and M Glasbeek. Optically detected spin coherence of the diamond n-v centre in its triplet ground state. *Journal of Physics C: Solid State Physics*, 21(23):4385–4391, aug 1988.

[55] H.Y. Chen, E.R. MacQuarrie, and G.D. Fuchs. Orbital state manipulation of a diamond nitrogen-vacancy center using a mechanical resonator. *Physical Review Letters*, 120(16):167401, Apr 2018.

[56] Max Glasbeek Eric van Oort. Fluorescence detected level-anticrossing and spin coherence of a localized triplet state in diamond. *Chemical Physics*, 152(3):365 – 373, 1991.

[57] D. Redman, S. Brown, and S. C. Rand. Origin of persistent hole burning of n-v centers in diamond. *J. Opt. Soc. Am. B*, 9(5):768–774, May 1992.

[58] L J Rogers, S Armstrong, M J Sellars, and N B Manson. Infrared emission of the nv centre in diamond: Zeeman and uniaxial stress studies. *New Journal of Physics*, 10(10):103024, Oct 2008.

[59] M W Doherty, J Michl, F Dolde, I Jakobi, P Neumann, N B Manson, and J Wrachtrup. Measuring the defect structure orientation of a single NV-centre in diamond. *New Journal of Physics*, 16(6):063067, jun 2014.

[60] H. Hanzawa, Y. Nisida, and T. Kato. Measurement of decay time for the nv centre in ib diamond with a picosecond laser pulse. *Diamond and Related Materials*, 6(11):1595 – 1598, 1997.

[61] J H N Loubser and J A van Wyk. Electron spin resonance in the study of diamond. *Reports on Progress in Physics*, 41(8):1201–1248, aug 1978.

[62] G. D. Fuchs, V. V. Dobrovitski, R. Hanson, A. Batra, C. D. Weis, T. Schenkel, and D. D. Awschalom. Excited-state spectroscopy using single spin manipulation in diamond. *Phys. Rev. Lett.*, 101:117601, Sep 2008.

[63] Hiraku Toida et al. Electron paramagnetic resonance spectroscopy using a single artificial atom. *Communications Physics*, 2(1):33, Mar 2019.

[64] T Delord, L Nicolas, L Schwab, and G Hétet. Electron spin resonance from NV centers in dimonds levitating in an ion trap. *New Journal of Physics*, 19(3):033031, mar 2017.

[65] Viva R. Horowitz, Benjamín J. Alemán, David J. Christle, Andrew N. Cleland, and David D. Awschalom. Electron spin resonance of nitrogen-vacancy centers in optically trapped nanodiamonds. *Proceedings of the National Academy of Sciences*, 109(34):13493–13497, 2012.

[66] Romana Schirhagl, Kevin Chang, Michael Loretz, and Christian L. Degen. Nitrogen-vacancy centers in diamond: Nanoscale sensors for physics and biology. *Annual Review of Physical Chemistry*, 65(1):83–105, 2014.

[67] D. M. Toyli, D. J. Christle, A. Alkauskas, B. B. Buckley, C. G. Van de Walle, and D. D. Awschalom. Measurement and control of single nitrogen-vacancy center spins above 600 k. *Phys. Rev. X*, 2:031001, Jul 2012.

[68] D. Le Sage, K. Arai, D. R. Glenn, S. J. DeVience, L. M. Pham, L. Rahn-Lee, M. D. Lukin, A. Yacoby, A. Komeili, and R. L. Walsworth. Optical magnetic imaging of living cells. *Nature*, 496(7446):486–489, Apr 2013.

[69] K. Chakrabarti, R. Chakrabarti, K.K. Chattopadhyay, S. Chaudhuri, and A.K. Pal. Nano-diamond films produced from cvd of camphor. *Diamond and Related Materials*, 7(6):845 – 852, 1998.

[70] Katherine B Holt. Diamond at the nanoscale: applications of diamond nanoparticles from cellular biomarkers to quantum computing. *Philosophical Transactions of the Royal Society A: Mathematical, Physical and Engineering Sciences*, 365(1861):2845–2861, 2007.

[71] V. A. Plotnikov, S. V. Makarov, D. G. Bogdanov, and A. S. Bogdanov. The structure of detonation nanodiamond particles. *AIP Conference Proceedings*, 1785(1):040045, 2016.

[72] Nicolaie Moldovan, Ralu Divan, Hongjun Zeng, and John A. Carlisle. Nanofabrication of sharp diamond tips by e-beam lithography and inductively coupled plasma reactive ion etching. *Journal of Vacuum Science & Technology B: Microelectronics and Nanometer Structures Processing, Measurement, and Phenomena*, 27(6):3125–3131, 2009.

[73] Moloud Kaviani, Peter Deak, Bálint Aradi, Thomas Frauenheim, Jyh-Pin Chou, and Adam Gali. Proper surface termination for luminescent near-surface nv centers in diamond. *Nano letters*, 14:4772–4777, 07 2014.

[74] Jennifer M. Schloss, John F. Barry, Matthew J. Turner, and Ronald L. Walsworth. Simultaneous broadband vector magnetometry using solid-state spins. *Phys. Rev. Applied*, 10:034044, Sep 2018.

[75] Ilya P. Radko, Mads Boll, Niels M. Israelsen, Nicole Raatz, Jan Meijer, Fedor Jelezko, Ulrik L. Andersen, and Alexander Huck. Determining the internal quantum efficiency of shallow-implanted nitrogen-vacancy defects in bulk diamond. *Opt. Express*, 24(24):27715–27725, Nov 2016.

[76] Christopher Jeffrey Hartley. *The Surface Chemistry of Diamond.* PhD thesis, Royal School of Mines, Imperial College of Science and Technology, University of London, 9 1978.

[77] P. Maletinsky and V. Jacques. 10 - diamond magnetic sensors. In Steven Prawer and Igor Aharonovich, editors, *Quantum Information Processing with Diamond*, pages 240 – 263. Woodhead Publishing, 2014.

[78] S. Steinert, F. Dolde, P. Neumann, A. Aird, B. Naydenov, G. Balasubramanian, F. Jelezko, and J. Wrachtrup. High sensitivity magnetic imaging using an array of spins in diamond. *Review of Scientific Instruments*, 81(4):043705, 2010.

[79] Sungkun Hong, Michael S. Grinolds, Linh M. Pham, David Le Sage, Lan Luan, Ronald L. Walsworth, and Amir Yacoby. Nanoscale magnetometry with nv centers in diamond. *MRS Bulletin*, 38(2):155–161, 2013.

[80] Thomas Wolf, Philipp Neumann, Kazuo Nakamura, Hitoshi Sumiya, Takeshi Ohshima, Junichi Isoya, and Jörg Wrachtrup. Subpicotesla diamond magnetometry. *Phys. Rev. X*, 5:041001, Oct 2015.

[81] M. W. Doherty, J. Michl, F. Dolde, I. Jakobi, P. Neumann, N. B. Manson, and J. Wrachtrup. Measuring the defect structure orientation of a single NV^- centre in diamond. *New Journal of Physics*, 16(6):063067, June 2014.

[82] Sebastain K.H. Andersen, Shailesh Kumar, and Sergey I. Bozhevolnyi. Coupling of nitrogen-vacancy centers in a nanodiamond to a silver nanocube. *Opt. Mater. Express*, 6(11):3394–3406, Nov 2016.

[83] R. Hanbury Brown and R. Q. Twiss. A Test of a new type of stellar interferometer on Sirius. *Nature*, 178:1046–1048, 1956.

[84] Akio Yamanaka Eiichi Hanamura, Yutaka Kawabe. *Quantum Nonlinear Optics*. Springer Science & Business Media, July 2007.

[85] L. Rondin, J.-P. Tetienne, P. Spinicelli, C. Dal Savio, K. Karrai, G. Dantelle, A. Thiaville, S. Rohart, J.-F. Roch, and V. Jacques. Nanoscale magnetic field mapping with a single spin scanning probe magnetometer. *Applied Physics Letters*, 100(15):153118, 2012.

[86] M. H. Anderson, J. R. Ensher, M. R. Matthews, C. E. Wieman, and E. A. Cornell. Observation of bose-einstein condensation in a dilute atomic vapor. *Science*, 269(5221):198–201, 1995.

[87] Andreas Bauch. Caesium atomic clocks: function, performance and applications. *Measurement Science and Technology*, 14(8):1159–1173, jul 2003.

[88] Jiahao Huang, Shuyuan Wu, Honghua Zhong, and Chaohong Lee. Quantum metrology with cold atoms. *Annual Review of Cold Atoms and Molecules*, page 365–415, Mar 2014.

[89] R. Chang, A. L. Hoendervanger, Q. Bouton, Y. Fang, T. Klafka, K. Audo, A. Aspect, C. I. Westbrook, and D. Clément. Three-dimensional laser cooling at the doppler limit. *Phys. Rev. A*, 90:063407, Dec 2014.

[90] Harold J Metcalf and Peter van der Straten. *Laser Cooling and Trapping.* Springer, Springer Nature Switzerland AG Picassoplatz 4 CH-4052 Basel Switzerland, 1999.

[91] R J Sewell, J Dingjan, F Baumgärtner, I Llorente-García, S Eriksson, E A Hinds, G Lewis, P Srinivasan, Z Moktadir, C O Gollasch, and et al. Atom chip for bec interferometry. *Journal of Physics B: Atomic, Molecular and Optical Physics*, 43(5):051003, Feb 2010.

[92] Mark Keil, Omer Amit, Shuyu Zhou, David Groswasser, Yonathan Japha, and Ron Folman. Fifteen years of cold matter on the atom chip: promise, realizations, and prospects. *Journal of Modern Optics*, 63(18):1840–1885, May 2016.

[93] Patrick Maletinsky, S Hong, Michael Grinolds, Birgit Hausmann, M Lukin, R. Walsworth, Marko Loncar, and Amir Yacoby. A robust scanning diamond sensor for nanoscale imaging with single nitrogen-vacancy centres. *Nature nanotechnology*, 7:320–4, 04 2012.

[94] Kevin Kai Chang. *Scanning Magnetometry with NV Centers in Diamond.* PhD thesis, ETH Zurich, ETH Zurich, Rämistrasse 101, 8092 Zürich, Switzerland, 2016.

[95] Felix M. Stürner. et al. Compact integrated magnetometer based on nitrogen-vacancy centres in diamond. *Diamond and Related Materials*, 93:59 – 65, 2019.

[96] James L. Webb, Joshua D. Clement, Luca Troise, Sepehr Ahmadi, Gustav Juhl Johansen, Alexander Huck, and Ulrik L. Andersen. Nanotesla sensitivity magnetic field sensing using a compact diamond nitrogen-vacancy magnetometer. *Applied Physics Letters*, 114(23):231103, 2019.

[97] Kento Sasaki, Yasuaki Monnai, Soya Saijo, Ryushiro Fujita, Hideyuki Watanabe, Junko Ishi-Hayase, Kohei M. Itoh, and Eisuke Abe. Broadband, large-area microwave antenna for optically detected magnetic resonance of nitrogen-vacancy centers in diamond. *Review of Scientific Instruments*, 87(5):053904, 2016.

[98] Xiangyang Xu, Zhiming Yu, Yongwei Zhu, and Baichun Wang. Influence of surface modification adopting thermal treatments on dispersion of detonation nanodiamond. *Journal of Solid State Chemistry*, 178(3):688 – 693, 2005.

[99] R. D. Strattan and F. J. Young. Fields in square helmholtz coils. *Applied Scientific Research, Section B*, 9(2):117–124, Mar 1961.

[100] E. R. Javor and T. Anderson. Design of a helmholtz coil for low frequency magnetic field susceptibility testing. In *1998 IEEE EMC Symposium. International Symposium on Electromagnetic Compatibility. Symposium Record (Cat. No.98CH36253)*, volume 2, pages 912–917 vol.2, Aug 1998.

[101] M. E. Rudd and J. R. Craig. Optimum Spacing of Square and Circular Coil Pairs. *Review of Scientific Instruments*, 39:1372–1374, September 1968.

[102] C. C. Finlay, S. Maus, C. D. Beggan, T. N. Bondar, et al. International Geomagnetic Reference Field: the eleventh generation. *Geophysical Journal International*, 183(3):1216–1230, 12 2010.

[103] Berkley Nucleonics Corporation. Model 845 rf / microwave signal generator. `https://www.berkeleynucleonics.com/sites/default/files/products/datasheets/845_datasheet_v2.59.pdf`, 2019.

[104] Swabian Instruments. Pulse streamer 8/2 documentation release 1.1. `https://www.swabianinstruments.com/static/documentation/PulseStreamer/PulseStreamer_User_Manual.pdf`, 8 2019.

[105] Jan M. Binder et al. Qudi: A modular python suite for experiment control and data processing. *SoftwareX*, 6:85 – 90, 2017.

[106] David Nečas and Petr Klapetek. Gwyddion: an open-source software for SPM data analysis. *Central European Journal of Physics*, 10:181–188, 2012.

[107] Dr. Roland Yingjie Tay. *Chemical Vapor Deposition Growth and Characterization of Two-Dimensional Hexagonal Boron Nitride*. Springer Theses, Singapore, 2018.

[108] G. Cassabois, P. Valvin, and B. Gil. Hexagonal boron nitride is an indirect bandgap semiconductor. *Nature Photonics*, 10(4):262–266, Jan 2016.

[109] Feipeng Sun, Zhuoran Hao, Guozhen Liu, Chenping Wu, Shiqiang Lu, Shengrong Huang, Chuan Liu, Qiming Hong, Xiaohong Chen, Duanjun Cai, and Junyong Kang. p-type conductivity of hexagonal boron nitride as a dielectrically tunable monolayer: modulation doping with magnesium. *Nanoscale*, 10:4361–4369, 2018.

[110] Yi-min Ding, Jun-jie Shi, Min Zhang, Xin-he Jiang, Hong-xia Zhong, Pu Huang, Meng Wu, and Xiong Cao. Improvement of n-type conductivity in hexagonal boron nitride monolayers by doping, strain and adsorption. *RSC Adv.*, 6:29190–29196, 2016.

[111] Toan Trong Tran et al. Quantum emission from hexagonal boron nitride monolayers. *Nature Nanotechnology*, 11(1):37–41, Jan 2016.

[112] Annemarie L. Exarhos, David A. Hopper, Richard R. Grote, Audrius Alkauskas, and Lee C. Bassett. Optical signatures of quantum emitters in suspended hexagonal boron nitride. *ACS Nano*, 11(3):3328–3336, 2017.

[113] U. D. Dzhuzeev and P. E. Ramazanov. Photoluminescence spectra of boron nitride activated by certain elements. *Soviet Physics Journal*, 12(7):890–893, Jul 1969.

[114] Bipin Kumar Gupta, Satbir Singh, Garima Kedawat, Kanika, Pawan Kumar, Amit Kumar Gangwar, Tharangattu N. Narayanan, Angel A. Marti, Robert Vajtai, and P. M. Ajayan. A novel electroluminescent device based on a reduced graphene oxide wrapped phosphor (zns:cu,al) and hexagonal-boron nitride for high-performance luminescence. *Nanoscale*, 9:5002–5008, 2017.

[115] Andrey K. Geim and Allan H. MacDonald. Graphene: Exploring carbon flatland. *Physics Today*, 60(8), 8 2007.

[116] Mark Zastrow. Meet the crystal growers who sparked a revolution in graphene electronics. *Nature*, 572(7770):429–432, Aug 2019.

[117] Simon A. Svatek et al. Triplet excitation and electroluminescence from a supramolecular monolayer embedded in a boron nitride tunnel barrier. *Nano Letters*, 20(1):278–283, 2020. PMID: 31821763.

[118] James L Wilbur, Amit Kumar, Hans A Biebuyck, Enoch Kim, and George M Whitesides. Microcontact printing of self-assembled monolayers: applications in microfabrication. *Nanotechnology*, 7(4):452–457, dec 1996.

[119] James Kerfoot. *The Growth and Fluorescence of Organic Monolayers and Heterostructures*. PhD thesis, University of Nottingham, School of Physics & Astronomy, The University of Nottingham, NG7 2RD, July 2018.

[120] Ryan Beams, Palash Bharadwaj, and Lukas Novotny. Electroluminescence from graphene excited by electron tunneling. *Nanotechnology*, 25(5):055206, jan 2014.

[121] Accurion. Nanofilm ep4. `https://www.accurion.com/thin-film-characterization-imaging-ellipsometry/nanofilm_ep4`, 2019.

[122] Lichao Guan, Jiexiong Ding, Li Du, Achyut Adhikari, and Anand Krishna Asundi. Spectroscopic imaging ellipsometry for thin film detection on uniaxial crystal. *Proceedings of SPEI*, 10449:377 – 384, 2017.

[123] Harand Tompkins Eugene A Irene. *Handbook of Ellipsometry*. William Andrew, 01 2005.

[124] D.V. Likhachev, N. Malkova, and L. Poslavsky. Modified tauc–lorentz dispersion model leading to a more accurate representation of absorption features below the bandgap. *Thin Solid Films*, 589:844 – 851, 2015.

[125] Maria Losurdo et al. Spectroscopic ellipsometry and polarimetry for materials and systems analysis at the nanometer scale: state-of-the-art, potential, and perspectives. *Journal of Nanoparticle Research*, 11(7):1521–1554, Oct 2009.

[126] A. J. Gatesman, R. H. Giles, and J. Waldman. Submillimeter optical properties of hexagonal boron nitride. *Journal of Applied Physics*, 73(8):3962–3966, 1993.

[127] Ronald Driggers Craig Hoffman. *Encyclopedia of Optical and Photonic Engineering.* Taylor & Francis, Boca Raton, FL, 2nd edition edition, 09 2015.

[128] M. A. McKay, J. Li, J. Y. Lin, and H. X. Jiang. Anisotropic index of refraction and structural properties of hexagonal boron nitride epilayers probed by spectroscopic ellipsometry. *Journal of Applied Physics*, 127(5):053103, 2020.

[129] A. Maity, T. C. Doan, J. Li, J. Y. Lin, and H. X. Jiang. Realization of highly efficient hexagonal boron nitride neutron detectors. *Applied Physics Letters*, 109(7):072101, 2016.

[130] T. Q. P. Vuong, G. Cassabois, P. Valvin, A. Ouerghi, Y. Chassagneux, C. Voisin, and B. Gil. Phonon-photon mapping in a color center in hexagonal boron nitride. *Phys. Rev. Lett.*, 117:097402, Aug 2016.

[131] Kenji Watanabe, Takashi Taniguchi, and Hisao Kanda. Direct-bandgap properties and evidence for ultraviolet lasing of hexagonal boron nitride single crystal. *Nature Materials*, 3(6):404–409, Jun 2004.

[132] Andrea Crovetto, Patrick Rebsdorf Whelan, Ruizhi Wang, Miriam Galbiati, Stephan Hofmann, and Luca Camilli. Nondestructive thickness mapping of wafer-scale hexagonal boron nitride down to a monolayer. *ACS Applied Materials & Interfaces*, 10(30):25804–25810, 2018.

[133] Y. Rah, Y. Jin, S. Kim, and K. Yu. Birefringence and dispersion analysis of hexagonal boron nitride (h-bn). In *2019 Conference on Lasers and Electro-Optics (CLEO)*, pages 1–2, May 2019.

[134] T Q P Vuong et al. Deep ultraviolet emission in hexagonal boron nitride grown by high-temperature molecular beam epitaxy. *2D Materials*, 4(2):021023, mar 2017.

[135] Yoonhyuk Rah, Yeonghoon Jin, Sejeong Kim, and Kyoungsik Yu. Optical analysis of the refractive index and birefringence of hexagonal boron nitride from the visible to near-infrared. *Opt. Lett.*, 44(15):3797–3800, Aug 2019.

[136] A. Segura, L. Artús, R. Cuscó, T. Taniguchi, G. Cassabois, and B. Gil. Natural optical anisotropy of h-bn: Highest giant birefringence in a bulk crystal through the mid-infrared to ultraviolet range. *Phys. Rev. Materials*, 2:024001, Feb 2018.

[137] S. Funke, U. Wurstbauer, B. Miller, A. Matković, A. Green, A. Diebold, C. Röling, and P.H. Thiesen. Spectroscopic imaging ellipsometry for automated search of flakes of mono- and n-layers of 2d-materials. *Applied Surface Science*, 421:435 – 439, 2017. 7th International Conference on Spectroscopic Ellipsometry.

[138] Olaf Stenzel. *The Kramers-Kronig Relations*, pages 85–93. Springer International Publishing, Cham, 2016.

[139] S. J.and others Haigh. Cross-sectional imaging of individual layers and buried interfaces of graphene-based heterostructures and superlattices. *Nature Materials*, 11(9):764–767, Sep 2012.

[140] Joshua O. Island et al. Mechanical manipulation and exfoliation of boron nitride flakes by micro-plowing with an afm tip, 2015.

[141] James Kerfoot et al. Substrate-induced shifts and screening in the fluorescence spectra of supramolecular adsorbed organic monolayers. *The Journal of Chemical Physics*, 149(5):054701, 2018.